Molecular Gas in Nearby Merging and Interacting Galaxies

MOLECULAR GAS IN NEARBY MERGING AND INTERACTING GALAXIES: THE WHIRLPOOL GALAXY (M51) AND THE ANTENNAE GALAXIES (NGC 4038/39)

By
Maximilien R. P. Schirm, B.Sc., M.Sc.

A Thesis
Submitted to the School of Graduate Studies
in Partial Fulfillment of the Requirements
for the Degree of

Doctor of Philosophy

McMaster University

DOCTOR OF PHILOSOPHY (2015) McMaster University
(Physics and Astronomy) Hamilton, Ontario

TITLE: Molecular Gas in Nearby Merging and Interacting Galaxies: the Whirlpool Galaxy (M51) and the Antennae Galaxies (NGC 4038/39)

AUTHOR: Maximilien R. P. Schirm, B.Sc. (University of Waterloo), M.Sc. (McMaster University)

SUPERVISOR: Professor Christine Wilson

NUMBER OF PAGES: xvi, 184

Abstract

I present a spectroscopic study of the molecular gas in the Whirlpool Galaxy (M51) and the Antennae Galaxies (NGC 4038/39) using data from the Herschel Space Observatory (*Herschel*) and the Atacama Large Millimeter/submillimeter Array (ALMA). Using data from the *Herschel* Spectral and Photometric Imaging REceiver (SPIRE) Fourier Transform Spectrometer (FTS), I perform an excitation analysis to determine the physical characteristics (temperature, density, column density) of the cold and warm molecular gas across both systems. I do not find significant variation in the cold molecular gas across an individual system or between the systems. The warm molecular gas temperature is greater in NGC 4038/39 than in M51, while the density in both M51 and the nucleus of NGC 4038 is greater than the rest of the Antennae system. Both galaxies exhibit a similar fraction of warm to cold molecular gas. I compare *Herschel* SPIRE-FTS data to models of photon dominated regions (PDRs) to determine the strength of the background far ultraviolet field (G_0) within both systems and find little variation across each system. I find that PDRs alone can explain the observed *Herschel* SPIRE-FTS data in both systems.

Using ALMA observations of dense molecular gas tracers in NGC 4038/39, I investigate the physical processes affecting the dense molecular gas. Ratios of various molecular gas tracers suggest that the contributions of mechanical heating relative to PDR heating are similar across the entire system. The dense gas fraction in the nucleus of NGC 4038 and the nucleus of NGC 4039 is higher than in the overlap region, which I attribute to an increase in the stellar potential within the two nuclei. Furthermore, I find evidence for an increased cosmic ray rate in the overlap region of NGC 4038/39 relative to the two nuclei, which I attribute to an increased supernova rate in the overlap region.

Most of the molecular gas in M51 and NGC 4038/39 is in the form of PDRs, while the increased temperature of the warm molecular gas in NGC

4038/39 compared to M51 is likely due to an increase in the mechanical heating from both supernova and stellar winds and the ongoing merger. Furthermore, a comparison of these results to previous studies of the interacting galaxy M82 and the late-stage merger Arp 220 suggests that mergers and interactions have a greater effect on the warm molecular gas compared to the cold molecular gas. The results from this thesis help to further our understanding of the effects of merging and interacting galaxies on molecular gas, while helping understand differences between interacting galaxies and merging galaxies.

To my wife

Co-Authorship

The central chapters of this thesis are a culmination of original scientific research written by myself, Maximilien R. P. Schirm. Chapter 2 has been published in the peer-reviewed journal The Astrophysical Journal (ApJ), with the following reference

Schirm, M. R. P., Wilson, C. D., Parkin, T. J., Kamenetzky, J., Glenn, J., Rangwala, N., Spinoglio, L., Pereira-Santaella, M., Baes, M., Barlow, M. J., Clements, D. L., Cooray, A., De Looze, I., Karczewski, O. L., Madden, S. C., Rémy-Ruyer, A., Wu, R., 2014, ApJ, Volume 781, Issue 2, article id. 101, 24 pages

The second author, Dr. Christine D. Wilson, is my supervisor. The third author, Dr, Tara J. Parkin, provided the CO $J = 3-2$ data cube used in this paper, from which I created the convolved CO $J = 3-2$ moment maps used throughout the paper. Dr. Julia Kamenetzky provided the single-component Bayesian likelihood code, which I modified to perform the iterative two-component fit. I participated in weekly teleconferences with Dr. Jason Glenn, Dr. Naseem Rangwala, Dr. Luigi Spinoglio and Dr. Miguel Pereira-Santaella, along with Dr. Wilson and Dr. Kamenetzky. Throughout these teleconferences, I engaged in discussion regarding the paper with these authors, who in addition provided comments on the written manuscript. Finally, I, along with all of the aforementioned authors. are members of SPIRE Special Astronomy Group 2 (SAG2), whose policy is to circulate drafts to the entire collaboration before publication. The remaining co-authors are members of SAG2 and provided comments on the manuscript, while they did not perform any additional analysis.

Chapter 3 has been prepared for submission to the peer-reviewed journal Monthly Notices of the Royal Astronomical Society (MNRAS). At the time of the submission of this thesis, it is in circulation within SAG2 for comments per the SAG2 policy. The current planned author list is as follows

Schirm, M. R. P., Wilson, C. D., Parkin, T. J., Glenn, J., Kamenetzky, J.,

Maloney, P., Rangwala, N., Spinoglio, L.
Once again, Dr. Christine D. Wilson, my supervisor, is the second author. Dr. Tara J. Parkin once again provided the CO $J = 3 - 2$ data cube, which I reduced into the convolved moment maps. Dr. Parkin also provided the schematic of M51 from her previous work which I used to derive the regions in this paper. In addition, Dr. Parkin provided the derived total-infrared luminosity map used in this work. I used the single-component Bayesian likelihood code provided by Dr. Julia Kamenetzky, as in Chapter 2. Finally, Dr. Jason Glenn, Dr. Phil Maloney, Dr. Naseem Rangwala and Dr. Luigi Spinoglio, along with Dr. Wilson and Dr. Kamenetzky, participated in discussions via teleconference with me regarding the paper, and provided comments on the written manuscript.

Chapter 4 has been prepared for submission to the peer-reviewed journal ApJ. The currently proposed author list is as follows
Schirm, M. R. P., Wilson, C .D.
Dr. Christine D. Wilson is my supervisor.

All of the material presented in this paper has been formatted to conform to the required thesis style as dictated by the School of Graduate Studies and McMaster University. I grant an irrevocable, non-exclusive license to McMaster University and the National Library of Canada to reproduce this material as part of this thesis.

Table of Contents

List of Figures

List of Tables

List of Acronyms

2MASS Two Micron All-Sky Survey

AD Anderson-Darling

AGN Active Galactic Nucleus

ALMA Atacama Large Millimeter/submillimeter Array

CASA Common Astronomy Software Package

CDF Cumulative Distribution Function

FIR Far InfraRed

FTS Fourier Transform Spectrometer

FUV Far UltraViolet

FWHM Full-Width Half-Maximum

GALEX GALaxy Evolution eXplorer

GMA Giant Molecular Association

GMC Giant Molecular Cloud

HIFI Heterodyne Instrument for the Far Infrared

HIPE Herschel Interactive Processing Environment

HPBW Half-Power Beam Width

HST Hubble Space Telescope

IAR Interaction Region

IR Infrared

IRAM Institut de Radioastronomie Millimétric

IRS Infrared Spectrograph

ISM Interstellar Medium

ISO Infrared Space Observatory

ISO-LWS Infrared Space Observatory Long-Wavelength Spectrometer

ISOCAM Infrared Space Observatory CAMera

JCMT James Clerk Maxwell Telescope

KAO Kuiper Airborne Observatory

KS Kolmogorov-Smirnov

LAMDA Leiden Atomic and Molecular Database

LVG Large Velocity Gradient

LINER Low Ionization Nuclear Emission Region

LIRG Luminous Infrared Galaxy

LTE Local Thermodynamic Equilibrium

MIPS Multiband Imaging Photometer for Spitzer

NGLS Nearby Galaxies Legacy Survery

OVRO Owens Valley Radio Observatory

PACS Photodetector Array Camera and Spectrometer

PAWS PdBI Arcsecond Whirlpool Survey

PdBI Plateau de Bure Interferometer

PDR Photon Dominated Region

SECT Semi-Extended Correction Tool

SFE Star Formation Efficiency

SFR Star Formation Rate

SGMC Super Giant Molecular Complex

SINFONI Spectrograph for INtegral Field Observations in the Near Infrared

SLED Spectral Line Energy Distribution

SLW SPIRE Long Wavelength Spectrometer Array

SNR Signal to Noise Ratio

SPS Spectrometer Point Source

SSC Super Star Cluster

SSW SPIRE Short Wavelength Spectrometer Array

SPIRE Spectral and Photometric Imaging REceiver

ULIRG Ultra Luminous Infrared Galaxy

VLA Karl G. Jansky Very Large Array

VLT Very Large Telescope

VNGS Very Nearby Galaxies Survey

XDR X-ray Dominated Region

Acknowledgements

First and foremost, I want to thank my supervisor, Christine Wilson, who gave me this opportunity and whose careful guidance has helped me complete this thesis. She provided me with the opportunity to work with data from two (at the time) leading-edge instruments throughout the course of my PhD. I have also been fortunate enough to travel to numerous conferences and workshops, and to present my work to a wide variety of audiences. Even when incredibly busy with other tasks, such as being CASCA president or department chair for a year, Chris has always found time to meet with me and to read paper and proposal drafts. While doing so, she has provided useful insights into my ongoing work and has quietly corrected my improper use of semi-colons and colons. Thank you, Chris, for giving me the chance to work in astronomy, to work with amazing data sets, and to meet fantastic people.

I also want to thank my supervisory committee members, Doug Welch and James Wadsley, who helped guide my project throughout the course of my yearly committee meetings. In particular, they led me away from studying Centaurus A, instead focusing my work on M51 so as to create a more cohesive project in the end. I also want to thank the secretaries in the Department of Physics and Astronomy - Tina, Cheryl, Rose and Mara - all of whom helped on the administrative side of things at one point or another, and who were always available to answer my questions, both painfully trivial and exceedingly complex, and for a quick chat during my visits to the office.

Numerous collaborators have been instrumental to me completing my degree. In particular, I want to thank the members of the Very Nearby Galaxies Survey who worked on the FTS data with me, including Naseem Rangwala, Jason Glenn, Julia Kamenetzky, Phil Maloney, and Luigi Spinoglio. The many discussions we have had on the FTS Telecon, along with your comments on paper drafts, were incredibly helpful in completing my degree.

I would be remiss if I did not acknowledge the many fantastic and amazing graduate students I have encountered throughout my years here at

McMaster. Within Christine Wilson's group, numerous students have come and gone, including Damien Robertson, Jonathan Newton, and Angus Mok, all of whom I have shared an office with. In particular, I want to thank Tara Parkin and Kazimierz Sliwa, who were both here for most (Tara) or all (Kaz) of my time at McMaster. Outside of Christine's group, the list of students grows large: Rachel Ward, Aaron Maxwell, Gwendolyn Eadie, Jeremy Webb, Mikhail Klassen, Rory Woods, Samantha Benincasa, Alex Cridland, Gandhali Joshi, Ben Keller, Ben Jackel, and Matt Alessi. I apologize if I have forgotten anyone, as the list is long!

Numerous friends outside of McMaster helped me keep my sanity throughout the course of my PhD, including: Adam, Nick, Dan, Jeff, Jason, Jason, Becky, Dave, James, Matt, Crystal, Samm, Tayler, Anita, Angie, Tina, Brian; the list is long and I am certain to have forgotten someone.

My family has played an important role both during my PhD. My parents, Ronald and Johanne Schirm, have supported me throughout my life, providing me with the opportunity to do what I wanted to do, and making sure I kept my options open. My brother, Samuel, and my sister, Geneviève, both have been the most awesome siblings a person could ask for, while still driving me completely nuts at times (I'm sure the feeling is mutual). Marc, Chad, Emily, Natalie, and Natasha are nothing but great people, and are the best siblings-in-law a person could ask for. My Oma, Rita Schirm, for being there whenever I needed her, and my late Opa, Karl Schirm, who was a huge influence in my pursuit of an education in Physics and Astronomy.

Last, and certainly most, I must absolutely thank my wife, Jenna Schirm. She is one of the most amazing people I have ever known. She puts up with my antics with nothing but a smile on her face, and it fills me with joy every moment I spend with her. She's always willing to listen to whatever stories I've compiled throughout the day, no matter how boring. Waking up next to her every morning gives me the strength to get through anything in life, which has been incredibly helpful at times throughout my PhD. Together, we have welcomed a little boy, Alexandre Schirm, into this world, whose currently-toothless smile is intoxicating and whose laugh can put a smile on my face at any moment. I look forward to our next set of adventures, and to continuing to build our lives together.

Chapter 1

Introduction

"Ten to fifteen billion years ago, the Universe is born."

Raymond Kurzwell (1948-present)

The best estimate for the age of the Universe is 13.7 billion years[1]. When the Universe became transparent, about ~ 400 thousand years after the Big Bang (Hinshaw et al., 2009), it consisted mostly of dark matter ($\sim 63\%$), radiation in the form of photons ($\sim 15\%$), baryonic matter ($\sim 12\%$) and neutrinos ($\sim 10\%$)[1]. Back then, the structure in the Universe was vastly different than what we observe today, with no galaxies and no stars. However, the seeds of our present day structure had already been set.

After about ~ 400 million years, the Universe progressed into the epoch of reionization. This epoch is significant as it signals the beginning of significant star formation in the Universe, when newly formed stars re-ionized the largely neutral gas found throughout the Universe. It is at this point that galaxies, collections of stars, gas, dust and dark matter, began to form and grow. These galaxies, however, were not completely isolated systems, and by merging with other galaxies would continue to grow into the larger galaxies we

[1] WMAP Five Year Results on the Oldest Light in the Universe. Available at `http://wmap.gsfc.nasa.gov/news/5yr_release.html`

see in the present day Universe (Steinmetz & Navarro, 2002). These galactic mergers are violent events, and the nature of the merger along with the properties of the progenitor galaxies has a profound effect on the final structure formed.

The present-day Universe is largely dominated by dark energy ($\sim 70\%$) followed by dark matter (25%). Most of the remaining $\sim 5\%$ of the content in the Universe is baryonic matter, with only a very small fraction $< 0.1\%$) in the form of radiation. Dark energy drives the expansion of the Universe and is important only on the largest of scales. Dark matter, on the other hand, is important when investigating individual galaxies, as it resides in the outer regions of galaxies (known as the halo) and dominates the total mass of these systems.

The remaining mass in galaxies consists of the baryonic matter, which includes stars, gas and dust. In the Milky Way, the mass of the baryonic matter is largely dominated by stars ($\sim 90\%$, McMillan 2011). Only $\sim 10\%$ of the mass is in the form of gas (Tielens, 2005), while $\sim 0.1\%$ is embedded in the form of solid dust grains (Draine, 2003). However, all three forms of matter are intrinsically linked: the gas will collapse to form stars, the most massive of which will die and enrich the surrounding interstellar medium (ISM) with metals. These metals can, in turn, form dust grains, which can shield gas from radiation and provide a catalyst for the formation of molecular hydrogen, allowing the gas to cool and collapse once again, leading to the formation of more stars. Therefore, to understand the entire star formation process, each individual part needs to be understood.

When two galaxies merge together, the ISM can undergo significant changes. In some cases, the ongoing merger can catalyze the formation of new stars, leading to star formation rates (SFR) upwards of 100 times what is observed in the Milky Way ($SFR \sim 1\,\mathrm{M_{\odot}/year}$). In the most extreme cases, the two merging galaxies will become either a luminous infrared galaxy (LIRG, $L_{IR} > 10^{11}\ L_{\odot}$) or an ultra luminous infrared galaxy (ULIRG, $L_{IR} > 10^{12}\ L_{\odot}$), whose enhanced infrared (IR) luminosity is due to the ongoing star formation within the system. These systems are similar to the submillimeter galaxies observed around a redshift of $z \sim 2$, systems in which the star formation can attain rates of $\sim 1000\,\mathrm{M}_{\odot}$/year (Hodge et al., 2013). As such, understanding star formation in merging and interacting galaxies in the local universe, where the spatial details of individual systems can be resolved, is fundamental to our understanding of merging galaxies, which is in turn important in our understanding in the overall evolution of the Universe.

In this thesis, I will discuss my work investigating the interstellar medium (ISM) of interacting and merging galaxies. In particular, this thesis focuses on the molecular gas of the nearby ($D < 100\,\mathrm{Mpc}$) galactic merger NGC 4038/39 and the nearby interacting spiral galaxy M51. The purpose of this introduction is to provide a framework for the reader to understand of my work. I will begin by discussing molecular gas and photon dominated regions, along with the molecular gas tracers used to study the molecular gas. I will then introduce merging and interacting galaxies, before presenting the two sources studied in this thesis: NGC 4038/39 and M51. Following this, I will briefly discuss the excitation analysis used in a large portion of this work. Finally, the two primary instruments used in this work, the *Herschel* SPIRE-FTS and ALMA, will be described.

1.1 Molecular gas

Molecular gas is generally regarded as the primary fuel for star formation, and is a necessary component for star formation to occur in the nearby universe. As with all baryonic matter in the universe, the star forming molecular gas consists primarily of hydrogen, predominantly in the form of H_2, along with inert helium gas, and varying amounts of metals. Molecular gas is typically found within the confines of giant molecular clouds (GMCs), where there is sufficient self-shielding for molecular hydrogen to form without being dissociated. While the names suggest a smooth, cloud-like structure, GMCs are in fact inhomogeneous, turbulent environments. Furthermore, the surrounding environment can have a significant effect on GMCs, especially if they are in the presence of a strong radiative source such as massive stars or an active galactic nucleus (AGN). Within merging and interacting galaxies, the turbulent motions generated by the merger along with radiation from massive stars have a profound effect on the physical state and ongoing chemistry of the molecular gas, and in turn can drive the gas to collapse and form stars at an accelerated rate.

1.1.1 Photon dominated regions

Photon dominated regions (PDRs), also known as photodissociation regions, are regions of molecular gas which are illuminated by far ultraviolet (FUV) photons (Tielens & Hollenbach, 1985). Young, massive OB stars are regarded as the primary source of this FUV radiation, and so PDRs are commonly associated with star forming regions. However some authors argue that as much as 90% of molecular gas is in the form of PDRs (Kaufman et al., 1999). The PDR surface lies at the interface between ionized and neutral gas, where the PDR itself is assumed to contain largely neutral hydrogen in the form of either HI or H_2. Within PDRs, electrons are liberated from dust grains via the photoelectric effect, which in turn transfer energy to the gas particles via collisions, heating the gas near the surface. In addition to heating the gas, this FUV radiation has a profound effect on the ongoing chemistry within PDRs (Kaufman et al., 1999).

In the classic PDR model by Tielens & Hollenbach (1985), the molecular gas is assumed to be in a semi-infinite slab with one edge illuminated by the FUV radiation. In this case, there are two parameters which must be accounted for: the strength of the background FUV field, and the molecular gas density. A consequence of this assumption is that the molecular gas exhibits stratified structure, with a surface layer of HI, followed by a transition layer containing both HI and H_2 at an extinction of $A_v \sim 3$. This leads to a region of molecular gas which is CO dark: a region where CO is dissociated and so does not emit any CO emission (Wolfire et al., 2010). Indeed, this model also leads to a thin layer dominated by atomic carbon, from which it is assumed [CI] emission arises.

In reality, PDRs are more complex than the simple stratified structure from Tielens & Hollenbach (1985). Molecular clouds are turbulent environments (Falgarone, 1997), which can lead to mixing of the surface layers of PDRs. This in turn affects the ongoing chemistry, which can become significant in more extreme star forming environments, such as LIRGs (Papadopoulos, 2007). For example, electrons near the surfaces of PDRs can be mixed deeper into the molecular cloud where molecular ions, such as HCO^+, are found. These molecular ions would then be destroyed via dissociative recombination reactions which in turn would lower their abundances relative to H_2.

This turbulent motion can have the additional effect of heating the molecular gas in PDRs through mechanical heating (Loenen et al., 2008). Heating due to the FUV radiation occurs near the surfaces of the PDR, while in the absence of mechanical heating, the temperature deeper within the cloud drops to $\sim 10\,\mathrm{K}$ (Kazandjian et al., 2012). Mechanical heating, on the other hand, can warm the entire cloud and can lead to temperatures $> 100\,\mathrm{K}$ throughout (Kazandjian et al., 2012, 2015). This has the effect of altering the excitation condition for molecular gas tracers excited via collisions with H_2.

Cosmic rays are high-energy particles, such as high-energy protons, and enhanced cosmic ray rates relative to the Milky Way have been observed both in starburst galaxies (VERITAS Collaboration et al., 2009; Acero et al., 2009) and ULIRGs (Papadopoulos, 2010). This enhancement is due to the increased star formation rate, which in turn leads to an increase of both supernova and stellar winds, both of which can produce cosmic rays (Binns et al., 2008; Papadopoulos, 2010). These cosmic rays can penetrate deep into PDRs and increase the abundances of some ionic species, such as the ${H_3}^+$ ion (Meijerink et al., 2011). This in turn can increase the abundances of molecules whose formation require these ions, such as HCO^+ (Kazandjian et al., 2012). Changes in the abundances will in turn drive changes in the emission of the same species; however this relation is not generally linear (Kazandjian et al., 2012, 2015).

In summary, PDR models are generally characterized by the FUV field strength and molecular gas density. However, in order to properly quantify observations of various molecular gas tracers, mechanical heating due to turbulent motion and cosmic rays must be considered. Mechanical heating alters the excitation conditions of the molecular gas, while cosmic rays play a fundamental role in the ongoing chemistry deep within PDRs. While not discussed in this work, metallicity also has an effect on the ongoing chemistry, as it alters the relative abundance of various molecules and atoms. This, in turn, alters the observed line ratio between two difference atomic or molecular species.

1.1.2 Molecular gas tracers

As stated previously, molecular gas consists primarily of hydrogen in the form of H_2. However, unlike atomic gas, where the total gas content can be observed via the HI 21 cm forbidden transition, H_2 is difficult to observe directly. First, it is a symmetric molecule and lacks a rotational dipole moment, such as in

CO. As such, molecular gas temperatures of $> 100\,\mathrm{K}$ are required for H_2 to be excited (Bolatto et al., 2013), while most of the molecular gas in the Universe is cold ($\sim 10\,\mathrm{K}$, Young & Scoville 1991).

Secondly, H_2 emits its lowest energy transition in the far-infrared (FIR) ($\lambda = 28.22\,\mu\mathrm{m}$), with higher energy transitions being emitted at shorter wavelengths. Atmospheric transparency at these wavelengths is poor, making observations of H_2 difficult from the ground. Thus, space missions, such as the Spitzer Space Telescope (*Spitzer*) are required to study the H_2 emitting molecular gas.

Because H_2 can be difficult or impossible to observe directly, molecular gas tracers are required to study the bulk of the molecular gas in the Universe. These molecular gas tracers are excited via collisions with H_2, and so their brightness is tied directly to the total molecular gas content within a system. The most commonly used molecular gas tracer is CO, with a less frequently used tracer being atomic carbon ([CI]). Dense molecular gas tracers that are tied directly to star formation are HCN, HCO^+ and HNC.

1.1.2.1 CO

Carbon monoxide (CO) is by far the most commonly used observational tracer of molecular gas. Its abundance relative to H_2 and the position of the lower energy transitions relative to atmospheric windows makes it easy to observe from the ground. The most common isotopologue of CO is $^{12}C^{16}O$ (hereafter CO), with relative abundances $1 - 2$ orders of magnitude larger than the next most common isotopologue, $^{13}C^{16}O$ (hereafter ^{13}CO) (Langer & Penzias, 1990). In addition, there are two less abundant isotopologues which have been observed, $^{12}C^{17}O$ and $^{12}C^{18}O$.

CO is excited both rotationally and vibrationally; however, the energies required to excite the molecule into higher vibrational states are high ($E_k =$

3086 K for the $v = 1$ state, Coxon & Hajigeorgiou 2004; Gendriesch et al. 2009). The energies of the rotational states are significantly smaller ($E_k = 5.5$ K for the $J = 1$ state). CO is excited into higher rotational states via collisions with H_2, which then de-excite, emitting a photon which we in turn observe. The transition from the first excited rotational state to the ground state ($J = 1-0$) emits at 115.27 GHz, while subsequent transitions are separated by roughly ~ 115 GHz in frequency space, forming what is known as the “CO ladder”. This, along with its relative brightness, makes CO useful for not only studying molecular gas in the nearby universe, but also as a redshift indicator at higher z (Weiß et al., 2013).

The molecular gas temperature and density required to excited CO $J = 1 - 0$ are relatively low, making it ideal for studying the total molecular gas content within GMCs. The measured CO $J = 1 - 0$ emission can be converted into a molecular gas mass via a CO-to-H_2 conversion factor ($\alpha_{\rm CO}$, in units of $M_\odot$ pc^{-2}(K km s^{-1})$^{-1}$), also known as the X-factor ($X_{\rm CO}$, in units of cm^2 (K km s^{-1})$^{-1}$) (See Bolatto et al. 2013 for a review of the CO-to-H_2 conversion factor).

The higher CO transitions ($J = 2 - 1$ and above) require increasingly greater temperatures and densities to excite. Using an excitation analysis, measurements of multiple CO transitions can be used to constrain the physical state of the molecular gas, along with ongoing physical processes such as heating via PDRs (Tielens & Hollenbach, 1985) or x-ray dominated regions (XDRs, Maloney et al. 1996).

Caution should be exercised when using only CO to study molecular gas. First, the lower J transitions of CO are often optically thick, and so trace only the surfaces of molecular clouds. This can be alleviated by including optically thin “secondary” molecular transitions, such as ^{13}CO (Kamenetzky et al., 2012) or [CI] (Papadopoulos et al., 2004) in the analysis. In this case, it is assumed that all of the included transitions trace the same molecular gas, which may not always be the case. For example, it is possible that a certain fraction of the molecular gas is "CO-dark", in particular near the surfaces of PDRs (Wolfire et al., 2010; Langer et al., 2014). In these cases, the [CI] is assumed to reside in a surface layer around the cloud where CO is dissociated.

In addition, CO and in particular the $J = 1-0$ transition can be subthermally excited in extended, diffuse molecular gas (Polk et al., 1988), which is not associated with ongoing or future star formation. This warm, diffuse gas emits more CO $= 1-0$ emission relative to its mass than colder, denser gas typically found in GMCs (Papadopoulos et al., 2012). For example, in the case of M51, up to 50% of the CO $J = 1-0$ emission originates from an extended component of the molecular gas, that corresponds to only $\sim 20\%$ of the total molecular gas content (Pety et al., 2013).

1.1.2.2 [CI]

Unlike CO, neutral atomic carbon ([CI]) is a less frequently used molecular gas tracer. However, like CO, it is excited via collisions with hydrogen. Early models of PDRs suggest that [CI] would be limited to tracing the surfaces of PDRs (e.g. Tielens & Hollenbach 1985 or Wolfire et al. 2010), while observations show that it is found throughout molecular clouds (e.g. see Shimajiri et al. 2013). Recent hydrodynamic simulations of PDRs support these observations (Offner et al., 2014).

[CI] is a three-level system and has two fine structure transitions: $^3\mathrm{P}_1 \longrightarrow {}^3\mathrm{P}_0$ at $\sim 492\,\mathrm{GHz}$, and $^3\mathrm{P}_2 \longrightarrow {}^3\mathrm{P}_1$ at $\sim 809\,\mathrm{GHz}$. While [CI] serves as a useful tracer of molecular gas (e.g. Papadopoulos et al. 2004), the rest-frame frequency of both transitions are in regions where the atmosphere is not as transparent, making observations difficult from the ground. Until recently, few instruments have had receivers which can be tuned to these frequencies. In fact, *Herschel* is the first observatory able to observe both transitions simultaneously.

These two transitions are useful for calculating the temperatures of molecular gas. If we assume that the [CI] emitting gas is in local thermodynamic equilibrium (LTE), we can calculate the molecular gas temperature strictly from the observed line ratio of the two [CI] transitions using the following equation (e.g. see Spinoglio et al. 2012)

$$T_k = -\frac{E_{21}}{k}\left[\ln\left(\frac{g_1}{g_2}\frac{A_{10}\nu_{10}F_{21}}{A_{21}\nu_{21}F_{10}}\right)\right]^{-1} \tag{1.1}$$

where $g_j = 2J + 1$ are the Gaunt factors, A_{ij} are the Einstein coefficients, $E_{21}/k = E_2 - E1$ is the difference in the energy of the first two excited states, ν_{ij} is the frequency of the transition, F_{ij} is the measured flux in units of W/m^2, and T_k is the kinetic temperature of the molecular gas. This equation is a variation of the Boltzmann equation; however, in this form, no knowledge of the relative transition populations ($\frac{n_2}{n_1}$) is necessary in order to calculate the temperature. In cases where the LTE assumption does not hold, this equation provides a lower limit to the kinetic temperature of the molecular gas.

While [CI] is useful for determining the molecular gas temperature, it has also been suggested as a tracer of the total molecular gas content within a system (e.g. see Papadopoulos et al. 2004). In that same vein, attempts to calculate a [CI]-to-H_2 conversion factor for the $^3P_1 \longrightarrow {}^3P_0$ transition, akin to the CO-to-H_2 conversion factor, have been made. These attempts have yielded vastly different results, varying from $\alpha_{[CI]} \sim 1.4\,M_\odot$ pc^{-2} (K km s^{-1})$^{-1}$ (Bell et al., 2007) to $\alpha_{[CI]} \sim 26\,M_\odot$ pc^{-2} (K km s^{-1})$^{-1}$(Offner et al., 2014). Recent observations of this transition using the Herschel Space Observatory SPIRE-FTS provide a new opportunity to constrain this factor.

1.1.2.3 HCN, HNC, and HCO+

Observations of CO do not discriminate between inert diffuse gas and the dense gas directly associated with the ongoing star formation within a system. Dense molecular gas tracers, such as hydrogen cyanide (HCN), hydrogen isocyanide (HNC), and HCO^+, allow us to focus solely on the dense ($n(H_2) \gtrsim 10^5\,cm^{-3}$) molecular gas within a star forming system. This is due to the higher critical density required to excite HCN ($n_{crit} \sim 2 \times 10^6\,cm^{-3}$), HNC ($n_{crit} \sim 4.0 \times 10^5\,cm^{-3}$), and HCO^+ ($n_{crit} \sim 2 \times 10^5\,cm^{-3}$, Kazandjian et al. 2015). As with CO, all three molecules have both rotational and vibrational excitation states. I focus my discussion on the rotational transitions due to the lower energies required to excite them.

All three molecules are susceptible to infrared pumping. In these cases, a background mid-infrared field ($\sim 10-20\,\mu$m) excites the molecule radiatively into its first vibrational state (Sakamoto et al., 2010). The excited molecule will then de-excite down to the ground state by cascading through multiple ro-vibrational transitions (Carroll & Goldsmith, 1981). This effect is particularly important when the IR pumping excitation rate is similar to the H_2 collisional excitation rate. Gao & Solomon (2004) argue that IR pumping does not have an appreciable effect on the HCN $J = 1-0$ transition in even IR bright galaxies. However, IR pumping has been seen in Arp 220 (Rangwala et al., 2011)

Chemistry plays an important role in the relative abundances of HCN, HNC, and HCO^+ (e.g. see Meijerink et al. 2011). Due to the similar collisional excitation conditions, these changes in abundance can be seen in ratios of the $J = 1-0$ transition of the three molecules. However, the relationship between abundance ratios and luminosity ratios is not linear due to optical depth effects (Meijerink et al., 2011; Kazandjian et al., 2012, 2015).

Both HCN and HNC are formed predominantly through the dissociative recombination of $HCNH^+$ ($HCNH^+ + e^- \longrightarrow H + HCN$ and $HCNH^+ + e^- \longrightarrow H + HNC$) (Talbi et al., 1996; Loison et al., 2014). These reactions favour neither isotopomer and form HCN and HNC at a 1-to-1 ratio. Variations in the ratio of HNC/HCN are driven largely by the exchange reaction $HNC + H \rightleftarrows HCN + H$ (Talbi et al., 1996). The activation barrier for the reaction of HNC + H is less then 1200 K, while for the reverse reaction (HCN + H), the activation barrier is $\sim 9000\,\mathrm{K}$ (Graninger et al., 2014). Thus, the exchange reaction favours the formation of HCN and the destruction of HNC. A minimum temperature of a few hundred K is required for this reaction to occur at an appreciable rate (Talbi et al., 1996; Meijerink et al., 2011; Kazandjian et al., 2015).

Both HCN and HNC can be "recycled" by reacting with ${H_3}^+$, which has $HCNH^+$ as one of its products. As before, HCN^+ will then undergo dissociative recombination to form either HCN or HNC. In cool environments ($T_{kin} \sim 10\,\mathrm{K}$), where neither HCN nor HNC is destroyed, this recycling will drive the ratio of HNC/HCN to unity on relatively rapid timescales ($\sim 10^5$ yrs, Loison et al. 2014). Thus, the ratio of HNC/HCN is a highly dependent upon temperature, and is a useful indicator of the molecular gas temperature (e.g. see Kazandjian et al. 2015).

Unlike the ratio of HNC/HCN, where values of unity are possible, the ratio of the isotopomers HOC^+/HCO^+ is very small, ranging between $\frac{1}{300}$ and $\frac{1}{6000}$ (Smith et al., 2002). HCO^+, however, is useful as a comparison to HCN due to the relative brightness of the emission lines of the two molecules. For example, ${H_3}^+$ is formed in abundance in cosmic ray-dominated regions and is an important ion in the formation of $HCNH^+$, which is used in the formation of both HCN and HCO^+ (Papadopoulos, 2007). The formation of ${H_3}^+$ leads to a free electron being ejected, which in turn can destroy HCO^+ via dissociative recombination. As a result, the ratio of HCN/HCO^+ is a potential indicator of the cosmic ray rate in dense molecular regions (Meijerink et al., 2011; Kazandjian et al., 2015). Furthermore, the critical density of HCO^+ is a factor of ~ 15 smaller than that of HCN, and so the ratio of HCN/HCO^+ may serve as an indicator of the density of the dense molecular gas (Juneau et al., 2009).

1.2 Merging and Interacting Galaxies

Merging and interacting galaxies are found at all epochs in the Universe, and play a fundamental role in the evolution of structure within the Universe. These ongoing interactions and mergers can have a profound effect on the structure and physics of the progenitor galaxies, including their ISM, morphology and star formation rates. In particular, an interaction or merger can induce star formation within these systems (Sanders & Mirabel, 1996). In fact, there is strong evidence to suggest that virtually all ULIRGs are the product of gas rich mergers, as evidenced by multiple observations of ULIRGs where two distinct nuclei are visible (Clements et al., 1996).

Merging and interacting galaxies often serve to catalyze and enhance star formation within the systems in the form of "starbursts", short, violent episodes of localized star formation (Mihos & Hernquist, 1996). Early simulations of merging and interacting galaxies suggested that the gravitational interaction served to drive molecular gas towards the nucleus of the progenitor galaxy, in turn enhancing the star formation rate (e.g. see Hernquist 1989). In this case, gravitational torques applied in the opposite direction of the progenitor galaxy's rotation serve to remove angular momentum from the gas, which drives the gas to smaller radii (e.g. Toomre & Toomre 1972). Whether star formation is enhanced in these systems and where this star formation is located depends upon the relative orientation of the two progenitor galaxy's gas disks (Moreno et al., 2015).

While nuclear starbursts are relatively well understood, off-nuclear starbursts are not. Furthermore, there is significant observational evidence of enhanced star formation in the off-nuclear regions of some interacting and merging systems, such as in the Tadpole galaxy (UGC 10214, Jarrett et al. 2006) or the Antennae (NGC 4038/39). A popular explanation for this off-nuclear star formation is shock-triggering, where collisions between large, diffuse HI clouds lead to an increase in pressure (Barnes, 2004). This process in turn increases the pressure of the molecular clouds contained within these diffuse HI clouds, causing star formation to occur at an increased rate. With this model, the star formation occurs at the interface between the two gas-disks of the progenitor galaxies, and occurs during the early stages of the merger (Jarrett et al., 2006).

My work focuses on two systems of galaxies in particular. The first is the merging pair NGC 4038/39, also known as the Antennae, while the second is the interacting galaxy M51, also known as the Whirlpool galaxy. A description of each system is given in the following two subsections.

1.2.1 NGC 4038/39 ("the Antennae")

NGC 4038/39 (Figure 1.1) is a nearby, ongoing merger between two gas-rich spiral galaxies, NGC 4038 and NGC 4039. Discovered in 1785 by Sir William Herschel (Herschel, 1786), the Antennae's relatively small distance ($D = 22 \pm 3\,\mathrm{Mpc}$, Schweizer et al. 2008) makes it one of the nearest major gas-rich mergers. As a result, it is one of the most well studied merger systems, having been observed at nearly every wavelength, from radio waves (e.g. van der Hulst 1979) to x-rays (e.g. Fabbiano et al. 2001). It is often viewed as the prototypical early-stage gas-rich merger, and may represent a step in the evolution of the extreme star forming galaxies knows as ULIRGs (Gao et al., 2001).

Figure 1.1 Hubble Space Telescope colour image of the Antennae (NGC 4038/39), an ongoing merger between two gas rich spiral galaxies. Credit: NASA, ESA, and the Hubble Heritage Team (STScI/AURA)-ESA/Hubble Collaboration. Used in accordance with STScI copyright policy.

The Antennae was identified as two separate objects as early as 1922 (e.g. Perrine 1922), while Duncan (1923) noted the "antennae"-like appearance of the faint, thin structures extending from the nuclei. These thin structures are tidal tails, created by the gravitational interaction of the two progenitor spiral galaxies (Toomre & Toomre, 1972). Roughly 60% of the HI gas within the system is found in the southern tidal tail, while only $\sim 9\%$ is in the northern tail (Hibbard et al., 2001). The lengths of the tails suggest that the interaction began about $\sim 400\,\mathrm{Myr}$ ago (Hibbard et al., 2001).

One of the earliest studies of the molecular gas in NGC 4038/39 was done by Stanford et al. (1990), who used the Owens Valley Millimeter Wave Interferometer to observe the molecular gas tracer CO in the $J = 1-0$ transition at high resolution, with a beam full-width half-maximum (FWHM) of $\sim 6''$. Stanford et al. (1990) detected CO both in the nucleus of NGC 4038 ($F_{\rm CO} = 159\,{\rm Jy\ km\ s^{-1}}$) and the nucleus of NGC 4039 ($F_{\rm CO} = 46\,{\rm Jy\ km\ s^{-1}}$). The brightest CO emission, however, was found to emanate from an extra-nuclear region located between the two galaxies ($F_{\rm CO} = 225\,{\rm Jy\ km\ s^{-1}}$), dubbed the "overlap region". The emission in the overlap region was in four distinct clumps located north, south, east and west within the overlap region.

The work by Stanford et al. (1990) was followed up by Wilson et al. (2000, 2003) who observed the same CO transition in the Antennae using the Caltech Millimeter Array. Wilson et al. (2000) identified 5 super giant molecular complexes (SGMCs) in the overlap region, with molecular gas masses of $\sim 1-6\times10^8 M_\odot$. Wilson et al. (2003) extended this analysis to identify ~ 100 clouds of molecular gas across the entire system, including a region west of the nucleus of NGC 4038 known as the "Western Loop". With masses ranging from $2\times10^6\ M_\odot$ to $9\times10^8\ M_\odot$, Wilson et al. (2003) found that these clouds were an order of magnitude more massive than the clouds found in the spiral galaxy M51.

Hubble Space Telescope (HST) observations of the Antennae show that the youngest star clusters ($\lesssim 5\,{\rm Myr}$) are located within the overlap region (Whitmore et al., 1999) and are found within the molecular clouds detected by Wilson et al. (2003). In addition, many of these star clusters are in the form of "super star clusters": massive, compact clusters of stars with masses $\sim$ a few $10^6\ M_\odot$ (Whitmore et al., 2010). In fact, recent observations of the overlap region in the CO $J = 3-2$ transition using the Atacama Large Millimeter/submillimeter Array (ALMA) have revealed a surprisingly bright cloud of molecular gas within SGMC 2 which has been suggested to be a precursor to a super star cluster (Whitmore et al., 2014; Johnson et al., 2015).

The current star formation peaks in the overlap region (Gao et al., 2001; Zhang et al., 2010), while the star clusters detected by Whitmore et al. (1999) are likely the result of a starburst triggered due to the interaction, having begun $\sim 7-8\,\mathrm{Myr}$ in the past (Fischer et al., 1996). In addition, the bulk of the star formation in the overlap region is obscured by dust (Mirabel et al., 1998), which may explain why initial observations of the Antennae referred only to the two nuclei.

In addition to the cold molecular gas detected by the CO $J = 1-0$ transition, there is a component of the molecular gas which is significantly warmer, with temperatures exceeding $\sim 100\,\mathrm{K}$. Zhu et al. (2003) first saw evidence for this warmer component. They performed a non-LTE excitation analysis of ratios of the CO $J = 1-0$, $J = 2-1$ and $J = 3-2$ transitions, along with the $J = 1-0$, $J = 2-1$ and $J = 3-2$ transitions of the isotopologue ^{13}CO. They performed both a single component and a two-component fit, where they assume all of the molecular gas traced by these CO transitions resides in either a single component or two distinct components. In all cases, a warm component ($T_{kin} \sim 100\,\mathrm{K}$) is either recovered or allowed by the temperature range returned by their analysis.

Star formation in the Antennae is ongoing, with examples of various phases of a star's life found throughout the overlap region. Whitmore et al. (2014) combined ALMA observations of CO $J = 3-2$ in the overlap region with optical, infrared and hydrogen recombination line observations from HST, and radio observations from the Karl G. Jansky Very Large Array (VLA) and found that the typical GMC lifetime in the overlap region is $\sim 10\,\mathrm{Myr}$. In addition, they detected the presence of a bright, compact source in SGMC 2, which was also similarly detected in H_2 (Herrera et al., 2012). Johnson et al. (2015) suggest that this cloud will form stars within $\sim 1\,\mathrm{Myr}$.

The spatial extent of NGC 4038/39 on the sky along with its star forming properties make it a unique system in which to star formation and molecular gas in the nearby universe. Furthermore, it represents one of the earliest stage gas-rich mergers in the local Universe, which helps us to understand how star formation is triggered in a merger. Its off-nuclear star formation makes it an interesting source to compare in relation to other mergers, such as Arp 299, where the star formation is occurring within the former nuclei of the progenitor galaxies (Alonso-Herrero et al., 2000).

1.2.2 M51

M51 (Figure 1.2), also known as M51a, NGC 5194 or the Whirlpool Galaxy, is a nearby grand-design spiral galaxy. Its popular name comes from its likeness to swirling water due to its prominent spiral arms. While it is generally regarded as a normal spiral galaxy, it has recently undergone an interaction with the nearby lenticular galaxy NGC 5195, also known as M51b, and the interaction may have enhanced M51's spiral arms (Koulouridis, 2014). Its distance (9.9 Mpc, Tikhonov et al. 2009) and relative brightness has led to it being one of the most well studied spiral galaxies. At the centre of M51 lies a low-luminosity active black hole, leading to M51 being classified as a Low Ionization Nuclear Emission Region (LINER) galaxy (Satyapal et al., 2004).

The comet hunter Charles Messier discovered M51 in the year 1773 and included it in the final edition of his catalogue of nebulae and star clusters (Messier, 1781), while its companion galaxy, NGC 5195, was not discovered until 1781 by Pierre Méchain. At the time of the discovery, it was not known whether the two galaxies were interacting, or if their close proximity was merely a projection effect. Early sketches and photographs of M51 revealed its distinct and prominent spiral arms traced by the stellar content of the galaxy (Roberts, 1889).

Rickard & Palmer (1981) mapped CO $J = 1-0$ in M51 and found that

Figure 1.2 Hubble Space Telescope colour image of the interacting spiral galaxy known as the Whirlpool Galaxy (M51). NGC 5195 is the dusty lenticular galaxy located above M51, and has recently undergone an interaction with the spiral galaxy. Credit: NASA, ESA, S. Beckwith (STScI), and The Hubble Heritage Team (STScI/AURA). Used in accordance with STScI copyright policy.

the molecular gas was confined to the optical disk and peaked in the centre of the galaxy. Scoville & Young (1983) found that the neutral gas within the central $\sim 10\,\mathrm{kpc}$ ($\sim 200''$) is dominated by H_2 as opposed to HI, with $\sim 75\%$ in the form of molecular hydrogen. Garcia-Burillo et al. (1993b,a) mapped both CO $J = 1-0$ and $J = 2-1$ in M51. Garcia-Burillo et al. (1993b) found thick molecular arms ($\sim 20''$ wide) and evidence for a molecular bar which coincides with the previously observed stellar bar.

It has been $\sim 200-300$ Myrs since the interaction between M51 and NGC 5195 began (Dobbs et al., 2010). This interaction may have enhanced the star formation throughout the system, which would be the result of cloud-cloud collisions (Nikola et al., 2001). However, it is not clear when, based upon the cluster formation history in M51, the triggered star formation occurred (Bik et al., 2003). The total SFR as measured via Hα emission is $4.2\,\mathrm{M}_\odot\ \mathrm{yr}^{-1}$ (Scoville et al., 2001), with a significant portion ($\sim 30\%$) of the star formation occurring in the inter-arm regions of M51 (Foyle et al., 2010).

The ongoing star formation has led to a population of OB stars throughout M51 (Scoville et al., 2001), which provide the necessary FUV radiation for PDRs. These PDRs in M51 have been studied by Nikola et al. (2001), Kramer et al. (2005) and Parkin et al. (2013). Nikola et al. (2001) modelled the [CII], CO $J = 2-1$ and FIR emission at three bright [CII] regions of M51. Their models yielded degenerate solutions for the FUV field strength and gas density; however, they estimated that $\sim 2\%$ of the total molecular gas content is in [CII] emitting gas, which arises near the surfaces of PDRs. Kramer et al. (2005) used additional lines ([CII], [CI], [OI]63 μm, CO $J = 3-2$, and CI $J = 1-0$) along with the total infrared luminosity. They recovered a field strength $G_0 \sim 20-30$, low when compared to other star forming regions.

The most recent PDR modelling in M51 was performed by Parkin et al. (2013), who used Herschel PACS and SPIRE observations to constrain the field strength and gas density. In their models, Parkin et al. (2013) were able to correct for the [CII] fraction from ionized gas. With the correction applied, the model yields gas of intermediate density ($n(\mathrm{H}_2) \sim 10^2 - 10^4\,\mathrm{cm}^{-3}$) with a background field strength greater than that recovered by Kramer et al. (2005)

($10^{1.5} - 10^{4.0}$). Both the density and radiation field strength peak in the nucleus of M51. Parkin et al. (2013) suggest that there could be contamination from the weak AGN of M51, which in turn would reduce both the density and FUV field strength derived for the PDR in this region.

Due to its face-on orientation and proximity to us, M51 is a useful source in which to study molecular gas. While it has undergone a recent interaction, it does not show the same enhancement to its star formation rate as seen in other interactions, such as the starburst galaxy M82. In fact, M51 is generally regarded as a "normal" spiral galaxy, even though the interaction has likely had an effect on the morphology, and star formation rate, albeit not to the same extent as in NGC 4038/39. Furthermore, M51 does not exhibit the same massive, compact super star clusters that are found in the Antennae. Thus, M51 and NGC 4038/39 are excellent observational counterparts in which to study molecular gas and star formation, as the systems are sufficiently different to provide a point of comparison, while sufficiently similar to ensure a fair and useful comparison.

1.3 Non-local thermodynamic equilibrium excitation analysis

In Section 1.1.2.2, I briefly discussed deriving molecular gas temperatures using a local thermodynamic equilibrium (LTE) analysis and observations of atomic carbon. The next step up from a LTE excitation analysis is one where the assumption that the molecular gas is in LTE is dropped. In this case, the excitation of the molecular tracers is still assumed to be local; the excited molecule or atom is assumed not to have traveled far from its excitation location before de-exciting and emitting the observed photon. Under this assumption, the molecular gas is in statistical equilibrium, where any molecule or atom excited by collisions with H_2 to a higher energy level is assumed to de-excite back to its original level. For example, if CO is excited from the $J = 4$ to $J = 5$ rotational state, it will then emit a photon corresponding to the $J = 5 - 4$ transition.

This method requires that collisions are the dominant source of the excitation of the molecular gas tracers and that any other sources of excitation are well quantified. As mentioned previously, radiative excitation in the form of IR pumping can become important in the presence of a strong background radiative field, such as with HCN, while in general this is not an issue for CO or [CI]. In addition, this method requires knowledge of the collisional data between the tracer and primary collision partner (in the case of molecular gas, this partner is H_2). Data for many molecules and atoms, along with their isotopologues and isotopes, have been calculated and compiled in the Leiden Atomic and Molecular DAtabase (LAMDA, Schöier et al. 2005).

1.3.1 RADEX and likelihood analysis

In this thesis, I use the publicly available non-LTE excitation code RADEX (Version 20nov08, van der Tak et al. 2007). RADEX does not perform the full radiative transfer calculations; instead it uses an escape probability formalism to calculate the line integrated intensities. The escape probability itself depends only upon the optical depth of the medium, and the assumed geometry, which can either be a semi-infinite slab, a uniform sphere or an expanding spherical shell. Using this formalism, RADEX requires only a few inputs to calculate a set of integrated intensities and optical depths for multiple atomic and molecular species concurrently. A list of the input parameters is given in Table 1.1.

A grid of integrated intensities can be created by varying the kinetic temperature, molecular gas density and the column density for each species

Table 1.1. List of RADEX input parameters

Parameter	Name	Notes
T_{kin}	Kinetic Temperature	
$n(H_2)$	Molecular gas density	
N_{mol}	Molecule column density	Different for each tracer
Φ_A	Area filling factor	Introduced by likelihood code
ΔV	Line width	Typically fixed at 1 km s^{-1}

of interest (e.g. CO and [CI]). A set of measured integrated intensities can then be compared to this grid of models to calculate a multi-dimensional likelihood distribution. From this distribution, it is possible to calculate the most probable values for each of the input parameters along with the likelihood distribution for each parameter.

I use a Bayesian likelihood code to constrain the temperature, density, and column density of the molecular gas (e.g. see Kamenetzky et al. (2012) and references therein). The code introduces an additional parameter Φ_A, known as the area filling factor, which is a measure of what fraction of the observed region contains emission. Furthermore, the product of the filling factor and column density yields the beam-averaged column density, which is directly related to the total molecular gas mass within the observed region.

By invoking Bayes' Theorem, it is possible to introduce additional information into the likelihood analysis in order to constrain the physical parameters to values which are physically realizable. In particular, the code places constraints on the total molecular gas mass contained within the observed region, the length of the observed region along the line of sight (the "column"), and the optical depth. The optical depth prior is based upon limitations of the RADEX code. For the length and mass priors, how the prior is calculated depends upon the nature of the observation. For example, in the case of a galaxy where the entire system is contained within one beam, the dynamical mass of the galaxy can be used as the mass prior (e.g. see Rangwala et al. 2011), while this assumption does not apply to a face-on, resolved spiral galaxy.

This analysis lends itself to data sets which contain observations of multiple transitions of the same molecule. CO is an excellent candidate as observations from $J = 1-0$ up to $J = 13-12$ and beyond now exist for many sources and so allow us to constrain the physical state of multiple phases of the molecular gas, such as cold and warm molecular gas traced by the low and high J CO transitions respectively. In fact, any instrument which can observe multiple transitions of multiple molecules concurrently provides a unique opportunity to study the physical state of the molecular gas.

1.4 Instrumentation

1.4.1 Herschel Space Observatory

Launched in 2009, the Herschel Space Observatory (*Herschel*, Pilbratt et al. 2010) served to unlock the far-infrared sky at unprecedented sensitivity and resolution. *Herschel* consists of a single 3.5 m dish, and was the largest spaced-based telescope at the time. The spacecraft was located at the Lagrange point L2, and served as a platform for 3 instruments: the Heterodyne Instrument for the Far-Infrared (HIFI, de Graauw et al. 2010), the Photodetector Array Camera and Spectrometer (PACS, Poglitsch et al. 2010) and the Spectral and Photometric Imaging REceiver (SPIRE, Griffin et al. 2010). All three instruments were kept in a supercooled helium cryostat. The spacecraft ran out of liquid helium in April of 2013. It has since been decommissioned and placed into orbit around the Sun. Together, the instruments covered a total wavelength range of $55-671\,\mu$m ($450-5450\,$GHz). My work uses data from 2 of the instruments, PACS and SPIRE.

PACS consists of both a photometer and an imaging spectrometer. The PACS photometer consists of 3 filters at 70 μm (blue), 100 μm (green), and 160 μm (red) and can image image two filters concurrently. The resolution of the instrument (beam size) is $\sim 5.5''$ (blue), $\sim 6.5''$ (green) and $\sim 12''$ (red)[2]. These beam sizes, coupled with the large field-of-view of the PACS photometer ($1.75' \times 3.5'$), makes the PACS photometer ideal for studying cold and warm dust in extended, extragalactic sources.

The PACS spectrometer is an integral-field spectrometer and covers a spectral range comparable to the PACS photometer ($51-220\,\mu$m). Within this spectral ranges lie numerous important atomic species, such as [CII]158μm, and [OI]63 μm, both of which are important transitions for the study of PDRs (e.g. see Parkin et al. 2013). The total field of view of the spectrometer ($47'' \times 47''$) is smaller than the PACS photometer[2], while the beam size varies from $\sim 9''-13''$[2] and is dependent upon the observed wavelength. The instantaneous spectral coverage of the PACS spectrometer also depends upon the observed wavelength, and varies between $\Delta\lambda = 0.14\,\mu$m and $\Delta\lambda = 1.06\,\mu$m.

Like the PACS instrument, the SPIRE instrument consists of both a photometer and an imaging spectrometer. The SPIRE photometer is complementary to the PACS photometer, with broadband filters at 250 μm, 350 μm, and 500 μm tracing colder duster than PACS. The instrument field of view is large ($4' \times 8'$), while the resolution is worse than the PACS photometer (FWHM $\sim 17.6'' - 35.2''$)[3].

The SPIRE-Fourier Transform Spectrometer (SPIRE-FTS, Naylor et al. 2010) is a low spatial and spectral resolution Fourier transform spectrometer of a Mach-Zehnder configuration(Swinyard et al., 2014). Within the SPIRE-FTS, an input signal is split upon entering the instrument, with both signals

[2]PACS Observers Manual, available at http://herschel.esac.esa.int/Docs/PACS/html/pacs_om.html

[3]SPIRE Handbook, formerly the SPIRE Observers Manual, available at http://herschel.esac.esa.int/Docs/SPIRE/spire_handbook.pdf

being sent along different paths. A moving mirror creates a path difference between the two signals, which creates an interference pattern known as an interferogram. When a Fourier transform is applied to this interferogram, a spectrum is generated with spectral units of wavenumber[3] (cm^{-1}). The spectral resolution of the SPIRE-FTS is $\Delta\nu = 1.2\,\mathrm{GHz}$, and is dictated by the largest path difference generated by moving the mirror.

The SPIRE-FTS consists of two sets of detectors covering overlapping spectral ranges[3]: the SPIRE Long Wavelength Spectrometer Array (SLW, $\lambda = 316 - 672\,\mu\mathrm{m}$, $\nu = 446.7 - 989.4\,\mathrm{GHz}$) and the SPIRE Short Wavelength Spectrometer Array (SSW, $\lambda = 194 - 324\,\mu\mathrm{m}$, $\nu = 959.3 - 1544\,\mathrm{GHz}$). Unlike the PACS spectrometer, the entire spectral ranges of both the SLW and the SSW of the SPIRE-FTS are observed simultaneously, allowing for unprecedented spectral coverage in a single observation. Within this spectral range lie numerous molecular and atomic transitions, including both [CI] transitions, CO transitions from $J = 4 - 3$ to $13 - 12$, and the [NII]$205\,\mu$m transition, which traces ionized gas. As such, the SPIRE-FTS is useful both as a tool to measure line strengths, and also as a means of surveying for lines within an individual source (e.g. see Rangwala et al. 2011).

The SLW and SSW consist of 19 (SLW) and 37 (SSW) detectors hexagonally packed, while only 7 (SLW) and 19 (SSW) of these detectors are within the unvignetted field of view of the instrument ($\sim 2.6''$) and are used for science (Figure 1.3). In addition, 2 of the SSW detectors are "dead", leaving 17 working detectors in the SSW (Swinyard et al., 2010). With this detector layout, three sampling modes are available when observing with the SPIRE-FTS: sparse, intermediate and full. In sparse-sampling mode, the bolometers observe at a single position, while in intermediate and full-sampling modes, a secondary mirror is moved, or "jiggled", such that 4 (intermediate) or 16 (full) positions are measured with the array of detectors. Using the latter two modes allows for mapping with the SPIRE-FTS. It is important to note that only the full-sampling mode produces Nyquist sampled observations, and provides full coverage of the mapped region.

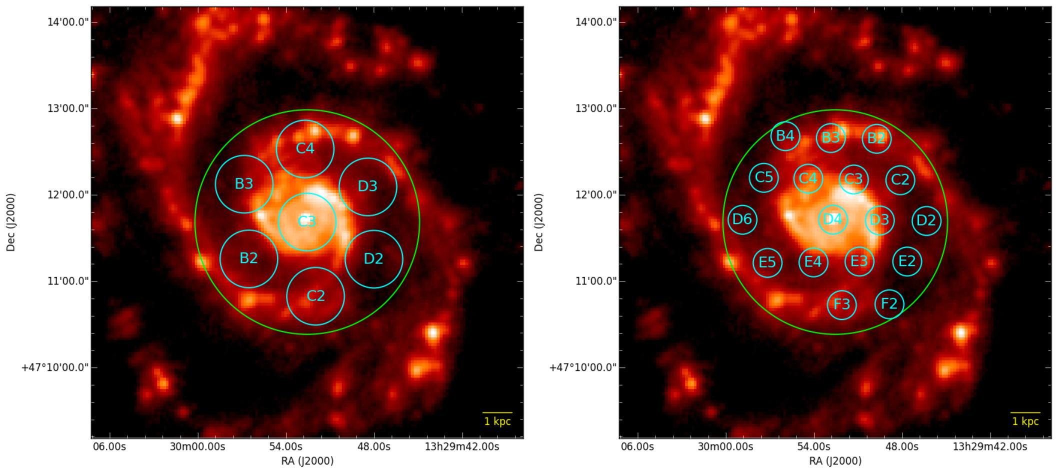

Figure 1.3 Schematic of the layout of the SPIRE-FTS detector arrays for the SLW (*left*) and SSW (*right*). The background image is the PACS 70 μm image (Parkin et al., 2013). The cyan circles indicate the location of the individual bolometric detectors, while the label combined with the array name corresponds to the detector name (e.g. C3 in the SLW image corresponds to detector SLWC3). The size of the cyan circles correspond to a representative beam size of $40''$ (for the SLW) and $20''$ (for the SSW). The large green circle indicates the unvignetted SPIRE-FTS field of view ($\sim 2.6'$). Note that detectors SSWD5 and SSWF4 are non-functioning and are not shown.

The unique feedhorn design leads to significant variations in the size and shape of the SPIRE-FTS beam over the observed frequency range (Makiwa et al. 2013), while the SLW beam (FWHM $\sim 29'' - 42''$, Figure 1.4) is larger than the SSW beam (FWHM$\sim 17'' - 21''$, Figure 1.4). The beam size and shape is easily accounted for when observing point ($\lesssim 5''$) sources or uniform, extended ($\gtrsim 1'$) sources with the SPIRE-FTS. However, for sources which are semi-extended and/or not uniform, the varying beam size and shape must be accounted for in order to accurately measure the line fluxes in the SPIRE-FTS spectrum. For full-sampled observations, line maps can be beam-matched by convolving the maps with the appropriate kernel (e.g. see Schirm et al. 2014 and Chapter 2). Intermediate-sampled observations require a more sophisticated correction (e.g. see Wu et al. 2013 and Chapter 3).

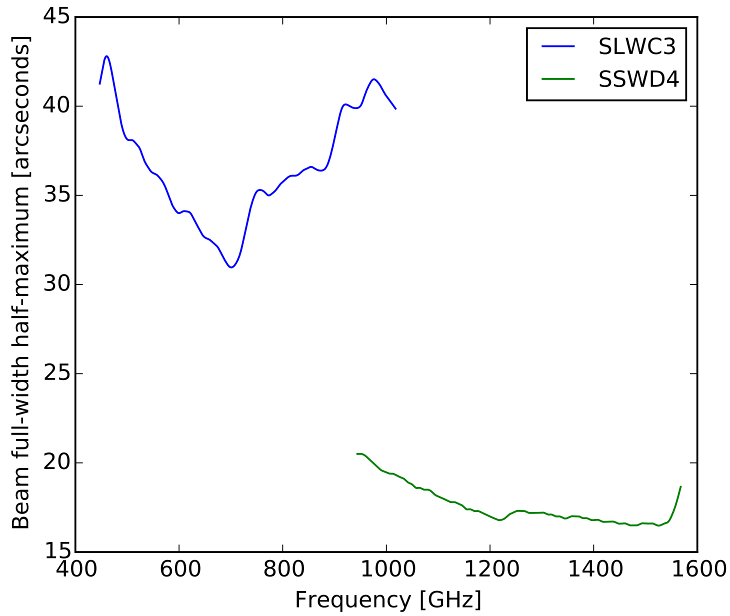

Figure 1.4 Plot of the beam size compared to the frequency in the form of the beam full-width half-maximum for the SPIRE-FTS. The blue line corresponds to the beam size of the SLWC3 detector, while the blue line corresponds to the beam size of SSWD4 detector. The beam size for the off-centre detectors in the SLW and SSW are similar to those of the central detectors (e.g. SLWC3 and SSWD4). The beam data was taken from the *Herschel* SPIRE-FTS calibration files.

1.4.2 Atacama Large Millimeter/submillimeter Array

The Atacama Large Millimeter/submillimeter Array (ALMA) is a newly commissioned interferometer located on the Atacama plateau in Chile. Like *Herschel*, the instrument takes advantage of Fourier transforms to observe sources both near and far. Unlike *Herschel*, these Fourier transforms are applied to position-space (and its Fourier transform) as opposed to frequency space (and its Fourier transform). As with other interferometers, ALMA takes advantage of the path difference generated when two (or more) individual antennas placed at some distance from each other observe the same source. Every pair of antennas generates what is known as a "baseline", while the distance between two antennas is the length of the baseline.

Each baseline generates a measurement in the $u - v$ plane which is the Fourier transform of the plane of the sky. As a result, small-scale structure in the $u - v$ plane corresponds to large-scale structure in the plane of the sky, and vice-versa. Longer baselines correspond to larger structures in the $u - v$ plane, while in turn filtering out the small scale structure in the $u - v$ plane. In order to fill in the $u - v$ plane as much as possible while still achieving the high resolutions interferometers are capable of, arrays ideally consist of ≥ 15 antennas. Physical limitations in how close two antennas can be placed always result in a lack of coverage at the smallest scales (the centre) of the $u - v$ plane. This in turn leads to the filtering of large scale structure on the sky, known colloquially as the "missing flux" problem.

ALMA has 2 separate arrays of dishes. The main array consists of a total of 50 12 m dishes, with a maximum number of baselines of $\frac{50\times49}{2} = 1225$, and a theoretical maximum baseline length of $\sim 16\,\mathrm{km}$[4]. These large baselines lead to resolutions $< 0.01''$[5]. Furthermore, the inclusion of so many dishes leads to a larger collecting area than any previous interferometer, which in turn leads to unprecedented sensitivity. The second array is the ALMA compact array (ACA), which consists of 12 7 m dishes and 4 12 m dishes and is used to recover the missing flux filtered out by the main array.

Currently, 7 bands are available for use on ALMA covering a spectral range from $\sim 84\,\mathrm{GHz}$ (3.57 mm) to 950 GHz (0.32 mm)[6]; however, there are

[4]ALMA Basics. Accessed June 10th, 2015. Available at `https://almascience.eso.org/about-alma/alma-basics`

[5]ALMA Early Science Primer. Accessed June 11th, 2015. Available at `https://almascience.nrao.edu/documents-and-tools/cycle3/alma-early-science-primer`

[6]ALMA Technical Handbook, available at `https://almascience.nrao.edu/documents-and-tools/cycle3/alma-technical-handbook`

gaps in the spectral range due to absorption lines in the Earth's atmosphere. In particular, large gaps in coverage exist at $492 - 610$ GHz and $720 - 787$ GHz, while another gap at $155 - 221$ GHz may be covered in the future by the implementation of an additional receiver band (Band 5).

With its high resolution and unprecedented sensitivity, ALMA provides the tools necessary to unlock the mysteries of the local Universe, the high-redshift Universe and everything in between. From circumstellar disks (Partnership et al., 2015) to high-redshift, luminous star forming galaxies (Ouchi et al., 2013), ALMA allows us to study systems at resolutions and sensitivities never before possible.

1.5 This thesis

Molecular gas is directly linked to star formation at most, if not all, epochs in the Universe. In interactions and mergers, the star formation can be enhanced significantly, and so understanding the molecular gas is paramount to understanding the entire interaction and merger process. Molecular gas tracers, such as CO, [CI] and the dense gas tracers HCN, HNC, and HCO^+, are useful tools to understanding the physical state of the molecular gas, and the dominant physical processes affecting the same gas.

In this thesis, I use observations from the *Herschel* SPIRE-FTS and ALMA to study the molecular gas within the nearby interacting galaxy M51, and the nearby merging galaxies NGC 4038/39. The *Herschel* SPIRE-FTS observations of NGC 4038/39 and M51 were performed as part of the "Very Nearby Galaxies Survey" (VNGS, PI: Christine Wilson), while the ALMA observations of NGC 4038/39 were an ALMA Cycle 1 program (PI: Maximilien Schirm). In addition, new observations of the CO $J = 2-1$ transition in NGC 4038/39 from the James Clerk Maxwell Telescope (JCMT) are presented (PI:

Maximilien Schirm).

The comparison between M51 and NGC 4038/39 is interesting. While there is little argument in the literature that NGC 4038/39 is an ongoing merger, M51 is often characterized as a "normal" spiral galaxy even though it has recently undergone an interaction with NGC 5195. In both cases, the interaction/merger has had an effect on the morphology and star formation of the progenitor galaxies, although both effects are more pronounced in NGC 4038/39. For the first time, the *Herschel* SPIRE-FTS coupled with ground-based observations of CO allows us to study the full CO spectral line energy distribution, up to the $J = 13-12$ transition, tracing molecular gas in a wide variety of excitation conditions. Furthermore, using the *Herschel* SPIRE-FTS mapping capabilities, we can investigate variations in the excitation conditions of CO within spatially extended systems, such as M51 and NGC 4038/39.

This thesis is organized as follows. In Chapter 2, I present *Herschel* SPIRE-FTS observations of CO and [CI] in NGC 4038/39, which are supplemented with ground based observations of CO, including the aforementioned JCMT observation of CO $J = 2-1$. In Chapter 3, I present *Herschel* SPIRE-FTS observations of CO and [CI] in the central $\sim$ 5 kpc of M51, which I supplement with ground based observations of CO from literature. In both Chapter 2 and 3, I present a non-LTE excitation analysis using the CO and [CI] observations, along with a discussion on heating sources within these systems. in Chapter 4, I present high resolution ALMA band 3 observations of HCN, HNC, and HCO^+ in the $J = 1-0$ transition. I summarized this thesis in Chapter 5, and present conclusions based upon this work, while also discussing potential future work to continue the study of M51 and NGC 4038/39.

Bibliography

Acero, F., Aharonian, F., Akhperjanian, A. G., et al. 2009, Science, 326, 1080

Alonso-Herrero, A., Rieke, G. H., Rieke, M. J., & Scoville, N. Z. 2000, ApJ, 532, 845

Barnes, J. E. 2004, MNRAS, 350, 798

Bell, T. A., Viti, S., & Williams, D. A. 2007, MNRAS, 378, 983

Bik, A., Lamers, H. J. G. L. M., Bastian, N., Panagia, N., & Romaniello, M. 2003, A&A, 397, 473

Binns, W. R., Wiedenbeck, M. E., Arnould, M., et al. 2008, New A Rev., 52, 427

Bolatto, A. D., Wolfire, M., & Leroy, A. K. 2013, ARA&A, 51, 207

Carroll, T. J., & Goldsmith, P. F. 1981, ApJ, 245, 891

Clements, D. L., Sutherland, W. J., McMahon, R. G., & Saunders, W. 1996, MNRAS, 279, 477

Coxon, J. A., & Hajigeorgiou, P. G. 2004, J. Chem. Phys., 121, 2992

de Graauw, T., Helmich, F. P., Phillips, T. G., et al. 2010, A&A, 518, L6

Dobbs, C. L., Theis, C., Pringle, J. E., & Bate, M. R. 2010, MNRAS, 403, 625

Draine, B. T. 2003, ARA&A, 41, 241

Duncan, J. C. 1923, ApJ, 57, 137

Fabbiano, G., Zezas, A., & Murray, S. S. 2001, ApJ, 554, 1035

Falgarone, E. 1997, in IAU Symposium, Vol. 170, IAU Symposium, ed. W. B. Latter, S. J. E. Radford, P. R. Jewell, J. G. Mangum, & J. Bally, 119–127

Fischer, J., Shier, L. M., Luhman, M. L., et al. 1996, A&A, 315, L97

Foyle, K., Rix, H.-W., Walter, F., & Leroy, A. K. 2010, ApJ, 725, 534

Gao, Y., Lo, K. Y., Lee, S.-W., & Lee, T.-H. 2001, ApJ, 548, 172

Gao, Y., & Solomon, P. M. 2004, ApJS, 152, 63

Garcia-Burillo, S., Combes, F., & Gerin, M. 1993a, A&A, 274, 148

Garcia-Burillo, S., Guelin, M., & Cernicharo, J. 1993b, A&A, 274, 123

Gendriesch, R., Lewen, F., Klapper, G., et al. 2009, A&A, 497, 927

Graninger, D. M., Herbst, E., Öberg, K. I., & Vasyunin, A. I. 2014, ApJ, 787, 74

Griffin, M. J., Abergel, A., Abreu, A., et al. 2010, A&A, 518, L3

Hernquist, L. 1989, Nature, 340, 687

Herrera, C. N., Boulanger, F., Nesvadba, N. P. H., & Falgarone, E. 2012, A&A, 538, L9

Herschel, W. 1786, Royal Society of London Philosophical Transactions Series I, 76, 457

Hibbard, J. E., van der Hulst, J. M., Barnes, J. E., & Rich, R. M. 2001, AJ, 122, 2969

Hinshaw, G., Weiland, J. L., Hill, R. S., et al. 2009, ApJS, 180, 225

Hodge, J. A., Karim, A., Smail, I., et al. 2013, ApJ, 768, 91

Jarrett, T. H., Polletta, M., Fournon, I. P., et al. 2006, AJ, 131, 261

Johnson, K. E., Leroy, A. K., Indebetouw, R., et al. 2015, ApJ, 806, 35

Juneau, S., Narayanan, D. T., Moustakas, J., et al. 2009, ApJ, 707, 1217

Kamenetzky, J., Glenn, J., Rangwala, N., et al. 2012, ApJ, 753, 70

Kaufman, M. J., Wolfire, M. G., Hollenbach, D. J., & Luhman, M. L. 1999, ApJ, 527, 795

Kazandjian, M. V., Meijerink, R., Pelupessy, I., Israel, F. P., & Spaans, M. 2012, A&A, 542, A65

—. 2015, A&A, 574, A127

Koulouridis, E. 2014, A&A, 570, A72

Kramer, C., Mookerjea, B., Bayet, E., et al. 2005, A&A, 441, 961

Langer, W. D., & Penzias, A. A. 1990, ApJ, 357, 477

Langer, W. D., Velusamy, T., Pineda, J. L., Willacy, K., & Goldsmith, P. F. 2014, A&A, 561, A122

Loenen, A. F., Spaans, M., Baan, W. A., & Meijerink, R. 2008, A&A, 488, L5

Loison, J.-C., Wakelam, V., & Hickson, K. M. 2014, MNRAS, 443, 398

Makiwa, G., Naylor, D. A., Ferlet, M., et al. 2013, Appl. Opt., 52, 3864

Maloney, P. R., Hollenbach, D. J., & Tielens, A. G. G. M. 1996, ApJ, 466, 561

McMillan, P. J. 2011, MNRAS, 414, 2446

Meijerink, R., Spaans, M., Loenen, A. F., & van der Werf, P. P. 2011, A&A, 525, A119

Messier, C. 1781, Catalogue des Nébuleuses & des amas d'Étoiles (Catalog of Nebulae and Star Clusters), Tech. rep.

Mihos, J. C., & Hernquist, L. 1996, ApJ, 464, 641

Mirabel, I. F., Vigroux, L., Charmandaris, V., et al. 1998, A&A, 333, L1

Moreno, J., Torrey, P., Ellison, S. L., et al. 2015, MNRAS, 448, 1107

Naylor, D. A., Baluteau, J.-P., Barlow, M. J., et al. 2010, in Society of Photo-Optical Instrumentation Engineers (SPIE) Conference Series, Vol. 7731, Society of Photo-Optical Instrumentation Engineers (SPIE) Conference Series, 16

Nikola, T., Geis, N., Herrmann, F., et al. 2001, ApJ, 561, 203

Offner, S. S. R., Bisbas, T. G., Bell, T. A., & Viti, S. 2014, MNRAS, 440, L81

Ouchi, M., Ellis, R., Ono, Y., et al. 2013, ApJ, 778, 102

Papadopoulos, P. P. 2007, ApJ, 656, 792

—. 2010, ApJ, 720, 226

Papadopoulos, P. P., Thi, W.-F., & Viti, S. 2004, MNRAS, 351, 147

Papadopoulos, P. P., van der Werf, P., Xilouris, E., Isaak, K. G., & Gao, Y. 2012, ApJ, 751, 10

Parkin, T. J., Wilson, C. D., Schirm, M. R. P., et al. 2013, ApJ, 776, 65

Partnership, A., Brogan, C. L., Perez, L. M., et al. 2015, ArXiv e-prints, arXiv:1503.02649

Perrine, C. D. 1922, MNRAS, 82, 486

Pety, J., Schinnerer, E., Leroy, A. K., et al. 2013, ApJ, 779, 43

Pilbratt, G. L., Riedinger, J. R., Passvogel, T., et al. 2010, A&A, 518, L1

Poglitsch, A., Waelkens, C., Geis, N., et al. 2010, A&A, 518, L2

Polk, K. S., Knapp, G. R., Stark, A. A., & Wilson, R. W. 1988, ApJ, 332, 432

Rangwala, N., Maloney, P. R., Glenn, J., et al. 2011, ApJ, 743, 94

Rickard, L. J., & Palmer, P. 1981, A&A, 102, L13

Roberts, I. 1889, MNRAS, 49, 389

Sakamoto, K., Aalto, S., Evans, A. S., Wiedner, M. C., & Wilner, D. J. 2010, ApJ, 725, L228

Sanders, D. B., & Mirabel, I. F. 1996, ARA&A, 34, 749

Satyapal, S., Sambruna, R. M., & Dudik, R. P. 2004, A&A, 414, 825

Schirm, M. R. P., Wilson, C. D., Parkin, T. J., et al. 2014, ApJ, 781, 101

Schöier, F. L., van der Tak, F. F. S., van Dishoeck, E. F., & Black, J. H. 2005, A&A, 432, 369

Schweizer, F., Burns, C. R., Madore, B. F., et al. 2008, AJ, 136, 1482

Scoville, N., & Young, J. S. 1983, ApJ, 265, 148

Scoville, N. Z., Polletta, M., Ewald, S., et al. 2001, AJ, 122, 3017

Shimajiri, Y., Sakai, T., Tsukagoshi, T., et al. 2013, ApJ, 774, L20

Smith, M. A., Schlemmer, S., von Richthofen, J., & Gerlich, D. 2002, ApJ, 578, L87

Spinoglio, L., Pereira-Santaella, M., Busquet, G., et al. 2012, ApJ, 758, 108

Stanford, S. A., Sargent, A. I., Sanders, D. B., & Scoville, N. Z. 1990, ApJ, 349, 492

Steinmetz, M., & Navarro, J. F. 2002, New Astron., 7, 155

Swinyard, B. M., Ade, P., Baluteau, J.-P., et al. 2010, A&A, 518, L4

Swinyard, B. M., Polehampton, E. T., Hopwood, R., et al. 2014, MNRAS, 440, 3658

Talbi, D., Ellinger, Y., & Herbst, E. 1996, A&A, 314, 688

Tielens, A. G. G. M. 2005, The Physics and Chemistry of the Interstellar Medium

Tielens, A. G. G. M., & Hollenbach, D. 1985, ApJ, 291, 722

Tikhonov, N. A., Galazutdinova, O. A., & Tikhonov, E. N. 2009, Astronomy Letters, 35, 599

Toomre, A., & Toomre, J. 1972, ApJ, 178, 623

van der Hulst, J. M. 1979, A&A, 71, 131

van der Tak, F. F. S., Black, J. H., Schöier, F. L., Jansen, D. J., & van Dishoeck, E. F. 2007, A&A, 468, 627

VERITAS Collaboration, Acciari, V. A., Aliu, E., et al. 2009, Nature, 462, 770

Weiß, A., De Breuck, C., Marrone, D. P., et al. 2013, ApJ, 767, 88

Whitmore, B. C., Zhang, Q., Leitherer, C., et al. 1999, AJ, 118, 1551

Whitmore, B. C., Chandar, R., Schweizer, F., et al. 2010, AJ, 140, 75

Whitmore, B. C., Brogan, C., Chandar, R., et al. 2014, ApJ, 795, 156

Wilson, C. D., Scoville, N., Madden, S. C., & Charmandaris, V. 2000, ApJ, 542, 120

—. 2003, ApJ, 599, 1049

Wolfire, M. G., Hollenbach, D., & McKee, C. F. 2010, ApJ, 716, 1191

Wu, R., Polehampton, E. T., Etxaluze, M., et al. 2013, A&A, 556, A116

Young, J. S., & Scoville, N. Z. 1991, ARA&A, 29, 581

Zhang, H.-X., Gao, Y., & Kong, X. 2010, MNRAS, 401, 1839

Zhu, M., Seaquist, E. R., & Kuno, N. 2003, ApJ, 588, 243

Chapter 2

Herschel SPIRE-FTS Observations of Excited CO and [CI] in the Antennae (NGC 4038/39): Warm and Cold Molecular Gas

Maximilien R.P. Schirm, Christine D. Wilson, Tara J. Parkin, Julia Kamenetzky, Jason Glenn, Naseem Rangwala, Luigi Spinoglio, Miguel Pereira-Santaella, Maarten Baes, Michael J. Barlow, Dave L. Clements, Asantha Cooray, Ilse De Looze, Oskar Ł. Karczewski, Suzanne C. Madden, Aurélie Rémy-Ruyer, and Ronin Wu

2014, The Astrophysical Journal, Volume 781, Issue 2, article id. 101, 24 pages, DOI: 10.1088/0004-637X/781/2/101. Reproduced with permission from The Astrophysical Journal and the American Astronomical Society

"All we have to decide is what to do with the time that is given us."

"Gandalf the Grey" from *The Fellowship of the Ring* by J.R.R. Tolkien (1954)

Abstract

We present *Herschel* SPIRE-FTS observations of the Antennae (NGC 4038/39), a well studied, nearby (22 Mpc) ongoing merger between two gas rich spiral galaxies. The SPIRE-FTS is a low spatial (FWHM $\sim 19'' - 43''$) and spectral (~ 1.2 GHz) resolution mapping spectrometer covering a large spectral range ($194 - 671\,\mu$m, $450\,$GHz $- 1545\,$GHz). We detect 5 CO transitions ($J = 4-3$ to $J = 8-7$), both [CI] transitions and the [NII]205μm transition across the entire system, which we supplement with ground based observations of the CO $J = 1-0$, $J = 2-1$ and $J = 3-2$ transitions, and Herschel PACS observations of [CII] and [OI]63μm. Using the CO and [CI] transitions, we perform both a LTE analysis of [CI], and a non-LTE radiative transfer analysis of CO and [CI] using the radiative transfer code RADEX along with a Bayesian likelihood analysis. We find that there are two components to the molecular gas: a cold ($T_{kin} \sim 10 - 30\,$K) and a warm ($T_{kin} \gtrsim 100\,$K) component. By comparing the warm gas mass to previously observed values, we determine a CO abundance in the warm gas of $x_{\rm CO} \sim 5 \times 10^{-5}$. If the CO abundance is the same in the warm and cold gas phases, this abundance corresponds to a CO $J = 1-0$ luminosity-to-mass conversion factor of $\alpha_{\rm CO} \sim 7\ M_\odot\,{\rm pc}^{-2}$ (K km s^{-1})$^{-1}$ in the cold component, similar to the value for normal spiral galaxies. We estimate the cooling from H_2, [CII], CO and [OI]63μm to be $\sim 0.01 L_\odot/M_\odot$. We compare PDR models to the ratio of the flux of various CO transitions, along with the ratio of the CO flux to the far-infrared flux in NGC 4038, NGC 4039 and the overlap region. We find that the densities recovered from our non-

LTE analysis are consistent with a background far-ultraviolet field of strength $G_0 \sim 1000$. Finally, we find that a combination of turbulent heating, due to the ongoing merger, and supernova and stellar winds are sufficient to heat the molecular gas.

2.1 Introduction

Luminous and ultra luminous infrared galaxies are a well studied class of infrared (IR) bright galaxies whose excess IR emission comes from dust heated by enhanced star formation activity (Cluver et al., 2010). Their enhanced star formation rate directly correlates with a star formation efficiency (SFE) $\sim 4-10$ times greater than in normal galaxies (Genzel et al., 2010) typically seen in the form of starbursts throughout the galaxy (Sanders & Mirabel, 1996). Many luminous infrared galaxies (LIRGs, $L_{IR} > 10^{11} L_\odot$) and almost all ultra luminous infrared galaxies (ULIRGs, $L_{IR} > 10^{12} L_\odot$) are found to be in an advanced merging state between two or more galaxies (Clements et al., 1996; Sanders & Mirabel, 1996); these starbursts are likely the result of the ongoing merger (Hibbard, 1997), triggered by the redistribution of material throughout the merging galaxies (Toomre & Toomre, 1972). It has been suggested that all mergers undergo a period of "super starbursts" (Joseph & Wright, 1985), where $\gtrsim 10^9 M_\odot$ of stars form in $\sim 10^8$ years (Gehrz et al., 1983).

The Antennae (NGC 4038/39, Arp 244) is a young, nearby, ongoing merger between two gas rich spiral galaxies, NGC 4038 and NGC 4039. At a distance of only 22 ± 3 Mpc (Schweizer et al., 2008), the Antennae may represent the nearest such merger. Its infrared brightness of $L_{IR} = 7.5 \times 10^{10} L_\odot$ (Gao et al., 2001) approaches that of a LIRG and is likely the result of merger triggered star formation. The majority of the star formation is occurring within the two nuclei (NGC 4038, NGC 4039), along with a third region where the two disks are believed to overlap (Stanford et al., 1990), also sometimes referred to as the interaction region (IAR, e.g. Schulz et al. 2007). A fourth star forming region of interest is located to the west of NGC 4038 and is known as the “western loop”. The X-ray luminosity in the Antennae is enhanced relative to normal spiral galaxies, with 50% of the X-ray emission originating from hot diffuse gas outside of these four regions (Read et al., 1995); however, the presence of an active galactic nucleus (AGN) has been ruled out (Brandl et al., 2009).

As a result of the star formation process, most of the star clusters in the Antennae are in the two nuclei and the overlap region, with the overlap region housing the youngest ($\lesssim 5\,$Myr) of these star clusters, and the second youngest found in the western loop ($5-10\,$Myr) (Whitmore & Schweizer, 1995; Whitmore et al., 1999). Some of the star clusters found near the overlap region are super star clusters with masses of a few $10^6\,M_\odot$ (Whitmore et al., 2010). Comparisons of *Spitzer*, GALEX, HST and 2MASS images by Zhang et al. (2010) showed that the star formation rate itself peaks in the overlap region and western loop, agreeing with previous results by Gao et al. (2001). The overlap region exhibits characteristics of younger, more recent star formation (Zhang et al., 2010). Far-infrared spectroscopy of the Antennae with the ISO-LWS spectrometer, together with ground-based Fabry-Perot imaging spectroscopy, has been used to constrain the age of the instantaneous starburst to $(7-8) \times 10^6\,$yr, producing a total stellar mass of $(2.5 \pm 1.5) \times 10^8\,M_\odot$ with a luminosity of $(7 \pm 4) \times 10^{10}\,L_\odot$ (Fischer et al., 1996).

The star forming molecular gas in the Antennae is well studied, with observations of the molecular gas tracer CO in the $J = 1-0$ (Wilson et al., 2000; Gao et al., 2001; Wilson et al., 2003; Zhu et al., 2003; Schulz et al., 2007), $J = 2-1$ (Zhu et al., 2003; Schulz et al., 2007; Wei et al., 2012), $J = 3-2$ (Zhu et al., 2003; Schulz et al., 2007; Ueda et al., 2012), $J = 6-5$ (Bayet et al., 2006) and $J = 7-6$ (Bayet et al., 2006) transitions. Interferometric observations of the ground state transition by Wilson et al. (2000) and Wilson et al. (2003) found ~ 100 super-giant molecular complexes (SGMCs) scattered throughout the Antennae. The 7 most massive of these SGMCs consist of the two nuclei (NGC 4038 and NGC 4039), and five others located in the overlap region. Assuming a CO-to-H_2 conversion factor of $3 \times 10^{20}\,H_2\,cm^{-2}\,(K\ km\ s^{-1})^{-1}$, the molecular gas masses of the SGMCs are on the order of $10^8\,M_\odot$. In addition, recent interferometric observations of the CO $J = 3-2$ transitions by Ueda et al. (2012) show that half of the $J = 3-2$ emission originates from the overlap region. Only 30% of the giant molecular clouds (GMCs) resolved in the $J = 3-2$ map coincide with star clusters which have been detected in the optical and near infrared, suggesting that the $J = 3-2$ emission may in fact be tracing future star forming regions.

Single-dish observations of the CO $J = 1-0$ line by Zhu et al. (2003) suggest that, assuming the same conversion factor as Wilson et al. (2000), the total molecular gas mass of the system is $1.2 \times 10^{10}\,M_\odot$, with about $\sim 40\%$ of the total gas mass in the overlap region ($4.5 \times 10^9\,M_\odot$). Large Velocity Gradient (LVG) models by Zhu et al. (2003) suggest that there are at least two phases to the molecular gas: a cold phase ($T_{kin} \sim 40\,K$) and a warm phase ($T_{kin} \sim 100\,K$). Bayet et al. (2006) performed a single component LVG analysis of NGC 4038 and the overlap region, finding that in the overlap region the molecular gas of their single component is warm ($T_{kin} \sim 140\,K$).

Launched in 2009, the Herschel Space Observatory (*Herschel*; Pilbratt et al. 2010) explores the largely unobserved wavelength range of $55-671\,\mu m$. The Spectral and Photometric Imaging Receiver (SPIRE; Griffin et al. 2010) spectrometer is the Fourier Transform Spectrometer (FTS; Naylor et al. 2010b), an imaging spectrometer covering a total spectral range from $194\,\mu m$ to $671\,\mu m$ ($\sim 450\,GHz$ to $\sim 1545\,GHz$). The SPIRE-FTS allows us to simultaneously observe all molecular and atomic transitions which lie within its spectral range. A total of 10 CO transitions, from $J = 4{-}3$ to $J = 13{-}12$, and both [CI] transitions at 492 GHz (609 μm) and 809 GHz (370 μm), lie within this spectral range, making the SPIRE-FTS ideal for studying both cold and warm molecular gas in extra-galactic sources (e.g. see Panuzzo et al. 2010; van der Werf et al. 2010; Rangwala et al. 2011; Kamenetzky et al. 2012; Spinoglio et al. 2012; Meijerink et al. 2013; Pereira-Santaella et al. 2013).

We have obtained observations of the Antennae using the SPIRE-FTS as part of the guaranteed time key project "Physical Processes in the Interstellar Medium of Very Nearby Galaxies" (PI: Christine Wilson), which we supplement with ground based observations of the CO $J = 1-0$, $J = 2-1$ and $J = 3-2$ transitions. In Section 2.2 we present the observations and method used to reduce these data. In Section 2.3 we present a radiative transfer analysis used to constrain the physical properties of the gas. We discuss the implications in Section 2.4, where we investigate the possible heating mechanisms of the molecular gas, including modeling of Photon Dominated Regions (PDRs).

2.2 Observations

We observed both the nucleus of NGC 4038 (hereafter NGC 4038) and the overlap region using the SPIRE FTS in high spectral resolution (FWHM $= 0.048\,\mathrm{cm}^{-1}$), full-sampling mode on December 12th, 2010 (OD 572). The observation of NGC 4038 is centered at ($12\,\mathrm{h}01\,\mathrm{m}53.00\,\mathrm{s}$, $-18°52'01.0''$) while the observation of the overlap region is centered at ($12\,\mathrm{h}01\,\mathrm{m}54.90\,\mathrm{s}$, $-18°52'45.0''$). The observation IDs for the observations of NGC 4038 and the overlap region are 1342210860 and 1342210859, respectively, and the total integration time for each observation is 17,843 seconds, for a total integration time of 35,686 seconds (~ 10 hours). In addition to the SPIRE observations, we also present here ground-based CO $J = 1-0$ from the Nobeyama Radio Observatory (Zhu et al., 2003), along with CO $J = 2-1$ and $J = 3-2$ maps from the James Clerk Maxwell Telescope (JCMT). We also include observations of [CII] and [OI]63 from the *Herschel* Photodetecting Array Camera and Spectrometer (PACS) instrument.

2.2.1 FTS Data reduction

We reduce the FTS data using a modified version of the standard Spectrometer Mapping user pipeline and the Herschel Interactive Processing Environment version 9.0, and SPIRE calibration context version 8.1. Fulton et al. (2010) and Swinyard et al. (2010) described an older version of the data reduction pipeline and process. The standard mapping pipeline assumes that the source is extended enough to fill the beam uniformly. Interferometric observations of NGC 4038/39 show that the molecular gas is partially extended (Wilson et al., 2000) and does not fill the beam (Figure 2.1). To account for this, we apply a point-source correction to all of the detectors in both of our bolometric arrays in order to calibrate the flux accurately across the entire mapped region. Furthermore, by applying this point source correction, we obtain a cube with the same calibration scale as our ground based observations. This point-source correction is calculated from models and observations of Uranus, and is the product of the beam area and of a point source coupling efficiency (see Chapter 5 of the SPIRE Observers Manual version 2.4[1]). The correction itself varies with frequency and is unique for each individual detector.

After applying the point-source correction, we combine the observations using the *spireProjection* task into two data cubes : one for the spectrometer long wave (SLW) bolometric array, the other for the spectrometer short wave

[1] Available at `http://herschel.esac.esa.int/Docs/SPIRE/html/spire_om.html`

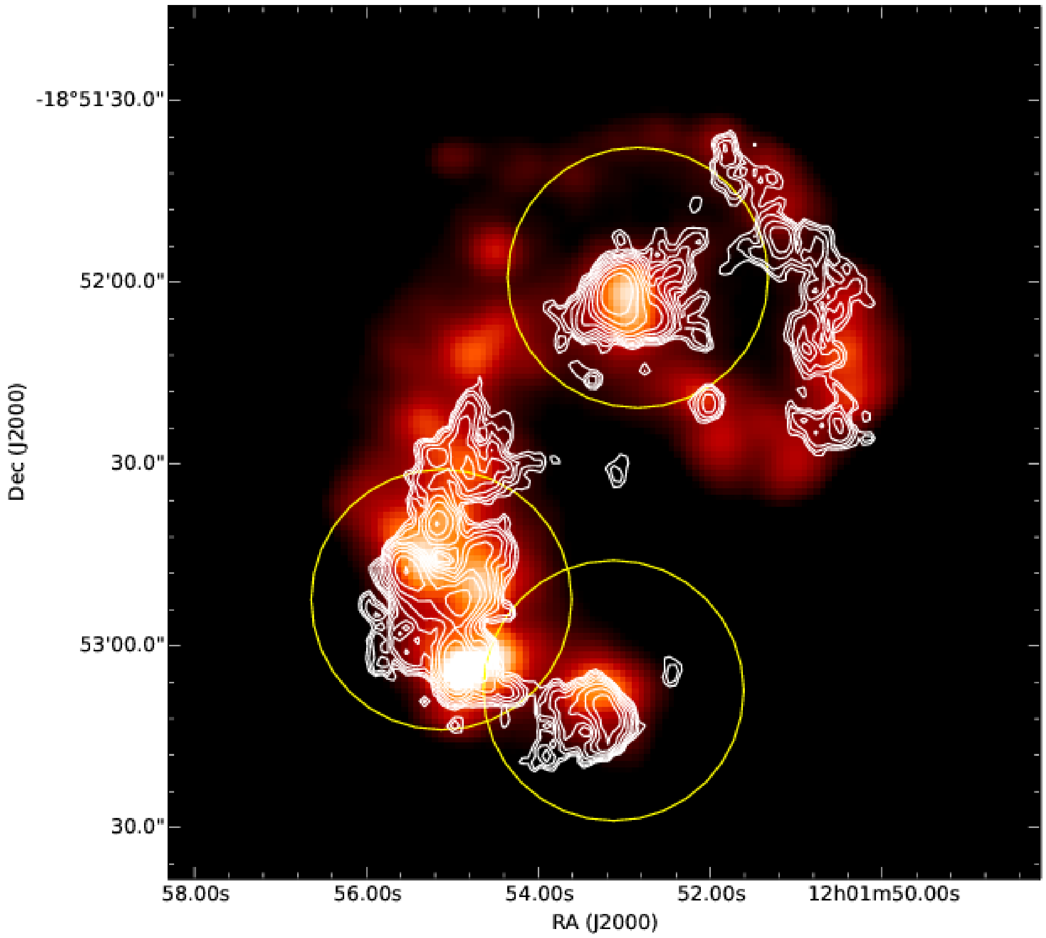

Figure 2.1 CO $J = 1-0$ contours from Wilson et al. (2003) overlaid on the PACS 70 μm observations of the Antennae from Klaas et al. (2010). The white contours correspond to 1%, 1.6%, 2.5%, 4%, 6%, 9.5%, 15%, 23%, 37%, and 57% the peak intensity. The yellow circles indicate the approximate region observed for NGC 4038 (*north-west*), the overlap region (*south-east*), and NGC 4039 (*south-west*) for the FTS beam at ~ 460 GHz ($\sim 43''$).

(SSW) bolometric arrays. We use a pixel size of $15''$ for both data cubes, which we determined empirically as a balance between a sufficient number of detector hits per pixel and small pixel sizes. In addition, we create a data cube for the SSW with $3''$ pixels for the purposes of correcting the [CII] ionized gas fraction (see Section 2.4.3.1). The FTS spectrum for the overlap region is shown in Figure 2.2.

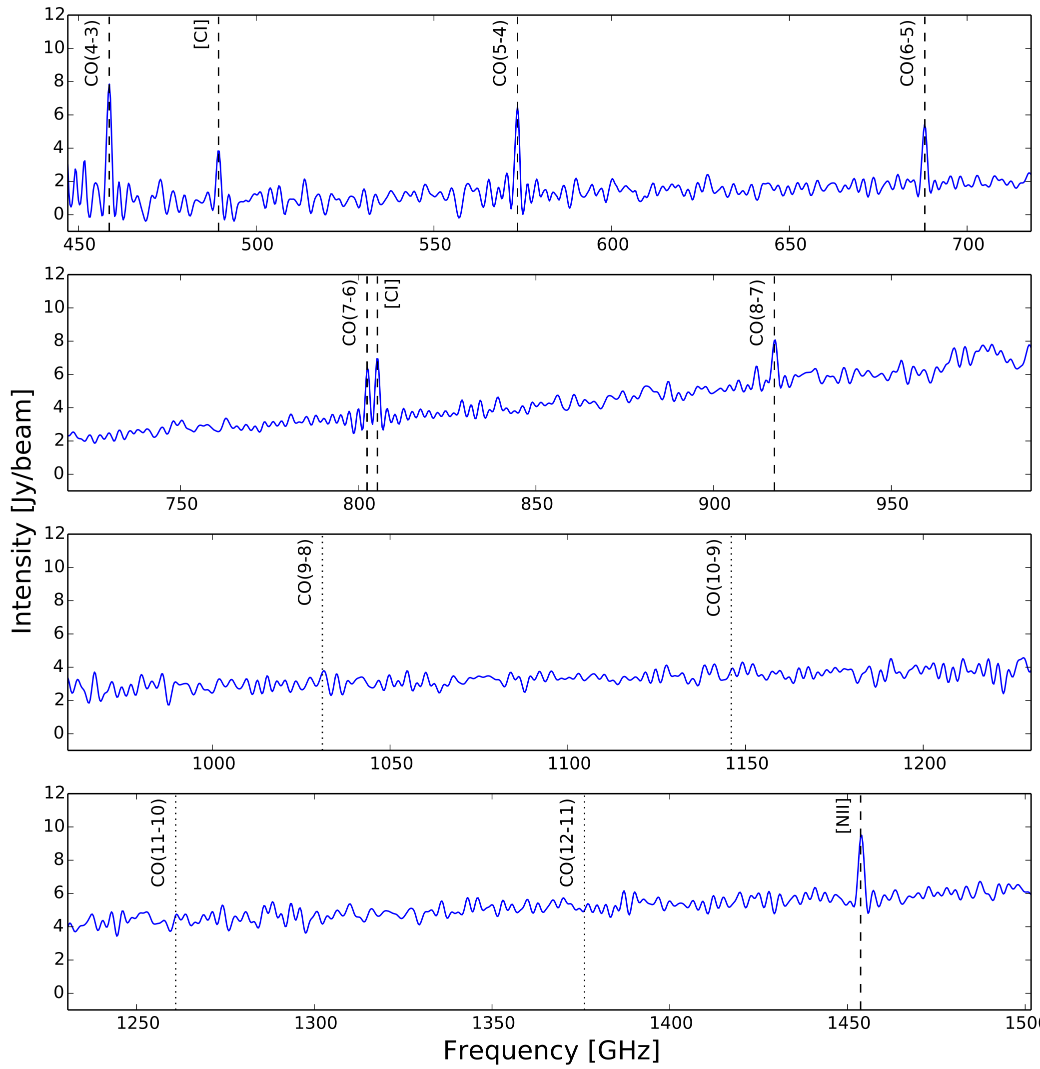

Figure 2.2 FTS spectrum for the overlap region covering the entire spectral range of the FTS. This position corresponds to the blue box in Figure 2.5. The top two panels correspond to the SLW and the bottom two panels correspond to the SSW, while the jump in the continuum between the second and third panels from the top is due to the large difference in beam size between the SLW ($\sim 37''$) and the SSW ($\sim 21''$) at the junction. The dashed lines indicate the detected and identified molecular and atomic transitions while the dotted lines indicate where we would expect to find the undetected higher J CO transitions.

2.2.1.1 Line Fitting

We detect 5 CO transitions in emission, from $J = 4-3$ to $J = 8-7$. We also detect the [CI] $^3\mathrm{P}_1 - ^3\mathrm{P}_0$ and $^3\mathrm{P}_2 - ^3\mathrm{P}_1$ transitions along with the [NII] ($^3\mathrm{P}_1 - ^3\mathrm{P}_0$) transition. We wrote a custom line fitting routine to measure the integrated intensities for all detected lines in the SLW and the SSW spectra across the entire data cube. In each pixel in the cube, the routine first removes the baseline by masking out all the lines in the spectrum and fitting a high-order polynomial to the remaining spectrum. Next, the routine fits a Sinc function to each line in the spectrum. To calculate the integrated intensity of each line we integrate over the entire Sinc function. In the case of the CO $\mathrm{J} = 7-6$ and [CI] $J = 2-1$ lines, the routine fits both lines simultaneously, each with its own Sinc function. The resulting integrated intensity maps are shown in Figures 2.3 and 2.4.

2.2.2 Ancillary Data

2.2.2.1 CO $J = 1-0$

We obtained CO $J = 1-0$ observations of the Antennae from Zhu et al. (2003). They obtained these observations from the Nobeyama Radio Observatory, with a telescope beam size of $15''$. The final map consists of three 64-point maps each covering $68'' \times 68''$, encompassing the CO emitting regions in NGC 4038, the overlap region and NGC 4039 in their entirety. We collapse the data cube using the `Starlink` software package (Currie et al., 2008). The total usable bandwidth was 350 MHz, corresponding to $\sim 640\,\mathrm{km\,s^{-1}}$. The FWHM of the CO $J = 1-0$ emission line across the Antennae is $\sim 100-200\,\mathrm{km\,s^{-1}}$; therefore, not enough bandwidth was available to estimate the uncertainty in each pixel reliably. We therefore estimate a total uncertainty, calibration included, of 20% in the final collapsed image.

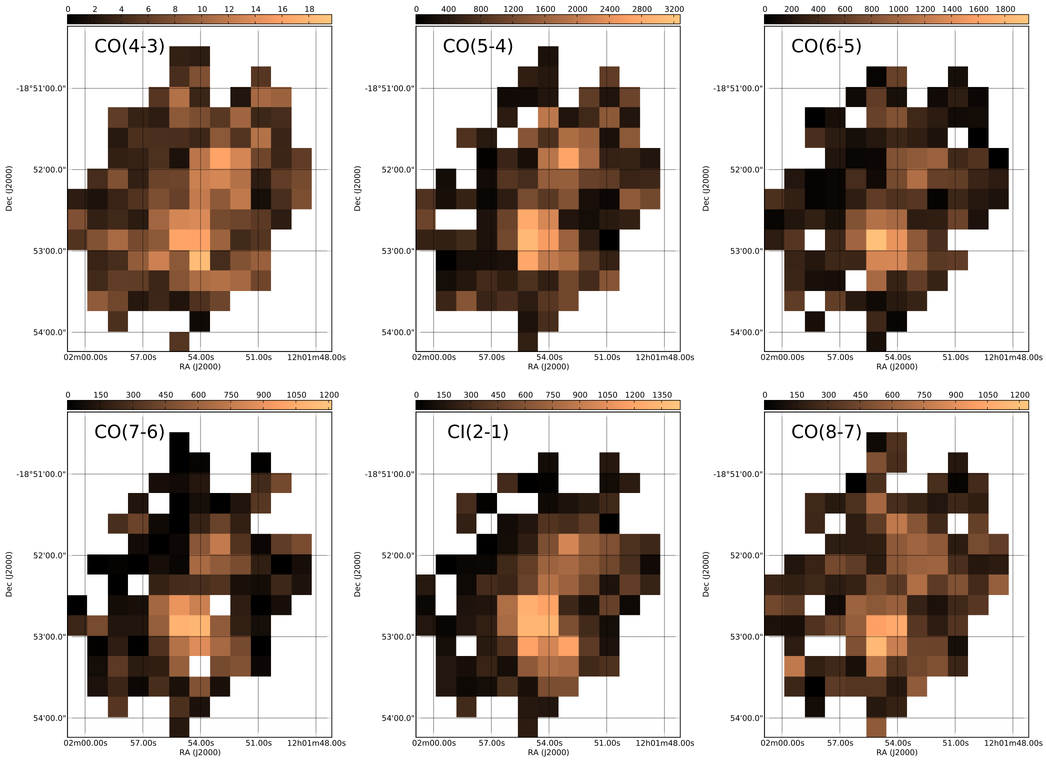

Figure 2.3 Integrated intensity maps for the SPIRE FTS CO and [CI] emission lines in units of Jy km s^{-1}. These maps are at the instrument resolution. The [CI] $1-0$ line map is shown in Figure 2.5.

2.2.2.2 CO $J = 2-1$ and CO $J = 3-2$

The CO $J = 2-1$ transition was observed in the Antennae using the JCMT on 2013 March 25 and 2013 April 3 as part of project M13AC09 (PI: Maximilien Schirm). These data were obtained using Receiver A3 in raster mapping mode. The resulting map is Nyquist sampled and covers the entire CO emitting region with a total area of $140'' \times 140''$ and a total integration time of 14, 940 seconds. The main-beam efficiency was $\eta_{MB} = 0.69$ and the beam size was $20.8''$ at 230.56 GHz. The JCMT CO $J = 3-2$ observations were obtained as part of project M09BC05 (PI: Tara Parkin) on 2009 December 10, 16 and 17. The beam size of the telescope was $14.5''$. We obtained a raster map over an area of $159'' \times 186''$ in position-switched mode with a total integration time of 2, 111

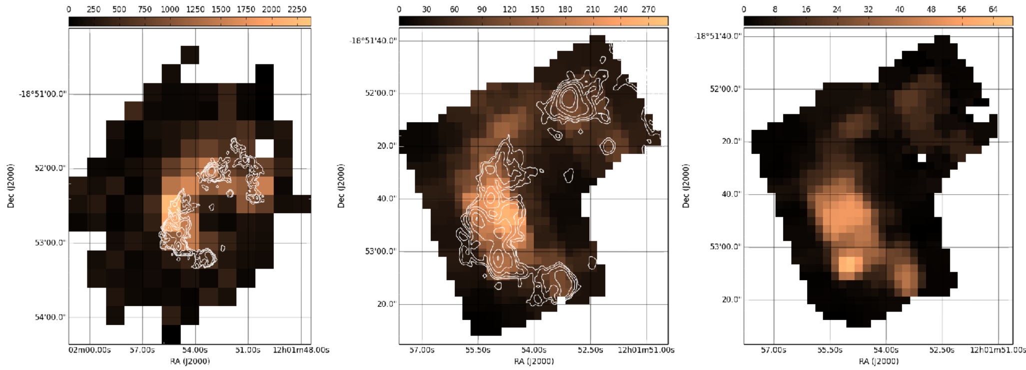

Figure 2.4 Integrated intensity maps for the [NII] 205 μm (left), [CII] 158 μm (centre), and [OI] 63 μm (right) atomic fine structure lines at the instrument resolution. The [NII] map is in units of Jy beam^{-1} km s^{-1}, while the [CII] and [OI] maps are in units of Jy sr^{-1} km s^{-1}. The CO $J = 1-0$ contours from Wilson et al. (2003) are overlaid in white on the [NII] and [CII] images, with the contours corresponding to 1%, 2.5%, 6% 15%, 37% and 57% the peak intensity.

seconds, and we used a bandwidth of 1 GHz across 2048 channels. We reduce both datasets using the methods described in Warren et al. (2010) and Parkin et al. (2012) using the `Starlink` software package, with the exception that we convolve the maps using custom convolution kernels described in section 2.2.3 rather than a Gaussian kernel.

2.2.2.3 [CII] 158 μm and [OI] 63 μm

The [CII] 158 μm and [OI] 63 μm transitions were observed in the Antennae using the *Herschel* PACS instrument each in three separate pointings: one centered on each of the nuclei of NGC 4038 (Observation IDs 1342199405 and 1342199406), NGC 4039 (Observation IDs 1342210820 and 1342210821), and the overlap region (Observation IDs 1342210822 and 1342210823). All of these observations were performed in a single pointing in chopping-nodding mode. The field-of-view for each observation is $47'' \times 47''$, and all observations were binned to a $3''$ pixel size. The beam sizes and spectral resolution were $\sim 11''$ and 239 km/s for [CII] 158 μm, and $\sim 9''$ and 98 km/s for [OI] 63 μm

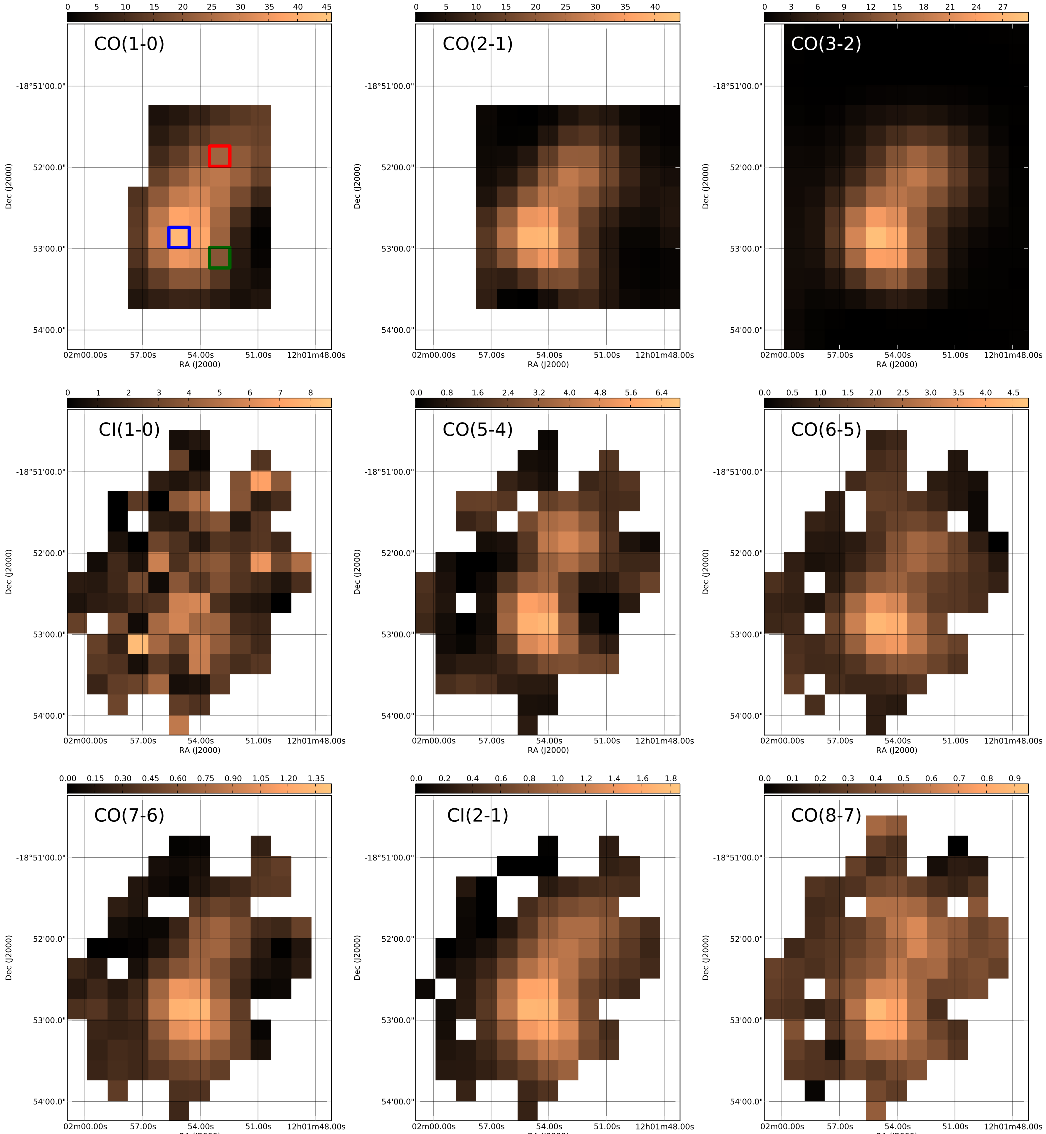

Figure 2.5 Convolved integrated intensity maps for CO and [CI] in units of K km s^{-1}. The CO $J = 1-0$ observations are from the NRO (Zhu et al., 2003), while the CO $J = 2-1$ and $J = 3-2$ observations are from the JCMT. All other observations are from the SPIRE-FTS. All of these maps except for the [CI] $J = 1-0$ maps have been convolved to match the largest beam size of the FTS at 43$''$. The red, blue and green squares on the CO $J = 1-0$ map indicate the location of NGC 4038, the overlap region and NGC 4039 (See Figure 2.1 for beam location). The CO $J = 4-3$ image is shown in Figure 2.3.

(PACS observers manual version 2.5.1[2]).

The level 2 data cubes were obtained from the *Herschel* Science Archive on October 10th, 2012 ([CII]158 μm) and December 12th, 2012 ([OI]63 μm). For each data cube, we fit and subtract the baseline in each pixel with a first-order polynomial before fitting the line with a Gaussian. We create an integrated intensity map for each transition by integrating across the fitted Gaussian in each pixel. For each transition, we combine the three maps using *wcsmosaic* in the `Starlink` software package. The resulting maps are shown in Figure 2.4.

2.2.3 Convolution

The FTS beam size and shape varies across both the SLW and SSW, from $\sim 17''$ to $\sim 43''$ (SPIRE Observers' Manual version 2.4, Swinyard et al. 2010), with the largest beam size occurring at the low frequency end of the SLW. We developed convolution kernels using the method described in Bendo et al. (2012) for the ground-based observations of the CO $J = 1-0$, $J = 2-1$ and $J = 3-2$ transitions, and for the SPIRE observations of $J = 5-4$ to $8-7$ transitions to match the CO $J = 4-3$ beam ($\sim 43''$). The kernels for the SPIRE CO transitions are the same kernels used in Kamenetzky et al. (2012) and Spinoglio et al. (2012). We use the CO $J = 7-6$ kernel to convolve the [CI] $J = 2-1$ map. Finally, we convert from Jy beam^{-1} km s^{-1} to K km s^{-1} using

$$I_{ij} = S_{ij} \left[0.0109 \theta_{ij}^2 \left(\frac{\nu_{ij}}{115} \right)^2 \right]^{-1} \tag{2.1}$$

where ν_{ij} is the frequency of the transition in GHz, θ_{ij} is the full-width half-maximum beam size in arcseconds, I_{ij} is the integrated intensity in units of

[2]Available at `http://herschel.esac.esa.int/Docs/PACS/html/pacs_om.html`

Table 2.1. Line flux measurements

Line	Rest frequency GHz	NGC 4038 [K km s^{-1}]	Overlap region [K km s^{-1}]	NGC 4039 [K km s^{-1}]	Calibration uncertainty %
CO $J = 1 - 0$	115.27	23.1	42.3	19.6	20
CO $J = 2 - 1$	230.54	20.6 ± 0.4	40.0 ± 0.4	25.6 ± 0.4	15
CO $J = 3 - 2$	345.80	15.0 ± 0.3	28.7 ± 0.4	15 ± 1	15
CO $J = 4 - 3$	461.04	16 ± 1	16.4 ± 0.2	8.5 ± 0.8	12
CO $J = 5 - 4$	576.28	4.5 ± 0.4	6.0 ± 0.5	3.4 ± 0.6	12
CO $J = 6 - 5$	691.47	2.5 ± 0.3	4.5 ± 0.3	3.0 ± 0.2	12
CO $J = 7 - 6$	806.65	0.8 ± 0.2	1.3 ± 0.4	1.0 ± 0.2	12
CO $J = 8 - 7$	921.80	0.7 ± 0.1	0.9 ± 0.1	0.55 ± 0.07	12
CO $J = 9 - 8$[a]	1036.91	< 0.8	< 0.9	< 1.2	12
[CI] $J = 1 - 0$	492.16	2.4 ± 0.4	5.7 ± 0.1	4.0 ± 0.5	12
[CI] $J = 2 - 1$	809.34	1.0 ± 0.2	1.7 ± 0.4	1.3 ± 0.2	12
[NII][b]	1461.13	2.9 ± 0.2	2.20 ± 0.04	1.09 ± 0.03	12

[a]3σ **upper limit**

[b]Measurements for [NII] are from the unconvolved map (beam size $\sim 17''$). All other measurements are at a beam size of $43''$.

K km s^{-1} and S_{ij} is in units of Jy beam^{-1} km s^{-1}. We use a beam size of $43.4''$ for the convolved maps. The convolved maps are shown in Figure 2.5 while the integrated intensities for the nuclei of NGC 4038 and NGC 4039, and the overlap region are given in Table 2.1 in units of K km s^{-1}.

2.3 Radiative Transfer Analysis

2.3.1 [CI] Local Thermodynamic Equilibrium Analysis

In this section we calculate the temperature of the gas using the two [CI] lines, $^3P_1 -^3 P_0$ and $^3P_2 -^3 P_1$, assuming local thermodynamic equilibrium (LTE). We calculate the kinetic temperature using a rewritten version of equation 3 from Spinoglio et al. (2012)

$$T_{kin} = -\frac{E_{21}}{k}\left[\ln\left(\frac{g_1}{g_2}\frac{A_{10}\nu_{21}^2 I_{21}}{A_{21}\nu_{10}^2 I_{10}}\right)\right]^{-1} \tag{2.2}$$

where ν_{ij} is the frequency of the transition in GHz, I_{ij} is the integrated intensity in units of K km s^{-1}, A_{ij} is the Einstein coefficient and γ_{ij} is the collisional rate. We use the values of $A_{10} = 7.93 \times 10^{-8}\,\mathrm{s}^{-1}$, $A_{20} = 2 \times 10^{-14}\,\mathrm{s}^{-1}$, and $A_{21} = 2.68 \times 10^{-7}\,\mathrm{s}^{-1}$ for the Einstein coefficients (Papadopoulos et al., 2004). For the collisional rate coefficients, we assume a temperature of 30 K and an ortho-to-para ratio of 3 and, using the tabulated data from Schroder et al. (1991), calculate $\gamma_{10} = 1.3 \times 10^{-10}\,\mathrm{cm}^3/\mathrm{s}$, $\gamma_{20} = 6.9 \times 10^{-11}\,\mathrm{cm}^3/\mathrm{s}$ and $\gamma_{21} = 8.3 \times 10^{-11}\,\mathrm{cm}^3/\mathrm{s}$.

We calculate the temperature in all pixels in our map where we detect both [CI] transitions (Figure 2.6). Our results suggest that the majority of the [CI] emission is associated with cold molecular gas with temperatures of $\sim 10 - 30$ K.

2.3.2 Non-LTE analysis

We model the CO and [CI] emission using the non-LTE code RADEX (van der Tak et al., 2007), available from the Leiden Atomic and Molecular Database (LAMDA, Schöier et al. 2005). RADEX iteratively solves for statistical equilibrium based on three input parameters: the molecular gas density ($n(\mathrm{H_2})$), the column density of the molecular species of interest (N_{mol}) and the kinetic temperature of the molecular gas (T_{kin}). From these three input parameters, RADEX will calculate the line fluxes and optical depths for any molecular or atomic species for which basic molecular data, including the energy levels, Einstein A coefficients and collision rates, are known. Molecular data files are available from LAMDA.

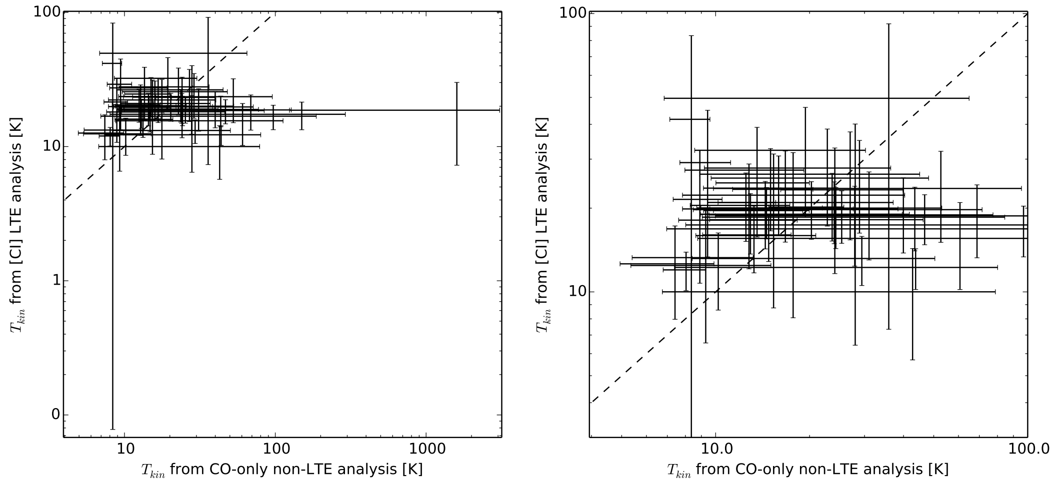

Figure 2.6 Left: Cold molecular gas temperature from the [CI] LTE analysis (*y-axis*) and the CO-only non-LTE radiative transfer analysis (*x-axis*). Right: Zoom in on the upper left portion of the *left* panel. The error bars correspond to the 1-sigma uncertainty in the respective temperatures. Note that where the error bars cross corresponds only to the midpoint of the 1-sigma ranges in log space and not the most probable value. The dashed diagonal line corresponds to where the two temperature are equal.

We calculate a grid of CO fluxes and optical depths with RADEX spanning a large parameter space in density, temperature and column density per unit line width ($N_{\text{mol}}/\Delta V$) using the uniform sphere approximation. In addition, we calculate a secondary grid of [CI] fluxes and optical depths based on the same parameter space while varying the [CI] abundance relative to CO ($x_{\text{[CI]}}/x_{\text{CO}}$). The Antennae itself is significantly more complex than a simple uniform sphere; however our results are averaged over the entire FTS beam. The complete list of grid parameters is shown in Table 2.2.

2.3.2.1 Likelihood analysis

We used a Bayesian likelihood code (Ward et al., 2003; Naylor et al., 2010a; Panuzzo et al., 2010; Kamenetzky et al., 2011) to determine the most likely solutions for the physical state of the molecular gas for a given set of measured

Table 2.2. RADEX grid parameters

Parameter	Range	# of Points
T_{kin} [K]	$10^{0.7} - 10^{3.8}$	71
$n(\mathrm{H_2})$ [cm^{-3}]	$10^{1.0} - 10^{7.0}$	71
Φ_A	$10^{-5.0} - 1$	71
$N_{\mathrm{CO}}/\Delta V$ [cm^{-2}]	$10^{12.0} - 10^{18.0}$	81
$N_{\mathrm{[CI]}}/N_{\mathrm{CO}}$	$10^{-2.0} - 10^{2.0}$	20
ΔV [km s^{-1}]	1.0	

Note. — Column density is calculated per unit linewidth, while the linewidth is held fixed at 1 km s^{-1} in the grid calculations (see text).

CO and [CI] line integrated intensities. We list the highlights of the code here, while further details can be found in Kamenetzky et al. (2012). The likelihood code includes an area filling factor (Φ_A) with the RADEX grid parameters (T_{kin}, $n(\mathrm{H_2})$, $N_{\mathrm{CO}}/\Delta V$) to create a 4 dimensional parameter space. Assuming Bayes' theorem, the code compares the measured fluxes to those in our RADEX grid to calculate the probability that a given set of parameters produces the observed set of emission lines. In addition, the source line width (ΔV) is included as an input parameter in order to properly compare measured and calculated integrated intensities. We use the convolved CO $J = 3-2$ second moment map for the source line widths of each pixel in our maps.

The code calculates three values for each parameter: the median, the 1DMax and the 4DMax. The 1DMax corresponds to the most probable value for the given parameter based upon the 1-dimensional likelihood distribution for that parameter, while the median is also calculated from the 1-dimensional likelihood distribution. The 4DMax is only calculated explicitly for the 4 grid parameters (T_{kin}, $n(\mathrm{H_2})$, N_{CO}, Φ_A) and is the most probable set of values based upon the 4-dimensional likelihood distribution of the 4 parameters. Finally, the 1σ range is calculated from the 1-dimensional likelihood distribution.

We use three priors to constrain our solutions to those which are physically realizable (Ward et al., 2003; Rangwala et al., 2011). The first prior places a limit on the column density ensuring that the total mass in the column does not exceed the dynamical mass of the system, or

$$N_{\mathrm{CO}} < \frac{M_{dyn} x_{\mathrm{CO}}}{\mu m_{\mathrm{H}_2} A_{\mathrm{CO}} \Phi_A} \tag{2.3}$$

where μ is the mean molecular weight, M_{dyn} is the dynamical mass of the system, x_{CO} is the CO abundance relative to H_2 and A_{CO} is the area of the CO emitting region. The dynamical mass is calculated as the sum of the virial masses of all of the SGMCs in the overlap region from Wilson et al. (2000), corrected for incompleteness as some of the mass will be found in unresolved SGMCs (e.g. see Wilson et al. 2003). This incompleteness correction is performed by calculating the fraction of CO emission in unresolved SGMCs in the overlap region. The corrected dynamical mass is $3.1 \times 10^9\ \mathrm{M}_{\odot}$. While the dynamical mass in other parts of the galaxy will be less than in the overlap region (e.g. see Zhu et al. 2003), it is very difficult to determine how much mass is observed by each pixel in our maps. Therefore we conservatively use the highest possible mass we expect in the beam for one pixel. Using these values along with those listed in Table 2.3, we limit the product of the column density and filling factor to

$$N_{\mathrm{CO}} \Phi_A < 10^{18.36}\ \mathrm{cm}^{-2} \tag{2.4}$$

The second prior limits the total length of the column to be less than the length of the molecular region on the plane of the sky, so that

$$\frac{N_{\mathrm{CO}}}{\sqrt{\Phi_A} x_{\mathrm{CO}} n(\mathrm{H}_2)} \leq L \tag{2.5}$$

where L is the size of the CO emitting region. We use the diameter of the

Table 2.3. Model Constraints

Parameter	Value	Units
CO abundance ($x_{\rm CO}$)	3×10^{-4}	...
Mean molecular weight (μ)	1.5	...
Angular size scale	107	pc/$''$
Source size	43	$''$
Length (L)	$\leq 1,930$[a]	pc
Dynamical Mass (M_{dyn})	$\leq 3.1 \times 10^{9}$[b]	$M_{\odot}$

[a]Physical size of the nucleus of NGC 4038 from Wilson et al. (2000) corrected to a distance of 22 pc

[b]Sum of the virial masses of all SGMCs in overlap region from Wilson et al. (2003) corrected for incompleteness; see text.

nucleus of NGC 4038 ($L = 1,900$ pc) from Wilson et al. (2000), corrected to a distance of 22 Mpc, since it is the largest single molecular complex in the Antennae. As such, this provides an upper limit on the true size of CO, regardless of which pixel is being considered. All of the physical parameters used to calculate the first two priors are shown in Table 2.3.

The third prior limits the optical depth to be $-1 < \tau < 100$ as recommended by the RADEX documentation (van der Tak et al., 2007). A negative optical depth is indicative of a "maser", which is nonlinear amplification of the incoming radiation. RADEX cannot accurately calculate the line intensities when the optical depth is less than $\tau < -1$, and masing is not expected, so these solutions should be disregarded. Conversely, a high optical depth can lead to unrealistic high calculated temperatures and so should be disregarded, and, in any case, our models do not approach that high optical depth limit.

2.3.3 RADEX results

2.3.3.1 CO only

We model the CO emission for each pixel in our map where we have a detection for all 8 of our observed CO transitions ($J = 1-0$ to $J = 8-7$) and both [CI] transitions. The pixels associated with NGC 4038, NGC 4039 and the overlap region are shown on the CO $J = 1-0$ map in Figure 2.5, while the beams associated with these pixels are shown in Figure 2.1. We assume that all of the molecular gas in each pixel is in one of two distinct components[3]: a cold component and a warm component. Studies of the Antennae have revealed that there is both cold gas (e.g. Wilson et al. 2000, Zhu et al. 2003) and warm gas (e.g. Brandl et al. 2009, Herrera et al. 2012); however the molecular gas likely populates a spectrum of temperature and density ranges. While a two component model is unlikely to represent the true physical state of the molecular gas, it does provide us with an average, along with a statistical range, of the temperature, density and column density of the molecular gas.

Under the two-component assumption, the cold component dominates the lower J CO emission while the warm component dominates the higher J CO emission. We begin by fitting the cold component to the lower J lines up to some transition $J_{up} \leq J_{break}$ and setting the measurements of the higher transitions ($J_{up} > J_{break}$) as upper limits. We subtract the resulting calculated cold component from the line fluxes and fit the residual high J CO emission as a "warm component", while keeping the residuals of the lower J CO transitions as upper limits. Following this fit, we subtract the warm component from our measured data and fit the cold component once again. We continue to iterate in this manner until we converge upon a set of solutions. We solve for values of $J_{break} = 3$, 4 and 5 and present a χ^2 goodness of fit parameter for each

[3] We performed 1-component fits in NGC 4038, NGC 4039 and the overlap region both with and without the two [CI] transitions in addition to our 8 CO transitions. In all three cases, we recovered only warm ($T_{kin} \gtrsim 100\,\mathrm{K}$), low density ($n(\mathrm{H_2}) \lesssim 10^3\,\mathrm{cm^{-3}}$) molecular gas. Furthermore, we recovered a molecular gas mass of $M_{beam} \sim 10^8 M_\odot$ or less in all three regions, which leads to a total molecular gas mass $\sim$ a few $10^8 M_\odot$ for the entire galaxy (assuming a CO abundance of 3×10^{-4}). CO $J = 1-0$ interferometric observations from Wilson et al. (2000) found that, in all three regions, the amount of molecular gas exceeds $5.0 \times 10^8 M_\odot$ using two different methods. Given the warm temperatures and low density of the gas we recovered with our 1-component fit, along with the low molecular gas mass, we feel that the 1-component fit does not represent a physical solution.

Table 2.4. χ^2 values of 2 component fit for various J_{break}

Model	J_{break}	NGC 4038 χ^2_{CO}	NGC 4038 $\chi^2_{\mathrm{[CI]}}$	Overlap region χ^2_{CO}	Overlap region $\chi^2_{\mathrm{[CI]}}$	NGC 4039 χ^2_{CO}	NGC 4039 $\chi^2_{\mathrm{[CI]}}$
CO only	3	31.2	–	27.7	–	**5.5**	
	4	12.2	–	**10.7**	–	13.1	
	5	**11.9**	–	16.0	–	15.3	
CO and [CI]	3	37.6	663.5	30.5	2431.9	**5.4**	969.7
	4	**10.2**	**4.8**	**22.2**	**1.2**	20.4	**2.2**
	5	10.4	**4.8**	25.5	3.9	10.1	563.6

Note. — The best χ^2 for each position is highlighted in bold

solution in Table 2.4. For the overlap region and NGC 4038, the $J_{break} = 3$ solution presents the worst fit, while the differences between the $J_{break} = 4$ and $J_{break} = 5$ solutions are minimal. Furthermore, for NGC 4039, all three solutions present reasonable fits with the $J_{break} = 3$ solution producing the best fit. Therefore, for consistency we report the $J_{break} = 4$ solution for each pixel in our map; however, it is important to note that the statistical ranges in the physical parameters for all 3 solutions do not depend appreciably on the value of J_{break}.

The measured and calculated CO spectral line energy distributions (SLEDs) are shown in Figure 2.7 while the optical depths are shown in Figure 2.8, both calculated from the 4DMax solutions (see Tables 2.5 and 2.6). In NGC 4038 and the overlap region, the cold component dominates the emission for all transitions where $J_{upper} \leq 5$, while the warm component is dominant only for the 2 highest J CO transitions. In NGC 4039, the cold component dominates only for the $J_{upper} \leq 4$ transitions. In all cases, the warm component is more optically thin than the cold component for almost all of the CO transitions (Figure 2.8).

The fitted physical parameters for NGC 4038, the overlap region and

Table 2.5. Cold Component Likelihood Results: CO only

Source	Parameter	Median	1σ Range	1D Max	4D Max	Unit
NGC 4038	T_{kin}	13	$10 - 20$	12	14	(K)
	$n(\mathrm{H_2})$	$10^{4.97}$	$10^{3.73} - 10^{6.33}$	$10^{4.00}$	$10^{5.54}$	($\mathrm{cm^{-3}}$)
	N_{CO}	$10^{18.95}$	$10^{18.53} - 10^{19.49}$	$10^{18.80}$	$10^{18.72}$	($\mathrm{cm^{-2}}$)
	Φ_A	$10^{-1.80}$	$10^{-2.02} - 10^{-1.62}$	$10^{-1.71}$	$10^{-1.79}$	
	P	$10^{6.05}$	$10^{5.01} - 10^{7.39}$	$10^{5.47}$	$10^{5.47}$	(K $\mathrm{cm^{-2}}$)
	$\langle N_{\mathrm{CO}} \rangle$	$10^{17.24}$	$10^{16.71} - 10^{17.76}$	$10^{17.33}$	$10^{17.33}$	($\mathrm{cm^{-2}}$)
Overlap region	T_{kin}	15	$10 - 38$	12	63	(K)
	$n(\mathrm{H_2})$	$10^{4.16}$	$10^{3.23} - 10^{6.01}$	$10^{3.40}$	$10^{3.40}$	($\mathrm{cm^{-3}}$)
	N_{CO}	$10^{18.91}$	$10^{18.35} - 10^{19.55}$	$10^{18.62}$	$10^{18.70}$	($\mathrm{cm^{-2}}$)
	Φ_A	$10^{-1.66}$	$10^{-1.94} - 10^{-1.42}$	$10^{-1.50}$	$10^{-1.93}$	
	P	$10^{5.37}$	$10^{4.66} - 10^{7.02}$	$10^{5.22}$	$10^{5.22}$	(K $\mathrm{cm^{-2}}$)
	$\langle N_{\mathrm{CO}} \rangle$	$10^{17.34}$	$10^{16.72} - 10^{17.99}$	$10^{16.87}$	$10^{16.87}$	($\mathrm{cm^{-2}}$)
NGC 4039	T_{kin}	15	$10 - 37$	12	28	(K)
	$n(\mathrm{H_2})$	$10^{4.27}$	$10^{3.33} - 10^{6.07}$	$10^{3.49}$	$10^{3.83}$	($\mathrm{cm^{-3}}$)
	N_{CO}	$10^{18.72}$	$10^{18.13} - 10^{19.48}$	$10^{18.61}$	$10^{18.76}$	($\mathrm{cm^{-2}}$)
	Φ_A	$10^{-2.00}$	$10^{-2.26} - 10^{-1.75}$	$10^{-1.93}$	$10^{-2.21}$	
	P	$10^{5.46}$	$10^{4.82} - 10^{7.11}$	$10^{5.22}$	$10^{5.22}$	(K $\mathrm{cm^{-2}}$)
	$\langle N_{\mathrm{CO}} \rangle$	$10^{16.75}$	$10^{16.24} - 10^{17.55}$	$10^{16.49}$	$10^{16.49}$	($\mathrm{cm^{-2}}$)

Table 2.6. Warm Component Likelihood Results: CO only

Source	Parameter	Median	1σ Range	1D Max	4D Max	Unit
NGC 4038	T_{kin}	1071	$368 - 3361$	647	5997	(K)
	$n(\mathrm{H_2})$	$10^{5.73}$	$10^{4.75} - 10^{6.60}$	$10^{7.00}$	$10^{4.26}$	($\mathrm{cm^{-3}}$)
	N_{CO}	$10^{17.04}$	$10^{15.30} - 10^{18.83}$	$10^{16.17}$	$10^{15.05}$	($\mathrm{cm^{-2}}$)
	Φ_A	$10^{-2.55}$	$10^{-4.27} - 10^{-0.81}$	$10^{-4.57}$	$10^{-0.71}$	
	P	$10^{9.28}$	$10^{8.15} - 10^{10.21}$	$10^{9.44}$	$10^{9.44}$	(K $\mathrm{cm^{-2}}$)
	$\langle N_{\mathrm{CO}} \rangle$	$10^{14.47}$	$10^{14.23} - 10^{14.85}$	$10^{14.43}$	$10^{14.43}$	($\mathrm{cm^{-2}}$)
Overlap region	T_{kin}	732	$279 - 2790$	389	3999	(K)
	$n(\mathrm{H_2})$	$10^{5.57}$	$10^{4.56} - 10^{6.55}$	$10^{4.43}$	$10^{4.26}$	($\mathrm{cm^{-3}}$)
	N_{CO}	$10^{17.08}$	$10^{15.32} - 10^{18.90}$	$10^{15.92}$	$10^{14.80}$	($\mathrm{cm^{-2}}$)
	Φ_A	$10^{-2.59}$	$10^{-4.32} - 10^{-0.82}$	$10^{-4.79}$	$10^{-0.36}$	
	P	$10^{8.92}$	$10^{7.86} - 10^{9.95}$	$10^{7.90}$	$10^{7.90}$	(K $\mathrm{cm^{-2}}$)
	$\langle N_{\mathrm{CO}} \rangle$	$10^{14.48}$	$10^{14.27} - 10^{14.79}$	$10^{14.41}$	$10^{14.41}$	($\mathrm{cm^{-2}}$)
NGC 4039	T_{kin}	324	$123 - 1276$	212	234	(K)
	$n(\mathrm{H_2})$	$10^{4.51}$	$10^{4.00} - 10^{5.22}$	$10^{4.34}$	$10^{4.69}$	($\mathrm{cm^{-3}}$)
	N_{CO}	$10^{16.34}$	$10^{15.11} - 10^{17.66}$	$10^{15.68}$	$10^{16.06}$	($\mathrm{cm^{-2}}$)
	Φ_A	$10^{-1.86}$	$10^{-3.16} - 10^{-0.63}$	$10^{-1.07}$	$10^{-1.43}$	
	P	$10^{7.13}$	$10^{6.95} - 10^{7.49}$	$10^{7.13}$	$10^{7.13}$	(K $\mathrm{cm^{-2}}$)
	$\langle N_{\mathrm{CO}} \rangle$	$10^{14.49}$	$10^{14.40} - 10^{14.64}$	$10^{14.61}$	$10^{14.61}$	($\mathrm{cm^{-2}}$)

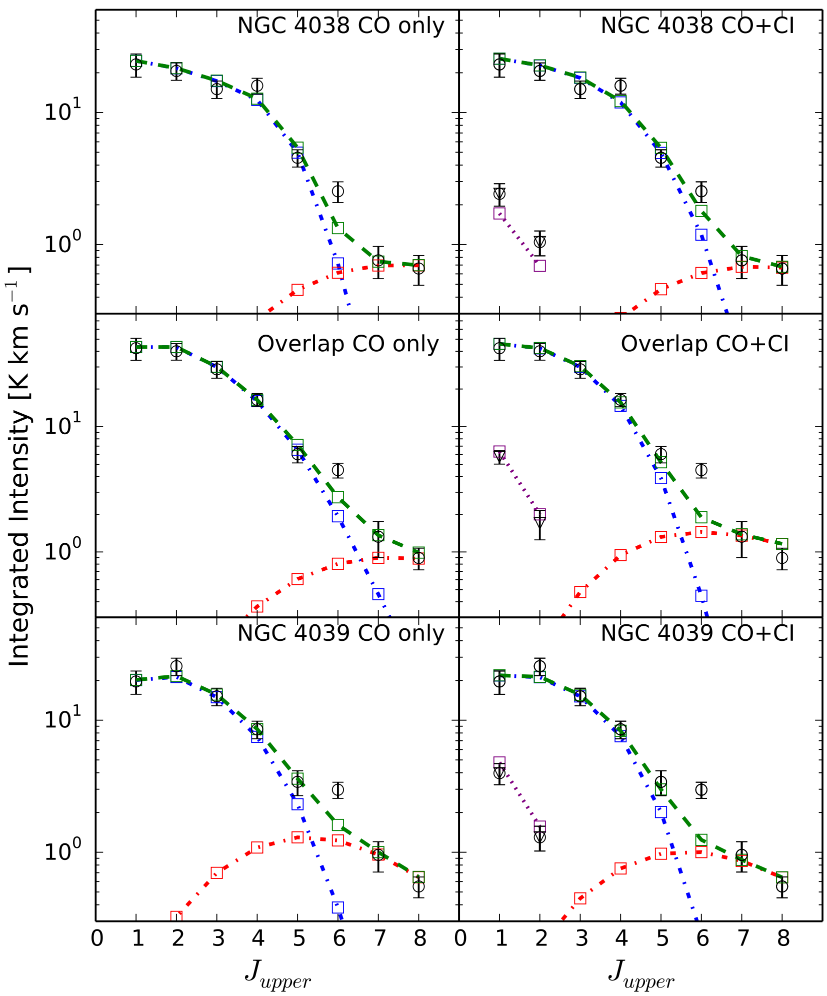

Figure 2.7 Measured and calculated CO spectral line energy distributions (SLED) for the nucleus of NGC 4038 (*top*), the overlap region (*middle*) and the nucleus of NGC 4039 (*bottom*) and for $J_{break} = 4$. The left panels correspond to solutions including only CO while the right panels correspond to solutions including both CO and [CI]. In all panels, the blue dashed-dot line and squares correspond to the cold component, the red dashed-dot line and squares to the warm component, the green dashed line and squares is the sum of the cold and warm component and the black circles correspond to the measured CO data. In the right column, the purple dotted line and squares correspond to the calculated [CI] flux while the black triangles correspond to the measured [CI] flux.

NGC 4039 are shown in Tables 2.5 (cold component) and 2.6 (warm component). In all three regions, the upper limits of the density for both the cold

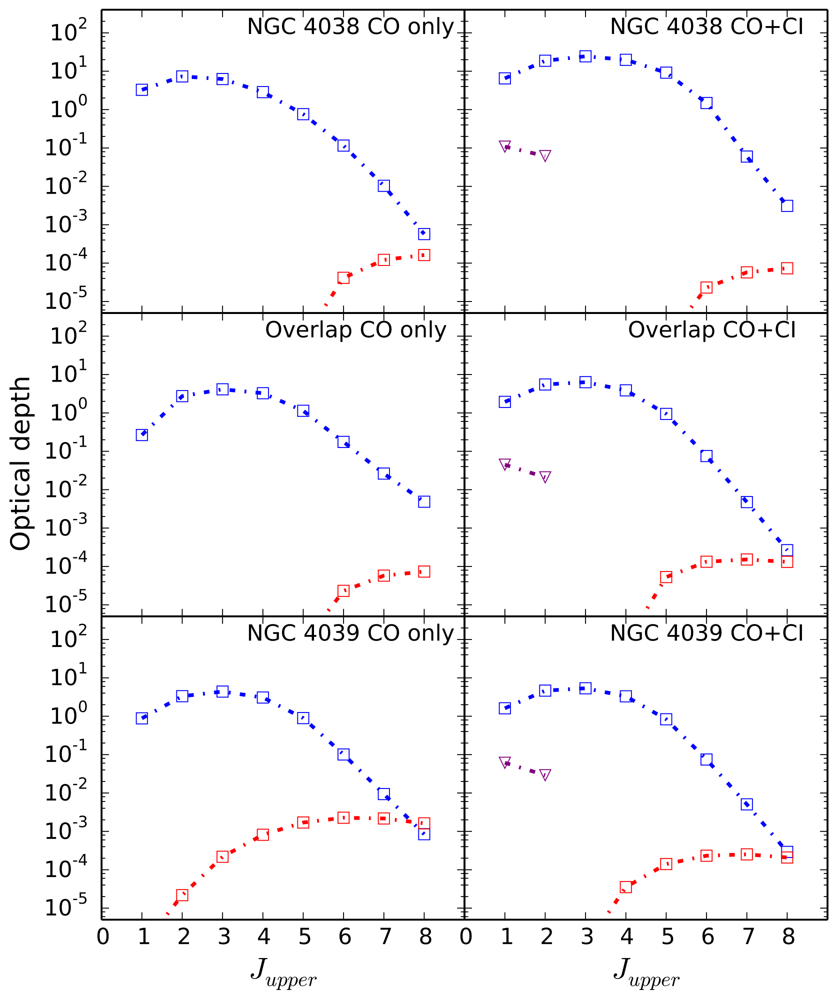

Figure 2.8 Best-fit model CO optical depth for the nucleus of NGC 4038 (*top*), the overlap region (*middle*) and the nucleus of NGC 4039 (*bottom*) and for $J_{break} = 4$. The left panels correspond to solutions including only CO while the right panels correspond to solutions including both CO and [CI]. In all panels, the blue dashed-dot line and squares correspond to the cold component, the red dashed-dot line and squares to the warm component. In the right column, the purple dotted line and squares correspond to the calculated [CI] optical depth. The warm component CO emission and the [CI] emission are optically thin.

and warm components are not well constrained (Figure 2.9 *top*). As a result, the upper limit on the pressure, which is the product of the temperature and density, is not well constrained. The 1σ range of the temperature of the cold component in all three regions is constrained to being cold ($T_{kin} \lesssim 40\,\mathrm{K}$), which agrees well with our [CI] LTE analysis (Figure 2.6). The filling factor and the CO column density for the cold component in all three regions is well constrained (Figure 2.9 *bottom*). The lack of constraint for the warm components of these three regions can be attributed to the degeneracy of Φ_A and N_{CO} (e.g. see Kamenetzky et al. 2012). Their product, which is equal to the beam-averaged column-density ($\langle N_{\mathrm{CO}} \rangle$) is well constrained for both the warm and cold component in all three regions (Figure 2.9 *bottom*). If we assume that the CO abundance (x_{CO}) is the same for both the warm and cold component, the warm component would correspond to $\sim 0.1\% - 0.3\%$ of the total molecular gas mass in the nucleus of NGC 4038 and the overlap region, and $\sim 1\%$ of the total gas mass in the nucleus of NGC 4039.

Results for the entire system are shown in Figure 2.10. In this figure, it is important to note that, since our pixel size ($15''$) is less than our beam size ($\sim 43''$), data points on these plots are not entirely independent. We compare the 1σ ranges for the temperature (*top row*) and beam-averaged column density (*bottom row*) to those for the density (*left column*) and pressure (*right column*). Both a cold and warm component are revealed outside of NGC 4038, NGC 4039, and the overlap region (Figure 2.10 *top row*). Furthermore, no distinction can be made between the density of the cold and warm components (Figure 2.10 *left column*). The pressure in each of the cold and warm components does not vary by more than $\sim 1 - 2$ orders of magnitude, (Figure 2.10 *right column*) which, given the large 1σ ranges, may in turn suggest that the conditions under which stars form are nearly constant across the entire system. In addition, the pressure of the warm component is higher than that of the cold component, which is likely attributable to the increased temperature.

Finally, the beam-averaged column density for both the warm and cold components are well constrained across the entire region, with the beam-

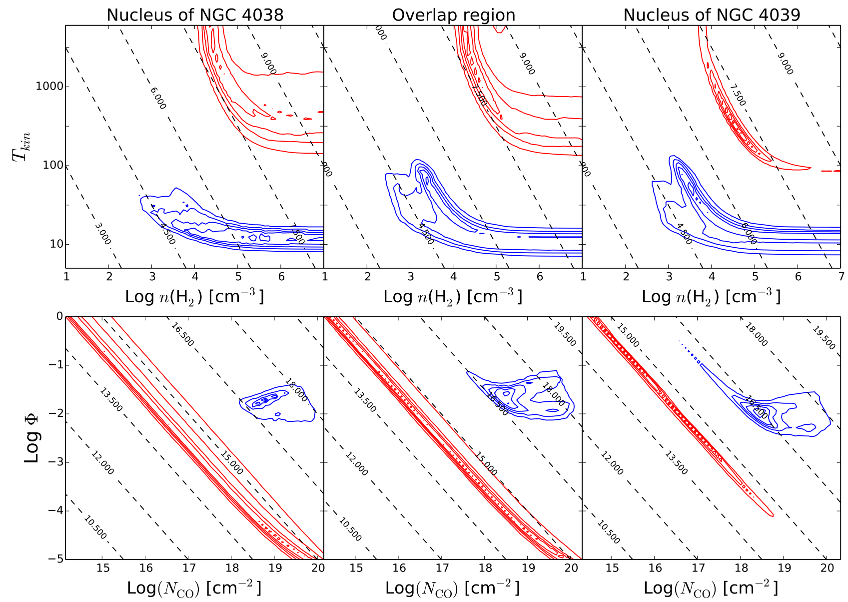

Figure 2.9 Contour probability plots for the CO-only solutions with $J_{break} = 4$ for the warm (red contours) and cold (blue contours) in the nucleus of NGC 4038 (*left*), the overlap region (*middle*) and the nucleus of NGC 4039 (*right*) and for kinetic temperature and density (*top*), and the filling factor and column density (*bottom*). The dashed diagonal lines correspond to the logarithm of the pressure in units of Log(K cm^{-2}) (*top*) and the beam-averaged column-density, denoted as $\langle N_{\rm CO} \rangle$ in the tables, in units of Log(cm^{-2}) (*bottom*). The contours correspond to 10%, 30%, 50%, 70% and 90% peak probability.

averaged column density of the warm component varying only by about an order of magnitude from pixel to pixel (Figure 2.10 *bottom row*). Furthermore, the beam-averaged column density of the warm component is $2 - 3$ orders of magnitude less than that of the cold component. Assuming a CO abundance of $x_{\rm CO} = 3 \times 10^{-4}$ (Kamenetzky et al., 2012), the total mass of the warm component across the entire map ($\log{(M_{warm}/M_\odot)} = 6.2^{+0.2}_{-0.2}$) is only $\sim 0.1\%$ that of the cold component ($\log{(M_{cold}/M_\odot)} = 9.1^{+0.3}_{-0.9}$).

2.3.3.2 CO and [CI]

We expand upon our likelihood analysis by assuming both [CI] transitions trace the same molecular gas as CO. Ikeda et al. (2002) found that in the Orion

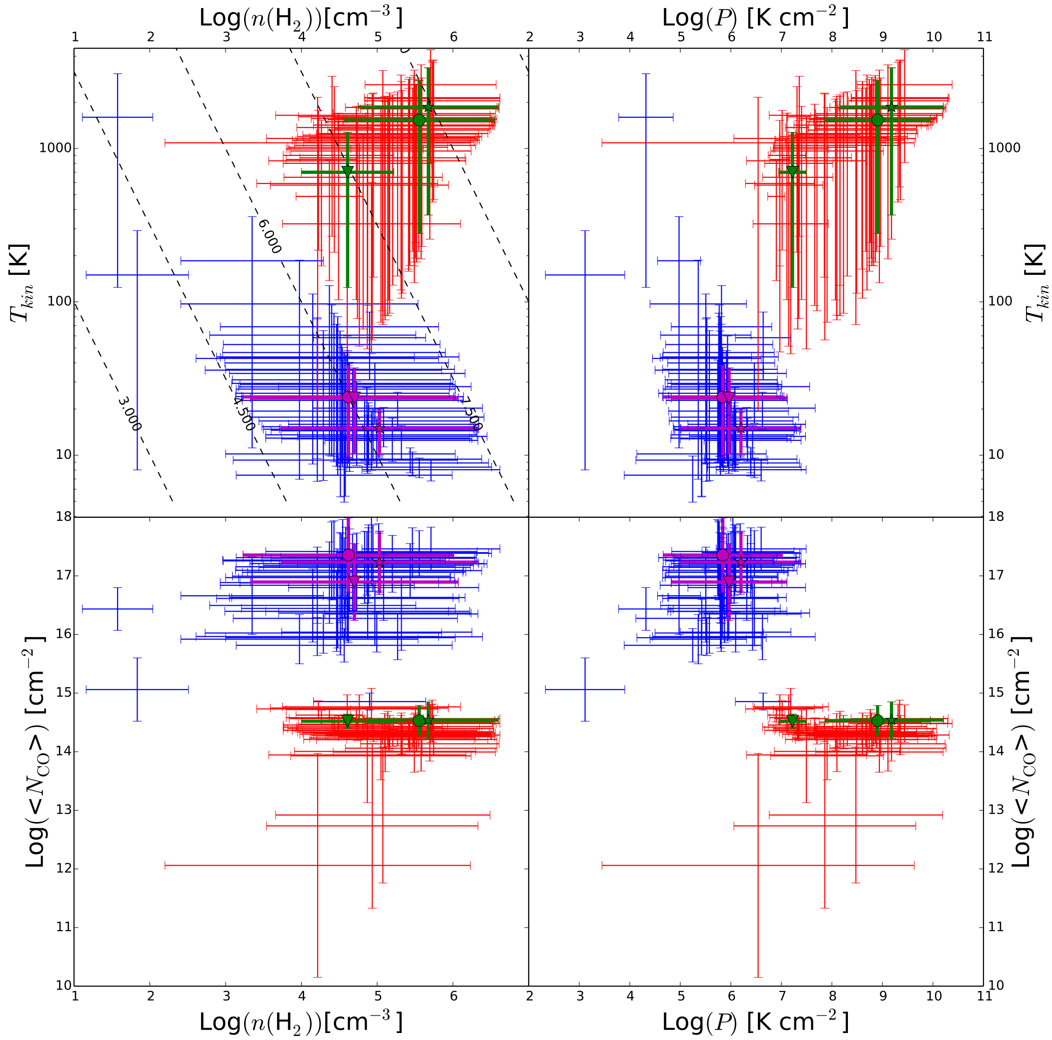

Figure 2.10 CO-only non-LTE radiative transfer results for every pixel in our maps for which we detect all 8 CO and both [CI] transitions. The temperature (top row) and beam-averaged column density (bottom row) are compared to the molecular gas density (left column) and pressure (right column) for both the cold (*blue*) and warm (*red*) components. The error bars correspond to the 1-sigma range for each physical parameter. The results for NGC 4038 (star), the overlap region (circle) and NGC 4039 (triangle) are indicated by the thick magenta (cold) and green (warm) symbols and lines. Note the location where the vertical and horizontal error bars cross corresponds to the midpoint of the 1σ range and not the most probable value. The dashed diagonal lines in the top-left plot correspond to contours of constant pressure.

Giant Molecular Cloud, [CI] $^3P_1 -^3 P_0$ and ^{13}CO $J = 1-0$ show structural similarities across the entire cloud both spatially and in velocity, suggesting that both transitions trace much of the same molecular gas especially in the denser regions of GMCs. Furthermore, our ratio of the two [CI] transitions along with the CO-only molecular gas temperature strongly suggests that it originates from cold, rather than warm molecular gas (Section 2.3.1).

We fit all of the pixels in our maps where we have a detection in all of the CO and both [CI] transitions with both a cold and warm component following the same procedure in section 2.3.3.1 with the following addition. We include the [CI] emission in the cold component only and not the warm component, assuming it does not contribute appreciably to the molecular gas traced by the higher J CO transitions. We report the χ^2 goodness of fit parameters for both the CO and [CI] measured and calculated SLEDs separately in Table 2.4. It is important to note that the CO SLED is calculated from the 4DMax solutions, while the [CI] solutions are calculated from the 1DMax solutions, as only the 1DMax is calculated for the [CI] abundance relative to CO. The best fit solution to CO for NGC 4038 and the overlap region is the $J_{break} = 4$ solution, while in NGC 4039, the $J_{break} = 3$ solution presents the best solution. Furthermore, the best-fit solutions for [CI] in all three regions is the $J_{break} = 4$ solution. Therefore, we report the $J_{break} = 4$ solution for consistency with our CO-only results.

The measured and calculated CO and [CI] SLEDs are shown in Figure 2.7 while the optical depths are shown in Figure 2.8. The behavior of the cold and warm components of the best fit SLED for all three regions is strikingly similar to the CO-only results. Furthermore, in all three regions the measured [CI] flux is reproduced. Once again, the warm component is more optically thin than the cold component (Figure 2.8). In addition, the [CI] emission is optically thin, as assumed in our [CI] LTE anlaysis. As in the CO-only

Table 2.7. Cold Component Likelihood Results: CO and [CI]

Source	Parameter	Median	1σ Range	1D Max	4D Max	Unit
NGC 4038	T_{kin}	24	$18-33$	25	25	(K)
	$n(\mathrm{H_2})$	$10^{3.66}$	$10^{3.08}-10^{4.26}$	$10^{3.74}$	$10^{3.57}$	($\mathrm{cm^{-3}}$)
	N_{CO}	$10^{19.12}$	$10^{18.58}-10^{19.62}$	$10^{19.40}$	$10^{19.40}$	($\mathrm{cm^{-2}}$)
	Φ_A	$10^{-2.09}$	$10^{-2.21}-10^{-1.96}$	$10^{-2.07}$	$10^{-2.07}$	
	P	$10^{5.03}$	$10^{4.51}-10^{5.57}$	$10^{5.22}$	$10^{5.22}$	(K $\mathrm{cm^{-2}}$)
	$\langle N_{\mathrm{CO}}\rangle$	$10^{17.09}$	$10^{16.58}-10^{17.58}$	$10^{17.62}$	$10^{17.62}$	($\mathrm{cm^{-2}}$)
	$X_{[\mathrm{CI}]}/X_{\mathrm{CO}}$	$10^{-0.65}$	$10^{-1.11}-10^{-0.16}$	$10^{-0.95}$	$10^{-0.95}$	
	$N_{[\mathrm{CI}]}$	$10^{18.50}$	$10^{18.34}-10^{18.71}$	$10^{18.65}$	$10^{18.65}$	
Overlap region	T_{kin}	20	$15-27$	21	21	(K)
	$n(\mathrm{H_2})$	$10^{3.67}$	$10^{2.90}-10^{4.42}$	$10^{4.00}$	$10^{3.91}$	($\mathrm{cm^{-3}}$)
	N_{CO}	$10^{19.13}$	$10^{18.44}-10^{19.69}$	$10^{19.59}$	$10^{18.84}$	($\mathrm{cm^{-2}}$)
	Φ_A	$10^{-1.83}$	$10^{-1.96}-10^{-1.66}$	$10^{-1.86}$	$10^{-1.79}$	
	P	$10^{4.91}$	$10^{4.28}-10^{5.61}$	$10^{4.32}$	$10^{4.32}$	(K $\mathrm{cm^{-2}}$)
	$\langle N_{\mathrm{CO}}\rangle$	$10^{17.38}$	$10^{16.76}-10^{17.87}$	$10^{17.59}$	$10^{17.59}$	($\mathrm{cm^{-2}}$)
	$X_{[\mathrm{CI}]}/X_{\mathrm{CO}}$	$10^{-0.49}$	$10^{-0.98}-10^{0.10}$	$10^{-0.74}$	$10^{-0.74}$	
	$N_{[\mathrm{CI}]}$	$10^{18.65}$	$10^{18.47}-10^{18.86}$	$10^{18.77}$	$10^{18.77}$	
NGC 4039	T_{kin}	21	$16-28$	21	21	(K)
	$n(\mathrm{H_2})$	$10^{3.79}$	$10^{3.07}-10^{4.44}$	$10^{4.00}$	$10^{4.00}$	($\mathrm{cm^{-3}}$)
	N_{CO}	$10^{19.01}$	$10^{18.38}-10^{19.65}$	$10^{19.65}$	$10^{18.83}$	($\mathrm{cm^{-2}}$)
	Φ_A	$10^{-2.21}$	$10^{-2.36}-10^{-2.03}$	$10^{-2.21}$	$10^{-2.14}$	
	P	$10^{5.09}$	$10^{4.45}-10^{5.66}$	$10^{5.34}$	$10^{5.34}$	(K $\mathrm{cm^{-2}}$)
	$\langle N_{\mathrm{CO}}\rangle$	$10^{16.86}$	$10^{16.33}-10^{17.44}$	$10^{16.49}$	$10^{16.49}$	($\mathrm{cm^{-2}}$)
	$X_{[\mathrm{CI}]}/X_{\mathrm{CO}}$	$10^{-0.17}$	$10^{-0.72}-10^{0.36}$	$10^{-0.53}$	$10^{-0.53}$	
	$N_{[\mathrm{CI}]}$	$10^{18.87}$	$10^{18.63}-10^{19.10}$	$10^{19.03}$	$10^{19.03}$	

solutions, when [CI] is included both a cold ($\lesssim 30\,\mathrm{K}$) and a warm ($\gtrsim 200\,\mathrm{K}$) component are recovered (Tables 2.7 and 2.8). However, in the CO and [CI] solution, the density of the cold component in all three components is better constrained than in the CO only solution (Figure 2.11), along with the density of the warm component in the overlap region and NGC 4039.

For the remaining pixels in the map, the addition of [CI] to the radiative transfer analysis does not change the resulting 1σ ranges for the various physical parameters (Figure 2.12). As in the CO solution, we find both a warm and cold component with comparable densities. The beam-averaged column density of the warm component is less than in the cold component. The pressure of the warm component is once again higher than in the cold component, while remaining nearly constant for each component separately. Furthermore, we find that the mass of the warm component ($\log\left(M_{warm}/M_{\odot}\right) = 6.2^{+0.3}_{-0.2}$) is

Table 2.8. Warm Component Likelihood Results: CO and [CI]

Source	Parameter	Median	1σ Range	1D Max	4D Max	Unit
NGC 4038	T_{kin}	1065	347 – 3397	647	3999	(K)
	$n(\mathrm{H_2})$	$10^{5.75}$	$10^{4.77} - 10^{6.61}$	$10^{7.00}$	$10^{4.26}$	(cm^{-3})
	N_{CO}	$10^{17.04}$	$10^{15.29} - 10^{18.83}$	$10^{16.10}$	$10^{14.68}$	(cm^{-2})
	Φ_A	$10^{-2.57}$	$10^{-4.30} - 10^{-0.81}$	$10^{-4.57}$	$10^{-0.36}$	
	P	$10^{9.29}$	$10^{8.17} - 10^{10.23}$	$10^{9.44}$	$10^{9.44}$	(K cm^{-2})
	$\langle N_{\mathrm{CO}} \rangle$	$10^{14.45}$	$10^{14.19} - 10^{14.83}$	$10^{14.29}$	$10^{14.29}$	(cm^{-2})
Overlap region	T_{kin}	1425	430 – 3811	2666	4425	(K)
	$n(\mathrm{H_2})$	$10^{4.23}$	$10^{4.00} - 10^{4.73}$	$10^{4.09}$	$10^{4.00}$	(cm^{-3})
	N_{CO}	$10^{16.39}$	$10^{15.12} - 10^{17.80}$	$10^{14.80}$	$10^{14.95}$	(cm^{-2})
	Φ_A	$10^{-1.86}$	$10^{-3.25} - 10^{-0.58}$	$10^{-0.14}$	$10^{-0.29}$	
	P	$10^{7.45}$	$10^{7.26} - 10^{7.73}$	$10^{7.39}$	$10^{7.39}$	(K cm^{-2})
	$\langle N_{\mathrm{CO}} \rangle$	$10^{14.55}$	$10^{14.40} - 10^{14.70}$	$10^{14.55}$	$10^{14.55}$	(cm^{-2})
NGC 4039	T_{kin}	629	203 – 2390	431	431	(K)
	$n(\mathrm{H_2})$	$10^{4.35}$	$10^{3.97} - 10^{5.00}$	$10^{3.91}$	$10^{4.51}$	(cm^{-3})
	N_{CO}	$10^{16.30}$	$10^{14.99} - 10^{17.73}$	$10^{14.78}$	$10^{15.15}$	(cm^{-2})
	Φ_A	$10^{-1.91}$	$10^{-3.33} - 10^{-0.59}$	$10^{-0.14}$	$10^{-0.64}$	
	P	$10^{7.27}$	$10^{7.09} - 10^{7.57}$	$10^{7.26}$	$10^{7.26}$	(K cm^{-2})
	$\langle N_{\mathrm{CO}} \rangle$	$10^{14.42}$	$10^{14.28} - 10^{14.51}$	$10^{14.47}$	$10^{14.47}$	(cm^{-2})

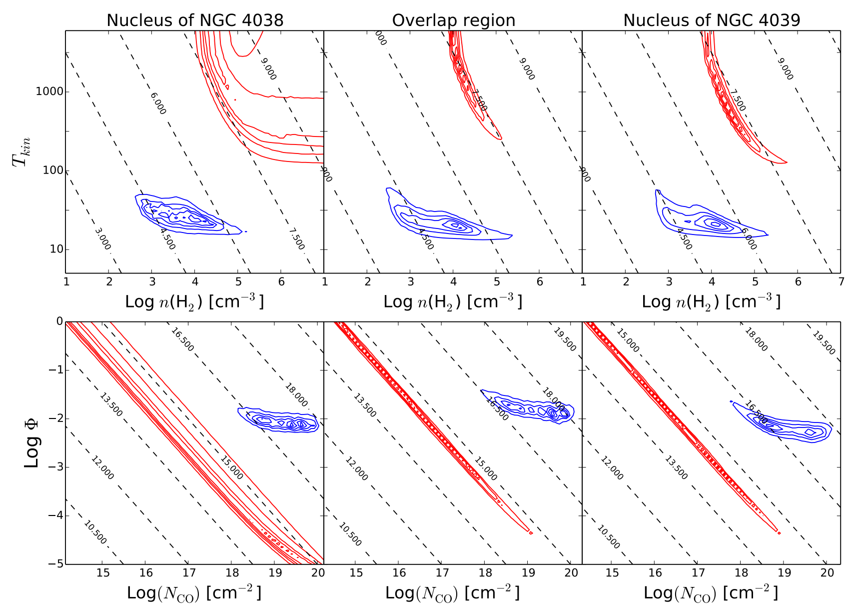

Figure 2.11 Same as figure 2.9 except for the solutions including both CO and [CI].

only $\sim 0.2\%$ that of the cold component ($\log{(M_{cold}/M_{\odot})} = 8.9^{+0.3}_{-0.7}$).

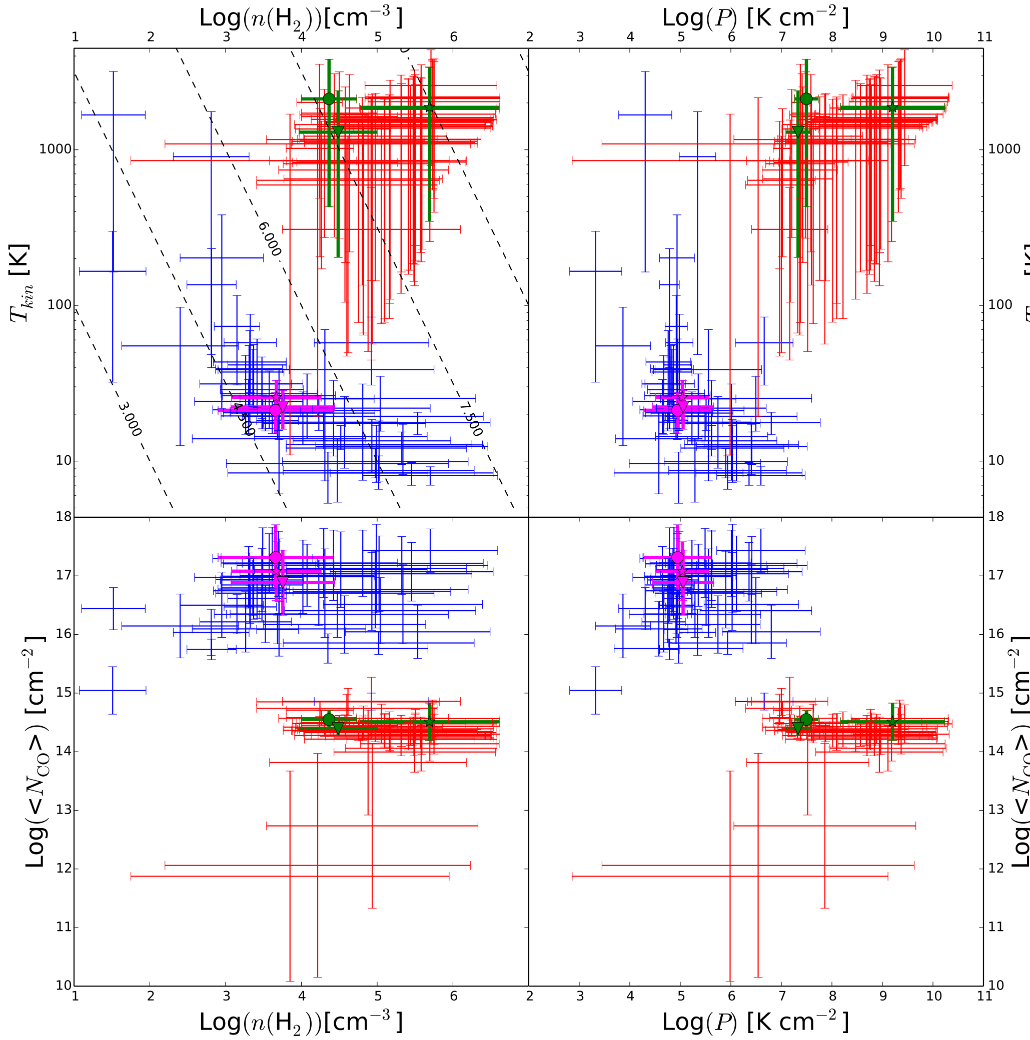

Figure 2.12 Same as figure 2.10 except for solutions including both CO and [CI].

2.3.4 Molecular gas mass correction

The total molecular gas mass calculated from our radiative transfer modeling will be slightly smaller than the true molecular gas mass as we only modeled the CO and [CI] emission in pixels where we detect both [CI] and all 8 CO transitions. We can estimate the missing mass using the CO $J = 3 - 2$ map as it encompasses the entire CO emitting region in the Antennae. The total integrated intensity in the CO $J = 3 - 2$ map is 724 K km s^{-1}, while the integrated intensity of the pixels used in RADEX modeling is 563 K km s^{-1}, corresponding to only $\sim 78\%$ of the total integrated intensity. Therefore, we apply a correction of $\sim 22\%$ to the total molecular gas masses calculated in sections 2.3.3.1 and 2.3.3.2.

In addition, the CO $J = 1-0$ map does not extend far beyond the bright CO emitting regions in the Antennae, suggesting that there could be missing flux from beyond the edges of the map. Using the CO $J = 3-2$ map, we estimate that only $\sim 88\%$ of the total integrated intensity is within the bounds of the CO $J = 1-0$ map. We correct for this missing flux when calculating the total cold molecular gas mass from the CO $J = 1-0$ map in Section 2.4.

2.4 Discussion

2.4.1 Radiative transfer modeling results

2.4.1.1 Comparison to previous results

Both Zhu et al. (2003) and Bayet et al. (2006) have previously performed a radiative transfer analysis using ground based CO data. Bayet et al. (2006) used the ratios of $\frac{^{12}\mathrm{CO}\ J=3-2}{^{12}\mathrm{CO}\ J=6-5}$, $\frac{^{12}\mathrm{CO}\ J=2-1}{^{12}\mathrm{CO}\ J=6-5}$, and $\frac{^{12}\mathrm{CO}\ J=3-2}{^{13}\mathrm{CO}\ J=3-2}$ to fit a single warm component in the nucleus of NGC 4038 and the overlap region. The primary difference between their model for a warm component and ours is that we consider the contributions of the cold component to the lower J CO transitions while they do not. They found that the temperature and density vary significantly between NGC 4038 and the overlap region. In NGC 4038, the temperature that their model predicts ($T_{kin} = 40$ K) does not fall within either the cold or warm component 1σ range for either the CO or the CO and [CI] solutions, while the density ($n(\mathrm{H}_2) = 3.5\times10^5\ \mathrm{cm}^{-2}$) agrees within 1σ of the CO-only cold component and both the CO-only, and the CO and [CI] warm components. In the overlap region, their model temperature (145 K) does not fall within any of our temperature ranges, while their density ($n(\mathrm{H_2}) = 8.0 \times 10^3\,\mathrm{cm^{-2}}$) agrees with both our cold component densities. Furthermore, their models predict that the ^{12}CO SLED peaks at the $J = 3-2$ transition, while our observations indicate that it instead peaks at the $J = 1-0$ transition (Figure 2.7). In our models we find that the warm component only contributes significantly to the $J = 6-5$, $J = 7-6$ and $J = 8-7$ transitions (Figure 2.7), suggesting that Bayet et al. (2006) is, at least in part, modeling a cold component of the molecular gas.

In comparison, using various ratios of the ^{12}CO $J = 1-0$ to $J = 3-2$ and the isotopologue ^{13}CO $J = 2-1$ and $J = 3-2$ transitions, Zhu et al. (2003) fit both a single and a two-component model in NGC 4038, NGC 4039 and the overlap region. The results from the single component fit suggest that these transitions are tracing a cold component($T_{kin} \sim 20-40\,\mathrm{K}$) with density $n(\mathrm{H_2}) \sim 10^3 - 10^4\,\mathrm{cm^{-3}}$, both comparable to our cold component. This agreement is unsurprising, as our models suggest that, in all 3 regions, the cold component dominates the emission from the ^{12}CO $J = 1-0$ to $J = 3-2$ transitions. For the two component fit, Zhu et al. (2003) argue that there must be a low density component ($n(\mathrm{H_2}) \sim 10^3\,\mathrm{cm^{-3}}$) which dominates the optically thick ^{12}CO emission and a high density component ($n(\mathrm{H_2}) \sim 10^5\,\mathrm{cm^{-3}}$) which dominates the optically thin ^{13}CO emission. As a result, they find two temperature components, a cold component ($T_{kin} = 36\,\mathrm{K} - 120\,\mathrm{K}$) and a warm component ($T_{kin} = 42\,\mathrm{K} - 220\,\mathrm{K}$), with the density and temperature of the two components depending upon the ratio of ^{12}CO/^{13}CO which varies from 40 to 70. In our case, the warm component dominates the high J CO transitions, which are optically thin, while the cold component dominates the optically thick lower J CO transitions (Figure 2.8). Furthermore, while the density is not well constrained, our results suggest that the cold component has a lower density than the warm component, indicating that our lower density component does coincide with the optically thick transitions, as found by Zhu et al. (2003).

2.4.1.2 Comparison across the Antennae

Both the LTE and non-LTE radiative transfer analyses suggest there is cold molecular gas across the Antennae with both sets of calculated temperatures agreeing within the uncertainties (Figure 2.6). Furthermore, the non-LTE analysis suggests that warm molecular gas ($T_{kin} \gtrsim 100\,\mathrm{K}$) is prevalent throughout the system; however the warm component temperature is poorly constrained (Figures 2.10 and 2.12). Both sets of RADEX solutions for the cold molecular gas suggest that the molecular gas has a similar temperature ($\sim 20\,\mathrm{K}$) and density ($\sim 10^3 - 10^4\,\mathrm{cm}^{-3}$) in all three regions. Similarly, the densities of the warm component in the overlap region and NGC 4039 are similar ($\sim 10^{4.5}\,\mathrm{cm}^{-3}$), while it is higher in NGC 4038 ($\gtrsim 10^{4.75}\,\mathrm{cm}^{-3}$). In addition, the CO and [CI] RADEX solution suggest the density of the warm component is slightly higher than that of the cold component; however for the overlap region and NGC 4039, the 1σ ranges of the densities of the cold and warm components overlap and so no firm conclusions can be drawn concerning these densities.

Brandl et al. (2009) calculated the temperature of the warm molecular gas from Infrared Spectrograph (IRS) Spitzer Space Telescope (*Spitzer*) observations of the H_2 S(1) and S(2) transitions and found a warm gas temperature of $270 - 370\,\mathrm{K}$ in both nuclei and at numerous locations in the overlap region. This temperature range falls within our warm component 1σ ranges for these three regions. This suggests that H_2 is tracing the same warm gas as the upper J CO transitions.

The pressure across the Antennae in each of the cold and warm components is nearly constant within uncertainties (Figures 2.10 and 2.12), while the pressure in the warm component is $\sim 2-3$ orders of magnitude larger than that in the cold component. The temperature is only $\sim 1-3$ orders of magnitude larger in the warm component over the cold component and may be sufficient to explain the increased pressure.

2.4.2 CO abundance and the CO-to-H_2 conversion factor

For the purpose of our RADEX modeling we have assumed a CO abundance of $x_{\rm CO} = 3 \times 10^{-4}$ (Kamenetzky et al., 2012). Using this abundance, we recover a corrected cold gas mass of $M_{cold} = 1.5^{+1.7}_{-1.3} \times 10^{9}\ M_{\odot}$ which would correspond to a CO $J = 1-0$ luminosity-to-mass conversion factor of $\alpha_{\rm CO} \sim 0.7\ M_{\odot}\,{\rm pc}^{-2}$ (K km s^{-1})$^{-1}$. This value is lower than the value for the Milky Way, but agrees with the value of $\alpha_{\rm CO} = 0.8\ M_{\odot}\,{\rm pc}^{-2}$ (K km s^{-1})$^{-1}$ from Downes & Solomon (1998), which is the value typically assumed for ULIRGs. Arp 299, another relatively nearby merger ($D_L = 46\,{\rm Mpc}$), is brighter in the infrared than the Antennae ($L_{IR} \sim 7\times10^{11} L_{\odot}$). Sliwa et al. (2012) found that for a CO abundance of 3×10^{-4}, $\alpha_{\rm CO} = 0.4\ M_{\odot}\,{\rm pc}^{-2}$ (K km s^{-1})$^{-1}$, which agrees with the value calculated for LIRGs ($\alpha_{\rm CO} \sim 0.6 \pm 0.2\ M_{\odot}\,{\rm pc}^{-2}$ (K km s^{-1})$^{-1}$, Papadopoulos et al. 2012).

However, the true CO abundance in the Antennae may be smaller (Zhu et al., 2003). We investigate the CO abundance by comparing the total warm molecular gas mass we calculate in the Antennae to those from previous studies. Brandl et al. (2009) measured the total warm ($\sim 300\,{\rm K}$) gas mass in the Antennae using *Spitzer* observations of the H_2 S(1), S(2) and S(3) transitions to be $2.5 \times 10^{7} M_{\odot}$. Our corrected warm component ($\gtrsim 100\,{\rm K}$) mass from the CO-only RADEX solution is $2.2^{+1.3}_{-1.0} \times 10^{6} M_{\odot}$, while for the CO and [CI] solution it is $2.2^{+1.5}_{-1.0} \times 10^{6} M_{\odot}$. Both of our calculated masses are a factor of

~ 10 less than the Brandl et al. (2009) mass. Assuming our warm gas solution is tracing the same gas as the H_2 lines, a CO abundance of $x_{\rm CO} = 3 \pm 2 \times 10^{-5}$ is required to recover this warm gas mass. This abundance ratio falls in the range of $\sim 10^{-5} - 10^{-4}$, which is typically assumed for starburst galaxies (Zhu et al., 2003; Mao et al., 2000).

Using this abundance ratio of 3×10^{-5}, we obtain a cold molecular gas mass for the CO-only solution of $M_{cold} = 1.5^{+1.7}_{-1.3} \times 10^{10}\ M_\odot$. In order to recover the same mass from our CO $J = 1-0$ map, we would require a CO $J = 1-0$ luminosity-to-mass conversion factor of $\alpha_{\rm CO} \sim 7\ M_\odot\,{\rm pc}^{-2}$ (K km s^{-1})$^{-1}$. This is consistent with the Milky Way value ($\alpha_{\rm CO} \sim 4-9\ M_\odot\,{\rm pc}^{-2}$ (K km s^{-1})$^{-1}$) and the value for M 31, M 33 and the Large Magellanic Cloud ($\alpha_{\rm CO} \sim 3-9\ M_\odot\,{\rm pc}^{-2}$ (K km s^{-1})$^{-1}$, Leroy et al. 2011). Wilson et al. (2003) calculated the CO-to-H_2 conversion factor in the Antennae by comparing the virial mass of resolved SGMCs to the integrated intensity. They found that the conversion factor in the Antennae agrees with the value for the Milky Way ($\alpha_{\rm CO} \sim 6.5\ M_\odot\,{\rm pc}^{-2}$ (K km s^{-1})$^{-1}$). As such, we adopt a value of $\alpha_{\rm CO} \sim 7\ M_\odot\,{\rm pc}^{-2}$ (K km s^{-1})$^{-1}$ and $x_{\rm CO} \sim 3 \times 10^{-5}$ for the CO-to-H_2 conversion factor and the CO abundance respectively.

2.4.3 Heating and cooling of the molecular gas

In this section we will discuss the possible heating and cooling mechanisms for the molecular gas in the Antennae.

2.4.3.1 Cooling

CO, [OI]63 μm, [CII] and H_2 will all contribute to the overall cooling budget of both the cold and warm molecular gas; however, which coolant dominates is dependent on the overall state of the molecular gas. In particularly warm molecular gas ($T_{kin} \gtrsim 1000$ K), H_2 will be the dominant coolant (e.g. Arp 220, Rangwala et al. 2011) while for cooler gas, [CII], [OI]63 μm, and CO will also contribute to the total cooling of molecular gas. We investigate the possible cooling mechanisms in order to determine the total rate of cooling of molecular gas in the Antennae.

H_2 cooling only becomes important in molecular gas where the temperature is $T_{kin} > 100\,$K. Le Bourlot et al. (1999) calculated curves for the total H_2 cooling per unit mass, which is dependent upon the molecular gas density ($n(H_2)$), the kinetic temperature T_{kin}, the H/H_2 ratio and the ratio of ortho-to-para H_2, all of which are input parameters for the calculated cooling curves. Le Bourlot et al. (1999) have provided a program which interpolates their cooling curves for a given set of input parameters, allowing us to estimate the H_2 cooling for each pixel in the Antennae using the RADEX calculated $n(H_2)$ and T_{kin} from the warm component, along with the mass of the warm molecular gas. We assume that $H/H_2 = 0.01$ and that the ratio of ortho-to-para is 1. It is important to note that changing the ortho-to-para ratio to 3 does not change the total H_2 cooling significantly (Le Bourlot et al., 1999). The H_2 cooling is highly dependent on the kinetic temperature and given that the temperature of our warm component is not particularly well constrained, we opt to use the 1σ lower bound on the temperature in each pixel to calculate a lower limit to the H_2 cooling. There is only a $\sim 10-15\%$ difference between the cooling rate calculated when using either the 1σ lower bound or the most probable value for the molecular gas density. We opt to use the most probable value as it likely represents a more realistic density (e.g. see Figures 2.9 and 2.11).

We assume a CO abundance of 3×10^{-5} as determined in Section 2.4.2 and apply the same pixel incompleteness correction as we did for the mass. We calculate the total H_2 cooling to be $\sim 4.9\times10^{7} L_{\odot}$ from the CO-only RADEX results, and $\sim 6.5\times10^{7} L_{\odot}$ from the CO and [CI] RADEX results. Brandl et al.

(2009) measured a luminosity of $9.2 \times 10^6 L_\odot$ for the H_2 S(3) transition. Given that the luminosity of the S(2) and S(1) transitions are comparable to the S(3) transition (Brandl et al., 2009), our calculated H_2 cooling is reasonably consistent with this measurement.

Next, we estimate the total cooling contribution from CO ($L_{\rm CO}$) by summing the total luminosity for all of our CO transitions. Each individual transition contributes between 1% and 25% of the total CO cooling, with the $J = 1-0$ transition contributing only 1%, and $J = 4-3$ and $J = 6-5$ transitions contributing $> 20\%$. The remaining 5 transitions each contribute between 6% and 14% to the total CO cooling. In addition, we apply the same pixel incompleteness correction as before, and we calculate the contribution of CO to the overall cooling to be $L_{\rm CO} = 1.8 \times 10^7 L_\odot$.

In order to calculate the total contribution from [CII] to the total cooling budget, we must correct for the fraction of emission which arises from ionized gas. The ratio of [CII] to the [NII] transition at 1461 GHz ($L_{\rm [CII]}/L_{\rm [NII]}$) provides a useful diagnostic for determining the contribution from ionized gas (Oberst et al., 2006), as emission from [NII] arises entirely from ionized gas (Malhotra et al., 2001). This ratio depends upon the ionized gas density, n_e, with the ratio varying from ~ 2.4 to ~ 4.3 (Oberst et al., 2006), assuming solar abundances for C^+ and N^+. We assume $L_{\rm [CII]}/L_{\rm [NII]} \sim 3.5$ for the ionized gas as it is near the midpoint between the two extremes for the ratio, and correct the [CII] emission by assuming any excess in $L_{\rm [CII]}$ cools the molecular gas. This value is an upper limit as some of the [CII] emission will originate from atomic gas.

We calculate the ratio of $L_{\rm [CII]}/L_{\rm [NII]}$ by first convolving our [CII] map to the beam of the [NII] map. We approximate the SSW beam at 1461 GHz as a $17''$ Gaussian and use the kernels from Aniano et al. (2011). We then align our [CII] map to the $3''$ pixel scale [NII] map, and calculate the ratio of $L_{[CII]}/L_{[NII]}$. We linearly interpolate any pixels in which we do not have measurements for [NII], due to the large beam size. We correct each pixel in our [CII] map before summing over the entire map. After this correction, we calculate that the contribution to the total molecular gas cooling from [CII] to be $L_{[CII]} = 5.5 \times 10^7 L_\odot$. In comparison, without the correction for [CII] from ionized gas, the total [CII] luminosity is $L_{[CII]} = 9.4 \times 10^7 L_\odot$ from the PACS observations.

The total [CII] luminosity corresponds to only $\sim$ 23% of the total [CII] luminosity calculated by Nikola et al. (1998) using observations from the Kuiper Airborne Observatory (KAO). Their map, however, covered a region of $5' \times 5'$ which is significantly larger than the region mapped by PACS. Furthermore, Nikola et al. (1998) compared their KAO observations to those from the Infrared Space Observatory (ISO) and found that the KAO flux is a factor of 2 larger across the same region. The KAO observations also have a calibration uncertainty of 30%. Given the large uncertainties in these previous observations, we elect to estimate the total [CII] flux from the PACS observations. We estimate the missing flux in our [CII] flux by comparing the total PACS 160 μm flux to the PACS 160 μm flux in the region mapped in our [CII] observation. The PACS 160 μm was graciously provided by Klaas et al. (2010), and covers a total region of approximately $8.5' \times 9.5'$ centered on the Antennae. We estimate that only $\sim$ 70% of the total [CII] luminosity is in our PACS map, which gives us an ionized gas corrected luminosity of $L_{[CII]} = 7.9 \times 10^7 L_\odot$. Due to the uncertainty in the KAO flux, we use this corrected luminosity for the contribution of [CII] to the total cooling budget.

We also calculate the total cooling due to [OI]63 μm to be $L_{[OI]63} = 3.6 \times 10^7 L_\odot$ from the PACS observations. The ratio of $L_{[CII]}/L_{[OI]63}$ is not constant, typically increasing further away from the nuclear regions of galaxies, as [CII] starts to dominate the cooling in more diffuse environments. As such, we do not correct the [OI]63 μm emission for missing flux when including it in our total cooling budget. We estimate the total cooling budget for the molecular gas in the Antennae to be $\sim 2.0 \times 10^8 L_\odot$. Assuming a molecular gas mass of $1.5 \times 10^{10} M_\odot$ (see Section 2.4.2), this would correspond to $\sim 0.01 L_\odot/M_\odot$, with [CII] dominating the cooling, followed by H_2, [OI]63 and CO. In comparison, the cooling per unit mass in M82 and Arp220 is $\sim 3L_\odot/M_\odot$ and $\sim 20L_\odot/M_\odot$ respectively (see Section 2.4.4).

2.4.3.2 Mechanical heating

We consider two forms of mechanical heating: turbulent heating (Bradford et al., 2005), and supernova and stellar wind heating (Maloney, 1999). Turbulent heating is caused by the turbulent motion of the molecular gas which can be be caused by a strong interaction or ongoing merger. We can calculate the energy per unit mass injected back into the Antennae using (Bradford et al., 2005)

$$\frac{L}{M} = 1.10 \left(\frac{\mathrm{v}_{rms}}{25\,\mathrm{km\ s^{-1}}}\right)^3 \left(\frac{1\,\mathrm{pc}}{\Lambda_d}\right) \frac{L_\odot}{M_\odot} \tag{2.6}$$

where v_{rms} is the turbulent velocity and Λ_d is the size scale. We assume the turbulent heating rate is equal to our calculated cooling rate ($L/M \sim 0.01 L_\odot/M_\odot$), and for a size scale of $\Lambda_d = 1$ pc we calculate a turbulent velocity of $\mathrm{v}_{rms} \sim 5\,\mathrm{km\ s^{-1}}$. For a size scale of $\Lambda_d = 1000$ pc the corresponding turbulent velocity is $\mathrm{v}_{rms} \sim 52\,\mathrm{km\ s^{-1}}$. The line widths for the resolved SGMCs from Wilson et al. (2003) are on the order of $10-50\,\mathrm{km\ s^{-1}}$, which correspond to turbulent velocities on the order of $\mathrm{v}_{rms} \sim 5-25\,\mathrm{km\ s^{-1}}$ on a size scale of 1 kpc. This is comparable to the values calculated for a 1 pc size scale, which is on the order of the Jeans length for our warm component. Furthermore, it is comparable to velocities from simulations of extreme star-forming galaxies ($\sim 30-140\,\mathrm{km\ s^{-1}}$, Downes & Solomon 1998). Given that the Antennae is both undergoing an intense starburst (Hibbard, 1997) and is in the process of merging, a turbulent velocity of $\sim 5\,\mathrm{km\ s^{-1}}$ is not unreasonable. Thus, turbulent velocity is a possible contributor to heating in the Antennae.

The mechanical energy due to supernovae is (Maloney, 1999)

$$L_{SN} \sim 3 \times 10^{43} \left(\frac{\nu_{SN}}{1\,\mathrm{yr}^{-1}}\right)\left(\frac{E_{SN}}{10^{51}\,\mathrm{erg}}\right) \mathrm{erg\ s^{-1}} \tag{2.7}$$

where ν_{SN} is the supernova rate and E_{SN} is the energy released per supernova ($\sim 10^{51}$ erg). In the Antennae, the observed global supernova rate is $\nu_{\mathrm{SN}} \sim 0.2 - 0.3\,\mathrm{yr}^{-1}$ (Neff & Ulvestad, 2000). This corresponds to a rate of $L_{SN} \sim (1.6-2.3)\times10^9\ L_\odot$ for the energy released from supernova. If we assume that the contribution from stellar winds is comparable (Rangwala et al., 2011), the total mechanical energy injected into the interstellar medium (ISM) from supernovae and stellar winds is $(3.2-4.6)\times10^9\ L_\odot$. Only $\sim 5\%$ of this energy would be required to balance the measured cooling rate of $\sim 2.0\times10^8 L_\odot$. This situation corresponds to a supernova heating efficiency of 0.05. In comparison, in the Milky Way only $\sim 10\%$ of the total energy from supernovae is injected back into the surrounding ISM in the form of kinetic energy, which in turn contributes to both moving and heating the gas (Thornton et al., 1998).

By comparing the position of the nonthermal radio sources in Neff & Ulvestad (2000), along with their respective derived supernova rates, to the beams in Figure 2.1, we estimate that 14%, 6% and 66% of the supernova originate from NGC 4038, NGC 4039 and the overlap region, respectively. In comparison, we estimate that 9%, 15% and 54% of the [CII] emission (corrected for the ionized gas fraction), which is the dominant coolant (see Section 2.4.3.1), originates from NGC 4038, NGC 4039 and the overlap region, respectively. The differences between the relative heating and cooling rates could be an indicator of a different balance between the varying sources of heating in the three regions.

Globally, supernovae and stellar winds are a possible source of heating in the Antennae. Given the turbulent nature of the molecular gas as a result of the ongoing merger, it is likely that both the merger induced turbulent motion as well as supernovae and stellar winds contribute to the heating, with their relative importance dependent on the local environment within the Antennae.

2.4.3.3 Photon dominated regions

Photon dominated regions (PDRs) are neutral regions located near the surfaces of molecular clouds which are irradiated by strong far-ultraviolet (FUV) radiation (Tielens & Hollenbach, 1985). The FUV photons are absorbed by dust grains and may liberate electrons through the photoelectric effect; the liberated electrons in turn heat the gas. The strength of the incident FUV field, G_0, is measured in units of the Habing interstellar radiation field, which is 1.3×10^{-4} ergs cm^{-2} s^{-1} sr^{-1} (Wolfire, 2010), and is the strength of the local interstellar field. This FUV radiation will photo-dissociate the CO located near the edge of the molecular cloud where the FUV radiation is the strongest. Typically, massive, young, hot stars are the source of the FUV radiation, and as such can have a profound effect on the chemical and physical state of the entire molecular cloud.

We use PDR models (Hollenbach et al. 2012 and M. Wolfire, private communication) to interpret the observed CO SLED for the three regions in the Antennae (Table 2.1). These models consist of a grid of CO fluxes for transitions from $J = 1-0$ to $J = 29-28$ spanning a large range of densities ($n(\mathrm{H}_2) = 10^{1.0}\,\mathrm{cm}^{-3}$ to $10^{7.0}\,\mathrm{cm}^{-3}$) and incident FUV fluxes ($G_0 = 10^{-0.5}$ to $10^{6.5}$). Furthermore, these models typically assume that the FIR flux is a factor of two larger than the incident FUV flux. Using these models along with the densities calculated from our radiative transfer analysis, we can constrain the FUV field strength. In this section, we model the ratio of two CO transitions

($J = 3-2$ and $J = 6-5$) to the FIR flux along with the ratios of numerous CO transitions to each other.

We estimate the FIR luminosity ($L_{\rm FIR}$) by first calculating the total infrared luminosity ($L_{\rm TIR}$) using equation 4 from Dale & Helou (2002). We acquired the Multiband Imaging Photometer for Spitzer (MIPS) 24 μm map from the Spitzer Space Telescope (*Spitzer*) archive, while we were graciously provided with the PACS 70 μm and 160 μm photometric maps by Klaas et al. (2010). All 3 maps are convolved to the $160 \mu m$ beam size ($12.13''$, PACS Observer's Manual version 2.4[4]) using the appropriate convolution kernels and scripts from Aniano et al. (2011)[5]. Next, we assume a ratio of $L_{\rm TIR}/L_{\rm FIR} \sim 2$ (Dale et al., 2001) and calculate a map of $L_{\rm FIR}$. This $L_{\rm FIR}$ map is convolved to the $43''$ beam of the FTS by first convolving it to a $15''$ Gaussian beam using the appropriate kernel from Aniano et al. (2011), and then to the $43''$ FTS beam using the same kernel used to convolve the CO $J = 3-2$ map.

We calculate the ratios of $L_{\rm CO}/L_{\rm FIR}$ for the CO $J = 3-2$ transition and CO $J = 6-5$ transition for NGC 4038 (Figure 2.13 bottom), NGC 4039 (Figure 2.14 bottom), and the overlap region (Figure 2.15 bottom). We further constrain the field strength by plotting various ratios of CO transitions for NGC 4038 (Figure 2.13), NGC 4039 (Figure 2.14) and the overlap region (Figure 2.15). For all three regions, we plot the ratio of CO $\frac{3-2}{1-0}$ (top-left), $\frac{3-2}{2-1}$ (middle-left), $\frac{8-7}{6-5}$ (top-right), and $\frac{8-7}{7-6}$ (middle-right). We associate the CO $J = 3-2$ transition ratios with the cold component and $J = 6-5$ transition ratios with the warm component, and as such we compare these ratios to the densities of the cold ($J = 3-2$) and warm ($J = 6-5$) components from the CO and [CI] non-LTE radiative transfer solutions. In the bottom two panels of all 3 figures, we combine the cold (bottom-left) and warm (bottom-right) CO transitions with the corresponding $L_{\rm CO}/L_{\rm FIR}$ ratio.

[4]Available from `http://herschel.esac.esa.int/Docs/PACS/html/pacs_om.html`
[5]Available from `http://www.astro.princeton.edu/~ganiano/Kernels.html`

The results for all three regions are similar: the various ratios for the warm component are consistent with a field strength of Log(G_0) ~ 3, while the various ratios for the cold component are consistent with a field strength of Log(G_0) ~ 2. It is important to note that the ratios of $L_{\rm CO}/L_{\rm FIR}$ are lower limits as there will be contributions to $L_{\rm FIR}$ from both the cold and warm components. These lower limits correspond to upper limits in the FUV field strength G_0 (see bottom of Figure 2.13, Figure 2.14 and Figure 2.15). We are unable to constrain the relative contributions from the warm and cold components to the total FIR luminosity, and so all values for G_0 are upper limits.

Given an FUV field strength of Log(G_0) = 3 for our warm PDR models, and assuming a ratio of $L_{\rm FIR}/L_{\rm FUV} \sim 2$, the corresponding FIR flux is $2.6 \times 10^{-1}\,{\rm ergs\ cm^{-2}\ s^{-1}\ sr^{-1}}$. The peak FIR flux, as estimated from our TIR map, in NGC 4038 is $4.9 \times 10^{-2}\,{\rm ergs\ cm^{-2}\ s^{-1}\ sr^{-1}}$, NGC 4039 is $2.6 \times 10^{-2}\,{\rm ergs\ cm^{-2}\ s^{-1}\ sr^{-1}}$ and the overlap region is $9.3 \times 10^{-2}\,{\rm ergs\ cm^{-2}\ s^{-1}\ sr^{-1}}$. In NGC 4039, the weakest of the three regions, our model PDRs would need to fill only $\sim 10\%$ of the $12''$ ($\sim 1.2\,$kpc) PACS beam in order to recover the measured peak flux. Given that the typical size scale of GMCs and stellar clusters is $10 - 100\,$pc, only a few model PDR regions are required to recover the measured FIR flux.

In comparison, our cold PDR models have a FUV field strength of Log(G_0) = 2, corresponding to a FIR flux of $2.6 \times 10^{-2}\,{\rm ergs\ cm^{-2}\ s^{-1}\ sr^{-1}}$. In NGC 4039, this would require that our model PDRs fill $\sim 100\%$ of the PACS beam. Given the face-on nature of the Antennae coupled with previous interferometric observations of CO (e.g. Wilson et al. 2003), we do not expect PDRs to fill the $12''$ PACS beam and thus the warm PDRs must make a significant contribution to L_{FIR}. For example, if cold PDRs filled 30% of the beam and so contributed 30% of L_{FIR}, then the warm PDRs would have to account for the remaining 70% of the far-infrared luminosity in NGC 4039.

Bayet et al. (2006) modeled various ratios of the CO $J = 3-2$, $J = 2-1$ and $J = 6-5$ transitions, along with the ^{13}CO $J = 3-2$ transition with PDR models in NGC 4038 and the overlap region. They find a FUV field strength, in units of the Habing field, of $\mathrm{Log}(G_0) \sim 5.4$ and density of $n(\mathrm{H_2}) = 3.5 \times 10^5\,\mathrm{cm^{-3}}$ for the overlap region, while for NGC 4038 they find that $\mathrm{Log}(G_0) \sim 5.6$ and $n(\mathrm{H_2}) = 3.5 \times 10^5\,\mathrm{cm^{-3}}$. In both cases, their field strength does not lie within the fields strengths allowed by our solutions for both regions (Figure 2.15 and Figure 2.13). Furthermore, our ratio of $L_{\mathrm{CO}}/L_{\mathrm{FIR}}$ for the $J = 6-5$ transition would need to be two orders of magnitude smaller to recover such a field strength, even at very high densities (e.g. see bottom-right of Figure 2.13 and Figure 2.15). Given that our ratio provides an upper limit on G_0, we can rule out their solutions.

In comparison, Schulz et al. (2007) modeled various ratios of the peak brightness of the ^{12}CO $J = 1-0$, $J = 2-1$, and $J = 3-2$ transitions, along with the ^{13}CO $J = 1-0$ and $J = 2-1$ transitions. They apply their model to NGC 4038, NGC 4039 and the overlap region (their "interaction region"). Their findings are consistent with ours: they are able to recover their line ratios with an FUV field strength equivalent to $\mathrm{Log}(G_0) \sim 3.2$ with densities of $n(\mathrm{H_2}) = 10^{4.5}$, $n(\mathrm{H_2}) = 10^{4.3}$ and $n(\mathrm{H_2}) = 10^{4.4}$ for NGC 4038, NGC 4039 and the overlap region. All of these densities lie either within our 1σ ranges for the respective cold and warm components, or lie near the boundary, further suggesting that our results are consistent with Schulz et al. (2007).

In summary, we model the ratios of CO $J = 3-2$ and $J = 6-5$ transitions to the FIR emission, along with various ratios of different CO transitions with PDRs. By comparing our densities as calculated from our non-LTE radiative transfer analysis, we find a field strength of $\mathrm{Log}(G_0) \sim 3$ for PDRs in all three regions. Our field strength and densities for our PDR models are both significantly less than the values from Bayet et al. (2006), but are both consistent with the results from Schulz et al. (2007). Thus, PDRs remain as a possible source of significant heating throughout the Antennae. Further study using transitions from atomic species, such as [CII] and [OI], will be useful in further constraining not only the physical characteristics of the PDRs throughout the Antennae, but the location of these PDRs.

2.4.4 Comparison to other galaxies

The Antennae is the fourth system from the VNGS-FTS sample to be analyzed using a non-LTE radiative transfer analysis and is the only early-stage merger from our sample. Furthermore, of these four systems, it is the only one in which large scale structure is resolved in our 43″ beam. Of the three previously studied galaxies, the Antennae has more similarities to M82 (Kamenetzky et al., 2012) and Arp 220 (Rangwala et al., 2011). The third galaxy, NGC 1068, is a Seyfert type 2 galaxy, whose nuclear physical and chemical state is driven by an active galactic nucleus (AGN) (Spinoglio et al., 2012).

M82 is a nearby galaxy (3.4 Mpc) currently undergoing a starburst (Yun et al., 1993) due to a recent interaction with the nearby galaxy M81. This starburst has led to an enhanced star formation rate, and as a result an infrared brightness ($L_{IR} = 5.6 \times 10^{10}\,\mathrm{L}_{\odot}$, Sanders et al. 2003) approaching that of a LIRG. Like in the Antennae, radiative transfer modeling of M82 found that there is both a cold ($\lesssim 100\,\mathrm{K}$) and warm ($\sim 450\,\mathrm{K}$) molecular gas, with the mass of the warm component ($\sim 1.5 \times 10^{6} M_{\odot}$) being on the order of $\sim 10\%$ of the mass of the cold component ($\sim 2 \times 10^{7} M_{\odot}$) (Kamenetzky et al., 2012). Arp 220, on the other hand, is a nearby (77 Mpc, Scoville et al. 1997) ULIRG with an increased star formation rate that is the result of an ongoing merger in an advanced state. As in M82 and the Antennae, both a cold ($T_{kin} \sim 50\,\mathrm{K}$) and a warm ($\sim 1300\,\mathrm{K}$) component are recovered from the radiative transfer analysis, albeit significantly warmer in Arp 220 (Rangwala et al., 2011). Similarly to M82, the warm gas mass ($\sim 4.7 \times 10^8 M_\odot$) is about $\sim 10\%$ that of the cold gas mass ($\sim 5.2 \times 10^9 M_\odot$, Rangwala et al. 2011).

Both Arp 220 and M82 have a significantly higher warm gas mass fraction than in the Antennae, where we found a warm gas mass fraction of $\sim 0.2\%$. This may be due to either Arp 220 and M82 having a larger source of heating or NGC 4038/39 cooling more efficiently. Evidence suggests Arp 220 hosts a central AGN (Clements et al., 2002; Iwasawa et al., 2005); however, the strongest candidates for heating are supernova and stellar winds, which contribute $\sim 200 L_\odot/M_\odot$ to the overall heating (Rangwala et al., 2011). (This value does not account for supernova feedback efficiency.) The majority of the cooling is from H_2 due to the high temperature of the warm molecular gas ($T_{kin} \sim 1300\,\mathrm{K}$) and the cooling rate is $\sim 20 L_\odot/M_\odot$. In Arp 220, a supernova heating efficiency $\gtrsim 0.1$ is required to match the cooling; however Arp 220 is compact in comparison to the Antennae with the size of its molecular region only $\sim 400\,\mathrm{pc}$. Therefore, the increase in both the temperature and mass fraction of the warm molecular gas in Arp 220 is likely a result of a larger amount of supernova and stellar wind energy being injected into the surrounding ISM, a higher supernova feedback efficiency and a larger difference between the heating and cooling rates.

Similarly to Arp 220, turbulent motions due to supernovae and stellar winds are the strongest candidate for molecular gas heating in M82 (Panuzzo et al., 2010; Kamenetzky et al., 2012). The cooling rate in M82 is greater than in NGC 4038/39 by two orders of magnitude ($3 L_\odot/M_\odot$). The supernova rate in M82 is $\sim 0.09\,\mathrm{yr}^{-1}$ (Fenech et al., 2010), which corresponds to $L_{SN} \sim (7 \times 10^8) L_\odot$, or $L_{SN}/M \sim 32 L_\odot/M_\odot$ assuming a molecular gas mass of $2.2 \times 10^7 M_\odot$ (Kamenetzky et al., 2012). A supernova feedback efficiency of ~ 0.1 is required to match the cooling in M82. As such, the higher warm gas fraction and temperature in M82 is possibly the result of a higher supernova heating rate, likely in part due to the increased supernova feedback efficiency.

2.5 Summary and conclusions

In this paper, we present maps of the CO $J = 4-3$ to $J = 8-7$ and two [CI] transitions of the Antennae observed using the *Herschel* SPIRE-FTS. We supplement the SPIRE-FTS maps with observations of CO $J = 2-1$ and $J = 3-2$ from the JCMT, CO $J = 1-0$ from the NRO, and observations of [CII] and [OI]63 μm from the *Herschel* PACS spectrometer.

1. We perform a local thermodynamic equilibrium analysis using the two observed [CI] transitions across the entire galaxy. We find that throughout the Antennae there is cold molecular gas with temperatures $\sim 10-30$ K. Our non-local thermodynamic equilibrium radiative transfer analysis using both CO and [CI] transitions shows that the [CI] emission is optically thin, which suggests that [CI] is in local thermodynamic equilibrium.

2. Using the non-local thermodynamic equilibrium radiative transfer code RADEX, we perform a likelihood analysis using our 8 CO transitions, both with and without the two [CI] transitions. We find that the molecular gas in the Antennae is in both a cold ($T_{kin} \sim 10-30$ K) and a warm ($T_{kin} \gtrsim 100$ K) state, with the warm molecular gas comprising only $\sim 0.2\%$ of the total molecular gas fraction in the Antennae. Furthermore, the physical state of the molecular gas does not vary substantially, with the pressure of both the warm and cold components being nearly constant within uncertainties and our angular resolution across the Antennae.

3. By considering the contributions of H_2, [CII], [OI]63 μm and CO, we calculate a total cooling rate of $\sim 2.0 \times 10^8 L_\odot$ for the molecular gas, or $\sim 0.01 L_\odot/M_\odot$, with [CII] as the dominant coolant. The contributions calculated for H_2 and [OI]63 μm are lower limits due to unconstrained temperatures from the radiative transfer analysis (H_2) and limits in the size of the map ([OI]63 μm). Furthermore, the contributions from [CII] is an upper limit as some of the [CII] emission likely originates from atomic gas. Mechanical heating is sufficient to match the total cooling and heat the molecular gas throughout the Antennae, with both turbulent heating due to the ongoing merger, and supernovae and stellar winds contributing to the mechanical heating.

4. We model the ratio of the CO flux to the FIR flux for CO $J = 3-2$ and $J = 6-5$, along with the ratio of various CO lines in the nucleus of NGC 4038, the nucleus of NGC 4039 and the overlap region using models of photon dominated regions. Using the densities calculated from our non-LTE radiative transfer analysis, we find that a photon dominated region with a field strength of $G_0 \sim 1000$ can explain the warm component CO and FIR emission in all three regions. We also find that this field strength is consistent with the observed peak FIR flux in all three regions. These results are consistent with a previous study by Schulz et al. (2007). While photon dominated regions are not necessary to heat the molecular gas, they remain as a possible contributor in heating the molecular gas in the star forming regions of the Antennae.

5. Both the warm gas fraction and temperature are smaller in NGC 4038/39 than in either Arp 220, or M82, both of which are likely heated by turbulent motion due to supernova and stellar winds. We suggest that this is due to increased supernova feedback efficiency in both Arp 220

and M82 due to their compactness.

6. In the warm molecular gas, we calculate a CO abundance of $x_{\rm CO} \sim 3 \times 10^{-5}$, corresponding to a warm molecular gas mas of $\sim 2.2 \times 10^{7} M_{\odot}$. If we assume the same CO abundance in the cold molecular gas, this corresponds to a cold molecular gas mass of $1.5 \times 10^{10} M_{\odot}$ and a CO luminosity-to-mass conversion factor of $\alpha_{\rm CO} \sim 7\ M_{\odot}\ {\rm pc}^{-2}$ (K km s^{-1})$^{-1}$, comparable to the Milky Way value. This value is consistent with previous results for the Antennae (Wilson et al., 2003) where the luminosity-to-mass conversion factor was determined using the virial mass of resoled SGMCs.

Acknowledgements

This research was supported by grants from the Canadian Space Agency and the Natural Sciences and Engineering Research Council of Canada (PI: C. D. Wilson). MPS has been funded by the Agenzia Spaziale Italiana (ASI) under contract I/005/11/0. PACS has been developed by a consortium of institutes led by MPE (Germany) and including UVIE (Austria); KU Leuven, CSL, IMEC (Belgium); CEA, LAM (France); MPIA (Germany); INAF-IFSI/OAA/OAP/OAT, LENS, SISSA (Italy); IAC (Spain). This development has been supported by the funding agencies BMVIT (Austria), ESA-PRODEX (Belgium), CEA/CNES (France), DLR (Germany), ASI/INAF (Italy) and CICYT/MCYT (Spain). SPIRE has been developed by a consortium of institutes led by Cardiff University (UK) and including Univ. Lethbridge (Canada); NAOC (China); CEA, LAM (France); IFSI, Univ. Padua (Italy); IAC (Spain); Stockholm Observatory (Sweden); Imperial College London, RAL, UCL-MSSL, UKATC, Univ. Sussex (UK); and Caltech, JPL, NHSC, Univ. Colorado (USA). This development has been supported by national funding agencies:

CSA (Canada); NAOC (China); CEA, CNES, CNRS (France); ASI (Italy); MCINN (Spain); SNSB (Sweden); STFC (UK); and NASA (USA). HIPE is a joint development by the Herschel Science Ground Segment Consortium, consisting of ESA, the NASA Herschel Science Center, and the HIFI, PACS and SPIRE consortia. This research has made use of the NASA/IPAC Extragalactic Database (NED) which is operated by the Jet Propulsion Laboratory, California Institute of Technology, under contract with the National Aeronautics and Space Administration. This research made use of the python plotting package matplotlib (Hunter, 2007). This research made use of APLpy, an open-source plotting package for Python hosted at http://aplpy.github.com. We would like to thank Mark Wolfire for providing the PDR model grids used in this paper. IDL is a postdoctoral researcher of the FWO-Vlaanderen (Belgium).

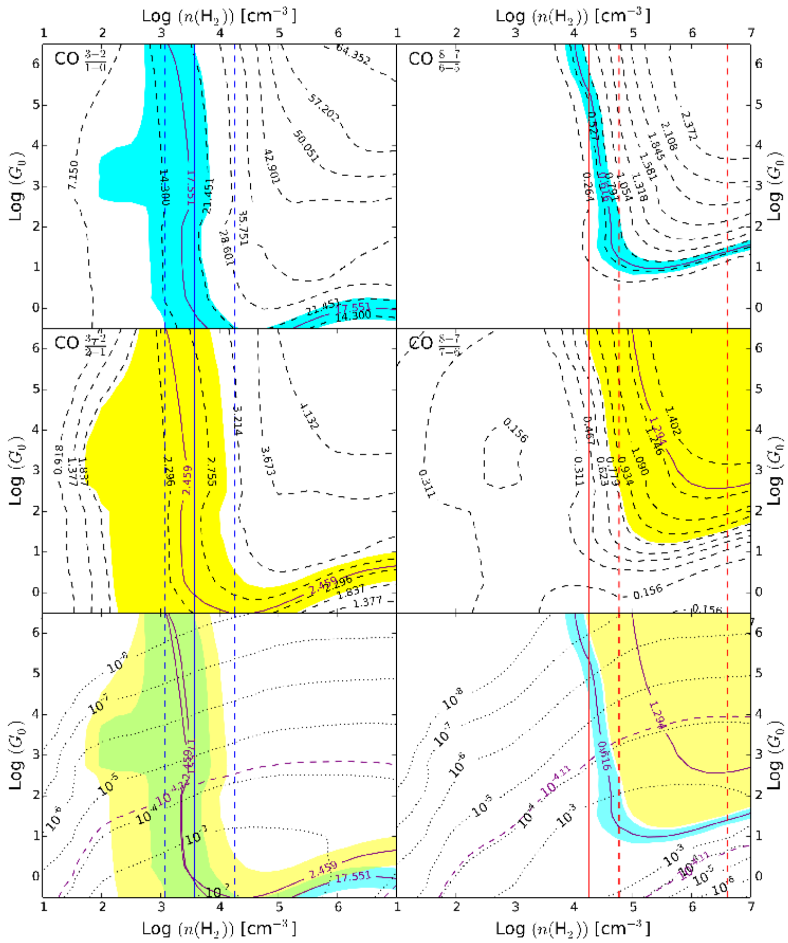

Figure 2.13 PDR models for NGC 4038 comparing CO line ratios to the field strength in units of the Habing field (G_0) and the gas density (n_{H_2}). Each of the panels in the top two rows correspond to a different CO ratio: $J = 3-2/1-0$ (*top-left*), $J = 3-2/2-1$ (*middle-left*), $J = 8-7/6-5$ (*top-right*) and $J = 8-7/7-6$ (*middle-right*). The $J = 3-2/1-0$ and $J = 3-2/2-1$ ratios are combined in the bottom-left panel, while the $J = 8-7/6-5$ and $J = 8-7/7-6$ ratios are combined in the bottom-right panel. The dashed black contours correspond to contours of constant ratios, while the purple contour corresponds to the measured ratio of the two lines. The blue and yellow shaded regions indicate the 1σ uncertainty range in the measured ratio. The blue and red solid lines correspond to the cold and warm component densities as determine from the $J_{break} = 4$ radiative transfer solution for both CO and [CI] while the blue and red dashed lines correspond to the 1σ range to this density for the cold and warm components respectively. In the bottom panels, the dashed purple contours corresponds to the measured ratio of CO $J = 3-2$/FIR (*bottom-left*) and CO $J = 6-5$/FIR (*bottom-right*) in units of erg cm^{-2} s^{-1} sr^{-1}, while the dotted black contours correspond to the model CO/FIR values.

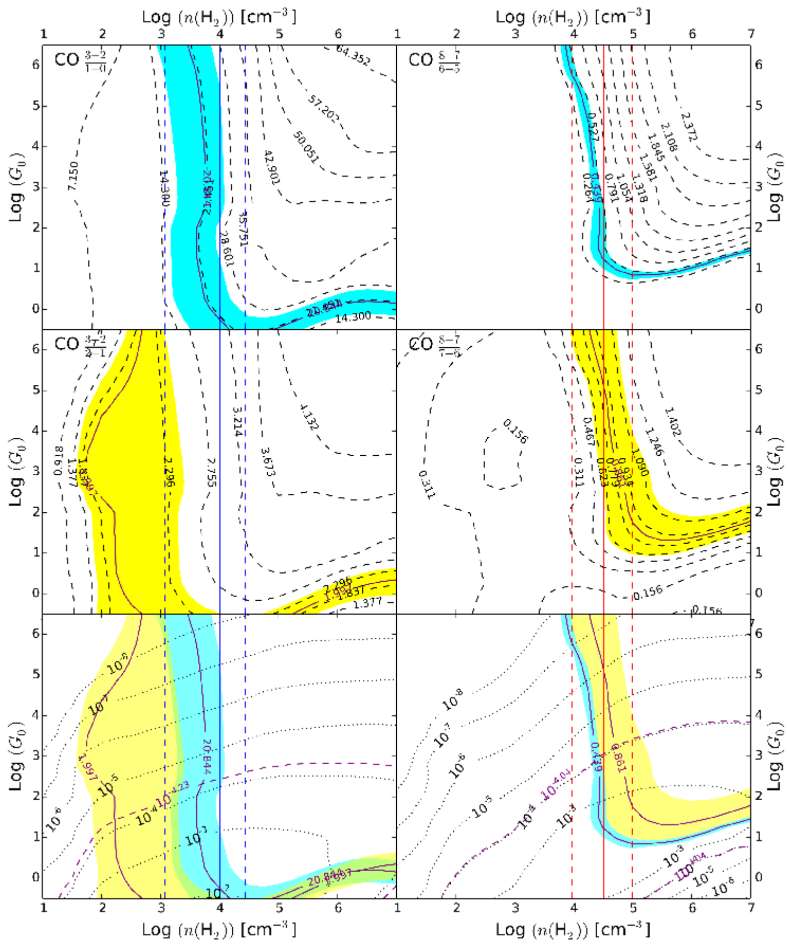

Figure 2.14 Same as figure 2.13 except for NGC 4039.

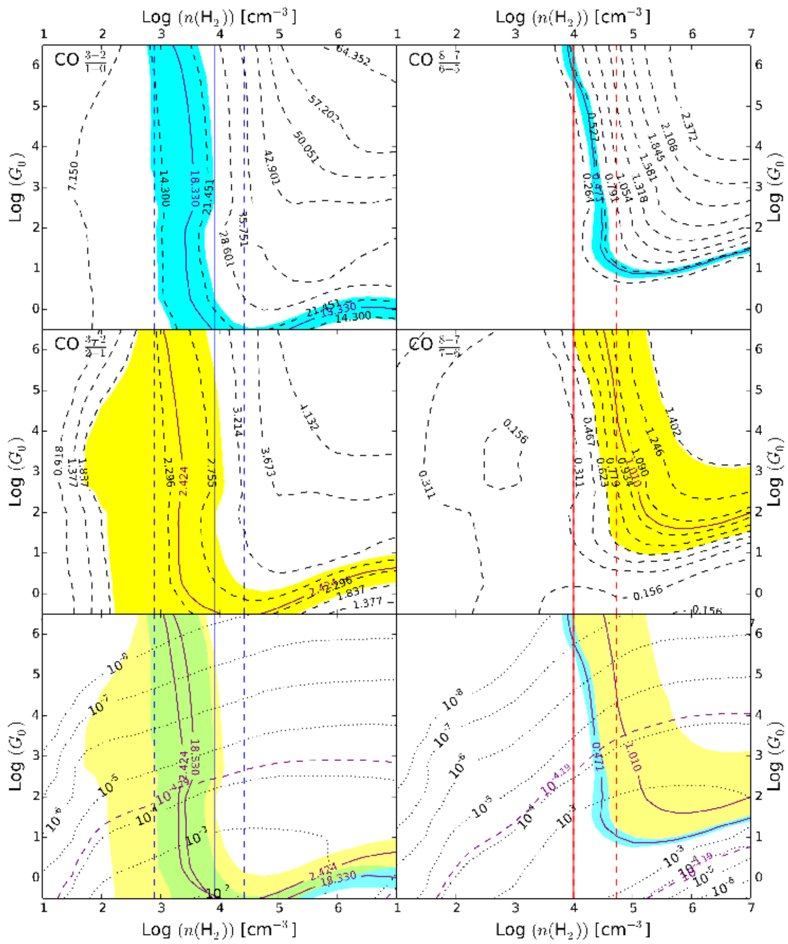

Figure 2.15 Same as figure 2.13 except for the overlap region. Note that in the right column, the solid red line coincides with the lower dashed red line.

Bibliography

Aniano, G., Draine, B. T., Gordon, K. D., & Sandstrom, K. 2011, PASP, 123, 1218

Bayet, E., Gerin, M., Phillips, T. G., & Contursi, A. 2006, A&A, 460, 467

Bendo, G. J., Boselli, A., Dariush, A., et al. 2012, MNRAS, 419, 1833

Bradford, C. M., Stacey, G. J., Nikola, T., et al. 2005, ApJ, 623, 866

Brandl, B. R., Snijders, L., den Brok, M., et al. 2009, ApJ, 699, 1982

Clements, D. L., McDowell, J. C., Shaked, S., et al. 2002, ApJ, 581, 974

Clements, D. L., Sutherland, W. J., McMahon, R. G., & Saunders, W. 1996, MNRAS, 279, 477

Cluver, M. E., Jarrett, T. H., Kraan-Korteweg, R. C., et al. 2010, ApJ, 725, 1550

Currie, M. J., Draper, P. W., Berry, D. S., et al. 2008, in Astronomical Society of the Pacific Conference Series, Vol. 394, Astronomical Data Analysis Software and Systems XVII, ed. R. W. Argyle, P. S. Bunclark, & J. R. Lewis, 650

Dale, D. A., & Helou, G. 2002, ApJ, 576, 159

Dale, D. A., Helou, G., Contursi, A., Silbermann, N. A., & Kolhatkar, S. 2001, ApJ, 549, 215

Downes, D., & Solomon, P. M. 1998, ApJ, 507, 615

Fenech, D., Beswick, R., Muxlow, T. W. B., Pedlar, A., & Argo, M. K. 2010, MNRAS, 408, 607

Fischer, J., Shier, L. M., Luhman, M. L., et al. 1996, A&A, 315, L97

Fulton, T. R., Baluteau, J., Bendo, G., et al. 2010, in Society of Photo-Optical Instrumentation Engineers (SPIE) Conference Series, Vol. 7731, Society of Photo-Optical Instrumentation Engineers (SPIE) Conference Series

Gao, Y., Lo, K. Y., Lee, S.-W., & Lee, T.-H. 2001, ApJ, 548, 172

Gehrz, R. D., Sramek, R. A., & Weedman, D. W. 1983, ApJ, 267, 551

Genzel, R., Tacconi, L. J., Gracia-Carpio, J., et al. 2010, MNRAS, 407, 2091

Griffin, M. J., Abergel, A., Abreu, A., et al. 2010, A&A, 518, L3

Herrera, C. N., Boulanger, F., Nesvadba, N. P. H., & Falgarone, E. 2012, A&A, 538, L9

Hibbard, J. E. 1997, in American Institute of Physics Conference Series, Vol. 393, American Institute of Physics Conference Series, ed. S. S. Holt & L. G. Mundy, 259–270

Hollenbach, D., Kaufman, M. J., Neufeld, D., Wolfire, M., & Goicoechea, J. R. 2012, ApJ, 754, 105

Hunter, J. D. 2007, Computing In Science & Engineering, 9, 90

Ikeda, M., Oka, T., Tatematsu, K., Sekimoto, Y., & Yamamoto, S. 2002, ApJS, 139, 467

Iwasawa, K., Sanders, D. B., Evans, A. S., et al. 2005, MNRAS, 357, 565

Joseph, R. D., & Wright, G. S. 1985, MNRAS, 214, 87

Kamenetzky, J., Glenn, J., Maloney, P. R., et al. 2011, ApJ, 731, 83

Kamenetzky, J., Glenn, J., Rangwala, N., et al. 2012, ApJ, 753, 70

Klaas, U., Nielbock, M., Haas, M., Krause, O., & Schreiber, J. 2010, A&A, 518, L44

Le Bourlot, J., Pineau des Forêts, G., & Flower, D. R. 1999, MNRAS, 305, 802

Leroy, A. K., Bolatto, A., Gordon, K., et al. 2011, ApJ, 737, 12

Malhotra, S., Kaufman, M. J., Hollenbach, D., et al. 2001, ApJ, 561, 766

Maloney, P. R. 1999, Ap&SS, 266, 207

Mao, R. Q., Henkel, C., Schulz, A., et al. 2000, A&A, 358, 433

Meijerink, R., Kristensen, L. E., Weiß, A., et al. 2013, ApJ, 762, L16

Naylor, B. J., Bradford, C. M., Aguirre, J. E., et al. 2010a, ApJ, 722, 668

Naylor, D. A., Baluteau, J.-P., Barlow, M. J., et al. 2010b, in Presented at the Society of Photo-Optical Instrumentation Engineers (SPIE) Conference, Vol. 7731, Society of Photo-Optical Instrumentation Engineers (SPIE) Conference Series

Neff, S. G., & Ulvestad, J. S. 2000, AJ, 120, 670

Nikola, T., Genzel, R., Herrmann, F., et al. 1998, ApJ, 504, 749

Oberst, T. E., Parshley, S. C., Stacey, G. J., et al. 2006, ApJ, 652, L125

Panuzzo, P., Rangwala, N., Rykala, A., et al. 2010, A&A, 518, L37

Papadopoulos, P. P., Thi, W.-F., & Viti, S. 2004, MNRAS, 351, 147

Papadopoulos, P. P., van der Werf, P., Xilouris, E., Isaak, K. G., & Gao, Y. 2012, ApJ, 751, 10

Parkin, T. J., Wilson, C. D., Foyle, K., et al. 2012, MNRAS, 422, 2291

Pereira-Santaella, M., Spinoglio, L., Busquet, G., et al. 2013, ApJ, 768, 55

Pilbratt, G. L., Riedinger, J. R., Passvogel, T., et al. 2010, A&A, 518, L1

Rangwala, N., Maloney, P. R., Glenn, J., et al. 2011, ArXiv e-prints, arXiv:1106.5054

Read, A. M., Ponman, T. J., & Wolstencroft, R. D. 1995, MNRAS, 277, 397

Sanders, D. B., Mazzarella, J. M., Kim, D.-C., Surace, J. A., & Soifer, B. T. 2003, AJ, 126, 1607

Sanders, D. B., & Mirabel, I. F. 1996, ARA&A, 34, 749

Schöier, F. L., van der Tak, F. F. S., van Dishoeck, E. F., & Black, J. H. 2005, A&A, 432, 369

Schroder, K., Staemmler, V., Smith, M. D., Flower, D. R., & Jaquet, R. 1991, Journal of Physics B Atomic Molecular Physics, 24, 2487

Schulz, A., Henkel, C., Muders, D., et al. 2007, A&A, 466, 467

Schweizer, F., Burns, C. R., Madore, B. F., et al. 2008, AJ, 136, 1482

Scoville, N. Z., Yun, M. S., & Bryant, P. M. 1997, ApJ, 484, 702

Sliwa, K., Wilson, C. D., Petitpas, G. R., et al. 2012, ApJ, 753, 46

Spinoglio, L., Pereira-Santaella, M., Busquet, G., et al. 2012, ArXiv e-prints, arXiv:1208.6132

Stanford, S. A., Sargent, A. I., Sanders, D. B., & Scoville, N. Z. 1990, ApJ, 349, 492

Swinyard, B. M., Ade, P., Baluteau, J.-P., et al. 2010, A&A, 518, L4

Thornton, K., Gaudlitz, M., Janka, H.-T., & Steinmetz, M. 1998, ApJ, 500, 95

Tielens, A. G. G. M., & Hollenbach, D. 1985, ApJ, 291, 722

Toomre, A., & Toomre, J. 1972, ApJ, 178, 623

Ueda, J., Iono, D., Petitpas, G., et al. 2012, ApJ, 745, 65

van der Tak, F. F. S., Black, J. H., Schöier, F. L., Jansen, D. J., & van Dishoeck, E. F. 2007, A&A, 468, 627

van der Werf, P. P., Isaak, K. G., Meijerink, R., et al. 2010, A&A, 518, L42

Ward, J. S., Zmuidzinas, J., Harris, A. I., & Isaak, K. G. 2003, ApJ, 587, 171

Warren, B. E., Wilson, C. D., Israel, F. P., et al. 2010, ApJ, 714, 571

Wei, L. H., Keto, E., & Ho, L. C. 2012, ApJ, 750, 136

Whitmore, B. C., & Schweizer, F. 1995, AJ, 109, 960

Whitmore, B. C., Zhang, Q., Leitherer, C., et al. 1999, AJ, 118, 1551

Whitmore, B. C., Chandar, R., Schweizer, F., et al. 2010, AJ, 140, 75

Wilson, C. D., Scoville, N., Madden, S. C., & Charmandaris, V. 2000, ApJ, 542, 120

—. 2003, ApJ, 599, 1049

Wolfire, M. G. 2010, Ap&SS, 380

Yun, M. S., Ho, P. T. P., & Lo, K. Y. 1993, ApJ, 411, L17

Zhang, H.-X., Gao, Y., & Kong, X. 2010, MNRAS, 401, 1839

Zhu, M., Seaquist, E. R., & Kuno, N. 2003, ApJ, 588, 243

Chapter 3

Probing the cold and warm molecular gas in the Whirlpool Galaxy: Herschel SPIRE-FTS Observations of the central region of M51 (NGC 5194)

M.R.P. Schirm, C.D. Wilson, T.J. Parkin, J. Glenn, J. Kamenetzky, P. Maloney, N. Rangwala, L. Spinoglio

Prepared for submission to Monthly Notices of the Royal Astronomical Society.

"And though we may not be alone in the universe, in our own separate ways, on this planet we are all alone."

"Jose Chung" from The X-Files episode "Jose Chung's From Outer Space" (1999-2013)

Abstract

We present Herschel SPIRE-FTS intermediate-sampled mapping observations of the central $\sim 8\,\mathrm{kpc}$ ($\sim 150''$) of M51, with a spatial resolution of $40''$. We detect 4 ^{12}CO transitions ($J = 4-3$ to $J = 7-6$) and both [CI] transitions in the nucleus, and centre regions. We supplement these observations with grounds based observations of ^{12}CO $J = 1-0$ to $J = 3-2$ and perform a two-component radiative transfer analysis. We find that most of the molecular gas resides in a cool ($T_{kin} \sim 20-40\,\mathrm{K}$) and moderately dense ($n(\mathrm{H_2}) \sim 10^{2.9} - 10^{3.8}\,\mathrm{cm^{-3}}$) component in the nucleus and centre regions, while $\sim 0.2-0.3\%$ of the molecular gas is in a warmer ($T_{kin} \sim 40-180\,\mathrm{K}$), higher density ($n(\mathrm{H_2}) \sim 10^{4.9} - 10^{6.6}\,\mathrm{cm^{-3}}$) component. Assuming a CO abundance of $x_{\mathrm{CO}} = 3\times10^{-5}$, we find values of $\alpha_{\mathrm{CO}} \sim 2M_{\odot}\,\mathrm{pc^{-2}(K\ km\ s^{-1})^{-1}}$ and $\alpha_{[\mathrm{CI}]} \sim 14M_{\odot}\,\mathrm{pc^{-2}(K\ km\ s^{-1})^{-1}}$ for the CO- and [CI]-to-H$_2$ conversion factors for the centre region. We compare our CO line ratios and calculated densities along with ratios of CO to far infrared luminosity to a grid of photon dominated region (PDR) models and find that the cold molecular gas likely resides in PDRs with a field strength of $G_0 \sim 10^2$. When compared to similar two-component models in other star-forming galaxies published as part of the VNGS (Arp220, M82 and NGC 4038/39), the warm component of M51 has the lowest temperature of the warm components, while the density and warm gas-mass fraction is comparable to the nucleus of NGC 4038. We attribute

these differences to the increased star formation rates in Arp220, M82 and NGC 4038/39.

3.1 Introduction

M51 (NGC 5194) is a well-studied, relatively normal, nearby spiral galaxy. Its recent interaction with the nearby dusty lenticular galaxy NGC 5195 has led to triggered star formation throughout the galaxy (Nikola et al., 2001), and there is evidence to suggest that the interaction is, at least in part, the cause for the prominent spiral arms of M51 (Zaritsky et al., 1993; Dobbs et al., 2010). Rose & Searle (1982) first suggested the presence of a non-stellar nuclear source of radiation at the centre of M51: it has been classified as a Seyfert type 2 galaxy, without any hidden broad line region (Tran, 2001) and later as a Low Ionization Nuclear Emission Region (LINER) galaxy (e.g., Satyapal et al. 2004). There is evidence to support the idea that the Seyfert-2 activity may have been triggered as a result of the interaction (Koulouridis, 2014).

M51 is an excellent source in which to study both cold and warm molecular gas, due to its nearly face-on orientation, the prominence of its spiral arms, and its recent interaction with NGC 5195. Observations of H_2 rotational lines have found that the ratio of warm ($T = 100-300\,\mathrm{K}$) to hot ($T = 400-1000\,\mathrm{K}$) molecular gas varies across the system, which may suggest a varying excitation mechanism (Brunner et al., 2008). Roussel et al. (2007) found that the H_2 is generally excited in photon dominated regions (PDRs, also known as photodissociation regions). Recently, Parkin et al. (2013) modelled PDRs in M51 using various transitions of [OI], [CII] and [NII], along with the total infrared luminosity, and found that the far-ultraviolet field strength necessary to reproduce PDRs in M51 varies between $G_0 \sim 10^{1.5} - 10^{4.0}$, with the highest values occurring in the nucleus.

The cold molecular gas has been studied predominantly through observations of the molecular gas tracer ^{12}CO (hereafter CO), and its isotopologues ^{13}CO and C^{18}O. M51 has been observed using ground-based single-dish telescopes in CO $J = 1-0$ (Scoville & Young, 1983; Garcia-Burillo et al., 1993; Nakai et al., 1994; Kramer et al., 2005; Koda et al., 2009), $J = 2-1$ (Garcia-Burillo et al., 1993; Kramer et al., 2005; Israel et al., 2006; Schuster et al., 2007; Leroy et al., 2009), $J = 3-2$ (Israel et al., 2006; Vlahakis et al., 2013) and $J = 4-3$ (Israel et al., 2006), and in ^{13}CO $J = 1-0$ (Kramer et al., 2005), $J = 2-1$ (Kramer et al., 2005; Israel et al., 2006) and $J = 3-2$ (Israel et al., 2006). In addition, Israel et al. (2006) presented observations of [CI] in the $^3P_1 -^3 P_0$ (hereafter $J = 1-0$) transition at 492 GHz, which has also been suggested as a molecular gas tracer (e.g. see Papadopoulos et al. 2004 and Offner et al. 2014).

Higher-resolution interferometric observations of CO $J = 2-1$, ^{13}CO $J = 1-0$ and ^{12}C^{18}O $J = 1-0$ in M51 have been performed using the Owens Valley Radio Observatory (OVRO) by Schinnerer et al. (2010). These observations were limited to two regions within the spiral arms of M51. Using non-local thermodynamic equilibrium (LTE) excitation models using an escape probability formalism, they found that the temperature of the molecular gas in the observed GMCs is $T_{kin} \sim 20$ K. This temperature is similar to those found in the Milky Way when observed at the same resolution (~ 180 pc), suggesting that the conditions inside GMCs found in the arms of M51 are Milky Way-like.

More recently, M51 was observed at arcsecond resolution in CO $J = 1-0$ and ^{13}CO $J = 1-0$ as part of the Plateau de Bure Interferometer (PdBI) Arcsecond Whirlpool Survey (PAWS, Schinnerer et al. 2013; Pety et al. 2013; Hughes et al. 2013b; Meidt et al. 2013; Hughes et al. 2013a; Colombo et al. 2014a,b). These observations were corrected for short-spacing using single dish observations. Colombo et al. (2014a) detected 1507 objects in CO $J = 1-0$, and found that the mass distribution, brightness and velocity dispersion of GMCs vary across the different environments in M51. There is evidence that some of these differences are dynamically driven (Meidt et al., 2013). Of particular interest is the extended CO $J = 1-0$ emission detected by Pety et al. (2013). This extended component resides in a thick molecular disk with a scale height $\sim 200\,$pc, and accounts for $\sim 50\%$ of the total CO $J = 1-0$ emission. Pety et al. (2013) suggest that this thick, extended disk could be the result of galactic fountains or chimneys due to the ongoing star formation.

In this paper, we present observations of M51 using the Spectral and Photometric Imaging Receiver (SPIRE; Griffin et al. 2010) Fourier Transform Spectrometer (FTS; Naylor et al. 2010b) on board the ESA Herschel Space Observatory (*Herschel*; Pilbratt et al. 2010). The SPIRE-FTS is a low spatial and spectral resolution imaging spectrometer covering a spectral range from $194\,\mu$m to $671\,\mu$m ($\sim 450\,$GHz $-$ $1545\,$GHz). At the redshift of M51 ($z \sim 0.002$), this spectral range includes a total of 10 CO transitions ($J = 4-3$ to $J = 13-12$), 10 ^{13}CO transitions ($J = 5-4$ to $J = 14-13$) and both [CI] transitions, all of which trace molecular gas. The SPIRE-FTS [NII]205 μm data were previously published by Parkin et al. (2013), while in this paper we present the detected CO and [CI] transitions for the first time. We adopt a distance of $9.9 \pm 0.7\,$Mpc (Tikhonov et al., 2009), based on observations of the red giant tip.

These observations were performed as part of the Very Nearby Galaxies Survey (VNGS; PI: C.D. Wilson) whose primary goal is to study the ISM of very nearby galaxies using both SPIRE and the Photoconductor Array Camera and Spectrometer (PACS; Poglitsch et al. 2010). From the sample of 13 galaxies in the VNGS, SPIRE-FTS CO data has been published for five: Arp 220 (Rangwala et al., 2011), M82 (Kamenetzky et al., 2012), NGC

1068 (Spinoglio et al., 2012), NGC 4038/39 (Schirm et al., 2014), and M83 (Wu et al., 2015). We present the observations and data reduction in Section 4.2. In Section 3.3, we present the radiative transfer analysis of our detected CO and [CI] transitions, while in Section 3.4 we present models of photon dominated regions (PDRs) in M51. We discuss the implications of the solutions of our radiative transfer models and our PDR models in Section 3.5. We include discussions of the CO- and [CI]-to-H_2 conversion factors, along with a comparison of the results for M51 to previously studied galaxies within our sample.

3.2 Observations

3.2.1 FTS Data reduction

M51 was observed using the SPIRE-FTS on OD 438 (July 25th, 2010) in intermediate sampling mode, with 32 repetitions per jiggle position (Observation ID 1342201202). The observation is centered at ($13\,\mathrm{h}29\,\mathrm{m}52.71\,\mathrm{s}, +47°11'42.60''$), covering a region roughly $\sim 160'' \times 180''$ with a total integration time of 17603 seconds ($\sim 5\,$hours). These data were reduced with the Herschel Interactive Processing Environment (HIPE) version 11.0 and SPIRE calibration 11.0. We used a modified version of the standard mapping pipeline, with the primary difference that we skip the map making step, instead saving each individual jiggle position as level 1 spectrometer point source (SPS) products.

The standard mapping pipeline assumes that the source is either a point source, or that the source is fully-extended, filling the entire beam uniformly. As with many of the sources in the VNGS sample, M51 cannot be characterized as either a point-source or fully-extended source relative to the FTS beam: instead, we characterize the source as being semi-extended. In addition, the beam size and shape of the SPIRE-FTS varies with frequency, with the size varying from $\sim 17''$ to $\sim 43''$. In previous works where we had fully Nyquist sampled maps of our sources (e.g. see Kamenetzky et al. 2012; Spinoglio et al. 2012; Schirm et al. 2014), we convolved our point-source calibrated integrated intensity maps using custom convolution kernels. The same technique cannot be used here as our map is not Nyquist sampled. Instead, we match the beam size across the entire spectrum using the recently developed semi-extended correction tool (SECT) in Hipe version 11.0. We discuss the highlights of the tool here while the method used by the tool is described in more detail in Wu et al. (2013).

When a source is semi-extended, correcting for the FTS beam requires correcting for the source-beam coupling at every frequency. The SECT corrects for the source-beam coupling by assuming that the distribution of the emitting gas or dust, whether it is [CI]- and CO-emitting molecular gas or [NII]-emitting ionized gas, follows the same distribution as some input image, such as the 70 μm photometry map. It first calculates the source-beam coupling in the form of a forward coupling efficiency, $\eta_f(\nu, \Omega_{source})$, for each bolometer at a given jiggle position using derived FTS beam profiles and a normalized input map. This source-beam coupling is frequency-dependent, and so must be calculated at every frequency. It then multiplies the intensity at each frequency by this factor. The resulting data cube has an equivalent beam size and shape of a $40''$ Gaussian beam. We opt to use the PACS 70 μm image (beam size $\sim 6''$) as our input image as we do not expect significant variations in the distribution of hot dust traced by the PACS 70 μm image and the molecular gas traced by CO and [CI]. We perform this correction on the level 1 SPS products at each jiggle position using the SECT.

We create a level 2 data cube for each set of detectors, the SLW and the SSW, from the semi-corrected level 1 products using the *spireProjection* task. We chose a pixel size of $10''$ for both cubes. It is important to note that the pixel size will have no significant effect on our data cubes, provided we limit the pixel size such that only one detector is assigned to each pixel. The resulting SLW and SSW data cubes contain 28 and 68 pixels with spectra, respectively. The complete semi-extended corrected FTS spectrum for the centre of M51 is shown in Figure 3.1.

3.2.1.1 Line Fitting

We wrote a custom line fitting routine in HIPE to fit all of the detected atomic and molecular transitions in every pixel of our cube. A list of detected transitions is shown in Table 3.1. The intrinsic line profile of the FTS is a Sinc function with a full-width half-maximum ranging from $280 - 450\,\mathrm{kms}^{-1}$ for the SSW, and $440 - 970\,\mathrm{km\ s}^{-1}$ for the SLW in high resolution mode. The maximum measured line width from observations from the James Clerk Maxwell Telescope of CO $J = 3 - 2$ convolved to a beam size of $40''$ (see Section 3.2.2.1) is only $\sim 50\,\mathrm{km\ s}^{-1}$ in the FTS field of view, less than the intrinsic line width of the instrument. Therefore, we do not resolve the line width in our observations.

For each pixel in our cubes, the routine fits each of the lines listed in Table 3.1 with a Sinc function using a Levenberg-Marquardt fitter, keeping the width of the line fixed to 1.4305 GHz, with the amplitude and centroid varying. The surrounding 30 GHz is fit with a quadratic at the same time in order to account for the continuum emission. With the exception of the CO $J = 7 - 6$ and [CI] $J = 2 - 1$ transitions, all of the lines listed in Table 3.1 are fit individually. In the case of the CO $J = 7 - 6$ and [CI] $J = 2 - 1$ transitions, both lines are fit concurrently, each with a Sinc function, along with the continuum emission. We integrate the resulting Sinc functions to calculate the total integrated intensity for each line, while the uncertainty is calculated from the uncertainty in the fitting parameters (Table 3.1). In

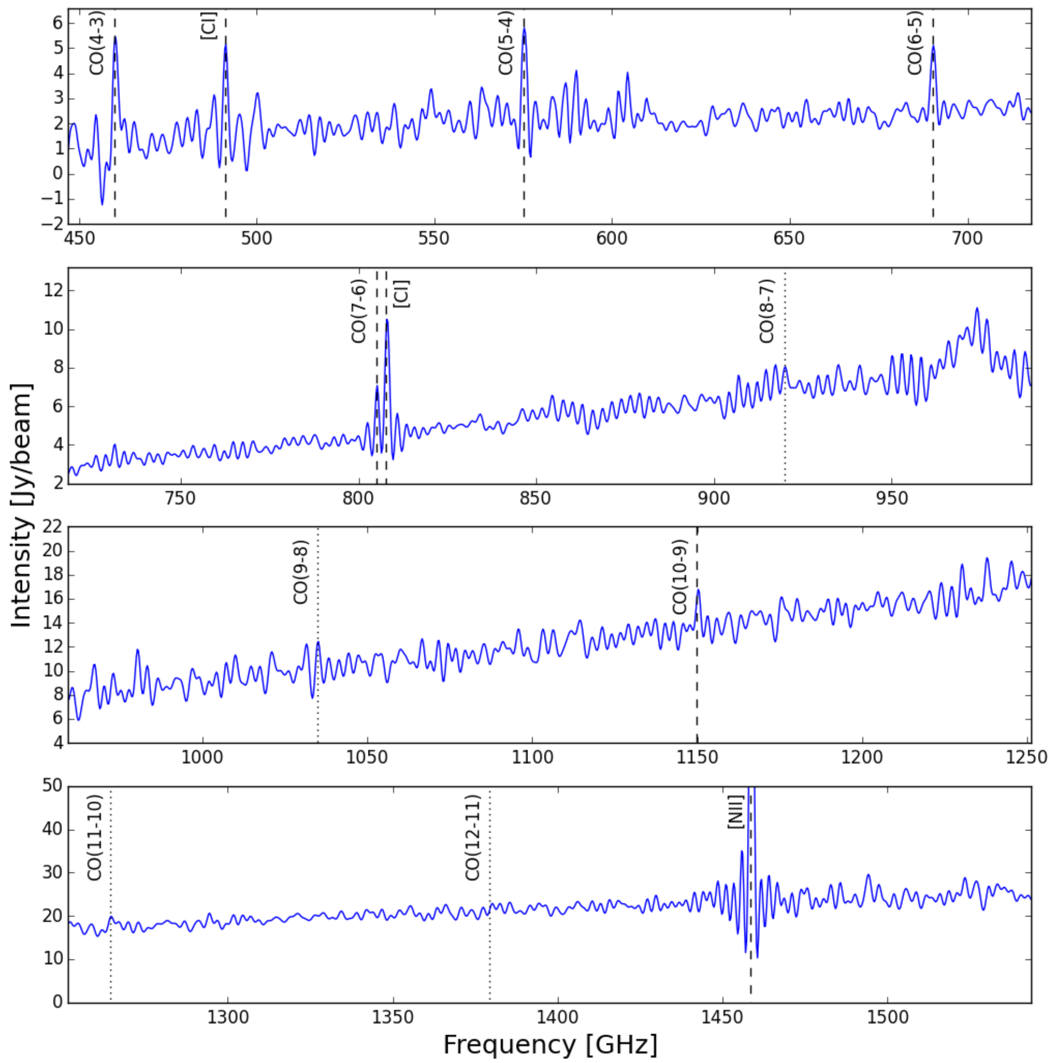

Figure 3.1 FTS spectrum for the nucleus of M51 in units of Jy beam^{-1}. All of the detected atomic and molecular transitions are indicated by a dashed line, while undetected CO transitions are indicated by a dotted line at the expected location. This spectrum has been corrected for the semi-extended nature of the emission (see Section 3.2.1 for details). Note that CO $J = 10-9$ is detected in the nucleus pixel only.

Table 3.1 Line flux measurements

Species	Transition	Rest frequency GHz	Average measured flux[1] K km s^{-1} Nucleus	Centre	Arm/inter-arm	All	Calibration uncertainty %
CO	$J = 1-0$	115.27	47.2 ± 0.2	41.2 ± 0.1	26.2 ± 0.1	33.1 ± 0.1	10.0[2]
	$J = 2-1$	230.54	37.8 ± 0.2	32.2 ± 0.2	20.0 ± 0.2	25.6 ± 0.2	20.0[3]
	$J = 3-2$	345.80	25.9 ± 0.2	20.9 ± 0.2	11.7 ± 0.2	16.0 ± 0.2	15.0[4]
	$J = 4-3$	461.04	12 ± 1	9 ± 1	$< 4.6 \pm 2.1$	7 ± 2	12.2
	$J = 5-4$	576.27	5.5 ± 0.9	4.2 ± 0.9	$< 1.8 \pm 0.9$	2.9 ± 0.9	12.2
	$J = 6-5$	691.47	2.2 ± 0.1	1.5 ± 0.4	$< 0.7 \pm 0.2$	1.1 ± 0.3	12.2
	$J = 7-6$	806.65	1.10 ± 0.06	0.6 ± 0.1	0.28 ± 0.07	0.47 ± 0.08	12.2
	$J = 8-7$	921.80	$< 0.4 \pm 0.2$	$< 0.3 \pm 0.1$	$< 0.3 \pm 0.1$	$< 0.3 \pm 0.1$	12.2
^{13}CO	$J = 1-0$	110.20	5.87 ± 0.06	5.09 ± 0.07	2.92 ± 0.06	3.91 ± 0.06	10.0[2]
[CI]	$J = 1-0$	492.16	8 ± 1	6 ± 2	$< 3.5 \pm 1.6$	$< 4.6 \pm 1.6$	12.2
	$J = 2-1$	809.34	3.08 ± 0.06	1.9 ± 0.1	0.85 ± 0.08	1.39 ± 0.09	12.2

[1]Quoted uncertainties are measurement uncertainties only
[2]Kramer et al. (2008)
[3]Leroy et al. (2009)
[4]Vlahakis et al. (2013)

addition, the CO $J = 10-9$ flux for the nucleus is 0.6 ± 0.2 K km s^{-1}. The calibration uncertainty of the SPIRE-FTS is 7%, while we add a total of 10% in quadrature to account for uncertainties in fitting the baseline, and uncertainties in the semi-extended source correction. The resulting maps for CO and [CI] are shown in Figures 3.2 and 3.3 respectively.

3.2.2 Ancillary Data

3.2.2.1 Ground based CO

We supplemented our FTS observations of M51 using previously published CO $J = 1-0$ to $J = 3-2$ maps from ground based instruments. M51 was observed in CO $J = 1-0$ and ^{13}CO $J = 1-0$ using the Institut de Radioastronomie Millimétrique (IRAM) 30 m telescope as part of the PAWS program (Schinnerer et al., 2013). The 30 m observations were used to fill in the short spacings for the interferometric observations using the PdBI. We use only the single-dish observations of CO $J = 1-0$ and ^{13}CO $J = 1-0$ as we are interested only in the very large scales (~ 40 pc) in M51. We acquired the

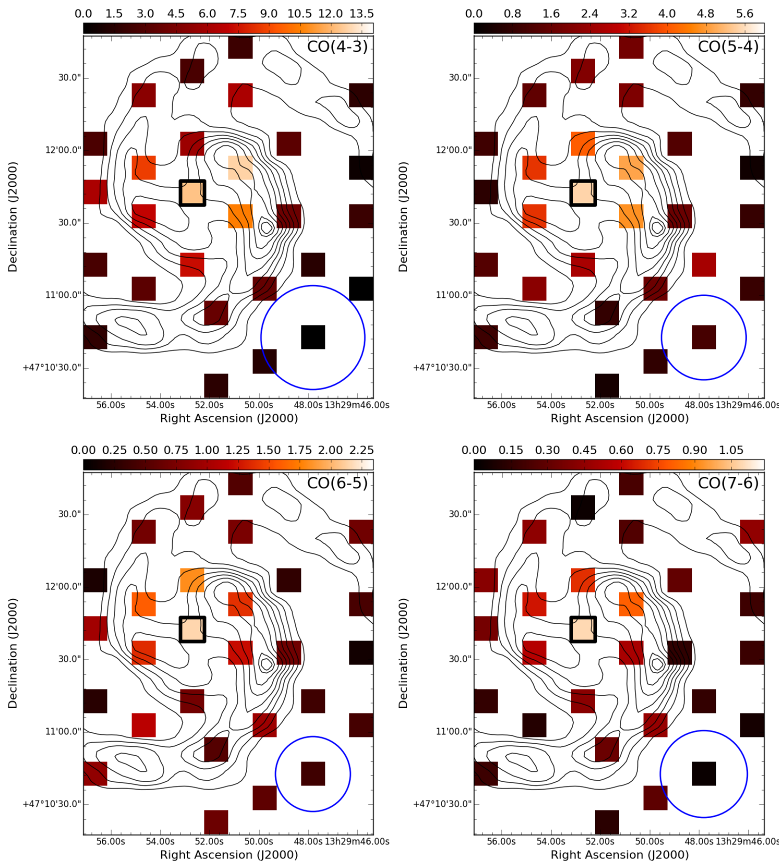

Figure 3.2 CO flux maps in units of K km s^{-1} from the Herschel SPIRE-FTS for the $J = 4-3$ (top left), $J = 5-4$ (top right), and $J = 6-5$ (bottom left), $J = 7-6$ (bottom right) transitions. The CO $J = 2-1$ contours from the IRAM 30 m telescope at a beam size of 13$''$ are overlaid (Leroy et al., 2009). The CO flux maps shown here have been corrected for the semi-extended nature of the source (see Section 3.2.1). The native FTS beam size at the observed frequencies is shown as a blue circle in the bottom-right corner for each of the CO maps, while the centre of M51 is denoted by a black box. The semi-extended corrected maps are characterized by a 40$''$ gaussian beam, which is the approximate size of the CO $J = 8-7$ beam.

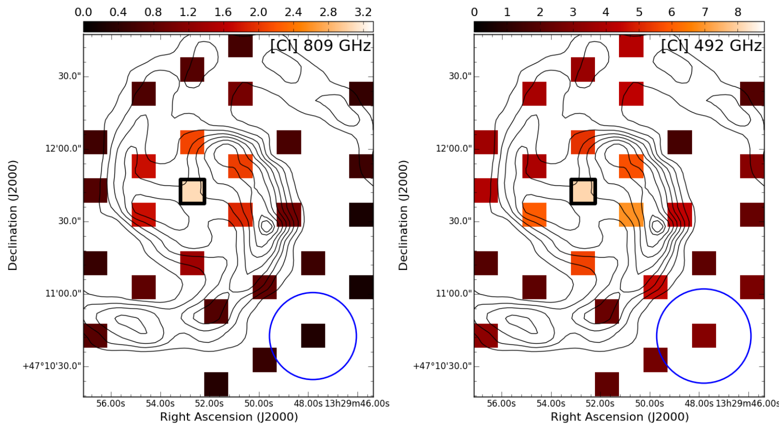

Figure 3.3 [CI] flux maps from the Herschel SPIRE-FTS observations of M51 for the $^3\mathrm{P}_1 -^3 \mathrm{P}_0$ (left) and $^3\mathrm{P}_2 -^3 \mathrm{P}_1$ (right) transitions. For more details see Figure 3.2.

CO $J = 1-0$ and ^{13}CO $J = 1-0$ data cubes published in Pety et al. (2013)[1], with a beam size of 22.5″.

We acquired previous observations of CO $J = 2-1$ in M51 from the IRAM 30 m telescope[2]. M51 had been observed as part of the HERA CO Line Extragalactic Survey (Schuster et al., 2007; Leroy et al., 2009). The IRAM 30 m beam FWHM is 11″, while the publicly available data cube has been smoothed to 13″, the smallest beam size of all the CO maps used in this work.

Finally, M51 was observed in the CO $J = 3-2$ transition by Vlahakis et al. (2013) using the HARP-B instrument on the James Clerk Maxwell Telescope (JCMT). This data was acquired as part of the JCMT Nearby Galaxies Legacy Survey (NGLS, Wilson et al. 2012). The beam size at the rest frequency of 345.79 GHz is 15″.

All four of the ground-based CO transitions (including ^{13}CO $J = 1-0$) were reduced in the same manner using the `Starlink` software package (Currie et al., 2008) and a similar method as for the CO $J = 3-2$ observations of NGC 4038/39 in Schirm et al. (2014). First, we convolved the data cubes to

[1] Downloaded from `http://www.mpia.de/PAWS/PAWS/Data.html`
[2] http://www.mpia-hd.mpg.de/HERACLES/Overview.html

a $40''$ gaussian beam using the `gausmooth` command. We then smoothed the cubes with a top hat with a width 2.5 times the half-power beam-width of the $40''$ beam and smoothed to a velocity width of 20 km/s. Using the `clumpfind` command, we identified regions of emission above 2σ in our smoothed cube to create a mask which we then used to creating moment 0, 1 and 2 maps from our original, $40''$ HPBW, data cubes. We estimated the noise in our moment 0 using the emission free channels from our $40''$ HPBW data cubes. Finally, we re-gridded our ground based observations of CO using the `wcsalign` task in `Starlink`, using our CO $J = 4-3$ integrated intensity map as a reference.

3.3 Non-LTE Excitation Analysis

Similar to the method used in Schirm et al. (2014), we perform a non-LTE excitation analysis to determine the physical state of the molecular gas across the entire observed region. Here, we present the highlights of the method used, along with any differences to the previous work. We use the non-LTE excitation code RADEX (van der Tak et al., 2007) along with a Bayesian likelihood code (Ward et al., 2003; Naylor et al., 2010a; Panuzzo et al., 2010; Kamenetzky et al., 2011) to determine the kinetic temperature ($T_{\rm kin}$), molecular gas density ($n({\rm H_2})$), area filling factor (Φ_A) and CO and [CI] column densities per unit line width ($N_{\rm CO}$ and $N_{\rm [CI]}$). By varying these 5 physical parameters, we create a grid of model fluxes for the CO and [CI] emission (see Table 3.2 for the grid parameters), where the grid parameters are spaced evenly in log space. We then use the Bayesian likelihood code to compare our measured fluxes to the grid of fluxes to calculate the likelihood distribution for each of the physical parameters. The code also determines the most probable value ("1DMax") and mean from each of the physical parameter's likelihood distribution, along with the most probable solution from the combined likelihood distribution for

Table 3.2 RADEX grid parameters

Parameter	Range	# of Points
T_{kin} [K]	$10^{0.7} - 10^{3.8}$	71
$n(\mathrm{H}_2)$ [cm^{-3}]	$10^{1.0} - 10^{7.0}$	71
Φ_A	$10^{-5.0} - 1$	71
$N_{\mathrm{CO}}/\Delta V$ [cm^{-2}]^3	$10^{12.0} - 10^{18.0}$	81
$N_{[\mathrm{CI}]}/N_{\mathrm{CO}}$	$10^{-2.0} - 10^{2.0}$	20
ΔV [km s^{-1}]	1.0	

the kinetic temperature, molecular gas density, CO column density and area filling factor ("4DMax"). By using Bayesian inference, we are able to include priors on the physical parameters based upon the physical characteristics of the observed region.

3.3.1 Regions

One of the aims of the VNGS is to investigate any regional variations in the interstellar medium of the galaxies which we resolve. Some of the galaxies in our sample which have been observed with the FTS are not resolved (e.g. Arp 220 Rangwala et al. 2011). In the case of M51, we resolve the central $\sim 2'$ at a beam size of $40''$. We investigate the regional variations in the physical state and heating mechanisms of the molecular gas by separating each pixel in our FTS map into one of four regions (see Figure 3.4): the nucleus, centre, arm and inter-arm. The selection is based on the schematic used by

For each region, we perform an unweighted average for each CO and [CI] transition, including all pixels where all of the transitions are detected with a signal-to-noise ratio (SNR) > 1. With the exception of the CO $J = 8-7$ line, all of the transitions listed in Table 3.1 are detected with a SNR > 3 for all pixels in the nucleus and centre regions. For the arm/inter-arm region, only a single pixel satisfies the same SNR > 3. As such, we choose a SNR > 1 in order to explore the parameter space in the arm and inter-arm regions of

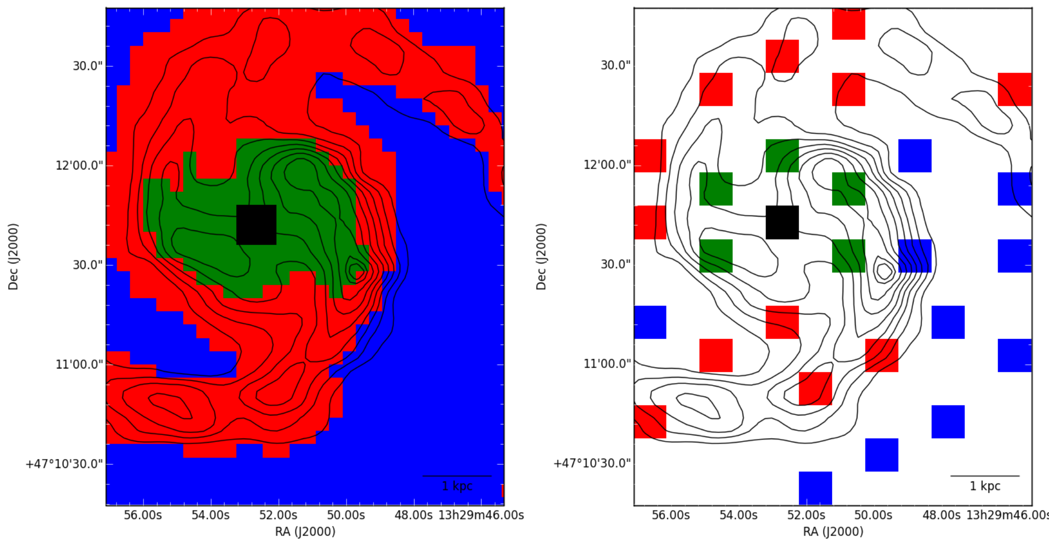

Figure 3.4 *Left:* Schematic of M51 as defined in Figure 6 of Parkin et al. (2013) with CO $J = 2-1$ contours overlaid. *Right:* The same regions of M51 except as defined for our FTS maps with the same CO $J = 2-1$ contours overlaid. In both figures, the colors correspond to the nucleus (black), centre (green), arm (red) and inter-arm(blue) regions of M51.

M51 (Figure 3.5). Even with this low SNR cut, few pixels are included from the arm and inter-arm regions (see Figure 3.5), while the included pixels all contain a portion of both regions within the 40″ beam. Therefore, we combine the arm and inter-arm regions into a single arm/inter-arm region. Finally, we combine the pixels included in the nucleus, centre and arm/inter-arm regions into a single "All" region.

The resulting spectral line energy distributions (SLEDs) for CO and [CI] are shown in Figure 3.6. Furthermore, the line width, which is used to calculate the resulting column densities, and the mass prior are taken as the average of each parameter from all the pixels included in the regional averages.

3.3.2 Priors

We introduce three priors into our modelling: a prior on the length along the line of sight, a prior on the total molecular gas mass and a prior on the optical

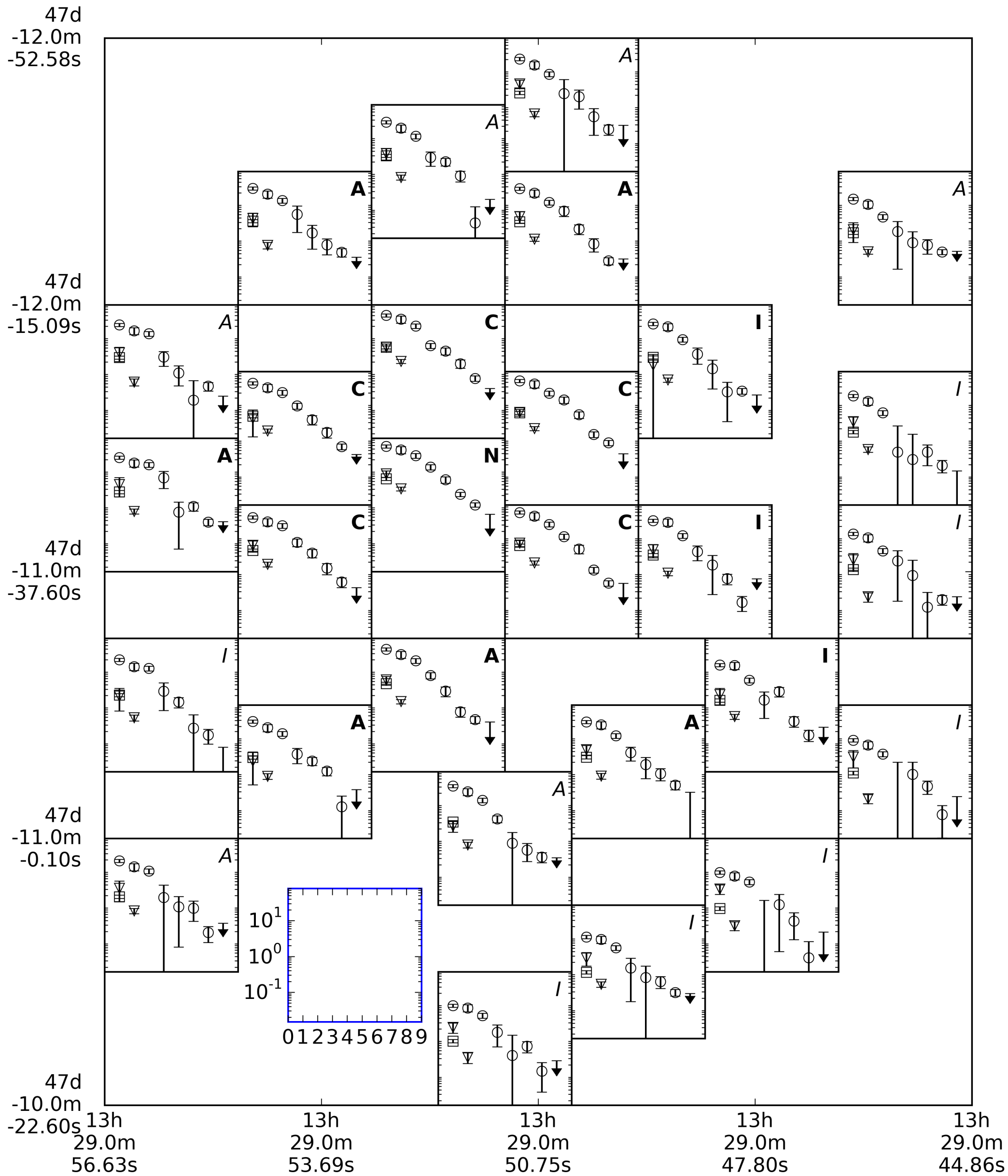

Figure 3.5 Measured CO (circles), [CI] (triangles), and ^{13}CO(squares) spectral line energy distribution in units of K km s^{-1} for each pixel in our FTS data cube. The scale is the same for each box and is shown by the empty blue box in the lower-left, where the y-axis corresponds to the integrated intensity in units of K km s^{-1} and the x-axis corresponds to J_{up}. The CO $J = 1-0$ to $J = 3-2$ and ^{13}CO $J = 1-0$ transitions are from ground based instruments (see Section 3.2.2.1). The error bars shown here do not include calibration uncertainties (see Table 3.1 for the calibration uncertainties). The letter in the upper right corner indicates the pixel's region, while only the bolded letters are included in our region averages, where "N" corresponds to the nucleus, "C" the centre, "A" the arm and "I" the inter-arm regions.

Table 3.3 Model Constraints

Parameter	Value	Units
CO abundance ($x_{\rm CO}$)	3×10^{-4}	...
Mean molecular weight (μ)	1.5	...
Angular size scale	48.9	pc/″
Source size	40	″
Length (L)	≤ 160	pc

depth. These are the same priors used in Schirm et al. (2014); however the derivation of some of the physical parameters differs. A list of the physical parameters used to calculate the priors is shown in Table 3.3. Note that the line width is derived for each region from the CO $J = 3 - 2$ moment 2 map. Here, we describe the three priors used, along with how we derive some of the physical parameters.

The first prior is on the total length (L) of the CO and [CI] emitting regions along the line of sight. This prior limits the column density, area filling factor, and molecular gas density via the following equation:

$$\frac{N_{\rm CO}}{\sqrt{\Phi_A} x_{\rm CO} n({\rm H_2})} \leq L \tag{3.1}$$

As with all grand design spiral galaxies, the molecular gas in M51 resides predominantly in a disk. As such, we derive our length prior based upon measurements of the scale height of this disk. Pety et al. (2013) calculated the scale height for their extended and compact components to be $\sim 190 - 250$ pc and $\sim 10 - 40$ pc, respectively (Figure 17 of their work). Their extended component corresponds to a warm, diffuse component, although we will not model here, while we will discuss the implications of not modelling this component in Section 3.5.1.3. We opt to use the scale height of their compact component to derive the length prior used in this work. For our work, we opt to use a length prior a factor of 4 times the maximum scale height (40 pc) derived for the compact component: a factor of 2 to account for both above and below the disk midplane, and a factor of 2 to account for the molecular gas beyond the scale height.

We use a second prior on the total mass of molecular gas in a single beam. In previous publications (e.g. Rangwala et al. 2011; Kamenetzky et al. 2012; Schirm et al. 2014), a dynamical mass prior was introduced to limit the total molecular gas mass within a single beam. The dynamical mass used was typically that of the entire system. This assumption is sensible for systems contained entirely within a single FTS beam, such as Arp 220 (Rangwala et al., 2011). However, in the case of galaxies which span multiple beams, such as NGC 4038/39 (Schirm et al., 2014) or M51, it is more difficult to isolate what the dynamical mass is per beam. Instead, we opt to calculate an upper limit to the molecular gas mass for each pixel using the CO $J = 1-0$ map along with an α_{CO} value of $9\,\mathrm{M}_\odot$ pc^{-2} (K km s^{-1})$^{-1}$. This value for the conversion factor corresponds to the largest values for α_{CO} seen in the Milky Way ($\alpha_{\mathrm{CO}} \sim 4-9\,\mathrm{M}_\odot$ pc^{-2} (K km s^{-1})$^{-1}$), along with M31, M33 and the Large Magellanic Cloud ($\alpha_{\mathrm{CO}} \sim 3-9\,\mathrm{M}_\odot$ pc^{-2} (K km s^{-1})$^{-1}$, Leroy et al. 2011).

The mass prior places a limit on the beam-averaged column density ($\langle N_{\mathrm{CO}} \rangle = N_{\mathrm{CO}}\Phi_A$)

$$N_{\mathrm{CO}}\Phi_A < \frac{M_{\mathrm{CO}(1-0)}x_{\mathrm{CO}}}{\mu m_{\mathrm{H}_2} A_{\mathrm{CO}}} \tag{3.2}$$

where $M_{\mathrm{CO}(1-0)}$ is our derived mass from the CO $J = 1-0$ map, x_{CO} is the CO abundance relative to H_2, μ is the mean molecular weight, and A_{CO} is the area of the CO emitting region, which is taken to be the area covered by one beam at the distance of M51.

The third prior limits the optical depth such that $0 < \tau < 100$. An optical depth < 0 is indicative of a maser, and we do not expect CO or [CI] masers to contribute appreciably to the emission from either CO or [CI] on the observed size scales. Furthermore, the line intensities calculated by RADEX become more uncertain the further the optical depth drops below 0. In addition, van der Tak et al. (2007) suggest limiting the optical depth to an upper limit of 100, as the one-zone approximation implied by its escape probability formalism breaks down at optical depths greater than $\tau > 100$.

3.3.3 Non-LTE Excitation Modelling

CO, [CI] and ^{13}CO are all tracers of molecular gas; all three species are excited via collisions with H_2. In the classic slab-geometry model of a photon dominated region (PDR) by Tielens & Hollenbach (1985), [CI] is a surface molecule, arising from the surfaces of molecular clouds. CO does not begin to form until deeper into the cloud. In this model, some of the molecular gas is "CO dark", and does not emit CO (Wolfire et al., 2010). However, there is strong evidence that [CI] and CO both trace the same molecular gas (Papadopoulos et al., 2004), as supported by observations of the Orion molecular cloud (Plume et al., 1999; Ikeda et al., 2002; Shimajiri et al., 2013) and, more recently, simulations of molecular clouds (e.g. Offner et al. 2014, Gaches et al. 2014). Furthermore, [CI] may be less sensitive to temperature than CO (Offner et al., 2014), and so may help constrain the density.

We fit a two-component model to our measured CO and [CI] emission in the nucleus, centre, and arm/inter-arm regions of M51. (A single-component model fit, which does not produce a physically realistic solution, is discussed in Appendix 3.7.) We include the CO transitions from $J = 1-0$ to $J = 7-6$, while leaving the $J = 8-7$ transitions as an upper limit. The total uncertainty used is the line fitting and calibration uncertainties added in quadrature. The molecular gas in M51 is unlikely to populate two distinct components in terms of the physical state of the gas, so in both cases both our single- and two-component fits will represent an average of the state of all the molecular gas within the 3 distinct regions. We are therefore investigating the bulk properties of the molecular gas in the three regions in both cases. (For an extensive discussion on one- and two-component modelling, see Kamenetzky et al. 2014)

Our two-component fit to the molecular gas consists of a "cold" component which dominates the lower-J CO transitions, and a "warm" component which dominates the upper-J CO transitions. We include the [CI] in the cold component model only. We begin by fitting the lower-J CO transitions, from $J = 1-0$ to $J = 4-3$, along with [CI]. The remaining CO transitions are set as 3σ upper limits by adding the flux to the 1σ uncertainty. We subtract the fitted 4DMax flux from the measured fluxes, and proceed to fit the residuals of the upper-J CO transitions, from $J = 5-4$ to $J = 7-6$, while leaving the remaining CO transitions as upper limits as before (including CO $J = 8-7$). We use the same priors for both components, and we iterate a total of 12 times for each region.

We check each iteration to verify convergence, which occurs after only $2-3$ iterations for the nucleus and all regions. In the case of the centre and arm/inter-arm regions, the solution does not converge to a single solution, instead cycling between 2 solutions (for the centre) or 3 solutions (for the arm/inter-arm). This is a result of the 4DMax solution changing, while the 1σ ranges for each of the physical parameters in both the cold and warm components for both regions do not change significantly from iteration to iteration. As such, we pick a representative iteration for the centre and arm/inter-arm regions, cautioning the reader that the 4DMax solution presented represents only the best-fit solution for the given iteration. The resulting measured and calculated SLEDs are shown in Figure 3.6, while the calculated optical depths are shown in Figure 3.7. The derived physical parameters are given in Table 3.4 and the 1σ ranges are shown in Figure 3.8.

Table 3.4 Two-Component RADEX results

		4DMax (1σ range)				
Comp.	Parameter	Nucleus	Centre[1]	Arm/inter-arm[1]	All	Units
Cold	$T_{\rm kin}$	30 (19 – 42)	28 (16 – 39)	6 (6 – 33)	28 (6 – 32)	[K]
	Log(n(H$_2$))	3.06 (2.94 – 3.68)	3.23 (2.91 – 3.75)	4.26 (2.85 – 5.58)	2.80 (2.95 – 5.62)	[Log(cm^{-3})]
	Log($N_{\rm CO}$)	19.05 (18.41 – 19.08)	18.85 (18.22 – 19.00)	18.80 (17.78 – 18.86)	19.07 (18.11 – 18.98)	[Log(cm^{-2})]
	Log(Φ_A)	−1.64 (−1.74 – −1.48)	−1.64 (−1.70 – −1.29)	−1.00 (−1.58 – −1.01)	−1.64 (−1.66 – −1.07)	[...]
	Log($< N_{\rm CO} >$)	17.35 (16.83 – 17.50)	17.14 (16.72 – 17.57)	17.32 (16.52 – 17.78)	17.37 (16.66 – 17.82)	[Log(cm^{-2})]
	Log(P)	4.96 (4.44 – 5.06)	4.96 (4.36 – 5.06)	4.83 (4.22 – 6.33)	4.83 (4.34 – 6.41)	[Log(K cm^{-2})]
	Log($N_{\rm [CI]}$)	18.73 (18.37 – 18.98)	18.47 (18.16 – 20.21)	20.35 (17.97 – 20.34)	18.40 (18.15 – 20.38)	[Log(cm^{-2})]
Warm /dense	$T_{\rm kin}$	212 (42 – 144)	37 (44 – 183)	69 (35 – 156)	30 (45 – 194)	[K]
	Log(n(H$_2$))	4.77 (4.85 – 6.41)	4.94 (4.87 – 6.57)	4.69 (4.71 – 6.54)	5.29 (4.87 – 6.57)	[Log(cm^{-3})]
	Log($N_{\rm CO}$)	14.85 (15.31 – 19.10)	19.29 (15.31 – 19.17)	15.42 (15.27 – 18.92)	18.92 (15.27 – 19.13)	[Log(cm^{-2})]
	Log(Φ_A)	−0.29 (−3.57 – −0.82)	−3.43 (−3.92 – −1.00)	−0.57 (−3.74 – −0.89)	−3.21 (−3.94 – −1.00)	[...]
	Log($< N_{\rm CO} >$)	14.60 (14.42 – 15.70)	14.54 (14.14 – 15.43)	14.71 (14.12 – 15.37)	14.48 (14.12 – 15.36)	[Log(cm^{-2})]
	Log(P)	7.13 (6.98 – 8.29)	7.13 (6.96 – 8.80)	6.88 (6.66 – 8.80)	7.13 (6.96 – 8.84)	[Log(K cm^{-2})]

[1] The centre and arm/inter-arm 4Dmax cycles between 2 solutions (centre) and 3 solutions (arm/inter-arm). The 1σ range is consistent with all the cycled solutions, while only the 4Dmax changes. See text.

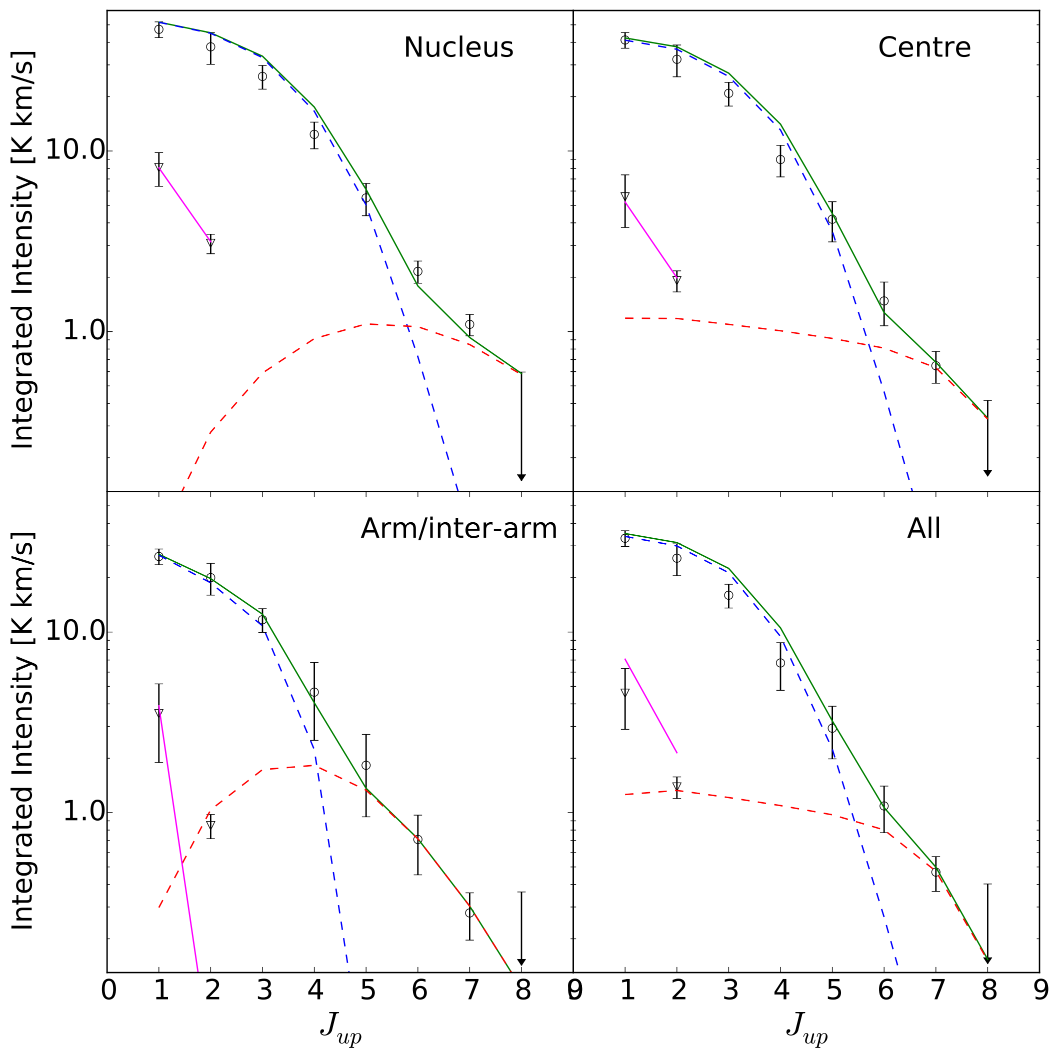

Figure 3.6 Measured and best-fit SLEDs for the two-component fit for the nucleus (top-left), centre (top-right), and arm/inter-arm (bottom-left) regions, and for all the regions combined (bottom right). The measured CO and [CI] SLEDs are shown by the black circles and triangles respectively. The cold component and warm component CO emission are shown by the blue and red dashed lines, respectively, while the total calculated CO emission is shown by the solid green line. The [CI] emission is indicated by the solid magenta line.

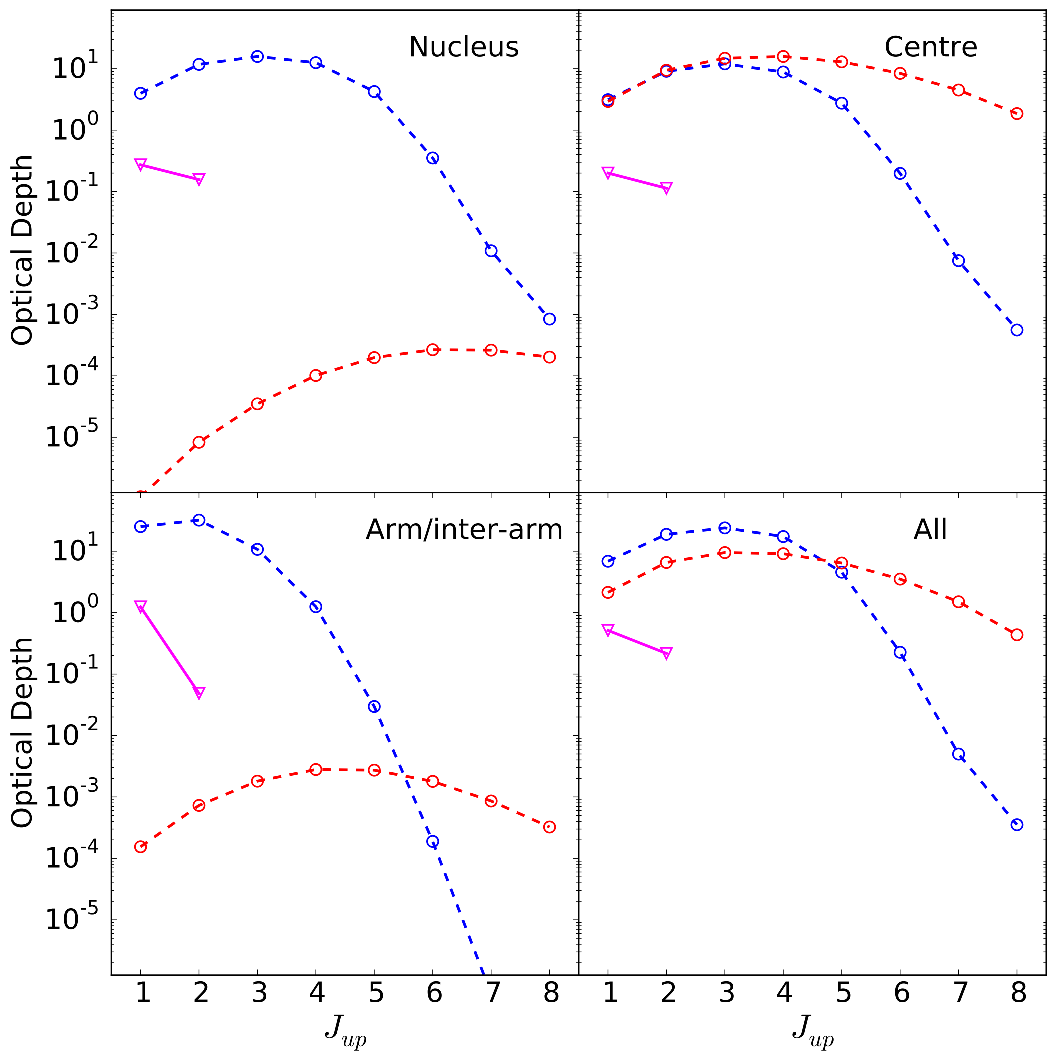

Figure 3.7 Best-fit optical depths for the two-component fit for the nucleus (top-left), centre (top-right), and arm/inter-arm (bottom-left) regions, and for all the regions combined (bottom right). The cold component and warm component CO optical depths are shown by the blue and red dashed lines and circles, respectively. The [CI] optical depths are indicated by the solid magenta line and triangles.

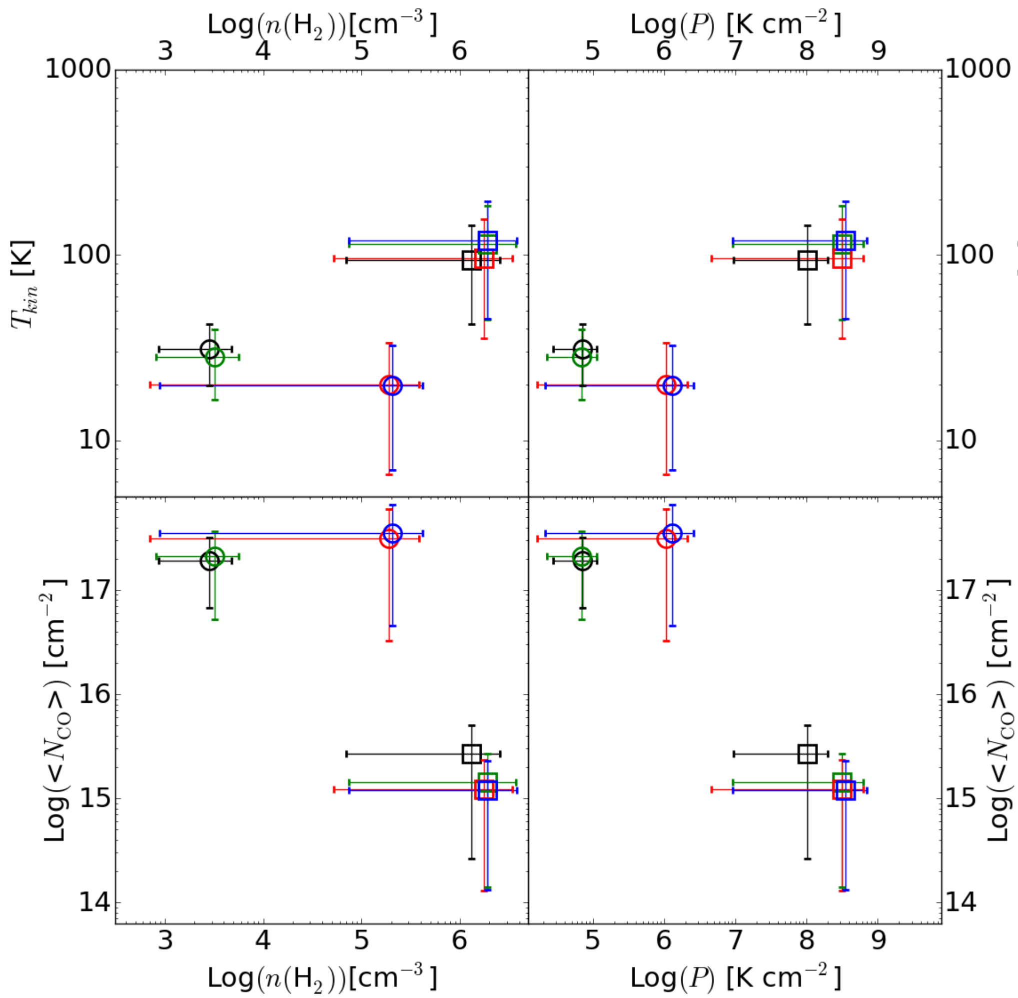

Figure 3.8 Derived physical parameters for the cold (*circles*) and warm (*squares*) components of the multi-component RADEX model averaged over the nucleus (*black*), centre (*green*),and arm/inter-arm (*blue*) regions of M51 (see Figure 3.4 and Section 3.3 for more details), and for the average of all the regions combined (*red*). CO is included in both the cold and warm components, while [CI] is included only in the cold component. The error bars correspond to the 1σ range of the combined likelihood distribution of each region for the kinetic temperature (*top row*), beam-averaged column density (*bottom row*), molecular gas density (*left column*), and pressure (*right column*).

3.4 Photon Dominated Regions

PDRs are regions of molecular gas illuminated by FUV radiation ($6.20\,\mathrm{eV} < E_{phot} < 13.6\,\mathrm{eV}$, Tielens & Hollenbach 1985). While FUV photons are typically not the right energy to dissociate molecular hydrogen, nevertheless this radiation can have a significant effect on the chemistry and heating of the illuminated region. Indeed, the FUV radiation will liberate electrons from dust grains through the photoelectric effect, which in turn will heat the molecular gas through collisions.

Using a PDR model grid (Hollenbach et al. 2012 and M. Wolfire, private communication), we model the ratio of CO transitions (e.g. CO $J = 3-2/J = 2-1$, etc.) for the nucleus, centre and arm/inter-arm regions of M51, along with the combination of all three regions. The model uses the molecular gas density ($n(\mathrm{H_2})$) and FUV field strength (G_0) in units of the Habing field (FUV flux $= 1.3 \times 10^{-4} G_0\,\mathrm{ergs\ cm^{-2}\ s^{-1}\ sr^{-1}}$). The model grid spans a large range of density ($n(\mathrm{H_2}) = 10^{1.0}\,\mathrm{cm^{-3}}$ to $10^{7.0}\,\mathrm{cm^{-3}}$) and FUV field strengths ($G_0 = 10^{-0.5}$ to $10^{6.5}$) to calculate the CO fluxes for the transitions from $J = 1-0$ up to $J = 29-28$. We present the CO model grid along with the results for the nucleus of M51 in Figure 3.9.

The CO ratios alone are unable to constrain both the density and FUV field strength (Figure 3.9). We include the cold and warm component densities calculated from our two-component RADEX fit to the low J (Figure 3.9, left column) and high J (Figure 3.9, right column) CO transitions, respectively. In addition, the ratio of $L_{\mathrm{CO}}/L_{\mathrm{FIR}}$ provides an upper limit to the FUV field strength.

We estimate L_{FIR} ($\lambda = 40 - 500\,\mu\mathrm{m}$) by first calculating the total infrared luminosity (L_{TIR}, $\lambda = 3 - 1100\,\mu\mathrm{m}$) using the following empirical relation from Galametz et al. (2013)

$$L_{\rm TIR} = c_{24}\nu_{24}L_{24} + c_{70}\nu_{70}L_{70} + c_{160}\nu_{160}L_{160} \tag{3.3}$$

where the subscripts 24, 70, and 160 correspond to the 24 μm, 70 μm, and 160 μm photometric maps respectively, while $c_{24} = 2.133 \pm 0.095$, $c_{70} = 0.681 \pm 0.028$ and $c_{160} = 1.125 \pm 0.010$. We use the *Spitzer Space Telescope* MIPS 24 μm photometric map reprocessed by Bendo et al. (2012), and the *Herschel* PACS 70 μm and 160 μm photometric maps from Mentuch Cooper et al. (2012). We beam-match and align all the maps before calculating the total infrared luminosity in each pixel. We then beam-match and align the $L_{\rm TIR}$ map to our FTS observations using the *imsmooth* command to beam-match, and the *imregrid* command to regrid, in Common Astronomy Software Package (CASA) version 4.2.1. We use a ratio of $L_{\rm TIR}/L_{\rm FIR} = 1.3$ to calculate our final FIR map, consistent with the value calculated for a sample of normal galaxies ($L_{\rm TIR} < 10^{11} L_\odot$) (Graciá-Carpio et al., 2008).

We calculate a grid of the ratio of $L_{{\rm CO}J=3-2}/L_{\rm FIR}$ and $L_{{\rm CO}J=6-5}/L_{\rm FIR}$ by estimating $L_{\rm FIR}$ as twice the FUV field strength (Kaufman et al., 1999). We show the resulting grid in the bottom panel of Figure 3.9, along with the measured ratio for the nucleus of M51. We show the measured $L_{{\rm CO}J=3-2}/L_{\rm FIR}$ ratios for the remaining regions in Figure 3.10, and the $L_{\rm CO(6-5)}/L_{\rm FIR}$ ratios in Figure 3.11.

For the low-J CO line ratio PDR model, the CO line ratios coupled with the ratio of $L_{{\rm CO}J=3-2}/L_{\rm FIR}$ constrain the field strength to $G_0 < 10^2$ in all the modelled regions, while the PDR model density agrees with the density from our radiative transfer analysis ($n({\rm H_2}) \sim 10^{2.75} - 10^{3.75}\,{\rm cm^{-3}}$, Figure 3.10). For the high-J CO line ratios PDR model, the CO line ratios limit the density to $n({\rm H_2}) \gtrsim 10^4\,{\rm cm^{-3}}$, while the ratio of $L_{{\rm CO}J=6-5}/L_{\rm FIR}$ limits the field strength to $G_0 \lesssim 10^3$ for all the modelled regions (Figure 3.11). The high density calculated from our radiative transfer analysis ($n(\mathrm{H_2}) \sim 10^{4.75} - 10^{6.5}\,\mathrm{cm^{-3}}$) constrains the field strength in the high-J CO PDR to $G_0 \sim 10^1 - 10^2$.

3.5 Discussion

3.5.1 Physical state of the molecular gas

3.5.1.1 Regional variations

The physical state of both the cold and warm molecular gas can vary significantly from source-to-source, depending upon the environment in which the molecular gas resides. Within an individual galaxy, the environment surrounding the molecular gas can vary. In Section 3.3, we investigated any differences in the physical state of the molecular gas for the nucleus, centre and arm/inter-arm regions of M51.

The results for the cold and warm components are shown in Table 3.4 and Figure 3.8. For each of the cold and warm components, no discernible differences are seen between any of the physical parameters across the 3 regions as all of the 1σ ranges overlap considerably. This suggests that either our observations are not sensitive to the differences in the physical states of the molecular gas, or that there are no appreciable changes to the physical state across the observed region.

The density of the cold molecular gas in the nucleus and centre regions ($n(\mathrm{H_2}) \sim 10^3\,\mathrm{cm^{-3}}$) is typical for GMCs in the Milky Way (e.g. Tielens 2005), while for the arm/inter-arm region the density is not very well constrained (Table 3.4). In the nucleus and centre, the temperature is slightly warmer than the typically quoted value of $\sim 10\,\mathrm{K}$ for Milky Way GMCs; however there may be contamination from a warmer, diffuse component (see Section 3.5.1.3). Furthermore, in both regions, the 1σ range for the beam-averaged

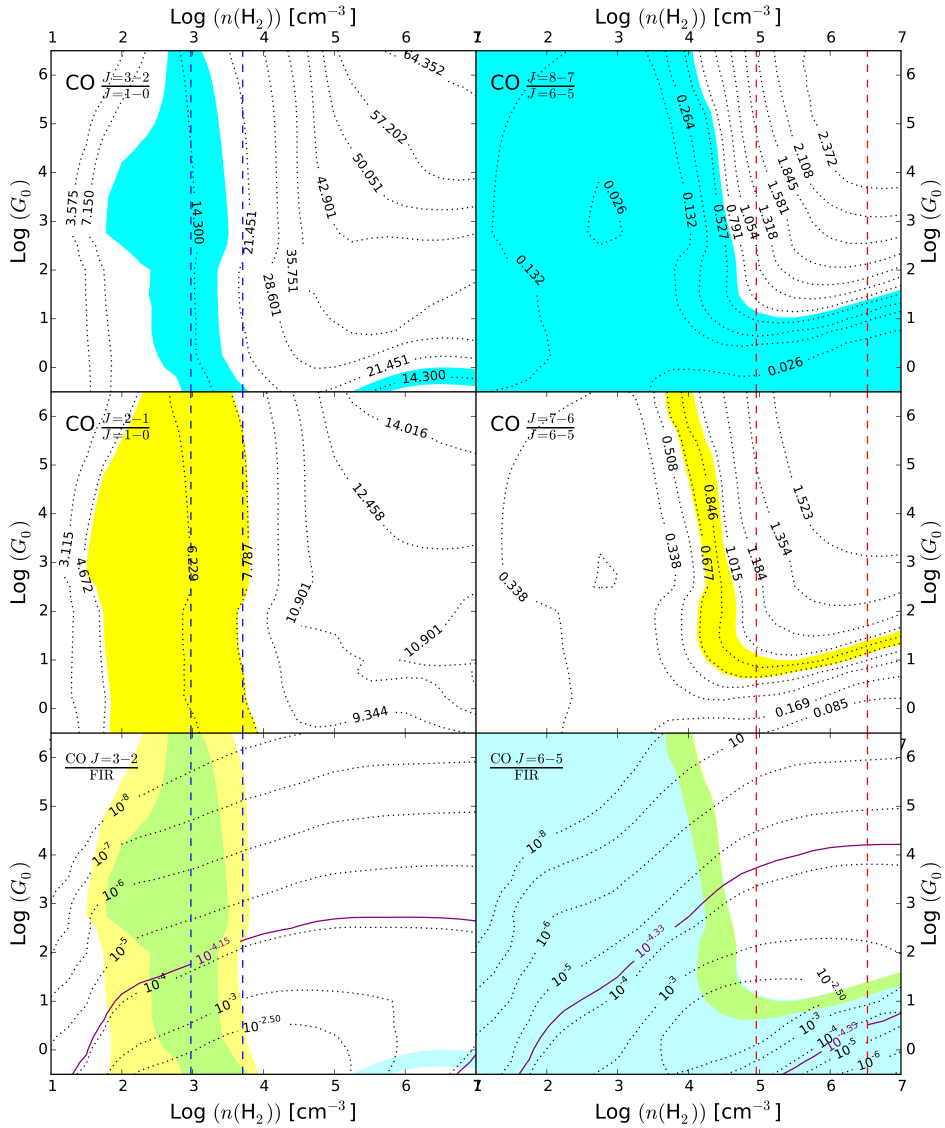

Figure 3.9 PDR model lines ratios for CO $\frac{J=3-2}{J=1-0}$ (*top-left*), $\frac{J=2-1}{J=1-0}$ (*middle-left*), $\frac{J=8-7}{J=6-5}$ (*top-right*), and $\frac{J=7-6}{J=6-5}$ (*middle-right*) for the nucleus of M51 in units of W m^2. The line ratios are in units of W m^{-2}. Note that the ratio of $\frac{J=8-7}{J=6-5}$ is an uper limit. In the top two rows, the dotted contours correspond to constant CO line ratios. The blue (*top-row*) and yellow (*middle-row*) shaded regions correspond to the uncertainty in the measured line ratio for the nucleus. In the bottom row, the dotted contours correspond to constant value of $\frac{L_{\rm CO\ J=3-2}}{L_{\rm FIR}}$ (*bottom-left*) and $\frac{L_{\rm CO\ J=6-5}}{L_{\rm FIR}}$ (*bottom-right*), while the solid purple line is the measured ratio for each. The shaded regions in the bottom-row panels correspond to the same CO line ratios of the two panels directly above, while the green region indicates where the two line ratios overlap. The blue (*left-column*) and red (*right-column*) dashed vertical lines correspond to the cold and warm component 1σ ranges for the densities from the two-component RADEX solutions.

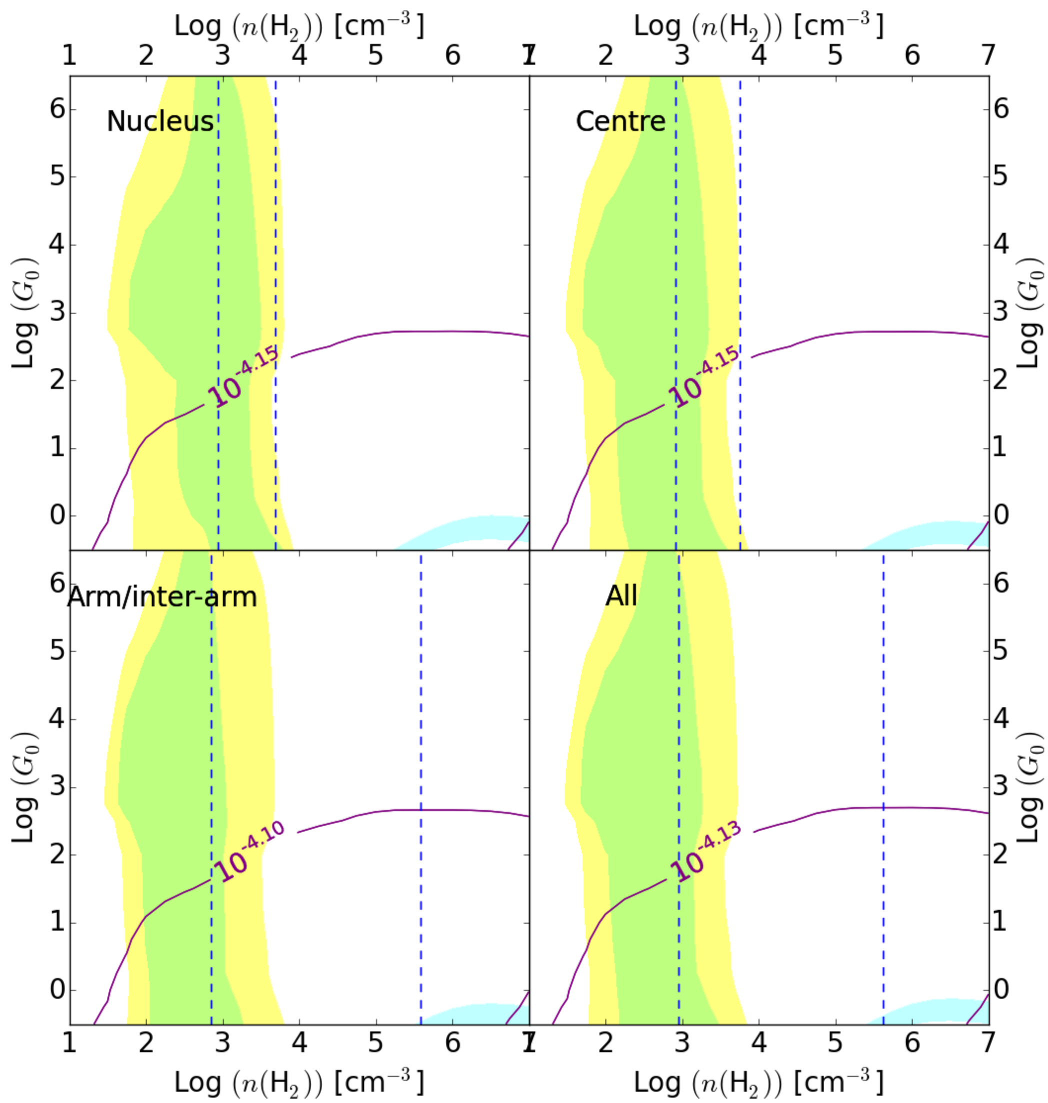

Figure 3.10 Same as the bottom-left panel of Figure 3.9 except for the cold-component PDR solutions for the nucleus (top-left), centre (top-right), and arm/inter-arm (bottom-left) regions of M51, and for all four regions combined (bottom-right). Note that the line ratios are calculated in units of W m^2.

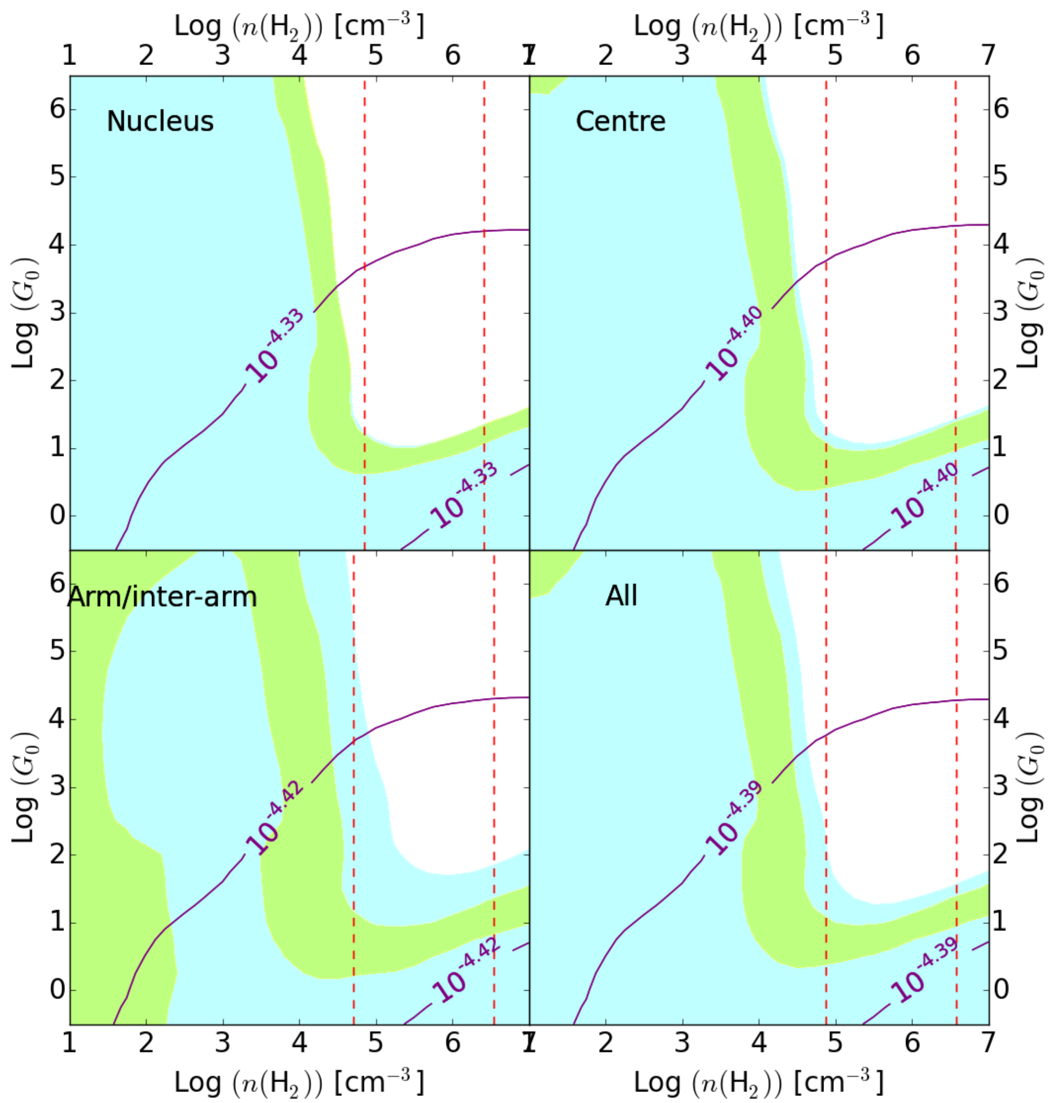

Figure 3.11 Same as the bottom-right panel of Figure 3.9 except for the warm-component PDR solutions for the nucleus (top-left), centre (top-right), and arm/inter-arm (bottom-left) regions of M51, and for all four regions combined (bottom-right). Note that the line ratios are calculated in units of W m^2.

column density covers half an order of magnitude, while in the arm/inter-arm region, it spans an order of magnitude. Any differences in the amount of molecular gas contained within a beam would need to be greater than a factor of ~ 5 (~ 10 for the arm/inter-arm region) to be seen in our results.

Similarly for the warm component, we detect no differences between the temperature, density or beam-averaged column density across the 3 regions. In the case of the temperature, the solutions suggest that the molecular gas is on the order of $\sim 100\,\mathrm{K}$ with a relatively high ($n(\mathrm{H_2}) \sim 10^5 - 10^6\,\mathrm{cm^{-3}}$) density. Unlike in previous results (e.g. Schirm et al. 2014), the difference in the temperature of the cold and warm component is not as clear, which may suggest we are tracing two different density components of the molecular gas as opposed to two temperature components.

The similarities in the nucleus and centre of M51 are likely due to contamination of the nucleus position beam by emission from the centre region. For example, Parkin et al. (2013) modelled PDRs in M51 using transitions of [CII], [OI] and [NII], along with the infrared flux. In their work, the nucleus consisted of a square $\sim 12''$ across with a beam size of $12''$. They found that the density recovered in their PDR models for the nucleus ($\sim 10^{3.5} - 10^{4.25}$) and centre ($\sim 10^{2.5} - 10^{4.0}$) overlapped, while the surface temperatures for the nucleus ($240 - 475\,\mathrm{K}$) and centre ($170 - 680$) overlap considerably. Given the larger beam size of our observations ($\sim 40''$), our nucleus region will be to a certain extent contaminated by emission from the centre region, and vice versa. As such, if the differences in our radiative transfer models are comparable to those seen in the PDR models of Parkin et al. (2013), we would not expect to detect them within our beam.

Our results suggest that the beam-averaged properties of the molecular gas in M51 do not vary by more than factors of a few in the case of both the cold and warm component, except for the warm component density which could vary by a few orders of magnitude. The larger beam size coupled with uncertainties in our line measurements contributes to our ability to detect any differences, while the results from Parkin et al. (2013) suggest that, if PDRs dominate the CO emission, we would not expect to see significant variations down to a beam size of at least $\sim 12''$.

3.5.1.2 Comparison to previous studies

Both Israel et al. (2006) and Schinnerer et al. (2010) modelled various ratios of CO and ^{13}CO in M51. In the case of Schinnerer et al. (2010), they used a non-LTE radiative transfer analysis to model ratios of ^{12}CO $J = 1-0$ and $J = 2-1$, and ^{13}CO $J = 1-0$ at multiple positions of the western arm and southern regions of M51 at resolutions of $2''.9$ and $4''.5$. They recovered cold $(14 - 20\,\mathrm{K})$, moderately dense $(n(\mathrm{H}_2) \sim 10^2 - 10^{2.4}\,\mathrm{cm}^{-3})$ gas; however these regions lie beyond our observed regions.

Israel et al. (2006) modelled ^{12}CO $J = 1-0$ to $J = 4-3$ and ^{13}CO $J = 1-0$ to $J = 3-2$ line ratios at two locations in M51: the centre and in a giant molecular association (GMA) offset from the nucleus $\Delta\alpha = -10'', \Delta\delta = +15''$. Given the small size of the offset and large nature of our beams $(40'')$, both of these positions correspond to our nucleus. Using an LVG radiative transfer model, they fit two components to the CO line ratios, assuming that $[^{12}\mathrm{CO}]/[^{13}\mathrm{CO}] = 40$. For the offset GMA, they find a warm $(\sim 100\,\mathrm{K})$, relatively diffuse $(\sim 10^{2.0}\,\mathrm{cm}^{-3})$ component, and a warmer $(\sim 150\,\mathrm{K})$, more dense $(\sim 10^{3.0}\,\mathrm{cm}^{-3})$ component. It is important to note that the density of the more diffuse component is at the lower limit of their modelled density space $(10^2\,\mathrm{cm}^{-3} \leq n(\mathrm{H}_2) \leq 10^5\,\mathrm{cm}^{-3})$, while the temperature of their warm component is at the upper limit of the modelled temperature space $(10\,\mathrm{K} \leq T_{kin} \leq 150\,\mathrm{K})$.

For the centre, they find a relatively warm $(\sim 100 - 1000\,\mathrm{K})$, lower density ($\sim 10^{2.0} - 10^{3.0}\,\mathrm{cm^{-3}}$) component, and a cooler ($\sim 20 - 60\,\mathrm{K}$, higher density ($10^{3.0} - 10^{3.5}\,\mathrm{cm^{-3}}$) component. In comparison, our cold component from our two-component fit agrees with their centre results ($T_{kin} \sim 19 - 42\,\mathrm{K}$, $n(\mathrm{H_2}) \sim 10^{2.94} - 10^{3.68}\,\mathrm{cm^{-3}}$). The temperature of our warm component agrees at the 1σ level with the warm component from Israel et al. (2006); however our warm component density ($n(\mathrm{H_2}) \sim 10^{4.85} - 10^{6.41}\,\mathrm{cm^{-3}}$) exceeds the Israel et al. (2006) density. Unlike Israel et al. (2006), we have observations of CO beyond the $J = 4 - 3$ transition, allowing us to probe warmer, denser gas.

In contrast, Brunner et al. (2008) probed the warm and hot molecular gas in M51 using the mid-infrared $\mathrm{H_2}$ rotational transitions $S(0) - S(5)$ in a strip. They found that the low-J $\mathrm{H_2}$ transitions ($S(0) - S(2)$) trace warm ($\sim 100-300\,\mathrm{K}$) molecular gas, likely the same component as our warm component. The high-J $\mathrm{H_2}$ transitions ($S(2) - S(5)$) trace hot molecular gas ($\sim 400 - 1000\,\mathrm{K}$). The mass of this hot component is small, with the peak surface density ($0.24\,\mathrm{M_\odot\ pc^{-2}}$) only $\sim 2\%$ of the peak surface density of the warm component ($11\,\mathrm{M_\odot\ pc^{-2}}$). The analysis by Kamenetzky et al. (2014) suggests that we do not detect this hot gas in our CO SLED as the high-J CO transitions are dominated by the warm component due to its significantly larger mass.

3.5.1.3 Diffuse molecular gas

As part of the PAWS collaboration to study the molecular gas in M51, Pety et al. (2013) used a combination of the Plateau de Bure Interferometer (PdBI) and the Institut de Radioastronomy Millimétrique (IRAM) 30m telescope to map the CO $J = 1 - 0$ emission at arcsecond resolution. By combining the PdBI interferometric data with the single dish IRAM-30m data, they are able to correct for the "missing flux" from the interferometric observations. They find that $\sim 50\%$ of the CO $J = 1 - 0$ emission is from unresolved molecular gas located in a thick, extended disk with a scale height $\sim 200\,\mathrm{pc}$. Pety et al.

(2013) argue that this emission originates from a warm ($\sim 50-100\,\mathrm{K}$), diffuse ($\sim 100-500\,\mathrm{cm}^{-3}$) component of molecular gas.

Some of the emission from the CO $J=1-0$ and $J=2-1$ transitions may in fact be coming from this extended component. We investigate the effects of the extended CO emission to the results of our two-component radiative transfer model by fitting various combinations of the CO and [CI] transitions (Table 3.5). We begin by setting the CO $J=1-0$ flux to half of the measured flux and fitting it along with the remaining CO and [CI] transitions as before (*half10*). Additionally, to investigate any contributions from the warm, diffuse component to the CO $J=2-1$ transition, we set the CO $J=2-1$ transition as an upper limit while fitting half of the CO $J=1-0$ flux (*half10 2ul*). We compare these solutions to our original two-component solutions (*all*).

We report the kinetic temperature (T_{kin}), molecular gas density ($n(\mathrm{H}_2)$), beam-averaged column-density ($< N_{\mathrm{CO}} >$) and pressure (P) for the centre region from each of the models in Table 3.5. The 1σ ranges for the kinetic temperatures do not shift significantly, with the range overlapping considerably for all three sets of solutions. The lower limit for the molecular gas density from both the *half10* and *half10 2ul* solutions ($n(\mathrm{H}_2) > 10^{3.72}\,\mathrm{cm}^{-3}$) lies at the upper limit of the range from the *all* solution ($n(\mathrm{H}_2) < 10^{3.75}\,\mathrm{cm}^{-3}$).

The increase in density for both the *half10* and *half10 2ul* solutions suggests that the diffuse molecular gas component from Pety et al. (2013) contributes to the CO $J=1-0$ emission, and possibly the CO $J=2-1$ emission. Determining the physical characteristics of this component using a radiative transfer model, such as the one presented in Section 3.3 would be difficult: the CO $J=1-0$ emission from the diffuse, extended component is already subthermally excited and there would be even less contribution from the diffuse component to higher J CO transitions. While Pety et al. (2013) use

Table 3.5 Comparing radiative transfer solutions

	Parameter 4DMax (1σ range)				
Solution	Log(n(H$_2$)) [Log(cm^{-3})]	T_{kin} [K]	Log($< N_{\mathrm{CO}} >$) [Log(cm^{-2})]	Log(P) [Log(K cm^{-2})]	Notes
all	3.23 (2.91 – 3.75)	28 (16 – 39)	17.14 (16.72 – 17.57)	4.96 (4.36 – 5.06)	
half10	4.09 (3.72 – 4.30)	22 (16 – 30)	16.27 (16.13 – 16.46)	5.34 (5.16 – 5.56)	CO $J = 1 - 0$ set to half
half10 2ul	4.09 (3.72 – 4.79)	22 (11 – 27)	16.42 (16.21 – 17.31)	5.34 (5.12 – 5.88)	*half10* with CO $J = 2 - 1$ set as upper limit

the ratio of $\frac{^{12}\mathrm{CO}}{^{13}\mathrm{CO}}$ to argue for the existence of this diffuse component, including only a single ^{13}CO transition in a radiative transfer analysis requires assuming a relative abundance ratio of ^{12}CO and ^{13}CO in the diffuse component.

It is important to note that the existence of this extended, diffuse component does not preclude the diffuse molecular gas, at least in part, being contained within GMCs. Diffuse GMCs exhibiting high ratios of $\frac{^{12}\mathrm{CO}}{^{13}\mathrm{CO}}$ have been observed at high latitudes within our own Galaxy (Blitz et al., 1984). In this case, the limited sensitivity of the interferometer along with the unresolved nature of the brightest clumps of the diffuse GMCs would lead to the interferometer filtering out these diffuse GMCs (Pety et al., 2013).

The critical densities of the [CI] $J = 1-0$ and $J = 2-1$ transitions are $n_{10} \sim 500\,\mathrm{cm}^{-3}$ and $n_{21} \sim 10^3\,\mathrm{cm}^{-3}$, respectively (Papadopoulos et al., 2004). These are comparable to the critical density of CO $J = 1-0$ ($n_{cr} \sim 1.1 \times 10^3\,\mathrm{cm}^{-3}$), which indicates that [CI] could also, at least in part, be tracing a diffuse molecular component. High-resolution observations of [CI] in galaxies like M51 coupled with single dish observations, as for CO in Pety et al. (2013), may be useful in constraining the physical state of this diffuse gas. Combining such observations with interferometric observations of dense gas tracers, such as HCN and HCO+ would allow us to discriminate between dense and diffuse GMCs. Finally, high-sensitivity, flux-recovered observations of a combination of these molecular gas-tracing species using the Atacama Large Millimeter/submillimeter Array (ALMA) would help differentiate between a truly extended component or a collection of diffuse GMCs. Unfortunately, M51 itself is not a viable target for ALMA due to its high declination.

3.5.2 CO-to-H_2 and [CI]-to-H_2 conversion factors

The CO-to-H_2 conversion factor (α_{CO}) is usually used to convert the luminosity of the CO $J = 1-0$ transition into a molecular gas mass. However, it remains

Table 3.6 CO- and [CI]-to-H_2 conversion factors ($x_{\rm CO} = 3 \times 10^{-4}$)

Region	Value (1σ range)	
	$\alpha_{\rm CO}$ $[M_\odot\,{\rm pc}^{-2}({\rm K\ km\ s}^{-1})^{-1}]$	$\alpha_{\rm [CI]}$ $[M_\odot\,{\rm pc}^{-2}({\rm K\ km\ s}^{-1})^{-1}]$
Nucleus	0.3 (0.07 – 0.4)	1.5 (0.4 – 2.8)
Centre	0.2 (0.06 – 0.6)	1.4 (0.4 – 5.4)
Arm/inter-arm	1.2 (0.08 – 1.7)	8.9 (0.4 – 21.5)
All	0.4 (0.07 – 1.2)	2.8 (0.4 – 12.7)

Note: both $\alpha_{\rm CO}$ and $\alpha_{\rm [CI]}$ depend on the assumed value for $x_{\rm CO}$. Adopting $x_{\rm CO} = 3 \times 10^{-5}$ would increase both conversion factors by a factor of 10.

rather uncertain, with estimates varying from $\sim 0.6{\pm}0.2 M_\odot\,{\rm pc}^{-2}({\rm K\ km\ s}^{-1})^{-1}$ for luminous infrared galaxies (Papadopoulos et al., 2012) to over an order of magnitude higher for the Milky Way ($\alpha_{\rm CO} \sim 4{-}9 M_\odot\,{\rm pc}^{-2}({\rm K\ km\ s}^{-1})^{-1}$, Leroy et al. 2011). Recently, Offner et al. (2014) investigated the use of a [CI]-to-H_2 conversion factor to calculate the total molecular gas mass.

We use the beam-averaged column densities calculated from our two-component radiative transfer model to determine the equivalent mass contained within a single beam for each region. We assume the same CO abundance as used to calculate our mass prior (3×10^{-4}). We then use the average measured CO $J = 1-0$ and [CI] $J = 1-0$ fluxes to calculate the necessary $\alpha_{\rm CO}$ and $\alpha_{\rm [CI]}$, respectively. We report the results in Table 3.6.

The value recovered for the arm/inter-arm and "all" regions of M51 are not very well constrained and span an order of magnitude due to the large range spanned by the beam-averaged column density. For $\alpha_{\rm CO}$, the value does not vary significantly across the three regions, with a value of $\sim 0.2^{+0.4}_{-0.1} M_\odot\,{\rm pc}^{-2}({\rm K\ km\ s}^{-1})^{-1}$ for the centre region. The value for $\alpha_{\rm [CI]}$ is more uncertain, varying between $\sim 0.4 - 5.4 M_\odot\,{\rm pc}^{-2}({\rm K\ km\ s}^{-1})^{-1}$ for the centre region. The larger range for $\alpha_{\rm [CI]}$ is due to larger measurement uncertainties in the [CI] $J = 1-0$ transition as opposed to the CO $J = 1-0$ transition. In the arm/inter-arm and "all" regions, the 1σ ranges for both $\alpha_{\rm CO}$ and $\alpha_{\rm [CI]}$

span over an order of magnitude. This is due to larger 1σ ranges for the beam-averaged column densities, and in the case of $\alpha_{[CI]}$, larger uncertainties on the measured luminosity.

It is important to note that the CO abundance is highly uncertain and could vary by an order of magnitude or more. As such, both α_{CO} and $\alpha_{[CI]}$ vary with the CO abundance as

$$\alpha'_{CO} = \alpha_{CO} \frac{3 \times 10^{-4}}{x_{CO}} \tag{3.4}$$

$$\alpha'_{[CI]} = \alpha_{[CI]} \frac{3 \times 10^{-4}}{x_{CO}} \tag{3.5}$$

where α_{CO} and $\alpha_{[CI]}$ are the values from Table 3.6, α'_{CO} and $\alpha'_{[CI]}$ are the values for the CO and [CI]-to-H_2 conversion factor, and x_{CO} is the CO abundance. Our choice of CO abundance is near the upper limit of observed values (Ward et al., 2003), and so the values for the conversion factors shown in Table 3.6 should be viewed as lower limits to the true conversion factors. If we instead adopt a value of $x_{CO} = 3 \times 10^{-5}$, as was found in the Antennae (Schirm et al., 2014), we recover values for α_{CO} and $\alpha_{[CI]}$ a factor of 10 larger than those shown in Table 3.6.

We compare the results for α_{CO} for the centre region to previous studies in Table 3.7. It is interesting to note that the two higher-resolution studies (Schinnerer et al., 2010; Hughes et al., 2013a) return values comparable to the Milky Way. These higher resolution studies focus on individual clumps of CO emission, as opposed to emission over a larger area as we have, and so are biased towards bright, compact CO emission. This in turn leads to a value of α_{CO} for only the bright, compact regions and not a global value. Our observations, on the other hand, do not distinguish between compact and extended emission, and so our values for α_{CO} represent a global value for the

Table 3.7 Comparing $\alpha_{\rm CO}$ to previous studies

Source	Beam size	$\alpha_{\rm CO}$ (1σ range)
Centre of M51 (This work, $x_{\rm CO} = 3 \times 10^{-4}$)	$40''$	0.2 (0.06 – 0.4)
Centre of M51 (This work, $x_{\rm CO} = 3 \times 10^{-5}$)	$40''$	2 (0.6 – 4)
Garcia-Burillo et al. (1993)	$\sim 14''$	1.9 (1.2 – 2.6)
Nakai & Kuno (1995)	$\sim 10''$	2.2 (1.9 – 2.4)
Schinnerer et al. (2010)	$\sim 4.5''$	(3.1 – 4.8)
Hughes et al. (2013a)	$\sim 1''$	3.8
Milky Way (Leroy et al., 2011)		(4 – 9)

observed region.

Historically, [CI] has not been used much as a tracer for the total molecular gas mass. Initially, it was thought that [CI] traced the surfaces of molecular clouds where CO was dissociated, while deeper within the molecular clouds all of the [CI] would be in CO (Tielens & Hollenbach, 1985). Observations of [CI] within our own Galaxy do not show the stratified structure expected at the surfaces of molecular clouds (e.g. see Plume et al. 1999; Ikeda et al. 2002; Shimajiri et al. 2013).

Bell et al. (2007) calculate theoretical values for $X_{\rm [CI]}$ based on the physical characteristics of M51 as derived from the `UCL_PDR` PDR model. They determine a value of $X_{\rm [CI]} \sim 0.6 \times 10^{20}\,{\rm cm}^{-2}$ (K km s^{-1})$^{-1}$, which corresponds to $\alpha_{[CI]} \sim 1.4\,{\rm M}_{\odot}$ pc^{-2}(K km s^{-1})$^{-1}$. It is important to note that the flux predicted for both [CI] transitions varies significantly depending upon which PDR model is used (for a comparison between models see Röllig et al. 2007), leading to large uncertainties in the model flux. Furthermore, PDR models generally predict [CI] to form in a surface layer (Röllig et al., 2007), due to the constant density slab-geometry assumed by most models. In reality, turbulent motion would lead to mixing of these surfaces layers deeper into the cloud, including [CI]. This is more in line with observations of [CI] which suggest it is found throughout molecular clouds (e.g. see Plume et al. 1999; Ikeda et al. 2002; Shimajiri et al. 2013).

More recently, Offner et al. (2014) simulated individual clouds of molecular gas with a full chemical network and determined a value of $X_{\rm [CI]} \sim 11 \times 10^{20}\,{\rm cm}^{-2}$ (K km s^{-1})$^{-1}$, corresponding to $\alpha_{[CI]} \sim 26\,{\rm M}_\odot$ pc^{-2}(K km s^{-1})$^{-1}$. This value is significantly higher than the values calculated in any of our regions, although with a lower $x_{\rm CO}$ value of 3×10^{-5} the measurements and predictions would agree with the 1σ ranges of our results. Offner et al. (2014) do not report a value for the CO abundance, making it difficult to compare results directly.

3.5.3 PDR modelling

Both Kramer et al. (2005) and Parkin et al. (2013) previously modelled PDRs in M51. Kramer et al. (2005) modelled various ratios of [CII](158 μm), [OI](63μm), [CI] $J = 1-0$, CO $J = 1-0$ and CO $J = 3-2$, using the PDR models from Kaufman et al. (1999). They find that the best fit solution to their line ratios at all 3 pointings is consistent with density of $n({\rm H}_2) \sim 4 \times 10^4\,{\rm cm}^{-3}$ and a field strength of $18 < G_0 < 32$ in an $80''$ beam.

Parkin et al. (2013) used the [CII]/[OI]63 μm and ([CII]+[OI]63 μm)/TIR ratios along with the PDR models from Kaufman et al. (1999) and Kaufman et al. (2006) to constrain the density and field strength in the nucleus, centre, arm and inter-arm regions of M51 (see Figure 3.4). Their results for the nucleus ($n({\rm H}_2) = 10^{3.75} - 10^{4.0}\,{\rm cm}^{-3}$, $G_0 = 10^{3.25} - 10^{3.75}$) do not agree with either our “cold” or “warm” PDR solutions, falling above the range allowed by our CO line ratios and our CO/FIR ratios.

The density Parkin et al. (2013) recover for the centre of M51 ($n({\rm H}_2) = 10^{3.0} - 10^{3.25}\,{\rm cm}^{-3}$) agrees with our “cold” PDR solution density, while their field strength ($G_0 = 10^{2.75} - 10^{3.0}$) exceeds what is allowed by our ratio of CO/FIR combined with various CO line ratios (Figure 3.10). The results Parkin et al. (2013) recover for both the arm and inter-arm regions are similar:

the ranges reported for the density ($n(\mathrm{H}_2) = 10^{2.75} - 10^{3.0}\,\mathrm{cm}^{-3}$) agree with our results, while the FUV field strength ($G_0 = 10^{2.25} - 10^{2.5}$) is larger than our allowed solutions.

In order to recover a $\frac{\mathrm{CO}\,J{=}6{-}5}{FIR}$ line ratio consistent with the $\frac{\mathrm{CO}\,J{=}8{-}7}{\mathrm{CO}\,J{=}7{-}6}$ and $\frac{\mathrm{CO}\,J{=}8{-}7}{\mathrm{CO}\,J{=}6{-}5}$ line ratios, we would require that only $\sim 1\%$ of the FIR flux comes from our "warm" PDRs. If we assume the remaining FIR flux arises from our "cold" PDRs, our results for the "cold" PDR do not change appreciably.

Our "cold" PDR results suggest a density of $n(\mathrm{H}_2 \sim 10^3\,\mathrm{cm}^{-3}$ and FUV field strength of $G_0 < 10^2$. In the Kaufman et al. (1999) and Kaufman et al. (2006) PDR models, this would correspond to $\frac{[\mathrm{CII}]}{[\mathrm{OI}](63\,\mu\mathrm{m})} \gtrsim 1.7$ and $\frac{[\mathrm{CII}]+[\mathrm{OI}](63\,\mu\mathrm{m})}{FIR} \gtrsim 1.3 \times 10^{-2}$. The average values of these ratios in each of the nucleus, centre, arm and inter-arm regions from Parkin et al. (2013) vary between $\frac{[\mathrm{CII}]}{[\mathrm{OI}](63\,\mu\mathrm{m})} \sim 0.2 - 1.2$ and $\frac{[\mathrm{CII}]+[\mathrm{OI}](63\,\mu\mathrm{m})}{FIR} \sim (5.0 - 8.1) \times 10^{-3}$. It is important to note that Parkin et al. (2013) corrected the [CII] emission for the ionized gas fraction and [OI]($63\,\mu$m) for orientation effects due to the plane-parallel slab-nature of the models (see Section 4.1 of Parkin et al. 2013 for details). For both ratios, the grid values for our "cold" PDR solution are a factor of ~ 1.5 greater than the values measured in Parkin et al. (2013).

We investigate the effects of our larger beam on our PDR results by convolving both the [CII] and [OI]($63\,\mu$m) maps from Parkin et al. (2013) to our $40''$ gaussian beam, and re-gridding the images to our SPIRE-FTS maps. Using these new maps, we find that the ratios vary between $\frac{[\mathrm{CII}]}{[\mathrm{OI}](63\,\mu\mathrm{m})} \sim 0.6 - 1.3$ and $\frac{[\mathrm{CII}]+[\mathrm{OI}](63\,\mu\mathrm{m})}{FIR} \sim (5.6 - 8.4) \times 10^{-3}$ across the region observed with SPIRE-FTS. These ratios are consistent with those from Parkin et al. (2013), suggesting that the beam sizes are not the cause of the differences in solutions.

The ranges for the measured ratios reported in Parkin et al. (2013) do not account for the calibration uncertainty of the PACS spectrometer, which is $\sim$ 30% (PACS observer manual[4]). Accounting for this uncertainty leads to a range for the ratio of $\frac{[\mathrm{CII}]+[\mathrm{OI}](63\,\mu\mathrm{m})}{FIR} \sim (3.5 - 10.5 \times 10^{-3})$, which agrees within 50% with $\frac{[\mathrm{CII}]+[\mathrm{OI}](63\,\mu\mathrm{m})}{FIR} \gtrsim 1.3 \times 10^{-2}$, the range necessary to reproduce our results using the Kaufman et al. (1999) and Kaufman et al. (2006) PDR models. The PACS calibration uncertainty would have a greater effect on the ratio of $\frac{[\mathrm{CII}]}{[\mathrm{OI}](63\,\mu\mathrm{m})}$, corresponding to an uncertainty of $\sim$ 40% in the line ratio. Accounting for the calibration uncertainty leads to a range of $\sim 0.4 - 1.8$ for the ratio of $\frac{[\mathrm{CII}]}{[\mathrm{OI}](63\,\mu\mathrm{m})}$, which agrees within uncertainties with the model value of > 1.7.

We attribute the remaining disagreement to the simplified geometries assumed by the PDR models, which can lead to differences in the model results (Röllig et al., 2007). Both the model used in Parkin et al. (2013) and the model used here assume a semi-infinite slab of gas illuminated by an FUV field. In reality, PDRs are clumpy media which are affected by other physical processes concurrently. Mechanical heating, for example, can have a significant effect on the atomic and ion line ratios reported by Parkin et al. (2013), and on the overall shape of the CO SLED (Kazandjian et al., 2015). Combining the measurements from Parkin et al. (2013) and our measured CO SLED, along with observations of other molecular gas tracers such as HCN and HCO+ would be necessary to quantify the contributions of mechanical heating to the PDRs in M51.

3.5.4 Comparison to other VNGS galaxies

M51 is the 6th galaxy in the VNGS sample for which the analysis of the SPIRE-FTS observations of CO have been published, and is the first normal, quiescent spiral galaxy from the sample. For the other 5 galaxies, only a single-

[4]PACS Observers Manual is available for download from the ESA Herschel Science Centre.

component was fit to the CO SLED for M83 (Wu et al., 2015), while for NGC 1068 (Spinoglio et al., 2012), the extended (star-forming ring) and compact (circumnuclear disk) CO emission was fit separately, taking advantage of the varying beam size of the SLW and SSW. In the case of Arp 220 (Rangwala et al., 2011), M82 (Panuzzo et al., 2010; Kamenetzky et al., 2012) and NGC 4038/39 (Schirm et al., 2014), a two-component fit was performed for the CO, ^{13}CO(M82) and [CI](NGC 4038/39) emission. As such, we compare our two-component fit for the centre region to those of Arp 220, M82 and NGC 4038/39 (Table 3.8). For NGC 4038/39, we distinguish between the region where the two merging gas disks overlap (the "overlap region") and the nucleus of NGC 4038 (hereafter NGC 4038). Note that in the case of Arp 220, the CO emission is point-like within the FTS beam (Rangwala et al., 2011), and so the actual column density is reported in Table 3.8.

Arp 220, M82 and NGC 4038/39 are all examples of either an interaction or an ongoing merger. Arp 220 ($D = 77\,$Mpc, Scoville et al. 1997) is an ultra luminous infrared galaxy and is an advanced merger between two galaxies. M82 ($D = 3.4\,$Mpc, Dalcanton et al. 2009) is a starburst galaxy (Yun et al., 1993) whose increased star formation rate is due to a recent interaction with the nearby M81. Finally, NGC 4038/39 ($D = 22\,$Mpc, Schweizer et al. 2008) is an ongoing merger between two gas rich spiral galaxies.

The characteristics of the cold component for the centre region of M51 are very similar to the two regions in NGC 4038/39. Besides the large temperature range for M82 ($T_{kin} = 12 - 472\,$K), the cold molecular gas in M51 is also similar to that of M82. The temperature of the cold molecular gas in Arp220 ($T_{kin} = 34 - 67\,$K) is higher than the temperature recovered in M51.

The warm component of M51 shows more differences than the cold component when compared to the other systems: it has a lower kinetic temperature ($T_{kin} = 44 - 183\,$K) than any of the other 3 systems ($T_{kin} > 300\,$K).

Table 3.8 Comparing radiative transfer solutions

Comp.	Source	Parameter 4DMax (1σ range) Log(n(H$_2$)) [Log(cm^{-3})]	$T_{\rm kin}$ [K]	Log($< N_{\rm CO} >$) [Log(cm^{-2})]	Log(P) [Log(K cm^{-2})]	Reference
Cold	Centre of M51	3.23 (2.91 – 3.75)	28 (16 – 39)	17.14 (16.72 – 17.57)	4.96 (4.36 – 5.06)	This work
	Arp220	2.80 (2.60 – 3.20)	50 (34 – 67)	20.30 (19.90 – 20.30)[1]	4.50 (4.50 – 4.80)	Rangwala et al. (2011)
	M82	3.20 (2.40 – 4.80)	40 (12 – 472)	18.20 (17.60 – 18.80)	5.10 (4.60 – 5.80)	Kamenetzky et al. (2012)
	NGC4038	3.60 (3.10 – 4.30)	25 (18 – 33)	17.60 (16.60 – 17.60)	5.20 (4.50 – 5.60)	Schirm et al. (2014)
	Overlap region	3.90 (2.90 – 4.40)	21 (15 – 27)	17.60 (16.80 – 17.90)	4.30 (4.30 – 5.60)	Schirm et al. (2014)
Warm	Centre of M51	4.94 (4.87 – 6.57)	37 (44 – 183)	14.54 (14.14 – 15.43)	7.13 (6.96 – 8.80)	This work
	Arp220	3.20 (3.00 – 3.20)	1343 (1247 – 1624)	19.40 (19.40 – 19.50)[1]	6.30 (6.20 – 6.40)	Rangwala et al. (2011)
	M82	4.00 (3.50 – 4.20)	414 (335 – 518)	16.70 (16.40 – 17.20)	6.60 (6.20 – 6.80)	Kamenetzky et al. (2012)
	NGC4038	4.30 (4.80 – 6.60)	3999 (347 – 3397)	14.30 (14.20 – 14.80)	9.44 (8.20 – 10.20)	Schirm et al. (2014)
	Overlap region	4.00 (4.00 – 4.70)	4425 (430 – 3811)	14.60 (14.40 – 14.70)	7.40 (7.30 – 7.70)	Schirm et al. (2014)

[1] Actual $N_{\rm CO}$ reported for Arp220; see text.

Furthermore, the density of the molecular gas ($n(\mathrm{H_2}) > 10^{4.87}\,\mathrm{cm^{-3}}$) is higher than in M82 ($n(\mathrm{H_2}) < 10^{3.20}\,\mathrm{cm^{-3}}$), Arp220 ($n(\mathrm{H_2}) < 10^{4.20}\,\mathrm{cm^{-3}}$) or the overlap region ($n(\mathrm{H_2}) < 10^{4.70}\,\mathrm{cm^{-3}}$), while it is comparable to NGC 4038.

The molecular gas mass is proportional to the beam size multiplied by the beam-averaged column density. Since the beam-size in any one system will be the same for the cold and warm components, we can calculate the warm gas mass as a fraction of the cold gas mass using the beam-averaged column densities. In M51, the warm gas mass is $\sim 0.3\%$ of the cold gas mass. This is comparable to the warm gas mass fraction in NGC 4038 and the overlap region ($\sim 0.1\%$), while it is a factor of $10 - 30$ smaller than the warm gas mass fraction in Arp 220 ($\sim 10\%$) and M82 ($\sim 3\%$). In comparison, the global star formation rates in Arp220 ($\sim 200\,\mathrm{M_\odot\ yr^{-1}}$, Barcos-Muñoz et al. 2015), M82 ($\sim 10\,\mathrm{M_\odot\ yr^{-1}}$, Yun et al. 1993) and NGC 4038/39 ($\gtrsim 5\,\mathrm{M_\odot\ yr^{-1}}$, Stanford et al. 1990) are all greater than the global star formation rate in M51 ($\sim 2.6\,\mathrm{M_\odot\ yr^{-1}}$ Schuster et al. 2007) by nearly a factor of 2 or more.

The primary heating source for the warm molecular gas in Arp 220 (Rangwala et al., 2011) and M82 (Kamenetzky et al., 2012) was found to be mechanical heating due primarily to supernova and stellar winds (Maloney, 1999), while it is unlikely that this warm gas resides primarily in PDRs. In NGC 4038/39, supernova and stellar winds were found to be sufficient to heat the warm molecular gas, while PDRs contributing significantly to the heating could not be ruled out (Schirm et al., 2014). The higher warm gas mass fraction in Arp 220 and M82 compared to NGC 4038/39 was attributed to an increase in the efficiency by which energy from supernova and stellar winds is injected as thermal energy into the molecular gas (Schirm et al., 2014).

For the nucleus of NGC 4038, the physical size corresponding to the beam of the observations ($\sim 43''$) is ~ 4.6 kpc. In comparison, our observations of M51 cover the central ~ 7 kpc ($\sim 150''$) of the galaxy, while the pixels used in our analysis cover the central $\sim 5\,\mathrm{kpc}$ ($\sim 100''$). As such, NGC 4038 provides us with a comparison of the effects of an early stage major merger to the less pronounced interaction seen between M51 and NGC 5195. The most striking difference is in the temperature of the warm molecular gas, where the temperature in the centre region of M51 ($T_{kin} \sim 44 - 183\,\mathrm{K}$) is $3 - 7$ times less than the lower limit of the temperature in NGC 4038 ($T_{kin} \gtrsim 350\,\mathrm{K}$).

It is not surprising to see an increase in the molecular gas temperature in NGC 4038 compared to M51, as M51 is generally regarded as a normal grand-design spiral galaxy, while NGC 4038/39 is an ongoing gas-rich merger. In NGC 4038 and the overlap region, Schirm et al. (2014) were unable to rule out PDRs as a possible source of heating, while evidence suggests the supernova and stellar winds contribute significantly to the heating. Conversely, in M51, there is strong evidence to suggest that PDRs are fundamental to the molecular gas heating (e.g. see Roussel et al. 2007 and Parkin et al. 2013). Both heating mechanisms, however, are tied to the star formation rate as both require the formation of O and B stars which are relatively short lived.

A relatively small amount of mechanical heating compared to heating due to PDRs ($\sim 1\%$) is required to have a significant effect on the temperature of the molecular gas (e.g. Kazandjian et al. 2012). In NGC 4038/39, the turbulent motion due to both the ongoing merger and supernova and stellar winds should exceed this minimum threshold (Schirm et al., 2014). On the other hand, the mechanical heating due to supernova and stellar winds has not been calculated for M51 as suitable supernova rate data do not exist. However, we would expect that, in NGC 4038/39, the contributions of both turbulent motion and star formation feedback in the form of supernova and stellar winds would have a larger effect on the overall heating of the molecular gas than in M51. Using more sophisticated PDR models which include contributions from mechanical heating, along with dense gas tracers such as HCN and HCO+ may allow us to calculate the contributions to the total gas heating from PDRs and mechanical heating in M51, NGC 4038/39, and other systems.

3.6 Summary and conclusions

In this paper, we have presented intermediate-sampled SPIRE-FTS observations of CO from $J = 4-3$ to $J = 8-7$ and both [CI] transitions of the central region of M51. We supplemented these observations with ground-based observations of CO $J = 1-0$ to $J = 3-2$. We separate M51 into 3 regions, the nucleus, centre and arm/inter-arm regions, by performing an unweighted average of the emission for each pixel contained with a region. We also combine all the pixels within the three into a single "All" region.

1. Using the non-LTE excitation code RADEX along with a Bayesian likelihood code, we perform a two-component fit to the CO and [CI] emission in the nucleus, centre and arm/inter-arm regions of M51, along with all three regions combined. We find that the results do not vary beyond 1σ for all three regions. The results for the nucleus and centre regions of M51 consist of a cold ($T_{kin} \sim 20-40\,\mathrm{K}$), moderately dense ($n(\mathrm{H_2}) = 10^{2.9} - 10^{3.8}$) component and a warm ($T_{kin} \sim 40-180\,\mathrm{K}$), higher density component ($n(\mathrm{H_2}) = 10^{4.9} - 10^{6.6}$). The results for the arm/inter-arm region, and for all regions combined are not as well constrained. The warm gas mass fraction for the centre of M51 is only $\sim 0.3\%$.

2. We calculate values for the CO-to-H$_2$ (α_{CO}) and [CI]-to-H$_2$ (α_{CI}) conversion factors using the $J = 1-0$ transition for both and the results from our non-LTE excitation analysis. Assuming a CO abundance of $x_{\mathrm{CO}} = 3\times10^{-5}$, we find $\alpha_{\mathrm{CO}} \sim 2$ and $\alpha_{\mathrm{[CI]}} \sim 10-50$ for the centre region of M51. The value for $\alpha_{\mathrm{[CI]}}$ is consistent with previous simulations,

while the value for α_{CO} are lower than those recovered from higher-resolution observations of M51 as part of the PAWS collaboration. We argue that the differences in α_{CO} are due to higher-resolution observations being biased towards the more compact CO emission in M51 and do not represent a global value for α_{CO}.

3. We investigate the contributions of an extended component of molecular gas to the CO $J = 1-0$ emission by setting CO $J = 1-0$ to half of the measured flux in our radiative transfer analysis. The density of the molecular gas increases in solutions where the CO $J = 1-0$ flux is set to half, which suggests that the remaining half may originate from a more diffuse, possibly extended component of the molecular gas. We suggest that this diffuse molecular gas may still arise from GMCs. High-resolution, high-sensitivity, flux-recovered observations of multiple molecular gas-tracing species, such as [CI], HCN and HCO+ along with CO would allow us to distinguish between dense and diffuse GMCs.

4. We compare line ratios of CO along with the $\frac{\mathrm{CO}J{=}3-2}{FIR}$ and $\frac{\mathrm{CO}J{=}6-5}{FIR}$ to a PDR model. Using the densities calculated from our non-LTE excitation analysis, our PDR modelling suggest a density of $n(\mathrm{H_2}) \sim 10^3\,\mathrm{cm^{-3}}$ and a field strength $G_0 < 10^2$. We compare our results to previous results (Parkin et al., 2013) which used various atomic line ratios and the total infrared flux to model the FUV field strength and gas density, and find that their FUV field strength ($G_0 > 10^{2.25}$) is greater than what is allowed by our models. We attribute the differences to calibration uncertainties in the atomic line ratios used by Parkin et al. (2013) and to differences in the models used in their work and our work.

5. We compare our two-component fit to the CO SLED of the centre region of M51 to radiative transfer results for the ULIRG Arp220, the starburst

galaxy M82 and the on-going merger NGC 4038/39. The characteristics of the cold component are comparable across all 4 systems, with the exception of the temperature of Arp220, which is slightly higher. In the case of the warm component, the temperature in the centre region of M51 ($T_{kin} \sim 44-183\,\mathrm{K}$) is less than the other 3 systems ($T_{kin} \gtrsim 350\,\mathrm{K}$), while the density in the centre of M51 ($n(\mathrm{H_2}) \sim 4.9-6.6$) is comparable to the nucleus of NGC 4038, and greater than the overlap region, Arp220 or M82. We suggest that the increase in the warm-component temperature in the nucleus of NGC 4038 compared to the observed regions in M51 is due to either the increased star-formation rate in the nucleus, or due to differences in the heating mechanism.

Acknowledgments

This research was supported by grants from the Canadian Space Agency and the Natural Sciences and Engineering Research Council of Canada (PI: C. D. Wilson). PACS has been developed by a consortium of institutes led by MPE (Germany) and including UVIE (Austria); KU Leuven, CSL, IMEC (Belgium); CEA, LAM (France); MPIA (Germany); INAF-IFSI/OAA/OAP/OAT, LENS, SISSA (Italy); IAC (Spain). This development has been supported by the funding agencies BMVIT (Austria), ESA-PRODEX (Belgium), CEA/CNES (France), DLR (Germany), ASI/INAF (Italy) and CICYT/MCYT (Spain). SPIRE has been developed by a consortium of institutes led by Cardiff University (UK) and including Univ. Lethbridge (Canada); NAOC (China); CEA, LAM (France); IFSI, Univ. Padua (Italy); IAC (Spain); Stockholm Observatory (Sweden); Imperial College London, RAL, UCL-MSSL, UKATC, Univ. Sussex (UK); and Caltech, JPL, NHSC, Univ. Colorado (USA). This development has been supported by national funding agencies: CSA (Canada); NAOC

(China); CEA, CNES, CNRS (France); ASI (Italy); MCINN (Spain); SNSB (Sweden); STFC (UK); and NASA (USA). HIPE is a joint development by the Herschel Science Ground Segment Consortium, consisting of ESA, the NASA Herschel Science Center, and the HIFI, PACS and SPIRE consortia. This research has made use of the NASA/IPAC Extragalactic Database (NED) which is operated by the Jet Propulsion Laboratory, California Institute of Technology, under contract with the National Aeronautics and Space Administration. This research made use of the python plotting package matplotlib (Hunter, 2007). This research made use of APLpy, an open-source plotting package for Python hosted at http://aplpy.github.com. We would like to thank Mark Wolfire for providing the PDR model grids used in this paper. This work made use of HERACLES, 'The HERA CO-Line Extragalactic Survey (Leroy et al., 2009).

Bibliography

Barcos-Muñoz, L., Leroy, A. K., Evans, A. S., et al. 2015, ApJ, 799, 10

Bell, T. A., Viti, S., & Williams, D. A. 2007, MNRAS, 378, 983

Bendo, G. J., Galliano, F., & Madden, S. C. 2012, MNRAS, 423, 197

Blitz, L., Magnani, L., & Mundy, L. 1984, ApJ, 282, L9

Brunner, G., Sheth, K., Armus, L., et al. 2008, ApJ, 675, 316

Colombo, D., Hughes, A., Schinnerer, E., et al. 2014a, ApJ, 784, 3

Colombo, D., Meidt, S. E., Schinnerer, E., et al. 2014b, ApJ, 784, 4

Currie, M. J., Draper, P. W., Berry, D. S., et al. 2008, in Astronomical Society of the Pacific Conference Series, Vol. 394, Astronomical Data Analysis Software and Systems XVII, ed. R. W. Argyle, P. S. Bunclark, & J. R. Lewis, 650

Dalcanton, J. J., Williams, B. F., Seth, A. C., et al. 2009, ApJS, 183, 67

Dobbs, C. L., Theis, C., Pringle, J. E., & Bate, M. R. 2010, MNRAS, 403, 625

Gaches, B. A. L., Offner, S. S. R., Rosolowsky, E. W., & Bisbas, T. G. 2014, ArXiv e-prints, arXiv:1412.2754

Galametz, M., Kennicutt, R. C., Calzetti, D., et al. 2013, MNRAS, 431, 1956

Garcia-Burillo, S., Guelin, M., & Cernicharo, J. 1993, A&A, 274, 123

Graciá-Carpio, J., García-Burillo, S., Planesas, P., Fuente, A., & Usero, A. 2008, A&A, 479, 703

Griffin, M. J., Abergel, A., Abreu, A., et al. 2010, A&A, 518, L3

Hollenbach, D., Kaufman, M. J., Neufeld, D., Wolfire, M., & Goicoechea, J. R. 2012, ApJ, 754, 105

Hughes, A., Meidt, S. E., Colombo, D., et al. 2013a, ApJ, 779, 46

Hughes, A., Meidt, S. E., Schinnerer, E., et al. 2013b, ApJ, 779, 44

Hunter, J. D. 2007, Computing In Science & Engineering, 9, 90

Ikeda, M., Oka, T., Tatematsu, K., Sekimoto, Y., & Yamamoto, S. 2002, ApJS, 139, 467

Israel, F. P., Tilanus, R. P. J., & Baas, F. 2006, A&A, 445, 907

Kamenetzky, J., Rangwala, N., Glenn, J., Maloney, P. R., & Conley, A. 2014, ApJ, 795, 174

Kamenetzky, J., Glenn, J., Maloney, P. R., et al. 2011, ApJ, 731, 83

Kamenetzky, J., Glenn, J., Rangwala, N., et al. 2012, ApJ, 753, 70

Kaufman, M. J., Wolfire, M. G., & Hollenbach, D. J. 2006, ApJ, 644, 283

Kaufman, M. J., Wolfire, M. G., Hollenbach, D. J., & Luhman, M. L. 1999, ApJ, 527, 795

Kazandjian, M. V., Meijerink, R., Pelupessy, I., Israel, F. P., & Spaans, M. 2012, A&A, 542, A65

—. 2015, A&A, 574, A127

Koda, J., Scoville, N., Sawada, T., et al. 2009, ApJ, 700, L132

Koulouridis, E. 2014, ArXiv e-prints, arXiv:1408.6233

Kramer, C., Mookerjea, B., Bayet, E., et al. 2005, A&A, 441, 961

Kramer, C., Moreno, R., & Greve, A. 2008, A&A, 482, 359

Leroy, A. K., Walter, F., Bigiel, F., et al. 2009, AJ, 137, 4670

Leroy, A. K., Bolatto, A., Gordon, K., et al. 2011, ApJ, 737, 12

Liszt, H. S., Pety, J., & Tachihara, K. 2009, A&A, 499, 503

Maloney, P. R. 1999, Ap&SS, 266, 207

Meidt, S. E., Schinnerer, E., García-Burillo, S., et al. 2013, ApJ, 779, 45

Mentuch Cooper, E., Wilson, C. D., Foyle, K., et al. 2012, ApJ, 755, 165

Nakai, N., Kuno, N., Handa, T., & Sofue, Y. 1994, PASJ, 46, 527

Naylor, B. J., Bradford, C. M., Aguirre, J. E., et al. 2010a, ApJ, 722, 668

Naylor, D. A., Baluteau, J.-P., Barlow, M. J., et al. 2010b, in Society of Photo-Optical Instrumentation Engineers (SPIE) Conference Series, Vol. 7731, Society of Photo-Optical Instrumentation Engineers (SPIE) Conference Series, 16

Nikola, T., Geis, N., Herrmann, F., et al. 2001, ApJ, 561, 203

Offner, S. S. R., Bisbas, T. G., Bell, T. A., & Viti, S. 2014, MNRAS, 440, L81

Panuzzo, P., Rangwala, N., Rykala, A., et al. 2010, A&A, 518, L37

Papadopoulos, P. P., Thi, W.-F., & Viti, S. 2004, MNRAS, 351, 147

Papadopoulos, P. P., van der Werf, P., Xilouris, E., Isaak, K. G., & Gao, Y. 2012, ApJ, 751, 10

Parkin, T. J., Wilson, C. D., Schirm, M. R. P., et al. 2013, ApJ, 776, 65

Pety, J., Lucas, R., & Liszt, H. S. 2008, A&A, 489, 217

Pety, J., Schinnerer, E., Leroy, A. K., et al. 2013, ArXiv e-prints, arXiv:1304.1396

Pilbratt, G. L., Riedinger, J. R., Passvogel, T., et al. 2010, A&A, 518, L1

Plume, R., Jaffe, D. T., Tatematsu, K., Evans, II, N. J., & Keene, J. 1999, ApJ, 512, 768

Poglitsch, A., Waelkens, C., Geis, N., et al. 2010, A&A, 518, L2

Rangwala, N., Maloney, P. R., Glenn, J., et al. 2011, ApJ, 743, 94

Röllig, M., Abel, N. P., Bell, T., et al. 2007, A&A, 467, 187

Rose, J. A., & Searle, L. 1982, ApJ, 253, 556

Roussel, H., Helou, G., Hollenbach, D. J., et al. 2007, ApJ, 669, 959

Satyapal, S., Sambruna, R. M., & Dudik, R. P. 2004, A&A, 414, 825

Schinnerer, E., Weiß, A., Aalto, S., & Scoville, N. Z. 2010, ApJ, 719, 1588

Schinnerer, E., Meidt, S. E., Pety, J., et al. 2013, ApJ, 779, 42

Schirm, M. R. P., Wilson, C. D., Parkin, T. J., et al. 2014, ApJ, 781, 101

Schuster, K. F., Kramer, C., Hitschfeld, M., Garcia-Burillo, S., & Mookerjea, B. 2007, A&A, 461, 143

Schweizer, F., Burns, C. R., Madore, B. F., et al. 2008, AJ, 136, 1482

Scoville, N., & Young, J. S. 1983, ApJ, 265, 148

Scoville, N. Z., Yun, M. S., & Bryant, P. M. 1997, ApJ, 484, 702

Shimajiri, Y., Sakai, T., Tsukagoshi, T., et al. 2013, ApJ, 774, L20

Spinoglio, L., Pereira-Santaella, M., Busquet, G., et al. 2012, ApJ, 758, 108

Stanford, S. A., Sargent, A. I., Sanders, D. B., & Scoville, N. Z. 1990, ApJ, 349, 492

Tielens, A. G. G. M. 2005, The Physics and Chemistry of the Interstellar Medium

Tielens, A. G. G. M., & Hollenbach, D. 1985, ApJ, 291, 722

Tikhonov, N. A., Galazutdinova, O. A., & Tikhonov, E. N. 2009, Astronomy Letters, 35, 599

Tran, H. D. 2001, ApJ, 554, L19

van der Tak, F. F. S., Black, J. H., Schöier, F. L., Jansen, D. J., & van Dishoeck, E. F. 2007, A&A, 468, 627

Vlahakis, C., van der Werf, P., Israel, F. P., & Tilanus, R. P. J. 2013, MNRAS, 433, 1837

Ward, J. S., Zmuidzinas, J., Harris, A. I., & Isaak, K. G. 2003, ApJ, 587, 171

Wilson, C. D., Warren, B. E., Israel, F. P., et al. 2012, MNRAS, 424, 3050

Wolfire, M. G., Hollenbach, D., & McKee, C. F. 2010, ApJ, 716, 1191

Wu, R., Polehampton, E. T., Etxaluze, M., et al. 2013, A&A, 556, A116

Wu, R., Madden, S. C., Galliano, F., et al. 2015, A&A, 575, A88

Yun, M. S., Ho, P. T. P., & Lo, K. Y. 1993, ApJ, 411, L17

Zaritsky, D., Rix, H.-W., & Rieke, M. 1993, Nature, 364, 313

3.7 Appendix: Single-component fit

We fit a single-component to the 7 detected CO transitions ($J = 1-0$ to $J = 7-6$), and both [CI] transitions, setting the CO $J = 8-7$ transition as an upper limit, in the nucleus, centre and arm/inter-arm regions of M51, along with all 3 regions combined. We show the calculated fluxes from the 4DMax solution compared to the measured fluxes in Figure 3.12. We report the mean, 1DMax, and 4DMax for each of the physical parameters in Table 3.9, along with the 1σ ranges for each parameter.

For all of the modelled regions, our single-component fits suggests that the CO emission is dominated by warm ($\sim 100-300\,\mathrm{K}$), relatively diffuse ($\lesssim 10^{2.4}-10^{2.8}\,\mathrm{cm}^{-3}$) molecular gas. While diffuse, CO emitting molecular gas has been observed within the Milky Way (e.g. see Pety et al. 2008 and Liszt et al. 2009), most of the star-forming molecular gas is much colder than 200 K. Furthermore, GMC scale observations of CO $J = 1-0$ in M51 by Hughes et al. (2013b) find that the CO peak brightness temperature ranges from $T_{mb} = 1-10\,\mathrm{K}$ on spatial scales of $\sim 50\,\mathrm{pc}$ ($\sim 1''$). Assuming the CO emission fills the beam, the CO peak brightness temperature corresponds to the molecular gas temperature. If the molecular gas were at a temperature of $\sim 200\,\mathrm{K}$, as recovered in our single-component model, only $\sim 0.5-5\%$ of the $1''$ beam would be filled. Given the typical size scale of GMCs ($10-100\,\mathrm{pc}$), our single-component model does not appear likely to accurately represent the bulk of the molecular gas in M51.

Table 3.9 Single Component RADEX results

	4DMax (1σ range)				
Parameter	Nucleus	Centre	Arm/inter-arm	All	Units
T_{kin}	234 (162 – 320)	141 (112 – 256)	104 (90 – 236)	141 (110 – 277)	[K]
$\mathrm{Log}(n(\mathrm{H_2}))$	2.37 (2.36 – 2.74)	2.54 (2.41 – 2.82)	2.46 (2.38 – 2.84)	2.54 (2.36 – 2.82)	$[\mathrm{Log(cm^{-3})}]$
$\mathrm{Log}(N_{\mathrm{CO}})$	18.68 (17.85 – 18.64)	18.70 (17.69 – 18.67)	18.74 (17.05 – 18.53)	18.56 (17.36 – 18.57)	$[\mathrm{Log(cm^{-2})}]$
$\mathrm{Log}(\Phi_A)$	-1.57 (-1.72 – -1.26)	-1.64 (-1.74 – -1.18)	-1.71 (-1.76 – -0.82)	-1.64 (-1.74 – -0.99)	[...]
$\mathrm{Log}(< N_{\mathrm{CO}} >)$	16.92 (16.57 – 17.02)	17.00 (16.49 – 17.01)	16.31 (16.21 – 16.83)	16.51 (16.35 – 16.91)	$[\mathrm{Log(cm^{-2})}]$
$\mathrm{Log}(P)$	5.09 (4.71 – 5.13)	5.09 (4.61 – 5.08)	4.96 (4.52 – 5.01)	5.09 (4.58 – 5.08)	$[\mathrm{Log(K\ cm^{-2})}]$

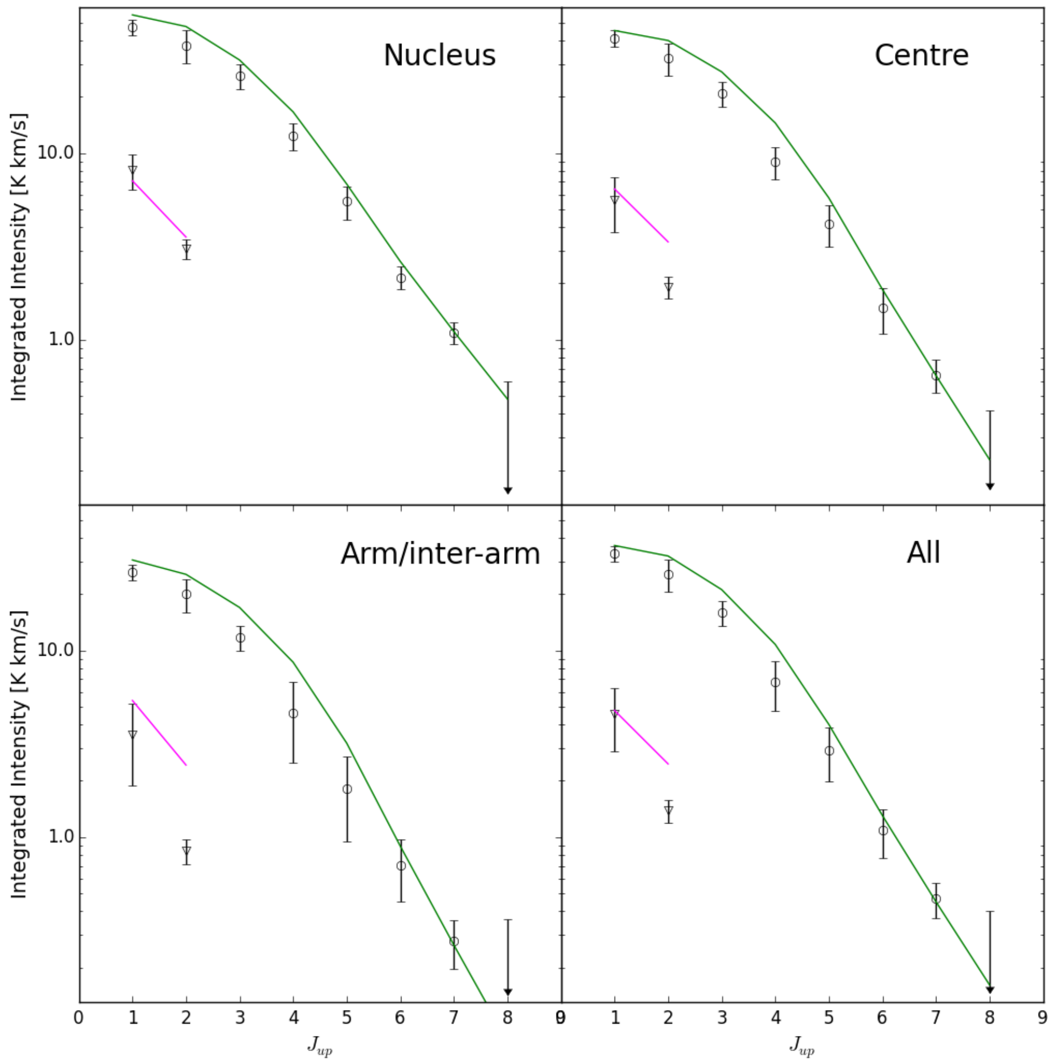

Figure 3.12 Measured and calculated spectral line energy distributions for the single component fit for the nucleus (top-left), centre (top-right), and arm/inter-arm (bottom-left) regions, and for all the regions combined (bottom right). The measured fluxes are shown by black circles (CO) and triangles ([CI]), while the calculated fluxes are shown by the green (CO) and magenta ([CI]) solid lines.

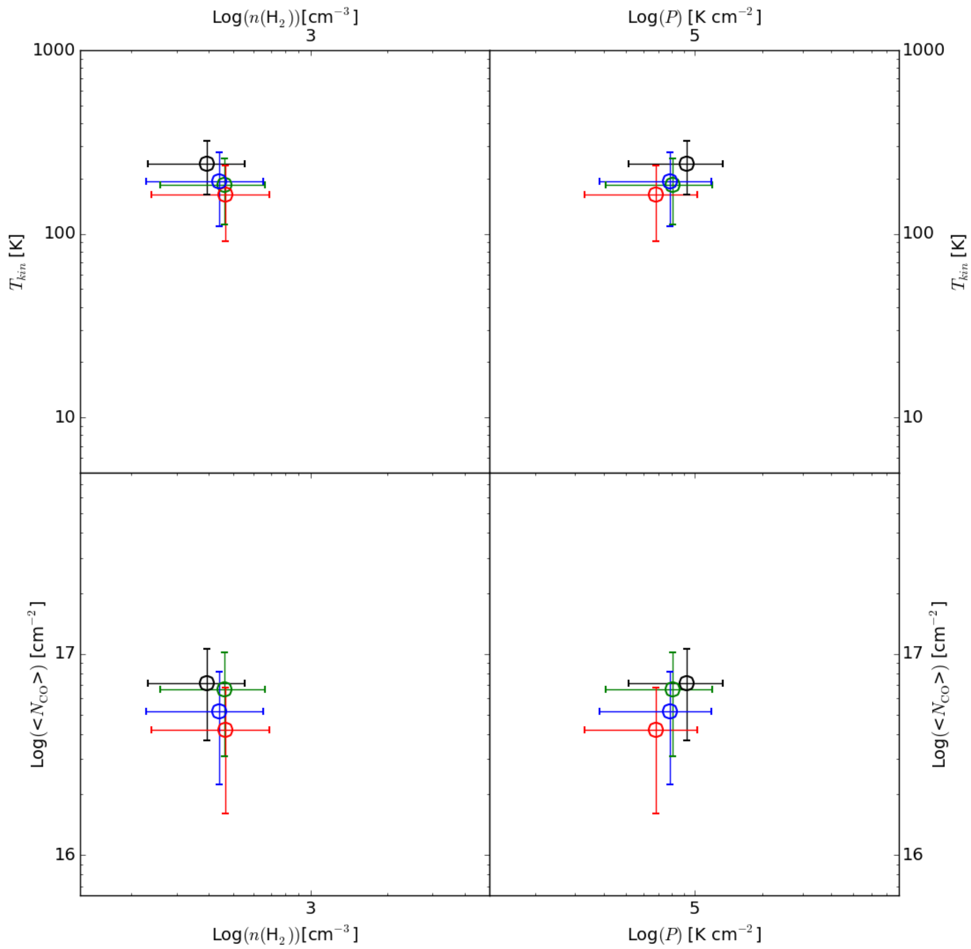

Figure 3.13 Derived physical parameters for the single-component RADEX model for the nucleus (*black*), centre (*green*), and arm/inter-arm (*blue*) regions of M51, and for all the regions combined (*red*, see Figure 3.4 and Section 3.7 for more details). Both CO and [CI] are modelled. The error bars correspond to the 1σ range of the combined likelihood distribution of each region for the kinetic temperature (*top row*), beam-averaged column density (*bottom row*), molecular gas density (*left column*), and pressure (*right column*).

Chapter 4

The dense gas in the largest molecular complexes of the Antennae (NGC 4038/39): HCN and HCO^+ observations of NGC 4038/39 using ALMA

Maximilien R.P. Schirm, Christine D. Wilson

Prepared for submission to The Astrophysical Journal.

"Voici mon secret. Il est très simple: on ne voit bien qu'avec le coeur. L'essentiel est invisible pour les yeux."

Le Petit Prince Antoine de Saint Exupéry (1943)

Abstract

We present observations of the dense molecular gas tracers HCN, HNC, and HCO^+ in the $J = 1-0$ transition using ALMA. These are the first ever detection of HNC and HCO^+ in the Antennae, while this is the first interferometric detections of HNC outside of the nucleus of NGC 4038. We supplement our datasets with previous observations of CO $J = 1-0$, which traces the total molecular gas content. We separate the Antennae into 7 bright regions in which we detect emission from all three molecules, including the nucleus of NGC 4038 and the nucleus of NGC 4039, 5 super giant molecular complexes in the overlap region and 2 additional bright clouds, and calculate the total emission along with line ratios of our molecular gas tracers. We find that the ratio of $L_{\rm HCN}/L_{\rm CO}$, which traces the dense molecular gas fraction, is greater in the two nuclei ($L_{\rm HCN}/L_{\rm CO}\sim 0.07-0.08$) than in the overlap region ($L_{\rm HCN}/L_{\rm CO}< 0.05$). We attribute this to an increase in pressure due to the stellar potential within the nuclei, similar to what has been seen previously in the Milky Way and nearby spiral galaxies. Furthermore, the ratio of $L_{\rm HNC}/L_{\rm HCN}\sim 0.3-0.4$ and does not vary by more than a factor of 1.5 between regions. By comparing our measured ratios to PDR models including mechanical heating, we find that the ratio of $L_{\rm HNC}/L_{\rm HCN}$ is consistent with mechanical heating contributing $\gtrsim 5\% - 10\%$ of the PDR surface heating to the total heating budget, where values $> 10\%$ indicate a molecular gas temperature $> 100\,$K. Finally, the ratio of $L_{\rm HCN}/L_{\rm HCO+}$ varies from ~ 1 in the nucleus of NGC 4038 down to ~ 0.5 in the overlap region. The lower ratio in

the overlap region is likely due to an increase in the cosmic ray rate, in turn driven by the increased supernova rate within this region.

4.1 Introduction

Merging and interacting galaxies play a fundamental role in the hierarchical evolution of galaxies (e.g. Steinmetz & Navarro 2002). In a major merger, the turbulent motion generated by the gravitational interaction between the two merging galaxies can lead to a significant increase in the star formation rate, usually in the form of starbursts (e.g. see Hopkins et al. 2006 and references therein). For the most extreme mergers, this enhancement can culminate in an ultra luminous infrared galaxy (URLIG, $L_{IR} > 10^{12}$, Sanders & Mirabel 1996). In fact, it has been shown that most, if not all, ULIRGs are the direct result of an ongoing merger (Sanders et al., 1988; Sanders & Mirabel, 1996; Clements et al., 1996).

In the nearby universe, the closest example of a major merger is the Antennae (NGC 4038/39, Arp 244), with the two progenitor galaxies, NGC 4038 and NGC 4039, still in a relatively early merger stage. Within this system, the region where the two initial gas disks are believed to overlap has been dubbed the "overlap region" (Stanford et al., 1990), while it has also been referred to as the "interaction region" (Schulz et al., 2007). Young, massive ($> 10^6 M_\odot$), compact "super star clusters" (SSCs) are found throughout the overlap region (Whitmore et al., 1999, 2010). The overlap region also plays host to 5 super giant molecular complexes (SGMCs, Wilson et al. 2000), massive ($> 10^8 M_\odot$) associations of molecular gas within which current and future star formation is expected.

The molecular gas in the Antennae has been studied predominantly using the molecular gas tracer CO, which is excited via collisions with H_2. The total molecular gas content within the Antennae, assuming a Milky Way-like CO-to-H_2 conversion factor, is $\sim 2{\times}10^{10}\,\mathrm{M}_\odot$ (Gao et al., 2001). Interferometric observations of CO $J = 1-0$ show the presence of 100 giant molecular associations (GMAs) throughout the system with a mass range $\sim 10^7-10^9 M_\odot$(Wilson et al., 2003). More recently, Schirm et al. (2014) analyzed observations of CO $J = 1-0$ to $J = 8-7$ using a non-local thermodynamic equilibrium (non-LTE) radiative transfer analysis. They found that most of the molecular gas in the system is cool ($T_{kin} \sim 10-30\,\mathrm{K}$) and intermediately dense ($n(\mathrm{H_2}) \sim 10^3 - 10^4\,\mathrm{cm^{-3}}$), while a small fraction ($\sim 0.3\%$) of the molecular gas is in a warm ($T_{kin} \gtrsim 100\,\mathrm{K}$), dense ($n(\mathrm{H_2}) \gtrsim 10^4\,\mathrm{cm^{-3}}$) phase.

Recently, Herrera et al. (2012) combined high-resolution Atacama Large Millimeter/submillimeter Array (ALMA) science verification observations of CO $J = 3-2$ in the Antennae with VLT/SINFONI imaging of the $\mathrm{H_2}\ 1-0\,\mathrm{S}(1)$ transition, while Whitmore et al. (2014) obtained ALMA cycle-0 observations of the overlap region in CO $J = 3-2$. By combining their data with observations from the Hubble Space Telescope (HST), and the Very Large Array (VLA), Whitmore et al. (2014) identify regions within the overlap region corresponding to the various stages of star formation, from diffuse giant molecular clouds (GMCs) all the way to intermediate and old stellar clusters. Of particular interest is the very bright CO $J = 3-2$ emission found within SGMC 2, which Whitmore et al. (2014) dubbed the “firecracker” and which is believed to be the precursor to a SSC. In addition, strong $\mathrm{H_2}\ 1-0\,\mathrm{S}(1)$ emission is associated with the bright CO $J = 3-2$ emission (Herrera et al., 2012). The mass and energetics of the cloud suggest a very high pressure ($P/k_B \gtrsim 10^8$ K cm^{-3}), while a lack of thermal radio emission indicates no star formation has yet occurred (Johnson et al., 2015).

While CO is the most commonly used tracer of molecular gas, due to its brightness and relatively high abundance in giant molecular clouds (GMCs), it may not be the ideal tracer for the star forming molecular gas. Often, the CO emission is converted to a molecular gas mass using the CO-to-H_2 conversion factor ($X_{\rm CO}$) or $\alpha_{\rm CO}$, also known as the "X" factor (for a review on the conversion factor, see Bolatto et al. 2013). However, the value of $X_{\rm CO}$ is highly uncertain, varying from $X_{\rm CO} = 2 \times 10^{20}\,{\rm cm}^{-2}({\rm K\ km\ s}^{-1})^{-1}$ in the Milky Way and other "normal" galaxies, down to $X_{\rm CO} \sim 0.4 \times 10^{20}\,{\rm cm}^{-2}({\rm K\ km\ s}^{-1})^{-1}$ in ultra luminous infrared galaxies.

Recent observations of the nearby spiral galaxy M51 found that $\sim 50\%$ of the CO $J = 1-0$ emission arises from an extended, inert component of molecular gas (Pety et al., 2013); this molecular gas is found at high latitudes above the galactic disk and is not directly related to the ongoing star formation. Instead, this gas is likely the by-product of star formation, having been ejected into a thick disk via galactic fountains or chimneys. Furthermore, it has been suggested that "CO-dark" gas, molecular gas which does not emit CO, may make up a significant fraction of molecular gas (e.g. see Wolfire et al. 2010). This "CO-dark" gas resides near the surfaces of photon dominated regions (PDRs), in the surface layers where CO is dissociated. This in turn can alter the value of $X_{\rm CO}$.

Dense gas tracers, such as HCN (Gao & Solomon, 2004a,b; Papadopoulos, 2007), HNC (Talbi et al., 1996), and HCO^+ (Graciá-Carpio et al., 2006), can be used to study the dense molecular gas most directly linked to star formation. This relation culminates in the form of a tight relationship between the luminosity of HCN ($L_{\rm HCN}$) and the infrared (IR) luminosity (L_{IR}), tighter than the correlation between CO and the infrared luminosity (Liu & Gao, 2010). In fact, this relationship holds in the form of a constant ratio of $L_{\rm HCN}/L_{IR}$ from individual giant molecular clouds (GMCs) all the way up to luminous infrared galaxies (LIRGs) (Wu et al., 2005). The critical densities of HCN, HNC, and HCO^+ are all $n_{cr} > 10^5\,{\rm cm}^{-3}$ for the $J = 1-0$ transition (Loenen et al., 2007), significantly higher than CO $J = 1-0$ ($n_{cr} \sim 3 \times 10^3\,\mathrm{cm}^{-3}$, Loenen et al. 2007).

Because HCN, HNC, and HCO^+ in the $J = 1-0$ transition all have similar critical densities ($n_{cr} > 10^5\,\mathrm{cm}^{-3}$, Loenen et al. 2007), the relative strengths of the lines of these molecules are driven largely by ongoing physical processes. Infrared (IR) pumping can enhance HCN emission in a system with a strong background mid-IR field (Sakamoto et al., 2010), while HCO^+ can be destroyed via dissociative recombination in the presence of a significant abundance of electrons. HCN and HNC are isotopomers, and their relative abundance is driven by the temperature of the dense molecular gas (Talbi et al., 1996). Furthermore, line ratios of these molecules can be used as a diagnostic for cosmic rays (Meijerink et al., 2011), photon dominated regions (PDRs, Kazandjian et al. 2012), and mechanical heating (Loenen et al., 2008; Kazandjian et al., 2012). As such, these tracers serve as a mechanism by which to study both the distribution and amount of dense molecular gas within a system, and also the physical processes affecting this gas.

In this paper, we present observations of the $J = 1-0$ transition of HCN, HNC, and HCO^+ in the Antennae using ALMA Band 3. We adopt a distance to NGC 4038/39 of $D = 22\,\mathrm{Mpc}$ (Schweizer et al., 2008), corresponding to an angular scale of $107\,\mathrm{pc}/''$. These are the first detections of HNC and HCO^+ $J = 1-0$ at any location in the Antennae, and the first detections of HCN $J = 1-0$ outside the nucleus of NGC 4038. We combine these observations with previous observations of CO $J = 1-0$ from Wilson et al. (2000, 2003). In this work, we detail the observations and data reduction in Section 4.2, while we discuss separating the emission into the brightest regions in Section 4.3. We present various line ratios of HCN, HNC, HCO^+, and CO in Section 4.4, and we discuss the implications of the measured line ratios in Section 4.5.

4.2 Observations

NGC 4038 was observed in two pointings over the course of 2 nights each in March, 2013 and April, 2014 as part of ALMA Cycle-1. One pointing was positioned to cover the nucleus of NGC 4038 and the western loop (12 h01 m51.7763 s, $-18°52'02.892''$), while the other was positioned to cover both the overlap region and the nucleus of NGC 4039 (12 h01 m54.5945 s, $-18°52'50.891''$), with a total on-source integration time of 20356 seconds. The antenna array configuration was C32-4. The bandpass calibrators used were J1256-0547, J1246-2547, and J1130-1449, while J1215-1731 was used as the phase calibrator and Titan was used as the amplitude calibrator throughout.

Band 3 was used, with one spectral window set to observed both HCN and HCO^+ simultaneously. A second spectral window was aligned to search for HNC emission throughout the Antennae. The total usable bandwidth for each of these spectral windows was 1875 MHz with a channel spacing of 0.488 MHz. The two remaining spectral windows were centred at 101.0 GHz and 102.875 GHz to observe the continuum emission across the Antennae. The bandwidth of the two continuum windows was 2000 MHz with a channel spacing of 15.625 MHz.

We reduce these data using the Common Astronomy Software Applications package version 4.2. We start by running the script provided to the PI as part of the data delivery in order to calibrate the *uv*-datasets before splitting out the target from the calibrated dataset. We further split out the spectral window which contains the HCN and HCO^+ lines, and the spectral window which contains the HNC line. We subtract the background continuum emission by fitting a first order polynomial to the line-free channels of each spectral window using the `uvcontsub` task.

We create dirty data-cubes for each of the HCN, HCO^+, and HNC

$J = 1-0$ transitions with a channel width of $5\,\mathrm{km\ s^{-1}}$ and cell size of $0.3''$. The restoring beams of the cleaned data cubes when using Briggs weighting with robust = 0.5 are $1.85'' \times 1.51'', -79.2^{\circ}$ for the HCO^+ line, $1.86'' \times 1.52'', -79.8^{\circ}$ for the HCN line, and $1.83'' \times 1.44'', -79.8^{\circ}$ for the HNC line. We set the restoring beam for the HCN and HCO^+ transitions to the HCN beam and create clean data-cubes, while the HNC emission was too weak at the native ALMA resolution. We place clean boxes around $> 5\sigma$ emission in the dirty data-cubes, being careful not to select artifacts. We clean down to a threshold of $1.1\,\mathrm{mJy\ beam^{-1}}$, corresponding to 2σ in all three dirty data cubes as measured in the line-free channels ($\sigma = 0.55\,\mathrm{mJy\ beam^{-1}}$).

In addition, we create dirty and clean data cubes to match the beam of the CO $J = 1-0$ data cube from Wilson et al. (2000, 2003). We set the uv-taper on the outer baselines to $5.0'' \times 2.0'', 1.45^{\circ}$ for both HCN, HCO^+, and HNC with a restoring beam of $4.91'' \times 3.15'', 1.45^{\circ}$. We use the same channel width and cell size as before, and draw clean boxes around 5σ emission. We clean down to a threshold of $1.6\,\mathrm{mJy\ beam^{-1}}$, corresponding to 2σ of the tapered dirty data cubes ($\sigma = 0.8\,\mathrm{mJy\ beam^{-1}}$).

We create moment maps for all of our clean HCN and HCO^+ data cubes, including emission above 2σ. The un-tapered moment 0 maps are shown in Figure 4.1, while the tapered moment 0 maps are shown in Figure 4.2, along with the CO $J = 1-0$ moment 0 map from Wilson et al. (2000, 2003). Finally, we correct all of our HCN, HCO^+, and HNC moment-0 maps for the primary beam. The largest correction occurs in the nucleus of NGC 4039, where the primary beam correction is on the order of $\sim 0.6 - 0.7$ for both the native ALMA resolution maps and the CO $J = 1-0$ resolution maps. The CO $J = 1-0$ map from Wilson et al. (2003) has already been corrected for the primary beam.

Gao et al. (2001) observed the Antennae in HCN $J = 1-0$ in two pointings: one centered on the nucleus of NGC 4038, and the other on the brightest CO emission from the overlap region. The full-width half-maximum of their beam was $\sim 72''$, and their two pointings include both nuclei and the overlap region. They calculate a total HCN $J = 1 - 0$ luminosity of 0.8×10^8 K km s^{-1} pc^2 (adjusted to our adopted distance of 22 Mpc). Conversely, we measure a total of HCN $J = 1 - 0$ luminosity of $\sim 0.7 \times 10^8$ K km s^{-1} pc^2 in our ALMA maps. Our detected HCN emission is well within their two beams, and we do not expect significant HCN emission outside of our observed region. As such. this comparison suggests that we recover $\sim 90\%$ of the total HCN emission in our ALMA observations.

We estimate the uncertainties in our moment maps by first determining the number of channels included in each pixel of the moment map (N_{chan}). We calculate the uncertainty in each pixel as $\sqrt{N_{chan}}\sigma\Delta v$, where σ is the root-mean squared uncertainty measured from our line-free channels of our data cubes and is the same for each pixel. $\Delta v = 5$ km/s is the channel width. Furthermore, when comparing our dense gas tracers to our CO $J = 1 - 0$ map, we add a 5% calibration uncertainty[1]. The calibration uncertainty of the CO $J = 1 - 0$ map is 20% (Wilson et al., 2003).

4.3 The brightest regions in the Antennae

In this paper, we will focus on the HCN, HNC, and HCO^+ emission from the brightest regions in the Antennae. A full catalogue of clouds in both HCN, HNC, and HCO^+ will be published in a future paper, along with a cloud-by-cloud analysis of the emission.

Wilson et al. (2000) identified and isolated the 7 brightest regions in their CO $J = 1 - 0$ map of the Antennae at a resolution of $4.91'' \times 3.15''$ using

[1] ALMA Cycle 1 Technical Handbook. Available at `https://almascience.nrao.edu/documents-and-tools/cycle-1/alma-technical-handbook`

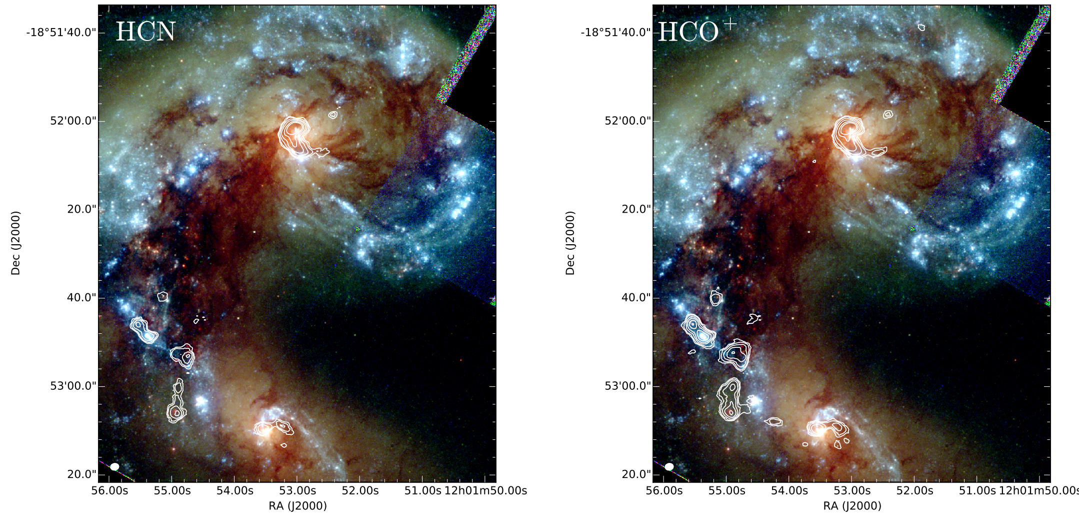

Figure 4.1 HCN (*left*) and HCO$^+$ (*right*) moment-0 contours overlaid on the same HST image of the Antennae. The contours shown have not been corrected for the primary beam. The HST image was created using data from Whitmore et al. (1999). The HCN and HCO$^+$ contours, shown in white, correspond to $(3, 5, 9, 15, 25, 35) \times (2.8 \times 10^{-2}$ Jy beam^{-1} km s$^{-1})$. The beam of the dense gas tracer observations is shown by a white ellipse in the lower left corner.

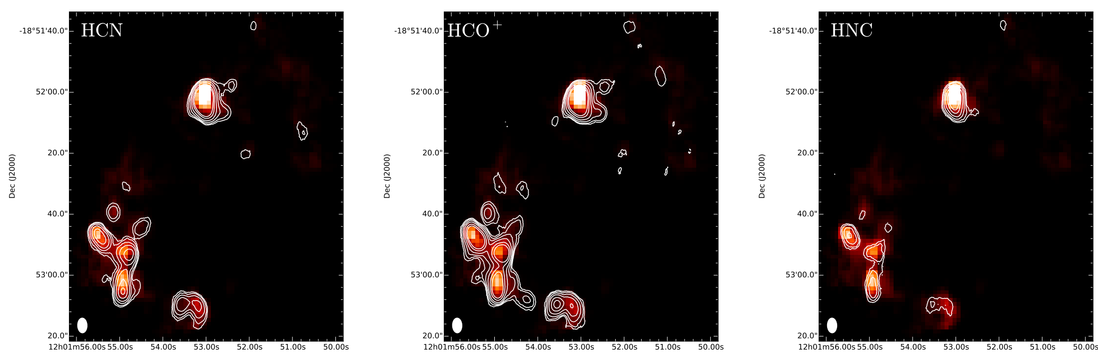

Figure 4.2 HCN (*left*), HCO$^+$ (*middle*), and HNC (*right*) moment-0 contours beam-matched to the CO $J = 1-0$ observations from Wilson et al. (2003) overlaid on the same CO $J = 1-0$ moment-0 map. The contours correspond to $(3, 5, 9, 15, 25, 35) \times (3.6 \times 10^{-2}$ Jy beam^{-1} km s$^{-1})$. The beam is shown by the white ellipse in the lower left corner of each image.

the clump identification algorithm CLFIND (Williams et al., 1994). These regions include both nuclei (NGC 4038 and NGC 4039), and 5 large clouds in the overlap region, dubbed Super Giant Molecular Complexes (SGMCs). In addition to these 7 regions, we identify two additional bright regions, C6 and C7. These clouds correspond to clouds 16, 17 and 18 (C6), and clouds 67 and 74 (C7) in the CO cloud catalogue published in Wilson et al. (2003).

We place elliptical apertures around each of the 9 brightest regions to measure the total HCN, HNC, HCO^+, and CO fluxes (S_{mol}, Table 4.1) in the moment-0 map for the $J = 1 - 0$ transition for each molecule (Figure 4.3). It is important to note that the total fluxes and total luminosities are measured at the CO $J = 1 - 0$ resolution for all 4 molecules, with the exception of the pre-super star cluster (see Section 4.3.1)

For the 5 SGMC regions, we are unable to distinguish between SGMC 3, 4 and 5 in the moment-0 map and so we combine these three SGMCs into SGMC 3+4+5. We can, however, distinguish between them in velocity-space. Using the measured local standard of rest velocity (V_{lsr}) along with the velocity width (ΔV_{FWHM}) from Wilson et al. (2000) for these three clouds, we create moment-0 maps for the velocity range spanned by each SGMC. We measure the flux and luminosity for each cloud in their own moment-0 map using the same aperture as used for SGMC 3+4+5. It is important to note that there are 2 channels of overlap in the velocity ranges for SGMC 3 and 4 as measured by Wilson et al. (2000). As such, we separate the two SGMCs by including one channel in each of the moment maps of SGMC 3 and 4.

4.3.1 A precursor to a super star cluster

Johnson et al. (2015) identified a small region in SGMC2 in their ALMA CO $J = 3 - 2$ map of the overlap region which they believe to be the precursor to a super star cluster, which we have dubbed "pre-SSC" in this work. The resolution of their CO $J = 3 - 2$ map is considerably better than that of our observations (beam size = $0.56'' \times 0.43''$), while the size of pre-SSC as measured using the CPROPS program (Rosolowsky & Leroy, 2006) is $\sim 0.66'' \times 0.55''$, less than the size of the beam of our HCN and HCO^+ observations.

As with SGMCs 3, 4 and 5, we create a moment-0 map around pre-SSC using the velocity range measured by Johnson et al. (2015). Using this map, we measure the HCN and HCO^+ fluxes of the pre-SSC at the location of the pre-SSC (Table 4.1), as the size of the pre-SSC is less than the size of our beam. We do not measure the emission in the CO $J = 1-0$ map from Wilson et al. (2000, 2003) as the beam of that map is comparable to the size of SGMC2 and as such we would be unable to distinguish between emission from SGMC2 and emission from the pre-SSC.

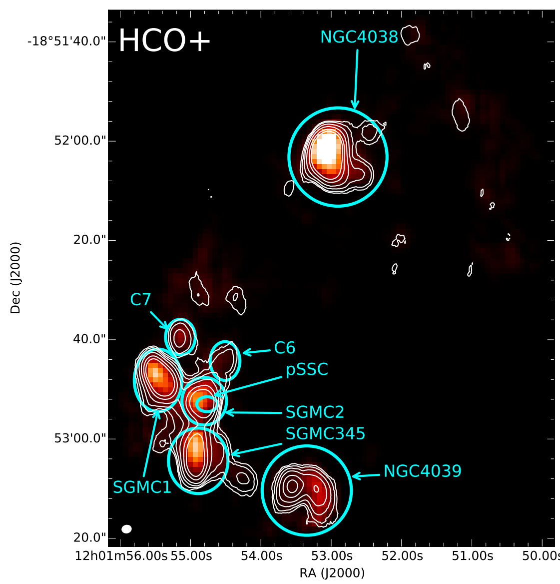

Figure 4.3 Map of the brightest regions in the Antennae. The background image is the CO $J = 1-0$ map from Wilson et al. (2000) while the HCO^+ $J = 1-0$ contours from Figure 4.2 are overlaid. The cyan ellipses indicate the location of the two nuclei, the 5 SGMCs and the two additional clouds, C6 and C7, along with the pre-super star cluster "pSSC".

4.4 Line Ratios

In this section, we calculate various line ratios of HCN, HNC, HCO^+, and CO.

Table 4.1. Measured flux densities of the molecular gas tracers

Region ID	S_{HCN}[a] (Jy km s^{-1})	S_{HCO^+}[a] (Jy km s^{-1})	S_{HNC}[a] (Jy km s^{-1})	S_{CO}[b] (Jy km s^{-1})
NGC 4038	14.32 ± 0.08	14.23 ± 0.08	5.58 ± 0.06	290 ± 5
NGC 4039	4.03 ± 0.08	6.51 ± 0.09	1.06 ± 0.05	100 ± 5
SGMC 1	2.59 ± 0.05	6.63 ± 0.06	1.01 ± 0.04	117 ± 2
SGMC 2	2.12 ± 0.04	4.50 ± 0.05	0.59 ± 0.03	92 ± 2
pre-SSC[c]	0.28 ± 0.01	0.45 ± 0.01	–	52 ± 5[d]
SGMC 3	0.69 ± 0.03	1.82 ± 0.03	0.25 ± 0.02	61 ± 2
SGMC 4	1.32 ± 0.03	3.03 ± 0.04	0.46 ± 0.02	67 ± 3
SGMC 5	0.94 ± 0.03	1.35 ± 0.03	0.30 ± 0.02	30 ± 2
SGMC 3+4+5	3.34 ± 0.06	6.18 ± 0.06	1.10 ± 0.04	128 ± 3
C6	0.40 ± 0.02	0.45 ± 0.02	0.14 ± 0.01	15 ± 1
C7	0.34 ± 0.02	0.53 ± 0.02	0.13 ± 0.01	22.5 ± 0.8

Note. — The reported uncertainties are the measurement uncertainties. To convert into luminosity with units of K km s^{-1} pc^2, multiply fluxes by $1.5666 \times 10^{10} (\nu_0/\mathrm{GHz})^{-2}$. See text for additional details.

4.4.1 Molecular line ratios for the brightest regions in the Antennae

4.4.1.1 Ratios of the dense gas tracers

We calculate the ratios of the luminosities of the dense gas tracers HCN, HNC, and HCO^+ for the brightest regions in the Antennae (see Section 4.3). We use the fluxes we measure in Table 4.1 at the OVRO beam size, and convert them to luminosities using the following formula (Wilson et al., 2008)

$$\frac{L'}{\mathrm{K\ km\ s^{-1}\ pc^2}} = 3.2546 \times 10^7 \left(\frac{S_{\mathrm{mol}}}{\mathrm{Jy\ km\ s^{-1}}}\right) \left(\frac{D_L}{\mathrm{Mpc}}\right)^2$$

$$\times \left(\frac{\nu_0}{\mathrm{GHz}}\right)^{-2} (1+z)^{-1} \quad (4.1)$$

where S_{mol} is the flux, $D_L = 22\,\mathrm{Mpc}$ is the distance, ν_0 is the rest frequency of the transition, and $z = 0.005477$ is the redshift. We show these ratios of $L_{\mathrm{HNC}}/L_{\mathrm{HCN}}$, $L_{\mathrm{HNC}}/L_{\mathrm{HCO+}}$, and $L_{\mathrm{HCN}}/L_{\mathrm{HCO+}}$in Table 4.2 and we plot the ratios of $L_{\mathrm{HNC}}/L_{\mathrm{HCO+}}$ and $L_{\mathrm{HCN}}/L_{\mathrm{HCO+}}$ in Figure 4.4.

For the nucleus of NGC 4038, the values of $L_{\mathrm{HCN}}/L_{\mathrm{HCO+}}$ and $L_{\mathrm{HNC}}/L_{\mathrm{HCO+}}$ are more than a factor of 1.5 greater than every other region, with the exception of C6. Of the remaining regions, SGMCs 1, 2, 3 and 4 exhibit similar values for both the ratio of $L_{\mathrm{HCN}}/L_{\mathrm{HCO+}}$ ($\sim 0.39 - 0.48$) and the ratio of $L_{\mathrm{HNC}}/L_{\mathrm{HCO+}}$ ($\sim 0.13 - 0.15$), suggesting similar heating mechanisms and dense gas properties across the 5 regions. The nucleus of NGC 4039 exhibits slightly larger values for both ($L_{\mathrm{HCN}}/L_{\mathrm{HCO+}}\sim 0.63$, $L_{\mathrm{HNC}}/L_{\mathrm{HCO+}}\sim 0.16$). Of the SGMCs, SGMC 5 exhibits the largest value for both line ratios ($L_{\mathrm{HCN}}/L_{\mathrm{HCO+}}\sim 0.7$, $L_{\mathrm{HNC}}/L_{\mathrm{HCO+}}\sim 0.22$).

The value of $L_{\mathrm{HNC}}/L_{\mathrm{HCN}}$ varies by less than a factor of 1.5 across all 10 regions. The largest deviations occurs for the nucleus of NGC 4039 and SGMC 2, with $L_{\mathrm{HNC}}/L_{\mathrm{HCN}}= 0.25$ and $L_{\mathrm{HNC}}/L_{\mathrm{HCN}}= 0.27$ respectively. Of the remaining 8 regions, $L_{\mathrm{HNC}}/L_{\mathrm{HCN}}$ is nearly constant, varying by only $\sim 20\%$ ($L_{\mathrm{HNC}}/L_{\mathrm{HCN}}\sim 0.31 - 0.38$).

4.4.1.2 Ratios to CO

The ratio of the detected dense gas tracers to the total CO luminosity is an indicator of the fraction of the dense molecular gas within the different regions in the Antennae. We calculate this ratio for all three dense gas tracers relative to CO (Table 4.3), and plot the ratio of $L_{\mathrm{HCN}}/L_{\mathrm{CO}}$ and $L_{\mathrm{HCO+}}/L_{\mathrm{CO}}$ in Figure 4.5.

The ratio of $L_{\mathrm{HCN}}/L_{\mathrm{CO}}$ varies by more than a factor of 4, with the two

Table 4.2. Luminosity ratios for the dense gas tracers for the brightest regions in the Antennae

Region ID	$L_{\mathrm{HCN}}/L_{\mathrm{HCO+}}$	$L_{\mathrm{HNC}}/L_{\mathrm{HCO+}}$	$L_{\mathrm{HNC}}/L_{\mathrm{HCN}}$
NGC 4038	1.019 ± 0.008	0.384 ± 0.005	0.377 ± 0.005
NGC 4039	0.63 ± 0.02	0.160 ± 0.008	0.25 ± 0.01
SGMC 1	0.396 ± 0.008	0.149 ± 0.006	0.38 ± 0.02
SGMC 2	0.48 ± 0.01	0.128 ± 0.006	0.27 ± 0.01
SGMC 3	0.39 ± 0.02	0.132 ± 0.010	0.34 ± 0.03
SGMC 4	0.44 ± 0.01	0.149 ± 0.008	0.34 ± 0.02
SGMC 5	0.70 ± 0.03	0.22 ± 0.02	0.31 ± 0.02
SGMC 3+4+5	0.55 ± 0.01	0.173 ± 0.006	0.32 ± 0.01
C6	0.90 ± 0.07	0.29 ± 0.03	0.33 ± 0.04
C7	0.65 ± 0.05	0.24 ± 0.03	0.36 ± 0.04

nuclei exhibiting larger values than the other regions in the Antennae. The smallest values are seen in SGMC 3 and C7, while the remaining 6 regions have values ~ 0.04. The ratio of $L_{\mathrm{HCO+}}/L_{\mathrm{CO}}$, on the other hand, varies by a factor of ~ 2.5. Once again, SGMC 3 and C7, along with C6, show the smallest values of $L_{\mathrm{HCO+}}/L_{\mathrm{CO}}$ ($\sim 0.04 - 0.05$), while the nucleus of NGC 4039 has the highest ratio of $L_{\mathrm{HCO+}}/L_{\mathrm{CO}}$ (~ 0.1). The remaining regions, including the nucleus of NGC 4038, all have a characteristic value of $L_{\mathrm{HCO+}}/L_{\mathrm{CO}}$ of ~ 0.08. It is important to note that there is a systematic uncertainty in both ratios of $\sim 21\%$ due to calibration uncertainties in both sets of observation.

4.4.2 The distribution of the HCN/HCO$^+$ line ratios

In this section, we discuss a pixel-by-pixel analysis of the $L_{\mathrm{HCN}}/L_{\mathrm{HCO+}}$ line ratio. We calculate the HCN/HCO$^+$ line ratio ($L_{\mathrm{HCN}}/L_{\mathrm{HCO+}}$) for the native resolution moment-0 maps by dividing the HCN moment-0 map by the HCO$^+$ moment-0 map (Figure 4.6). The difference between the primary beam correction for the HCN and HCO$^+$ moment-0 maps is minimal, and so we use the

Table 4.3. Luminosity ratios relative to CO for the brightest regions in the Antennae

Region ID	$L_{\rm HCN}/L_{\rm CO}$	$L_{\rm HCO+}/L_{\rm CO}$	$L_{\rm HNC}/L_{\rm CO}$
NGC 4038	0.083 ± 0.001	0.082 ± 0.001	0.0314 ± 0.0006
NGC 4039	0.068 ± 0.004	0.109 ± 0.006	0.017 ± 0.001
SGMC 1	0.0376 ± 0.0009	0.095 ± 0.002	0.0142 ± 0.0006
SGMC 2	0.039 ± 0.001	0.082 ± 0.002	0.0105 ± 0.0006
SGMC 3	0.019 ± 0.001	0.050 ± 0.002	0.0066 ± 0.0005
SGMC 4	0.033 ± 0.002	0.075 ± 0.003	0.0111 ± 0.0008
SGMC 5	0.053 ± 0.005	0.075 ± 0.006	0.016 ± 0.002
SGMC 3+4+5	0.044 ± 0.001	0.081 ± 0.002	0.0140 ± 0.0006
C6	0.047 ± 0.005	0.052 ± 0.005	0.015 ± 0.002
C7	0.026 ± 0.002	0.039 ± 0.002	0.009 ± 0.001

Note. — The reported uncertainties are measurement uncertainties only. The uncertainties in these line ratios are dominated by the calibration uncertainties. We add the calibration uncertainties from the two instruments in quadrature to obtain a total line ratio uncertainty of 21%. See text for additional details.

non-primary beam corrected maps. In addition, we include only pixels with a 3σ detection of both molecular transitions. As before, we separate the emission into the same regions as detailed in Section 4.3. We plot the distribution function for NGC 4038, NGC 4039, SGMC 1, SGMC 2, SGMC 3+4+5, C6 and C7 in the top of Figure 4.7, while we show the cumulative distribution functions in the bottom of Figure 4.7.

In addition, we use the moment maps created for SGMC 3, SGMC 4, SGMC 5 and pSSC to create $L_{\rm HCN}/L_{\rm HCO+}$ ratio maps for each of these regions. We plot the corresponding distribution functions, along with the distribution function for SGMC 3+4+5 in Figure 4.8.

We compare the distributions of line ratios between each region using

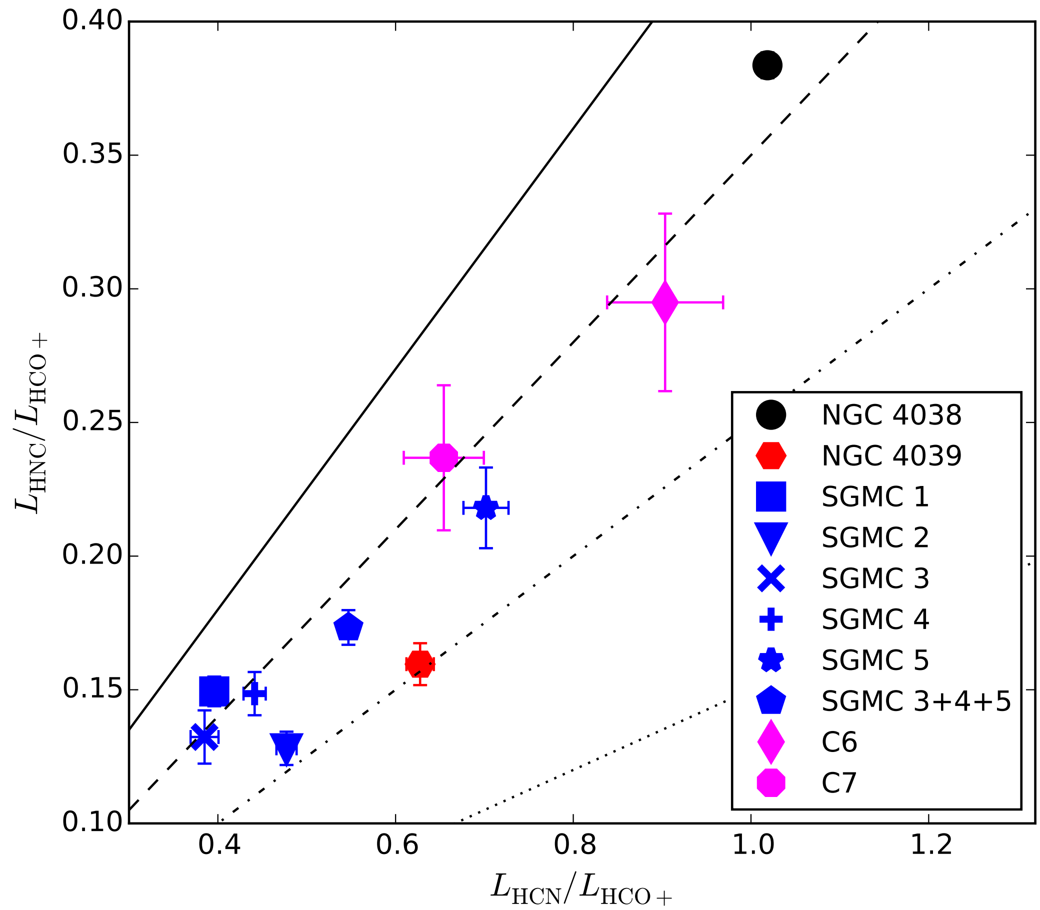

Figure 4.4 Luminosity ratios of the dense gas tracers for the brightest regions in the Antennae calculated at the CO $J = 1-0$ beam. The error bars correspond to measurement uncertainties in the line ratios. The lines correspond to lines of constant $L_{\rm HNC}/L_{\rm HCN}$, with $L_{\rm HNC}/L_{\rm HCN}$= 0.15 (dotted line), 0.25 (dash-dot line), 0.35 (dashed line) and 0.45 (solid line). The region SGMC 3+4+5 corresponds to the region in the moment-0 map spanned by SGMC 3, 4 and 5, while the values for SGMC 3, 4 and 5 were calculated from moment maps created based on the velocity range calculated in Wilson et al. (2000)

a K-sample Anderson-Darling (AD) test. The AD test is a modification of the Kolmogorov-Smirnov (KS) test, where for both tests the cumulative distribution function (CDF) of two samples are compared. In the KS test, the test statistic is calculated based upon the distance between the two CDFs. The AD test statistic, on the other hand, calculates the total squared distance between

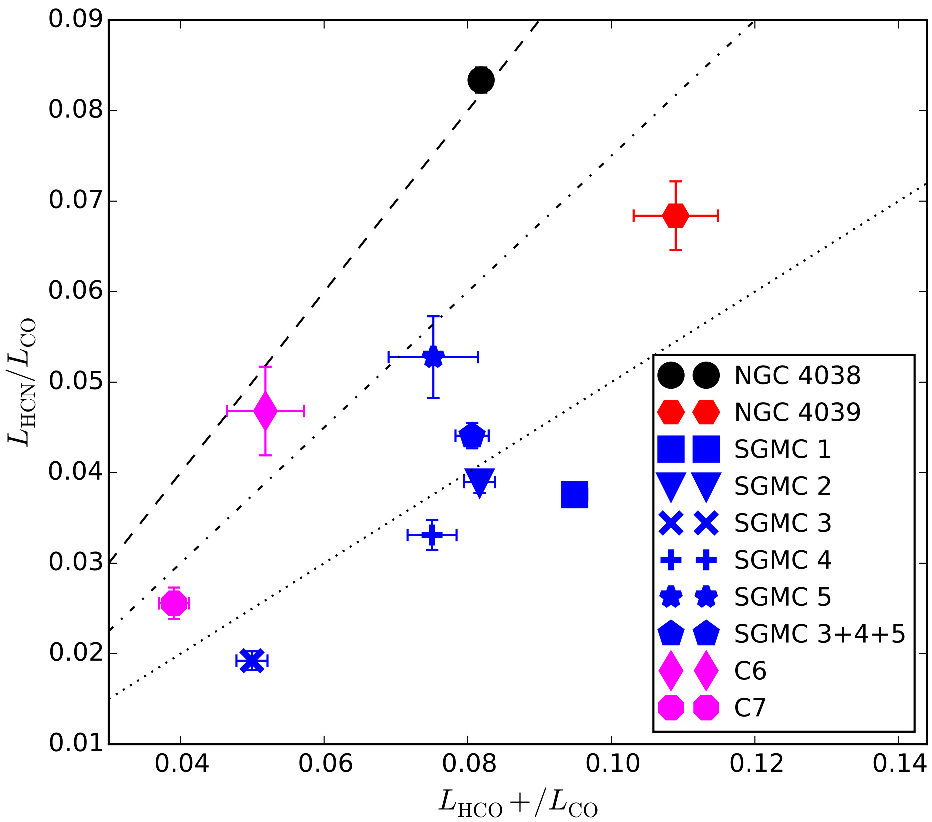

Figure 4.5 Plot of the dense gas fraction calculated at the CO $J = 1-0$ beam using $L_{\rm HCN}/L_{\rm CO}$(y-axis) and $L_{\rm HCO+}/L_{\rm CO}$(x-axis) for the brightest regions in the Antennae. The errors bars correspond to the measurement uncertainties in the ratios, while the calibration uncertainty of these line ratios is $\sim 21\%$. The lines correspond to lines of constant $L_{\rm HCN}/L_{\rm HCO+}$, with $L_{\rm HCN}/L_{\rm HCO+}$= 0.5 (dotted line), 0.75 (dash-dotted line) and 1.0 (dashed line). The region SGMC 3+4+5 corresponds to the region in the moment-0 map spanned by SGMC 3, 4 and 5, while the values for SGMC 3, 4 and 5 were calculated from moment maps created based on the velocity range calculated in Wilson et al. (2000)

two CDFs, while providing more weight to the tails of the distribution. This leads to a more sensitive test statistic. Neither the KS test nor the AD test assumes a particular distribution of the data, such as a normal distribution in the case of Student's t-test or Welch's t-test. For consistency, we *a priori* calculate the KS test statistic and resulting p-value for each of our pairs to

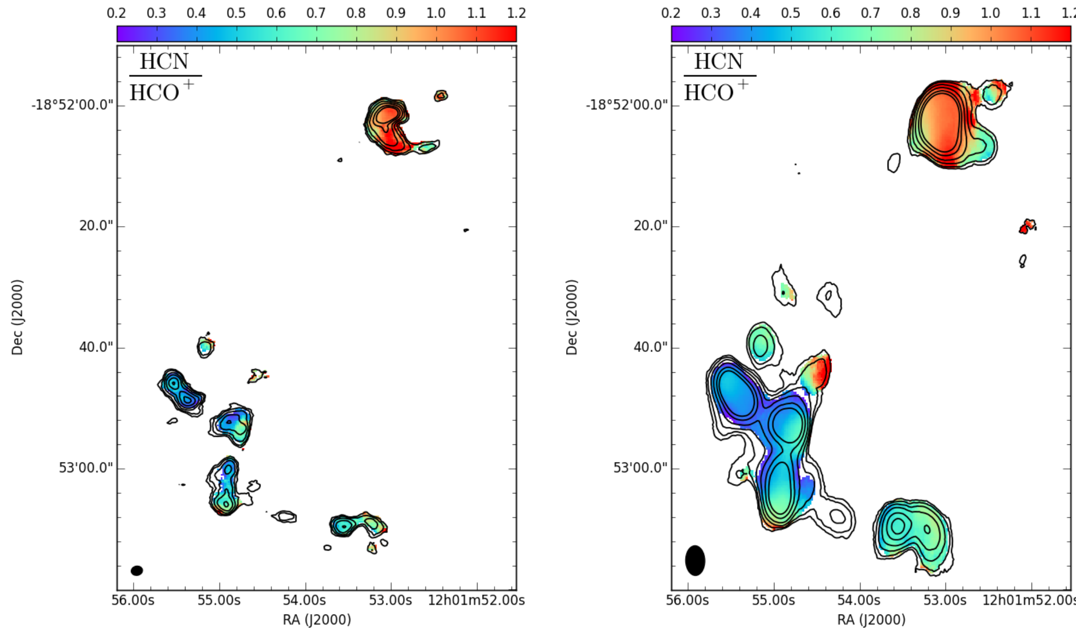

Figure 4.6 HCN/HCO$^+$ line ratio maps at the native ALMA beam (*left*) and CO $J = 1-0$ beam (*right*). The contours are the same HCO$^+$ contours shown in Figure 4.1 (*left*) and Figure 4.2 (*middle*) . The line ratios are calculated in units of Jy km s^{-1}. The nucleus of NGC 4038 exhibits the highest ratio (~ 1) while the ratio in the overlap region is about a factor of 2 smaller. The distribution functions for each of the regions in Figure 4.3 are shown in Figures 4.7 and 4.8.

check that the results obtained from the AD test and KS test are consistent with each other.

We calculate the normalized AD test statistic, A^2, and compare the statistic to a set of critical values for $p = 25\%$, 10%, 5%, 2.5%, and 1%. If the test statistic exceeds the critical value at $p = 1\%$, we reject the null hypothesis that both datasets are drawn from the same distribution,which we interpret as the ratio of HCN/HCO$^+$ between two regions being statistically different. We then proceed to calculate p by interpolating our set of critical values.

We compare the 7 regions plotted in Figure 4.7, along with the 3 SGMCs and the pre-SSC plotted in Figure 4.8 in pairs using the AD test. For the regions plotted in Figure 4.7, we are unable to reject the null hypoth-

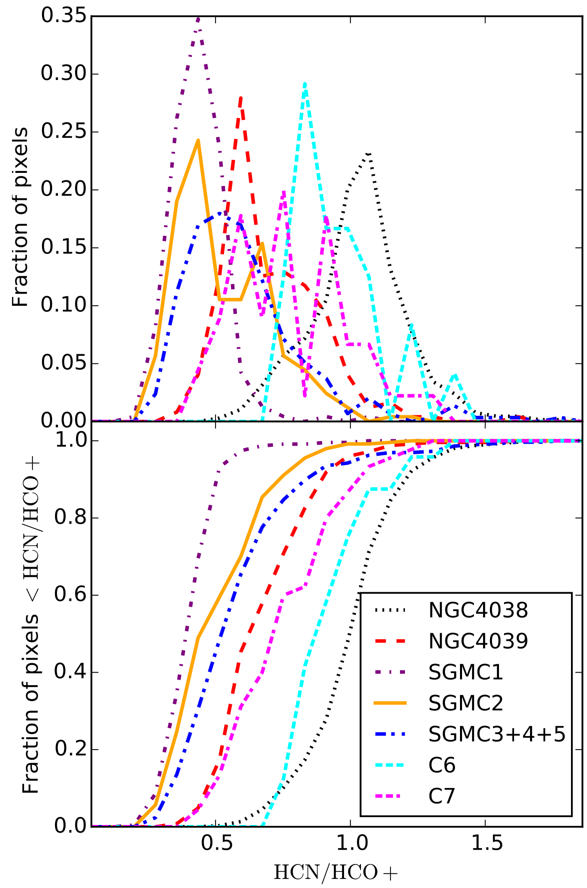

Figure 4.7 *Top:* Distribution function for the ratio of HCN/HCO$^+$ for the brightest regions in the Antennae. *Bottom:* Cumulative distribution function for these same regions. The distribution functions were calculated from the moment map spanning the entire velocity range of the emission. SGMC 3, 4 and 5 cover the same spatial region and are combined as SGMC 3+4+5. These clouds are shown individually in Figure 4.8.

esis for three pairs of regions: NGC4038 and C6 (p = 1.1%), SGMC5 and C7 (p = 12%), and NGC4039 and C7 (p = 2.7%). Furthermore, we *a priori* calculate the KS test statistic and resulting p-value for each of our pairs of regions and find that the same 3 pairs of regions reject the null hypothesis, while no additional pairs of regions reject the null hypothesis.

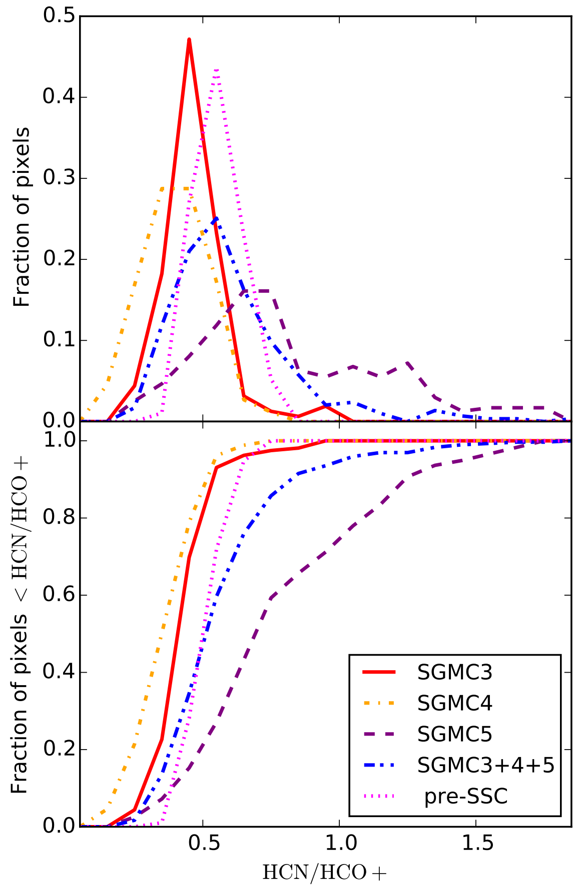

Figure 4.8 Same as Figure 4.7 except for SGMC 3, 4 and 5. These SGMCs are separated only in velocity space, and moment maps were created for each individual SGMC. We include SGMC 3+4+5 from Figure 4.7, along with the pre-super star cluster (pSSC) from Johnson et al. (2015).

For SGMC3, SGMC 4 and SGMC5, the null hypothesis is rejected for all 3 pairs of regions with $p < 1\%$, while the null hypothesis is rejected between SGMC3+4+5 region, and SGMC3, SGMC4 and SGMC5 individually. Furthermore, Figure 4.8 suggests that SGMC3+4+5 is not dominated by any one of the SGMCs in particular, and instead represents an average of the 3 regions.

4.5 Discussion

4.5.1 On the global line ratio of $L_{\mathrm{HCN}}/L_{\mathrm{CO}}$

Gao et al. (2001) measured the HCN $J = 1-0$ emission at two locations in the Antennae with a beam FWHM = 72″: the nucleus of NGC 4038 and the overlap region, including a large portion of NGC 4039. They calculated a global value of $L_{\mathrm{HCN}}/L_{\mathrm{CO}}$= 0.02. This is comparable to the value we calculate for SGMC 3 ($L_{\mathrm{HCN}}/L_{\mathrm{CO}}$= 0.019), the smallest value of our 10 regions. $L_{\mathrm{HCN}}/L_{\mathrm{CO}}$ ratios in five of our regions are a factor of 2 or more larger than the global value calculated by Gao et al. (2001), while the value calculated for the nucleus of NGC 4038 is a factor of 4 larger.

There are two major contributions which could lead to such a large difference in our ratios compared to the global ratio from Gao et al. (2001): missing flux in the CO interferometric observations, and CO emitting gas beyond the boundaries of our defined regions. Wilson et al. (2003) compared their interferometric map of CO $J = 1-0$ to the same region in the Gao et al. (2001) single dish map and found that only $\sim 65\%$ of the flux is recovered in the interferometric map. In comparison, we determined that most of the HCN emission is recovered in our map (see Section 4.2).

The total CO luminosity in our interferometric map across the 7 regions (with SGMC 3, 4 and 5 combined as SGMC 3+4+5) is $L_{\mathrm{CO}} = 9.0 \times 10^8$ K km s^{-1} pc^2, while the total luminosity from the single dish map used in Gao et al. (2001), scaled to our adopted distance of 22 Mpc, is $L^G_{\mathrm{CO}} = 40 \times 10^8$ K km s^{-1} pc^2. Similarly, the total HCN luminosity from our regions is $L_{\mathrm{HCN}} = 5.4 \times 10^7$ K km s^{-1} pc^2, while from Gao et al. (2001), $L^G_{\mathrm{HCN}} = 8 \times 10^7$ K km s^{-1} pc^2. Based on this, $\sim 68\%$ of the total HCN emission originates from the brightest regions of the Antennae, while in comparison, only $\sim 23\%$ of the total CO emission originates from these regions.

If we assume that the $\sim$ 32% of the HCN emission found outside of these regions is associated with CO emission, we can assume a ratio of $L_{\rm HCN}/L_{\rm CO}\sim 0.02$ and calculate that these regions account for another $\sim$ 33% of the total CO emission. This leaves $\sim$ 45% of the CO emission unaccounted for and presumably not within relative dense GMCs. This value represents a lower limit as, based upon our measurements (e.g. see Table 4.3), the ratio of $L_{\rm HCN}/L_{\rm CO}$ is likely greater than the global value of 0.02 from Gao et al. (2001). A higher ratio would decrease the amount of CO emission associated with the HCN emission found outside of our brightest regions, which in turn would increase the amount of CO emission we are unable to account for.

Recent observations of CO $J = 1-0$ in M51 were performed as part of the Plateau de Bure interferometer (PdBI) Arcsecond Whirlpool Survey (PAWS) in which M51 was observed using both the PdBI and the IRAM-30m single dish telescope to produce a high-resolution flux-recovered CO $J = 1-0$ map (Schinnerer et al., 2013). $\sim$ 50% of the flux is missing from the CO $J = 1-0$ PdBI map, which Pety et al. (2013) attribute to an extended, diffuse component of the molecular gas, with the CO $J = 1-0$ emission being subthermally excited.

It is possible that a significant fraction of the 45% of the CO emission that is unaccounted for is subthermally excited CO from a diffuse, extended component such as in M51. The critical density of the CO $J = 1-0$ transition ($n_{cr} \sim 10^3\,{\rm cm}^{-1}$) is significantly less than that of HCN ($n_{cr} \sim 10^5\,{\rm cm}^{-1}$), and so we would not expect any HCN emission from an extended, diffuse component. This would lead to a suppression of the global $L_{\rm HCN}/L_{\rm CO}$ ratio when compared to smaller regions. High-resolution, flux-recovered observations of CO $J = 1-0$ in the Antennae using ALMA would allow us to detect the presence of this extended diffuse component.

4.5.2 Infrared pumping of HCN and HCO^+

Pumping of HCN due to a background mid-IR field could lead to an enhancement of the HCN luminosity (Carroll & Goldsmith, 1981), which in turn would enhance the ratio of $L_{\mathrm{HCN}}/L_{\mathrm{CO}}$. IR-pumping of HCN requires a 14 μm field, which in turn vibrationally excites the molecule (Sakamoto et al., 2010), enhancing the rotational line emission as the molecule de-excites back to its ground state. For IR-pumping to become significant in HCN, the brightness temperature at 14 μm must exceed $T_B > 85$ K (Aalto et al., 2007, 2012); otherwise the excitation of HCN is dominated via collisions with H_2.

Mirabel et al. (1998) mapped the 15 μm flux ($12 - 17\,\mu$m, $F_{15\,\mu\mathrm{m}}$) in the Antennae using the Infrared Space Observatory Camera (ISOCAM), while Brandl et al. (2009) measured the mid-IR flux at 15 μm ($F_{15\,\mu\mathrm{m}}$, $14.75 - 15.25\,\mu$m) at 8 peaks using the *Spitzer* Infrared Spectrograph. We continue the analysis using the mapped observations from Mirabel et al. (1998) using the measurements made by Klaas et al. (2010); using the Brandl et al. (2009) measurements of the peaks yields the same conclusion.

We plot the values of $F_{15\,\mu\mathrm{m}}$ measured by Klaas et al. (2010) from the ISOCAM map and the luminosity ratio of HCN and CO in Figure 4.9, where their K2b, K2a, K1, NN, and NS regions correspond to SGMC 1, SGMC 2, SGMC 3+4+5, NGC 4038 and NGC 4039. The two nuclei show the highest ratio of $L_{\mathrm{HCN}}/L_{\mathrm{CO}}$, while their measured 15 μm fluxes are comparable to SGMC 1 and SGMC 2. Conversely, the strongest 15 μm flux is seen in SGMC 3+4+5, which exhibits similar values of $L_{\mathrm{HCN}}/L_{\mathrm{CO}}$ to SGMC 1 and SGMC 2. If IR-pumping were enhancing the HCN emission, we would expect to see an increase in the ratio of $L_{\mathrm{HCN}}/L_{\mathrm{HCO^+}}$ in SGMC 3+4+5. However, the ratio in SGMC 3+4+5 is comparable to the ratio measured in the other regions of the overlap region, while individually, SGMC 3, 4 and 5 do not exhibit any significant enhancement (Figure 4.5).

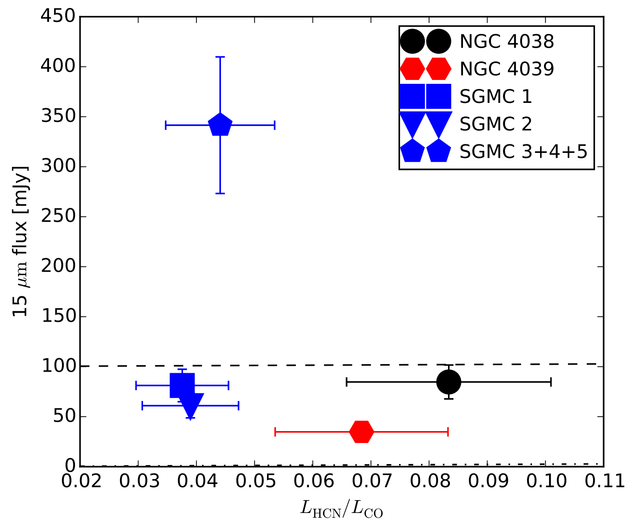

Figure 4.9 Comparing the strength of the background mid-IR field at 15 μm and the dense gas fraction traced by $L_{\rm HCN}/L_{\rm CO}$. The 15 μm fluxes are taken from Klaas et al. (2010) and their error bars correspond to a 20% photometric accuracy, while the x-axis error bars correspond to the measurement uncertainties and calibration uncertainties added in quadrature. In their work, knots K2b, K2a and K1 correspond to our SGMC 1, SGMC 2 and SGMC 3+4+5, respectively, while NN and NS correspond to NGC 4038 and NGC 4039, respectively.. The lack of positive correlation between the 15 μm emission and $L_{\rm HCN}/L_{\rm CO}$ line ratio indicates that radiative pumping of HCN does not have an appreciable effect on the measured HCN emission.

These results suggest that IR-pumping does not have an appreciable effect on $L_{\rm HCN}$ in the Antennae. The lack of evidence of IR pumping in individual SGMCs in the Antennae is reassuring, albeit not entirely surprising. Gao & Solomon (2004a) compared $L_{\rm HCN}$ to the 12 μm flux for a sample of 53 galaxies, including normal spiral galaxies, LIRGs and ULIRGs, and found no correlation between either $\rm L_{HCN}$ or $L_{\rm HCN}/L_{\rm HCO+}$ and the 12 μm flux. Their results suggest that IR-pumping is not typically seen on galactic scales, while our results show that this extends down to SGMCs in the Antennae for the HCN $J = 1-0$ transition. As such, we take the ratio of $L_{\rm HCN}/L_{\rm CO}$ to directly reflect the dense gas fraction across the Antennae.

4.5.3 Dense gas fraction

We use the ratio of $L_{\rm HCN}/L_{\rm CO}$ as an indicator of the dense gas fraction throughout the Antennae, and show this ratio compared to $L_{\rm CO}$ in Figure 4.10 for the 9 brightest regions in the Antennae. Typical values for normal spiral galaxies are $L_{\rm HCN}/L_{\rm CO} \sim 0.02 - 0.05$ (Gao & Solomon, 2004a,b), while this fraction can increase to $L_{\rm HCN}/L_{\rm CO} > 0.06$ in the case of some extreme star forming LIRGs and ULIRGs. In comparison, the global value for the Antennae is $L_{\rm HCN}/L_{\rm CO} \sim 0.02$ (Gao et al., 2001), near the lower end of the values for spiral galaxies, while only SGMC 3 has a dense gas fraction this low.

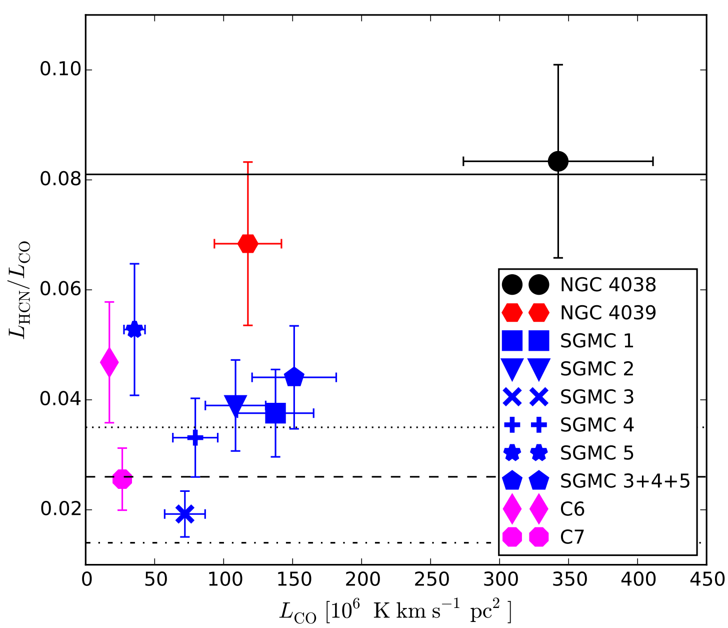

Figure 4.10 Dense gas fraction as measured by $L_{\rm HCN}/L_{\rm HCO+}$ (y-axis) as a function of CO luminosity (x-axis). The data points are the values measured for the brightest regions in the Antennae while the error bars correspond to the measurement uncertainty and the calibration uncertainty added in quadrature. The solid and dashed horizontal lines correspond to the average values of $L_{\rm HCN}/L_{\rm HCO+}$ as measured in the bulge and plane of the Milky Way, while the dot-dashed line corresponds to the average value measured in local GMCs (Helfer & Blitz, 1997a). The dashed line corresponds to typical values of $L_{\rm HCN}/L_{\rm HCO+}$ in normal spiral galaxies (Gao & Solomon, 2004b; Graciá-Carpio et al., 2006).

The two nuclei, NGC 4038 and NGC 4039, show a higher dense gas fraction than the rest of the system, by roughly a factor of $\sim 2-3$. In comparison, Helfer & Blitz (1997a) measured $I_{\rm HCN}/I_{\rm CO}$, comparable to $L_{\rm HCN}/L_{\rm CO}$, in the galactic plane of the Milky Way and found that the dense gas fraction was greater towards the bulge ($I_{\rm HCN}/I_{\rm CO} \sim 0.081$) than the rest of the galactic plane ($I_{\rm HCN}/I_{\rm CO} \sim 0.026$). Helfer & Blitz (1997b) saw a similar increase in NGC 6946, a grand-design spiral galaxy, and NGC 1068, a Seyfert-2 galaxy with a starburst, with the ratio of $I_{\rm HCN}/I_{\rm CO}$ increasing by a factor of $5-10$ towards the bulge.

Helfer & Blitz (1997a) argue that the increased dense gas fraction in the bulge is due to an increase in the average gas pressure towards the centre of the Milky Way, with $I_{\rm HCN}/I_{\rm CO} \propto P^{0.19}$. As such, a factor of 2 difference in the ratio of $I_{\rm HCN}/I_{\rm CO}$ would correspond to a factor of ~ 40 difference in the average gas pressure. This increase in gas pressure is due in part to the increased stellar density in the bulge, which increases the gravitational potential, and in turn increases the gas pressure required to support hydrostatic equilibrium.

Schirm et al. (2014) calculated the pressure using a non-LTE excitation analysis of CO and [CI] in each of NGC 4038, NGC 4039 and the overlap region in relatively large beams (FWHM $\sim 43''$, $\sim 5\,$kpc). Their cold component results suggest that the pressure in all three regions is similar ($P \sim 10^{4.5} - 10^{5.5}\,$K cm^{-2}); however the 1σ ranges span an order of magnitude. Their warm component, traced largely by the CO $J=7-6$ and $J=8-7$ transitions, shows a much higher pressure in NGC 4038 ($P \sim 10^{9}\,$K cm^{-2}) than in either NGC 4039 or the overlap region ($P \sim 10^{7.5}\,$K cm^{-2}). It is important to note that, due to the large beams, NGC 4039 contains some emission from the overlap region, and this may be reflected in the non-LTE excitation analysis.

As in the Milky Way, the high ratio of $I_{\rm HCN}/I_{\rm CO}$ seen in the two nuclei could be due to an increase in the stellar density compared to the overlap region. It is possible that Schirm et al. (2014) do not detect this increased pressure in their cold component due to relatively large 1σ ranges for the calculated pressures. In addition, the two nuclei are only a fraction the size of the large beams used by Schirm et al. (2014), which in turn would lead to gas not associated with the nuclei being included in their analysis. It is possible that some, or even most, of the HCN emission is associated with their warm component; however the $J = 1-0$ transition is often associated with cold, dense gas. Observations of higher J HCN and HNC transitions coupled with a non-LTE excitation analysis similar to the method used by Schirm et al. (2014) would help determine whether this HCN emission is associated with cold or warm dense molecular gas, while also enabling direct calculations of the pressure in the dense, molecular gas in these regions.

4.5.3.1 Distribution of the dense gas fraction

In this section, we investigate the distribution of the dense gas fraction within each individual region. We show the ratio of $I_{\rm HCN}/I_{\rm CO}$ in Figure 4.11. In both NGC 4038 and NGC 4039, there is a region towards the very center where the ratio of $I_{\rm HCN}/I_{\rm CO}$ increases by a factor of ~ 2 compared to the surrounding regions. These high ratio regions are approximately the size of the CO beam, which corresponds to $\sim 500\,$pc, similar to the size of the bulges measured by Helfer & Blitz (1997b). Interestingly, the peak value of $I_{\rm HCN}/I_{\rm CO}$ is greater in NGC 4039 than in NGC 4038, while overall, the dense gas fraction is greater in NGC 4038. These high-dense gas fraction regions are likely the result of an increase in the stellar density within the nuclei, similar to what is seen in Helfer & Blitz (1997a).

In the overlap region, most of the molecular gas is characteristic of SGMC 1, where $L_{\rm HCN}/L_{\rm CO} \sim 0.04$. There are two interesting peaks in the distribution of the dense gas ratio in the overlap region, one in the south-west

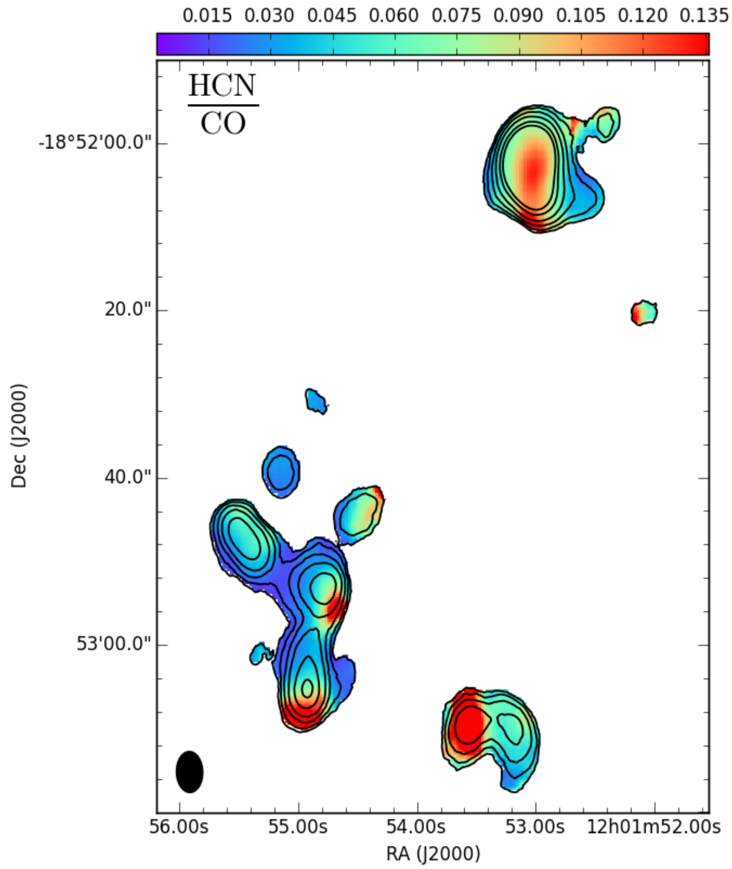

Figure 4.11 Ratio map of $I_{\mathrm{HCN}}/I_{\mathrm{CO}}$ with the HCN contours from Figure 4.2 *left* overlaid. The contours correspond to 3σ, 5σ, 9σ, $= 15\sigma$, 25σ, and 35σ, while $I_{\mathrm{HCN}}/I_{\mathrm{CO}}$ is calculated in units of K km s^{-1}.

of SGMC 2, and another to the south of SGMC 3+4+5. The centre of the peak in SGMC 2 is offset from the centre of pSSC by $\sim 3'' - 4''$, which corresponds to roughly a beam. Both peaks exhibit a higher ratio of $I_{\mathrm{HCO+}}/I_{\mathrm{CO}}$ and, to a lesser extent, $I_{\mathrm{HCN}}/I_{\mathrm{HCO+}}$ (Figure 4.12).

No significant emission is detect at a 3σ level at either peak in either HCN or HCO$^+$at the native ALMA resolution. However, both peaks are detected in the CO beam-matched maps of both dense gas tracers at a 5σ level. Moreover, there is no obvious CO $J = 3-2$ emission detected at this location either (Whitmore et al., 2014).

Whitmore et al. (2010) observed the Antennae with the Hubble Space Telescope using multiple filters, including the F435W, F814W, and F658N, which correspond to B-band, I-band and Hα emission. We compare the HCN emission to each of these filters in the bottom row of Figure 4.12. At both dense gas fraction peaks, there are no significant B-band or I-band optical counterparts to the increased dense gas fraction. However, there is Hα emission at the northern edge of the SGMC 3+4+5 peak, and near the eastern edge of the SGMC 2 peak. Furthermore, there is no 70 μm emission associated with either peak (Figure 4.12, Klaas et al. 2010).

The lack of emission in the B- and I-band images, along with the Hα image, is likely due to high dust extinction in the overlap region. The 70 μm flux correlates strongly with star formation (Calzetti et al., 2010), and so we attribute the deficiency in the 70 μm emission to a lack of recent star formation within the two dense gas peaks in the overlap region. As such, these high-dense gas fraction regions are likely the result of turbulent motion due to the ongoing merger, and may indicate sites of future star formation within the overlap region. However, if this gas has been heated by the turbulent motion, it may never cool sufficiently to collapse and begin star formation.

4.5.4 Mechanical heating and photon dominated regions

HCN and HNC are isotopomers with similar excitation energies. As such, the line ratio of $L_{\mathrm{HNC}}/L_{\mathrm{HCN}}$ is driven in large part by the relative abundance of the two molecules, while the exchange reaction $\mathrm{H} + \mathrm{HNC} \rightleftarrows \mathrm{H} + \mathrm{HCN}$ is an important factor in their relative abundances (Schilke et al., 1992; Talbi et al., 1996). At temperatures $< 100\,\mathrm{K}$, the rate coefficients of either the forward or reverse reactions are small, and this reaction is not important (Talbi et al., 1996). At temperatures of a few hundred K, the energies are sufficient to exceed the activation energy of the H + HNC reaction, leading to a higher

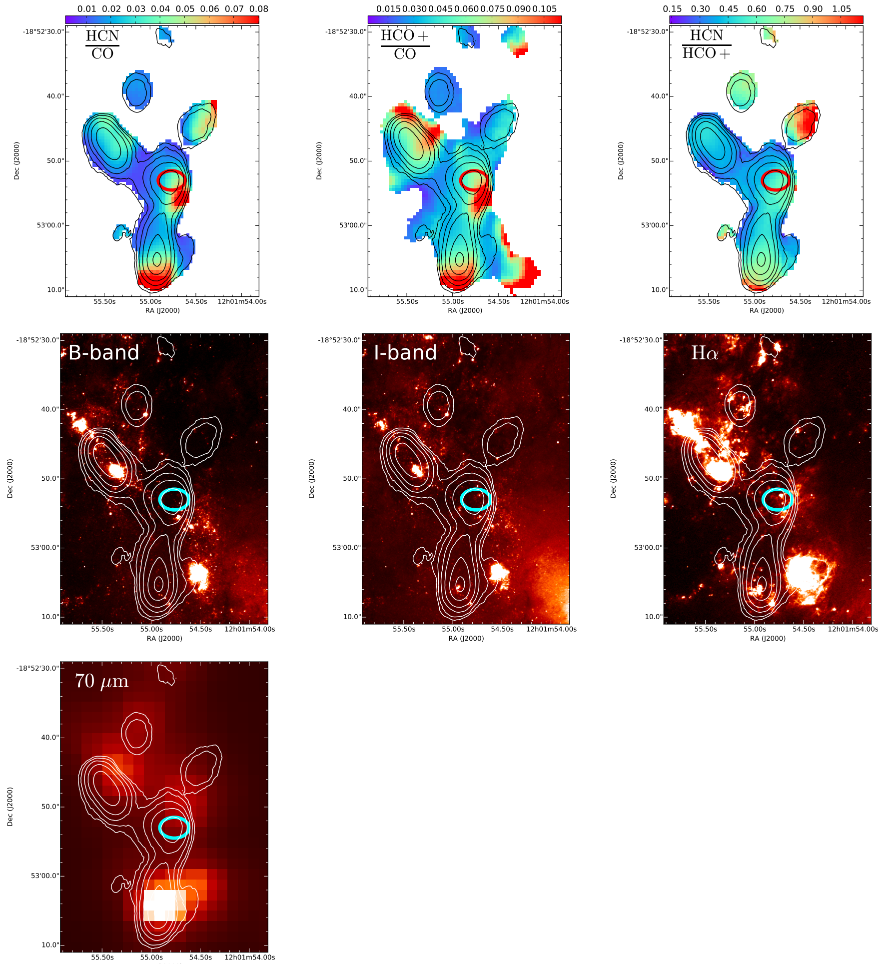

Figure 4.12 HCN contours beam-matched to the CO observations overlaid on various ratio maps and emission maps. The contours correspond to $(3, 5, 9, 15, 25, 35) \times (3.6 \times 10^{-2}$ Jy beam^{-1} km s^{-1}). **Top row:** Line ratio maps for HCN/CO (*left*), HCO^+/CO (*middle*) and HCN/HCO^+ (*right*). **Middle row:** Hubble space telescope images of the B-band (F435W, *left*), I-band (F814W, *middle*) and Hα (F658N, *right*) emission from Whitmore et al. (2010).**Bottom row:** *Herschel* PACS 70 μm emission, tracing star forming regions, from Klaas et al. (2010). The location of the pre-SSC is shown by the red (*top row*) and cyan (*bottom row*) ellipses. None of the emission maps have any significant emission towards the high-dense fraction regions as traced by HCN/CO in the overlap region (see text for more details).

relative abundance of HCN to HNC, and as such a lower ratio of $L_{\rm HNC}/L_{\rm HCN}$.

It has been suggested that most molecular gas is in the form of PDRs, while in the past, mechanical heating has been ignored by most PDR models (e.g. see the PDR model comparison study by Röllig et al. 2007). In the absence of mechanical heating, the heating occurs only at the surface of the PDR, where the photon energies are high enough to liberate elections from the surfaces of dust grains (via the photoelectric effect), which can in turn heat the gas. Recent PDR models have investigated the effects of mechanical heating on the molecular gas within PDRs (Meijerink et al., 2011; Kazandjian et al., 2012, 2015). In particular, these studies are concerned largely with the effects of mechanical heating on the observed atomic and molecular line ratios. They find that mechanical heating begins to have a measurable effect on the chemistry of the PDR, and consequently the line ratios, with contributions of as little as $\sim 1\%$ to the total heating (Kazandjian et al., 2012).

In the Antennae, the ratio of $L_{\mathrm{HNC}}/L_{\mathrm{HCN}}$ varies by less than a factor of 1.5 across the brightest regions, ranging from $\sim 0.25 - 0.38$ (Table 4.2 and Figure 4.4). We compare our measured line ratio of $L_{\mathrm{HNC}}/L_{\mathrm{HCN}}$to the PDR models with mechanical heating from Kazandjian et al. (2015). In their models, the mechanical heating is parameterized as α, which is equal to the total amount of mechanical heating relative to the PDR surface heating. For values of $\alpha < 0.05$, their reference models report a value of $L_{\mathrm{HNC}}/L_{\mathrm{HCN}}$ either near or above unity. Our measured line ratios are consistent with $\alpha > 0.05$ for their intermediate ($n(\mathrm{H_2}) = 10^{3.0}\,\mathrm{cm^{-3}}$) and high-density ($n(\mathrm{H_2}) = 10^{5.5}\,\mathrm{cm^{-3}}$) models, with the exception of their $n(\mathrm{H_2}) = 10^{5.5}\,\mathrm{cm^{-3}}$, $G_0 = 10^{3.0}$ model (M3 in their work), which reports $L_{\mathrm{HNC}}/L_{\mathrm{HCN}}\sim 1$ for all amounts of mechanical heating.

In comparison, Schirm et al. (2014) modelled various line ratios of CO from $J = 1-0$ to $J = 8-7$ along with the FIR luminosity using PDR models which did not include mechanical heating. In all three region, they found that line ratios of the low-J CO transitions ($J = 1-0$ to $J = 3-2$) are consistent with a "cold" PDR with a field strength of $G_0 \sim 100$ and a warm molecular gas density of $n(\mathrm{H_2}) \sim 10^3 - 10^4\,\mathrm{cm^{-3}}$. Line ratios of the high-J CO transitions ($J = 6-5$ to $J = 8-7$) are consistent with a "warm" PDR with a field strength of $G_0 \sim 1000$ and a molecular gas density of $n(\mathrm{H_2}) \sim 10^4 - 10^5\,\mathrm{cm^{-3}}$. As such, their warm PDR models are similar to model M3 from Kazandjian et al. (2015), for which $L_{\mathrm{HNC}}/L_{\mathrm{HCN}} \sim 1$ for all amounts of mechanical heating, while the field strength of their cold PDR models lies outside of the range of G_0 modelled by Kazandjian et al. (2015). Furthermore, the beam size of the observations from Schirm et al. (2014) is $\sim 43''$, which is considerably larger than the beam sizes used in our work.

We can draw a few conclusions based upon our measured line ratios of $L_{\mathrm{HNC}}/L_{\mathrm{HCN}}$. First, our measured line ratios are consistent with at least some ($> 5\%$) contribution of mechanical heating towards the total heating budget in all the bright regions in the Antennae. Future PDR modelling within the Antennae should include mechanical heating as it has to have a fundamental effect on the chemistry within these regions.

Secondly, the higher ratio of $L_{\mathrm{HNC}}/L_{\mathrm{HCN}}$ seen in the nucleus of NGC 4038 and SGMC 1 indicates that the relative contribution of mechanical heating is lower within these regions compared to PDR surface heating. Conversely, the lower ratio seen in the nucleus of NGC 4039 and SGMC 2 indicates a higher relative contribution of mechanical heating. An increase (decrease) in the relative contribution of mechanical heating could either be due to an increase (decrease) in the total mechanical heating, or due to a decrease (increase) in the total PDR surface heating. All four regions show similar star formation efficiencies (SFEs), ranging from $2.19\,\mathrm{L_\odot M_\odot^{-1}}$ for NGC 4038, to $3.33\,\mathrm{L_\odot M_\odot^{-1}}$ for SGMC 2 (Klaas et al., 2010). As PDR surface heating is tied to the background FUV field strength, which is emitted from young, massive stars, the similar SFEs within these four regions likely indicate variations in the amount of mechanical heating as opposed to the PDR surface heating. This, in turn, agrees with the results from Schirm et al. (2014) who found similar values for G_0 and $n(H_2)$ in NGC 4038, NGC 4039 and the overlap region.

Lastly, our ratios of $L_{\mathrm{HNC}}/L_{\mathrm{HCN}}$ are consistent with models from Kazandjian et al. (2015) with $\alpha > 0.1$. They note that the molecular gas temperature of these models is high ($T_{kin} > 100\,\mathrm{K}$), which would indicate that the HCN and HNC emission originates from warm, dense molecular gas similar to the warm component found by Schirm et al. (2014). However, the $J = 1 - 0$ transition of both these molecules is typically assumed to be associated with cold, dense, star forming molecular gas. It could be that this cold, dense gas is quickly heated by the ongoing star formation within these systems, via supernovae and stellar winds, or that the turbulent motion due to the ongoing merger heats this dense gas.

A multi-transitional non-LTE excitation analysis can be used to assess whether the HCN and HNC $J = 1 - 0$ emission is from cold or warm dense gas. Currently, the only other observations of either tracer in the Antennae is the HCN $J = 4 - 3$ transition observed in the overlap region at the same time as CO $J = 3 - 2$ by Whitmore et al. (2014). Currently, the HCN and HNC $J = 2 - 1$ transitions ($\nu_{\mathrm{HCN}} = 176.3\,\mathrm{GHz}$ and $\nu_{\mathrm{HNC}} = 180.3\,\mathrm{GHz}$ in the Antennae) fall outside of the frequency ranges of ALMA, while also lying at a frequency of relatively poor atmospheric transmission. The HCN and HNC $J = 3-2$ transitions ($\nu_{\mathrm{HCN}} = 264.4\,\mathrm{GHz}$ and $\nu_{\mathrm{HNC}} = 270.5\,\mathrm{GHz}$) lie within the ALMA band 6 and could be observed. As such, enough current and possible future observations are available to perform a full non-LTE excitation analysis to constrain the temperature of the dense molecular gas, along with other physical parameters including the density, pressure and relative abundance of HCN and HNC.

Table 4.4. Mean and standard deviation for the ratio of $I_{\mathrm{HCN}}/I_{\mathrm{HCO+}}$

Region ID	$< I_{\mathrm{HCN}}/I_{\mathrm{HCO+}} >$	$\sigma_{\mathrm{HCN/HCO+}}$	n_{pixels}
NGC 4038	1.03	0.18	668
NGC 4039	0.70	0.18	247
SGMC 1	0.43	0.10	233
SGMC 2	0.53	0.18	247
pre-SSC	0.64	0.00	1
SGMC 3	0.47	0.11	159
SGMC 4	0.40	0.12	261
SGMC 5	0.82	0.34	236
SGMC 3+4+5	0.61	0.23	295
C6	0.95	0.15	24
C7	0.78	0.21	45

Note. — All values are calculated at the ALMA beam size.

4.5.5 Cosmic rays and the abundances of HCN and HCO^+

Differences in the ratio of HCN and HCO^+ of over a factor of 2 are seen in both the total global line ratio in the form of $L_{\mathrm{HNC}}/L_{\mathrm{HCO+}}$ (Table 4.2) and in the distribution of $I_{\mathrm{HCN}}/I_{\mathrm{HCO+}}$ (Figures 4.7 and 4.8, and Table 4.4). In particular, the nucleus of NGC 4038 exhibits a ratio ~ 1, while in the SGMCs, the ratio is typically $\sim 0.4-0.6$ (Figure 4.6). These differences in the line ratio suggest either different excitation conditions for the two molecules (e.g. see Juneau et al. 2009) or changes in the relative abundances. In order to discern between varying excitation conditions, additional transitions are required of both molecules. As such, we discuss the implications of varying abundances of HCN and HCO^+ in the context of the measured line ratios.

HCO^+, unlike HCN, is an ion and is easily destroyed through recombination in the presence of free electrons. In addition, free electrons can combine with $HCNH^+$ to form HCN (Lintott & Viti, 2006; Juneau et al., 2009), simultaneously enhancing the abundance of HCN while the abundance of HCO^+ is suppressed. These free electrons are generated in the formation of the H_3^+ ion, which occurs via $2H_2 + \zeta \rightarrow H_3^+ + H$ (McCall et al., 2003). Papadopoulos (2007) argue that deep within molecular clouds, where the dense gas is found, this reaction with cosmic rays is the primary source of free electrons; however H_3^+ is also important in the formation of HCO^+. As such, interpreting variations in the line ratio of HCN and HCO^+ is not as straightforward as, say, HNC and HCN.

Meijerink et al. (2011) investigated the effects of cosmic rays on the abundances of various molecules, atoms and ions within PDRs. They modelled a dense ($n(\mathrm{H_2}) = 10^{5.5}\,\mathrm{cm^{-3}}$) PDR region with a strong background UV field ($10^5 G_0$), along with an intermediate density ($n(\mathrm{H_2}) = 10^3\,\mathrm{cm^{-3}}$) PDR with a PDR field strength of $G_0 = 10^3$. They varied the cosmic ray rate from $5 \times 10^{-17}\,\mathrm{s^{-1}}$ to $5 \times 10^{-13}\,\mathrm{s^{-1}}$. In the dense PDR, they found that the abundances of both HCN and HNC are insensitive to changes in the cosmic ray rates. The abundance of HCO^+, however, increases with increasing cosmic ray rates, except at very high cosmic ray rates. In the intermediate density PDR case, the HCO^+, HCN and HNC abundances all decrease with increasing cosmic ray rate.

These cosmic rays are assumed to originate largely from supernova remnants (Schulz et al., 2007). Neff & Ulvestad (2000) measured the supernova rate (ν_{SN}) across the Antennae using nonthermal radio sources which trace compact supernova, and found a global rate of $\nu_{SN} \sim 0.2 - 0.3\,\mathrm{yr^{-1}}$. Schirm et al. (2014) compared the location of these supernova to their $\sim 43''$ beams for each of NGC 4038, NGC 4039 and the overlap region and determined that $\sim 66\%$ of the supernova originate from the overlap region, 14% from the nucleus of NGC 4038 and $\sim 6\%$ from the nucleus of NGC 4039. Based upon the number of pixels determined within each region from Table 4.4 (n_{pixels}), the SGMCs in the overlap region along with C6 and C7 are comprised of ~ 850 pixels. NGC 4038 is of similar size (~ 650 pixels), while NGC 4039 is a factor of ~ 3 smaller (250 pixels). Given this, we estimate that the surface density of supernova in the overlap region is roughly 4 times greater than in NGC 4038 and NGC 4039.

The increased supernova surface density in the overlap region could indicate an increase in the cosmic ray rate in the supernova. This could in turn explain the decreased ratio of $L_{\rm HCN}/L_{\rm HCO+}$ found in the overlap region. NGC 4039, however, has a similar supernova rate and star formation rate to NGC 4038 and yet exhibits a lower $L_{\rm HCN}/L_{\rm HCO+}$ ratio. An active galactic nucleus (AGN) can also be the source of cosmic rays (Pierre Auger Collaboration et al., 2007); however multi-wavelength studies of the Antennae suggest that there is no AGN at the centre of NGC 4039 (Neff & Ulvestad, 2000; Brandl et al., 2009; Ueda et al., 2012). Ueda et al. (2012) suggest that the high line ratio of CO $J = 3-2/J = 1-0$ seen in NGC 4039 is not due to star formation activity, but could possibly be due to a hidden AGN. If that is the case, the lower value of $L_{\rm HCN}/L_{\rm HCO+}$ seen in NGC 4039 would be explained by the presence of such a hidden AGN. However, we present no additional evidence here to indicate the presence of an AGN in NGC 4039.

In summary, the high ratio of HCN/HCO^+ in the nucleus of NGC 4038 compared to the overlap region is likely due to an enhanced HCO^+ abundance in the overlap region which is caused by an increase in the cosmic ray rate. This increase in the cosmic ray rate is likely due to an increase in the supernova rate. The lower ratio seen in NGC 4039 compared to NGC 4038 is not due to an increase in the supernova rate, as there is no evidence for an increase in either the supernova rate or the star formation rate in NGC 4039. We postulate that a hidden AGN within NGC 4039 could explain the difference in the ratio between the two nuclei.

4.6 Summary and conclusions

In this paper, we presented high-resolution observations of HCN, HCO^+, and HNC $J = 1-0$ transition in the Antennae using ALMA band 3. All three of these molecules are tracers of dense gas. These observations are beam matched and compared to previously obtained lower resolution CO $J = 1-0$ observations by Wilson et al. (2000, 2003). We isolate the emission from the nucleus of NGC 4038 and NGC 4039, and from the 5 SGMCs in the overlap region. We also identify two other bright regions, clouds C6 and C7, located to the north of the overlap region. These regions are selected as they are the brightest regions in the Antennae.

1. We compare our interferometric observations of HCN and CO $J = 1-0$ to single-dish observations of the same transitions by Gao et al. (2001). We find that $\sim 68\%$ of the total HCN flux from the Gao et al. (2001) observations is located within the nuclei, SGMCs and clouds C6 and C7, while only $\sim 23\%$ of the COemission is from these same regions. Furthermore, assuming a line ratio of $L_{\rm HCN}/L_{\rm CO}\sim 0.02$, we find that we are unable to account for $\gtrsim 45\%$ of the CO emission is not associated with any HCN emission. We suggest that this CO is subthermally excited and the emission originates from relatively diffuse molecular gas, similar to what is seen in M51.

2. We find no correlation between the 15 μm flux measured by Klaas et al. (2010) and the ratio of $L_{\rm HCN}/L_{\rm CO}$ for the $J = 1-0$ transition. Given that $L_{\rm HCN}/L_{\rm CO}$ is IR pumped at 14 μm, we suggest that this lack of correlation indicates that there is no appreciable IR pumping of the

HCN $J = 1 - 0$ transition. As such, we suggest using $L_{\rm HCN}/L_{\rm CO}$ as a measure of the dense gas fraction throughout the Antennae.

3. The dense gas fraction as measured by $L_{\rm HCN}/L_{\rm CO}$ is higher in the two nuclei (0.083 and 0.068 respectively) than in any other region of the Antennae (< 0.053). Furthermore, the line ratio peaks in the centre of the two nuclei. This increase is consistent with what is seen within the bulges of nearby spiral galaxies, where the stellar potential is larger. As such, we attribute this increase in the dense gas fraction to an increase in the pressure within the two nuclei due to the higher stellar potential in the nuclei.

4. The ratio of $L_{\rm HNC}/L_{\rm HCN}$ is a tracer of mechanical heating within PDRs. We find that this ratio varies by less than a factor of 1.5 across our defined regions in the Antennae, ranging from $0.25 - 0.38$. By comparing these values to PDR models which include mechanical heating, we find that mechanical heating is at minimum > 0.05 of the PDR surface heating in the Antennae. In these PDR models, a value of 0.1 indicates temperatures > 100 K, which is consistent with the values we measure. This would indicate that both HCN and HNC $J = 1 - 0$ are tracers of warm, dense molecular gas in the Antennae as opposed to cold, dense molecular gas. We suggest that a multi-transitional non-LTE excitation analysis can be used to determine the temperature of this gas.

5. We investigate variations in $L_{\rm HCN}/L_{\rm HCO+}$between regions, along with the distribution of $I_{\rm HCN}/I_{\rm HCO+}$ within individual regions. We find that this ratio peaks in the nucleus of NGC 4038 ($L_{\rm HCN}/L_{\rm HCO+}\sim 1.0$), while it is approximately a factor of 2 smaller in the overlap region. We attribute this difference to a increase in the abundance of HCO^+ in the overlap region due to an increase in the cosmic ray rate from an increased super-

nova rate. We also find a difference in the ratio between NGC 4038 and NGC 4039 (~ 0.6). We suggest that this could be once again due to an increase in the cosmic ray rate, however the only possible source would be a hidden AGN in NGC 4039. Few studies have shown any evidence of a hidden AGN, and so its existence is inconclusive.

This research made use of the python plotting package matplotlib (Hunter, 2007). This research made use of APLpy, an open-source plotting package for Python hosted at http://aplpy.github.com.

Bibliography

Aalto, S., Garcia-Burillo, S., Muller, S., et al. 2012, A&A, 537, A44

Aalto, S., Spaans, M., Wiedner, M. C., & Hüttemeister, S. 2007, A&A, 464, 193

Bolatto, A. D., Wolfire, M., & Leroy, A. K. 2013, ARA&A, 51, 207

Brandl, B. R., Snijders, L., den Brok, M., et al. 2009, ApJ, 699, 1982

Calzetti, D., Wu, S.-Y., Hong, S., et al. 2010, ApJ, 714, 1256

Carroll, T. J., & Goldsmith, P. F. 1981, ApJ, 245, 891

Clements, D. L., Sutherland, W. J., McMahon, R. G., & Saunders, W. 1996, MNRAS, 279, 477

Gao, Y., Lo, K. Y., Lee, S.-W., & Lee, T.-H. 2001, ApJ, 548, 172

Gao, Y., & Solomon, P. M. 2004a, ApJS, 152, 63

—. 2004b, ApJ, 606, 271

Graciá-Carpio, J., García-Burillo, S., Planesas, P., & Colina, L. 2006, ApJ, 640, L135

Helfer, T. T., & Blitz, L. 1997a, ApJ, 478, 233

—. 1997b, ApJ, 478, 162

Herrera, C. N., Boulanger, F., Nesvadba, N. P. H., & Falgarone, E. 2012, A&A, 538, L9

Hopkins, P. F., Hernquist, L., Cox, T. J., et al. 2006, ApJS, 163, 1

Hunter, J. D. 2007, Computing In Science & Engineering, 9, 90

Johnson, K. E., Leroy, A. K., Indebetouw, R., et al. 2015, ArXiv e-prints, arXiv:1503.06477

Juneau, S., Narayanan, D. T., Moustakas, J., et al. 2009, ApJ, 707, 1217

Kazandjian, M. V., Meijerink, R., Pelupessy, I., Israel, F. P., & Spaans, M. 2012, A&A, 542, A65

—. 2015, A&A, 574, A127

Klaas, U., Nielbock, M., Haas, M., Krause, O., & Schreiber, J. 2010, A&A, 518, L44

Lintott, C., & Viti, S. 2006, ApJ, 646, L37

Liu, F., & Gao, Y. 2010, ApJ, 713, 524

Loenen, A. F., Baan, W. A., & Spaans, M. 2007, in IAU Symposium, Vol. 242, IAU Symposium, ed. J. M. Chapman & W. A. Baan, 462–466

Loenen, A. F., Spaans, M., Baan, W. A., & Meijerink, R. 2008, A&A, 488, L5

McCall, B. J., Huneycutt, A. J., Saykally, R. J., et al. 2003, Nature, 422, 500

Meijerink, R., Spaans, M., Loenen, A. F., & van der Werf, P. P. 2011, A&A, 525, A119

Mirabel, I. F., Vigroux, L., Charmandaris, V., et al. 1998, A&A, 333, L1

Neff, S. G., & Ulvestad, J. S. 2000, AJ, 120, 670

Papadopoulos, P. P. 2007, ApJ, 656, 792

Pety, J., Schinnerer, E., Leroy, A. K., et al. 2013, ApJ, 779, 43

Pierre Auger Collaboration, Abraham, J., Abreu, P., et al. 2007, Science, 318, 938

Röllig, M., Abel, N. P., Bell, T., et al. 2007, A&A, 467, 187

Rosolowsky, E., & Leroy, A. 2006, PASP, 118, 590

Sakamoto, K., Aalto, S., Evans, A. S., Wiedner, M. C., & Wilner, D. J. 2010, ApJ, 725, L228

Sanders, D. B., & Mirabel, I. F. 1996, ARA&A, 34, 749

Sanders, D. B., Soifer, B. T., Elias, J. H., et al. 1988, ApJ, 325, 74

Schilke, P., Walmsley, C. M., Pineau Des Forets, G., et al. 1992, A&A, 256, 595

Schinnerer, E., Meidt, S. E., Pety, J., et al. 2013, ApJ, 779, 42

Schirm, M. R. P., Wilson, C. D., Parkin, T. J., et al. 2014, ApJ, 781, 101

Schulz, A., Henkel, C., Muders, D., et al. 2007, A&A, 466, 467

Schweizer, F., Burns, C. R., Madore, B. F., et al. 2008, AJ, 136, 1482

Stanford, S. A., Sargent, A. I., Sanders, D. B., & Scoville, N. Z. 1990, ApJ, 349, 492

Steinmetz, M., & Navarro, J. F. 2002, New Astron., 7, 155

Talbi, D., Ellinger, Y., & Herbst, E. 1996, A&A, 314, 688

Ueda, J., Iono, D., Petitpas, G., et al. 2012, ApJ, 745, 65

Whitmore, B. C., Zhang, Q., Leitherer, C., et al. 1999, AJ, 118, 1551

Whitmore, B. C., Chandar, R., Schweizer, F., et al. 2010, AJ, 140, 75

Whitmore, B. C., Brogan, C., Chandar, R., et al. 2014, ApJ, 795, 156

Williams, J. P., de Geus, E. J., & Blitz, L. 1994, ApJ, 428, 693

Wilson, C. D., Scoville, N., Madden, S. C., & Charmandaris, V. 2000, ApJ, 542, 120

—. 2003, ApJ, 599, 1049

Wilson, C. D., Petitpas, G. R., Iono, D., et al. 2008, ApJS, 178, 189

Wolfire, M. G., Hollenbach, D., & McKee, C. F. 2010, ApJ, 716, 1191

Wu, J., Evans, II, N. J., Gao, Y., et al. 2005, ApJ, 635, L173

Chapter 5

Summary and Future Work

"Space. It seems to go on and on forever. But then you get to the end and a gorilla starts throwing barrels at you."

"Phillip J. Fry" from Futurama episode "Space Pilot 3000" (1999-2013)

In this thesis, I presented new observations and analysis of the nearby interacting spiral galaxy M51 and the nearby merging galaxies NGC 4038/39 using the Herschel Space Observatory (*Herschel*, M51 and NGC 4038/39) and the Atacama Large Millimeter/sudmillimeter Array (NGC 4038/39). These observations were used to study the molecular gas, which is the primary fuel for star formation, in order to better understand the effects of mergers and interactions on the molecular gas and star formation within these systems. In particular, these observations were used to study the physical state of both the cold and warm molecular gas in M51 and NGC 4038/39, along with the physical processes affecting the molecular gas, such as photon dominated regions (PDRs) and mechanical heating.

In Chapter 2, I presented observations of the molecular gas tracers CO ($J = 4-3$ to $J = 8-7$ and [CI] (^{3}P$_1$–^{3}P$_0$ and ^{3}P$_2$–^{3}P$_1$) in the Antennae (NGC 4038/39) obtained using the *Herschel* Spectral and Photometric Imaging REceiver (SPIRE) Fourier Transform Spectrometer (FTS), which I supplemented with ground-based observations of CO ($J = 1-0$ to $J = 3-2$). I performed both a local thermodynamic equilibrium (LTE) excitation analysis of the [CI] transitions, and a non-LTE excitation analysis of both CO and [CI] to constrain the physical state of the molecular gas across the system, particularly in the nucleus of NGC 4038, the nucleus of NGC 4039 and the overlap region. I found that in all three regions, CO and [CI] emission can be modelled with two-components: a cold ($T_{kin} \sim 15-30\,\mathrm{K}$), moderately dense ($n(\mathrm{H_2}) \sim 10^{2.9}-10^{4.4}\,\mathrm{cm^{-3}}$) component, and a warm ($T_{kin} \gtrsim 200\,\mathrm{K}$), dense component ($n(\mathrm{H_2}) \gtrsim 10^{4.0}\,\mathrm{cm^{-3}}$). There is little variation in these parameters across the system, except that the density of the warm component is greater in the nucleus of NGC 4038 ($n(\mathrm{H_2}) > 10^{4.75}\,\mathrm{cm^{-3}}$) than in the overlap region ($n(\mathrm{H_2}) < 10^{4.75}\,\mathrm{cm^{-3}}$). In all three regions, I found that both mechanical heating and heating due to PDRs are sufficient to explain the warm molecular gas. This in turn suggests that both processes play an important role in the physical state of the molecular gas within the Antennae.

In Chapter 3, I presented *Herschel* SPIRE-FTS observations of CO ($J = 4-3$ to $J = 7-6$) and [CI] ($^3\mathrm{P}_1{-}^3\mathrm{P}_0$ and $^3\mathrm{P}_2{-}^3\mathrm{P}_1$) in the Whirlpool Galaxy (M51), which I supplemented with ground based observations of CO from literature. For the analysis, I separated the galaxy into 3 regions based on the schematic from Parkin et al. (2013): the nucleus, centre and arm/inter-arm regions. For each region, I performed a two-component non-LTE excitation analysis. In the nucleus, centre and arm/inter-arm regions, most of the molecular gas is in a cold ($T_{kin} \sim 20-40\,\mathrm{K}$), moderately dense ($n(\mathrm{H_2}) \sim 10^{2.9}-10^{3.8}\,\mathrm{cm^{-3}}$) component, while a small fraction ($\sim 0.2-0.3\%$) is in a warm ($T_{kin} \sim 40-180\,\mathrm{K}$), dense ($n(\mathrm{H_2}) \sim 10^{4.9}-10^{6.6}\,\mathrm{cm^{-3}}$) component. PDR modelling of the CO line ratios along with the far-infrared luminosity suggests that most of the cold molecular gas is in PDRs with a field strength $G_0 \sim 100$, where G_0 is in units of the Habing field.

Finally, in Chapter 4, I reported on high resolution observations of the dense ($n(\mathrm{H_2}) \gtrsim 10^4\,\mathrm{cm^{-3}}$) molecular gas tracers HCN, HNC, and $\mathrm{HCO^+}$ in the Antennae (NGC 4038/39) using ALMA. Emission of all three molecules was mapped in the $J = 1-0$ transition, and these were the first detections of this transition in the Antennae for $\mathrm{HCO^+}$ and HNC. I supplemented these observations with observations of CO $J = 1-0$ from literature, which traces the total molecular gas content. I found that the ratio of the luminosities of HCN and CO ($L_{\mathrm{HCN}}/L_{\mathrm{CO}}$) is higher in the nucleus of NGC 4038 and the nucleus of NGC 4039 ($L_{\mathrm{HCN}}/L_{\mathrm{CO}} \sim 0.07-0.08$) than in the overlap region ($L_{\mathrm{HCN}}/L_{\mathrm{CO}} \lesssim 0.05$), which indicates that the fraction of molecular gas which is dense is lower in the overlap region than in either nucleus. Furthermore, I argued that this was due to an increase in the pressure due to the stellar potential within the two nuclei. The ratio of $L_{\mathrm{HNC}}/L_{\mathrm{HCN}}$, on the other hand, is nearly constant across the system ($L_{\mathrm{HNC}}/L_{\mathrm{HCN}} \sim 0.3-0.4$), which suggests that mechanical heating accounts for $\gtrsim 5\%$ of the total heating budget for the molecular gas throughout the Antennae. Finally, the ratio of $L_{\mathrm{HCN}}/L_{\mathrm{HCO+}}$ is highest in the nucleus of NGC 4038, followed by the nucleus of NGC 4039, and then the overlap region. In the overlap region, this decrease in the ratio of $L_{\mathrm{HCN}}/L_{\mathrm{HCO+}}$ can be explained by an increase in the cosmic ray rate from supernova in the overlap region. Furthermore, I suggested that the decrease in the ratio in NGC 4039 could be explained by an increase in the cosmic ray rate from a hidden active galactic nucleus; however, I provided no additional evidence for its existence.

A number of conclusions can be drawn from this study. First, the physical state of the cold component in both M51 (Chapter 3) and NGC 4038/39 (Chapter 2) is similar: in both systems, the cold component temperature is

$\sim 20\,\mathrm{K}$, with a density of $\sim 10^3 - 10^4\,\mathrm{cm}^{-3}$. In fact, similar characteristics are seen in the nearby starburst galaxy M82 (Kamenetzky et al., 2012), while the cold component temperature is warmer ($\sim 35 - 70\,\mathrm{K}$) in the nearby Ultra Luminous Infrared Galaxy (ULIRG) Arp 220 (Rangwala et al., 2011), which is also a late stage merger. This suggests that the properties of the cold molecular gas in star formation-dominated systems are quite similar.

Differences within NGC 4038/39, and between NGC 4038/39 and M51 arise when comparing the warm component of both systems. In NGC 4038/39, we find that both the density of the warm component from Chapter 2, and the dense molecular gas fraction from Chapter 4 is greater in the nucleus of NGC 4038 than in the overlap region. I argue in Chapter 4 that the increased dense gas fraction is due to the increased stellar potential in the nucleus of NGC 4038; however, this may also explain the higher density found in the nucleus of NGC 4038. Furthermore, the density of the molecular gas in the warm component in M51 is comparable to the nucleus of NGC 4038, while the temperature is lower in M51. In both systems, I found that it is likely that most of the molecular gas is found in PDRs, while in NGC 4038/39 I found the mechanical heating is contributing an appreciable amount to the total heating budget of the molecular gas in the system. While I do not calculate the contributions from mechanical heating in M51, it is highly unlikely to exhibit as large a fraction as I found in NGC 4038/39. This difference could explain the temperature difference between the two warm components as only a $\sim 10\%$ contribution to the total heating is required to increase temperatures $> 100\,\mathrm{K}$ in PDRs (Kazandjian et al., 2012, 2015).

5.1 Future Work

ALMA is a powerful observatory with which to study molecular gas in the nearby universe. Its high resolution, high sensitivity and large total spectral range will make it fundamental in the study of star formation and molecular gas at all redshifts. As such, much of the future work in studying molecular gas in merging and interacting galaxies within the nearby universe involves using ALMA to its full potential.

The work in Chapter 4 is a first step in understanding and studying the dense molecular gas in the Antennae; however, the data set presented has not been exhausted. The analysis presented in Chapter 4 focused on the brightest and largest regions in the Antennae. Using a cloud identification program, such as CPROPS (Rosolowsky & Leroy, 2006), a cloud-by-cloud analysis can be done at the native resolution of the ALMA maps for HCN and HCO^+ dense molecular gas tracers. For clouds with sufficient signal to noise, the virial mass can be calculated, which can then be compared to the HCN and HCO^+ emission to determine conversion factors for both tracers, similar to what has been done in the past for CO. Furthermore, a cloud-by-cloud analysis will help further identify any variations in the properties of the dense molecular gas in the Antennae.

ALMA can be used to observe more transitions of the dense molecular gas tracers presented in Chapter 4 in the Antennae and other sources. As part of their program to observe CO $J = 3-2$ in the overlap region using ALMA, Whitmore et al. (2014) observed the $J = 4-3$ transition for HCN and HCO^+; however, the data itself is currently unpublished. The $J = 3-2$ transitions of these tracers lie within ALMA Band 6, while the $J = 5-4$ transitions lies in ALMA Band 7. By combining observations of these transitions with my observations of the $J = 1-0$ of HCN and HCO^+, it would be possible to apply a similar non-LTE excitation analysis as used in Chapters 2 and 3 to determine the physical state of the dense molecular gas within the Antennae. Furthermore, the resolution of these ALMA observations provides the tools necessary to study variations within, say, the overlap region or the nucleus of NGC 4038, as opposed to comparing the regions as a whole as done in Chapter 2. Once again, using CPROPS, this analysis could be done on a cloud-by-cloud basis. Furthermore, as more CO transitions are observed in the Antennae, the same method could be applied to the CO at higher resolutions.

Beyond the dense gas tracers and CO, it has been suggested that [CI] could be a better tracer of the total molecular gas content (Papadopoulos et al., 2004), while recent simulations have been used to try to constrain a [CI]-to-H_2 conversion factor (e.g. see Offner et al. 2014). The two [CI] transitions discussed in Chapters 2 and 3, at 492 GHz and 809 GHz, lie within the observable frequency range of ALMA. Observations of the ${}^3P_1-{}^3P_0$ transition, the lower energy transition, in the Antennae, and other nearby galaxies, could be used to constrain the [CI]-to-H_2 conversion factor in a wide variety of environments. It is well known that the value for the CO-to-H_2 conversion factor varies by about an order of magnitude between the Milky Way and more extreme ULIRGs (e.g. see Bolatto et al. 2013), while this may not be the case for [CI]. Furthermore, by combining observations of both [CI] transitions, a high resolution LTE analysis could be used to look for temperature variations.

Finally, in both Chapters 3 and 4, I discussed CO tracing both diffuse and dense molecular gas, as found in M51 by Pety et al. (2013). In their study, they used high-resolution, flux-recovered observations of CO $J = 1-0$ in M51, while such observations of NGC 4038/39 do not exist: the observations by Wilson et al. (2000, 2003) of CO $J = 1-0$ of the Antennae are not flux-recovered. As a first step, ALMA can be used to observe CO $J = 1-0$ in the Antennae at subarcsecond resolutions, while the ALMA Compact Array can be used in addition to produce flux-recovered observations. By using a cloud identification program, such as CPROPS, the emission associated with relatively dense super giant molecular complexes can be subtracted from the total map to determine how much of the CO emission is not associated with relatively dense clouds. Furthermore, such a map can be compared to my dense molecular gas tracer maps from Chapter 4 to see how the distribution of the dense molecular gas fractions varies both in right ascension and declination within the Antennae, and along the velocity dimension of data cubes.

For the first time, ALMA provides us with an opportunity to study molecular gas tracers other than CO in a wide variety of merging and interacting galaxies. Observations of [CI] may provide better estimates of the total molecular gas mass within systems; constraining the [CI]-to-H_2 will be useful for determining molecular gas mass for unresolved and/or high-redshift sources. Furthermore, HCN, HNC and HCO^+ are useful in constraining the dense molecular gas mass in extra-galactic sources, while their relative line strengths provide a useful tool for studying molecular gas heating in these sources. In both nearby sources and beyond, understanding what physical processes are affecting the molecular gas in complicated systems such as mergers and interactions is fundamental in understanding the entire merger process.

Bibliography

Bolatto, A. D., Wolfire, M., & Leroy, A. K. 2013, ARA&A, 51, 207

Kamenetzky, J., Glenn, J., Rangwala, N., et al. 2012, ApJ, 753, 70

Kazandjian, M. V., Meijerink, R., Pelupessy, I., Israel, F. P., & Spaans, M. 2012, A&A, 542, A65

—. 2015, A&A, 574, A127

Offner, S. S. R., Bisbas, T. G., Bell, T. A., & Viti, S. 2014, MNRAS, 440, L81

Papadopoulos, P. P., Thi, W.-F., & Viti, S. 2004, MNRAS, 351, 147

Parkin, T. J., Wilson, C. D., Schirm, M. R. P., et al. 2013, ApJ, 776, 65

Pety, J., Schinnerer, E., Leroy, A. K., et al. 2013, ApJ, 779, 43

Rangwala, N., Maloney, P. R., Glenn, J., et al. 2011, ApJ, 743, 94

Rosolowsky, E., & Leroy, A. 2006, PASP, 118, 590

Whitmore, B. C., Brogan, C., Chandar, R., et al. 2014, ApJ, 795, 156

Wilson, C. D., Scoville, N., Madden, S. C., & Charmandaris, V. 2000, ApJ, 542, 120

—. 2003, ApJ, 599, 1049